A Mixed-Mode GPS Network Processing Approach for Volcano Deformation Monitoring

By

Volker Janssen

Dipl.-Ing., University of Bonn, Germany, 1997

A thesis submitted to The University of New South Wales
in partial fulfilment of the requirements for the degree of
Doctor of Philosophy

School of Surveying and Spatial Information Systems
The University of New South Wales
Sydney NSW 2052, Australia

July 2003

UNIVERSITY OF NEW SOUTH WALES
Thesis/Project Report Sheet

Surname or Family name: JANSSEN
First name: Volker Other name/s:
Abbreviation for degree as given in the University calendar: Ph.D.
School: School of Surveying and Spatial Information Systems Faculty: Engineering
Title: A Mixed-Mode GPS Network Processing Approach for Volcano Deformation Monitoring

Abstract 350 words maximum:

Ground deformation due to volcanic magma intrusion is recognised as an important precursor of eruptive activity at a volcano. The Global Positioning System (GPS) is ideally suited for this application by being able to measure three-dimensional coordinate changes of the monitoring points over time. Due to the highly disturbed ionosphere in equatorial regions, particularly during times of maximum solar activity, a deformation monitoring network consisting entirely of single-frequency GPS receivers cannot deliver baseline solutions at the desired accuracy level. In this thesis, a mixed-mode GPS network approach is proposed in order to optimise the existing continuous single-frequency deformation monitoring system on the Papandayan volcano in West Java, Indonesia. A sparse network of dual-frequency GPS receivers surrounding the deformation zone is used to generate empirical ‘correction terms’ in order to model the regional ionosphere. These corrections are then applied to the single-frequency data of the inner network to improve the accuracy of the results by modelling the residual atmospheric biases that would otherwise be neglected.

This thesis reviews the characteristics of existing continuously operating GPS deformation monitoring networks. The UNSW-designed mixed-mode GPS-based volcano deformation monitoring system and the adopted data processing strategy are described, and details of the system’s deployment in an inhospitable volcanic environment are given. A method to optimise the number of observations for deformation monitoring networks where the deforming body itself blocks out part of the sky, and thereby significantly reduces the number of GPS satellites being tracked, is presented. The ionosphere and its effects on GPS signals, with special consideration for the situation in equatorial regions, are characterised. The nature of the empirically-derived ‘correction terms’ is investigated by using several data sets collected over different baseline lengths, at various geographical locations, and under different ionospheric conditions. Data from a range of GPS networks of various sizes, located at different geomagnetic latitudes, including data collected on Gunung Papandayan, were processed to test the feasibility of the proposed mixed-mode deformation monitoring network approach. It was found that GPS baseline results can be improved by up to 50% in the midlatitude region when the ‘correction terms’ are applied, although the performance of the system degrades in close proximity to the geomagnetic equator during a solar maximum.

Declaration relating to disposition of project report/thesis

....
Signature Witness Date

FOR OFFICE USE ONLY Date of completion of requirements for Award

Registrar and Deputy Principal

THIS SHEET IS TO BE GLUED TO THE INSIDE FRONT COVER OF THE THESIS

ABSTRACT

Ground deformation due to volcanic magma intrusion is recognised as an important precursor of eruptive activity at a volcano. The Global Positioning System (GPS) is ideally suited for this application by being able to measure three-dimensional coordinate changes of the monitoring points over time. Due to the highly disturbed ionosphere in equatorial regions, particularly during times of maximum solar activity, a deformation monitoring network consisting entirely of single-frequency GPS receivers cannot deliver baseline solutions at the desired accuracy level. In this thesis, a mixed-mode GPS network approach is proposed in order to optimise the existing continuous single-frequency deformation monitoring system on the Papandayan volcano in West Java, Indonesia. A sparse network of dual-frequency GPS receivers surrounding the deformation zone is used to generate empirical 'correction terms' in order to model the regional ionosphere. These corrections are then applied to the single-frequency data of the inner network to improve the accuracy of the results by modelling the residual atmospheric biases that would otherwise be neglected.

This thesis reviews the characteristics of existing continuously operating GPS deformation monitoring networks. The UNSW-designed mixed-mode GPS-based volcano deformation monitoring system and the adopted data processing strategy are described, and details of the system's deployment in an inhospitable volcanic environment are given. A method to optimise the number of observations for deformation monitoring networks where the deforming body itself blocks out part of the sky, and thereby significantly reduces the number of GPS satellites being tracked, is presented. The ionosphere and its effects on GPS signals, with special consideration for the situation in equatorial regions, are characterised. The nature of the empirically-derived 'correction terms' is investigated by using several data sets collected over different baseline lengths, at various geographical locations, and under different ionospheric conditions. Data from a range of GPS networks of various sizes, located at different geomagnetic latitudes, including data collected on Gunung Papandayan, were processed to test the feasibility of the proposed mixed-mode deformation monitoring network approach. It was found that GPS baseline results can be improved by up to

50% in the mid-latitude region when the ‘correction terms’ are applied, although the performance of the system degrades in close proximity to the geomagnetic equator during a solar maximum.

TABLE OF CONTENTS

1. INTRODUCTION

2. VOLCANO DEFORMATION MONITORING WITH GPS

3. OPTIMISING THE NUMBER OF DOUBLE-DIFFERENCED OBSERVATIONS FOR GPS NETWORKS IN SUPPORT OF DEFORMATION MONITORING APPLICATIONS

4. IONOSPHERIC CORRECTIONS TO IMPROVE GPS-BASED VOLCANO DEFORMATION MONITORING

5. DATA PROCESSING AND ANALYSIS

6. SUMMARY AND CONCLUSIONS

LIST OF FIGURES

Figure

LIST OF TABLES

Table

ACKNOWLEDGEMENTS

As I complete this thesis, I would like to express my sincere gratitude to those who have contributed to my study and helped to make it all possible.

First and foremost, I would like to especially thank my supervisor Prof. Chris Rizos for his encouragement, support, valuable suggestions, and patient guidance throughout my study. Much gratitude also goes to my co-supervisor Dr. Bruce Harvey. Many thanks to A/Prof. Peter Morgan for his enthusiastic advice and support.

I wish to thank all the current and former members of the Satellite Navigation and Positioning (SNAP) group at the School of Surveying and Spatial Information Systems for their support during the period this research has been conducted. Special thanks to Dr. Craig Roberts – I have truly enjoyed our very educational and productive field trips to Gunung Papandayan in Indonesia. Also many thanks to the fantastic support staff of the School for their help during my study.

I would like to gratefully acknowledge the support given to me in form of an International Postgraduate Research Scholarship (IPRS) awarded by The University of New South Wales and funding from the Australian Research Council (ARC).

My gratitude goes out to my friends and colleagues at the ITB: Dr. Hasanuddin Abidin, Prof. Joenil Kahar, Mipi Kusuma, Dudy Darmawan, Dina Sarsito, Irwan Meilano, Gamal, and the ever cheerful driver Ohan. Thanks also to the many students who volunteered their help in the field: Deni, Heri, Asep, Susilo, Irawan, Deni, Marlon and Iing.

I would also like to express my appreciation to the Director of the Volcanological Survey of Indonesia, Dr. A.D. Wirakusumah and several staff members, especially Ony Suganda, for their expert advice. Many thanks to the VSI observers Momon, Achmad and Kresno at the Papandayan volcano observatory.

The invaluable help of several local farmers during the fieldwork on the volcano is gratefully acknowledged. An extra special thanks to Sarip for his initiative, skill, responsibility and reliability during the course of this project.

Many thanks to the staff at the VSI observatory at Gunung Guntur, the staff at the LAPAN observatory in Pameungpeuk, and Astri Pusana and her husband Ferry Augusta in Pangalengan for hosting the ‘fiducial’ GPS sites.

Finally I would like to express my deepest gratitude to my parents for their love, encouragement and support during all these years.

Chapter 1

INTRODUCTION

1.1 Volcanoes and their Hazards

1.1.1 Volcanoes

A volcano can be defined as an opening in the earth's crust through which hot magma (gas-rich, molten rock) from beneath the crust reaches the surface (Tazieff & Sabroux, 1983). Frequently, gases disrupt the magma and hurl the resulting clumps of rock of various sizes into the atmosphere (or, in the case of submarine volcanoes, into the water). This debris falls back around the eruptive vent and accumulates to form a hill around the erupting crater. At the same time molten, degassed (or originally gas-poor) magma pours out as lava flows. These flows can, depending on their viscosity, the slope of the ground and the volume of output, reach varying distances from the vent (from a few metres to over 100km) before solidifying into rock.

The location of volcanoes is closely associated with plate tectonic boundaries. Most of the world's volcanoes occur along the boundaries of converging plates (the subduction zones), plate rifting zones or the boundaries of diverging plates (the spreading zones). In fact, two thirds of the world's volcanoes are situated along the Pacific plate boundary, the so-called 'Ring of Fire' (Blong, 1984). As the Pacific plate is forced down into the earth's mantle, it is dehydrated and molten rock rises through the overlying continental crust to form subduction zone volcanoes (Fig. 1.1). Subduction zone volcanoes are of special interest because, while they do not erupt as frequently and as long as rift or spreading zone volcanoes, they produce the most explosive eruptions and are generally located in densely populated areas, such as in the Indonesian archipelago. Other well-known volcanoes, such as the Hawaiian Island chain, occur due to the location of a hotspot deep in the earth's mantle, feeding magma to the surface through the overlying plate.

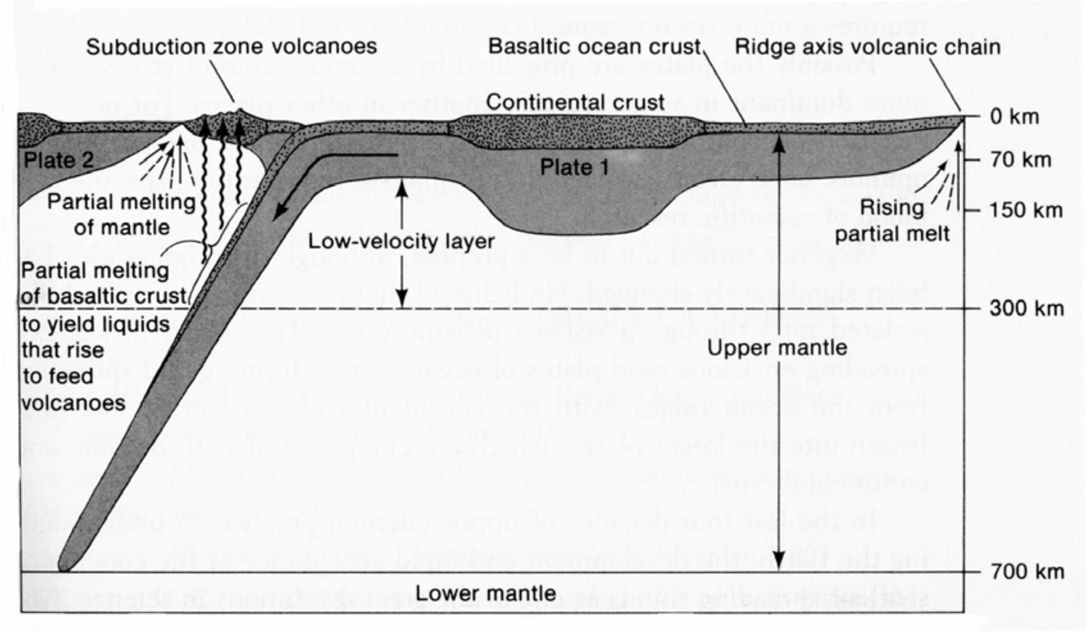

Fig. 1.1: The formation of subduction zone volcanoes (Decker & Decker, 1997)

Volcanoes appear in different shapes and sizes, and are categorised as active, dormant or extinct. However this classification is based on records obtained during a very short time, in geological terms, and can be misleading because officially extinct volcanoes may suddenly become active after several hundreds or even thousands of years of repose. The eruptions of Mt. Lamington in Papua New Guinea (1951), Mt. Arenal in Costa Rica (1968) and Helgafell in Iceland (1973) are examples of such behaviour (Tazieff & Sabroux, 1983). As historical records suggest that over 1300 separate volcanoes have erupted somewhere on the earth in the past 10,000 years, all those volcanoes showing some activity during this period are identified as *historically active* or *Holocene volcanoes* (Simkin & Siebert, 2000).

The size of a volcanic eruption can be estimated in a number of ways. For example, by the total volume of erupted products (magnitude), by the volumetric or mass rate at which these products left the vent (intensity), by the area over which the products are distributed (dispersive power), by the explosive violence or by the destructive potential of the eruption (Blong, 1984). The volcanic explosivity index (VEI) introduced by Newhall & Self (1982) provides a simple descriptive measure of the size of an eruption. This index combines the total volume of eruptive material, the height of the eruption cloud, duration of the main eruptive phase and several descriptive terms into a simple logarithmic scale of increasing explosivity ranging from 0-8. It is interesting to note that of all the historic eruptions only the 1815 eruption of Tambora (Indonesia) has been assigned a VEI of 7, while there are no recorded VEI 8 eruptions. The well-known and widely documented eruption of Mount St. Helens (USA) in 1980 has been assigned a VEI of 5.

1.1.2 Volcanic Hazards

Volcanic activity can cause several hazards (Fig. 1.2). The most prominent of these are briefly described in this section.

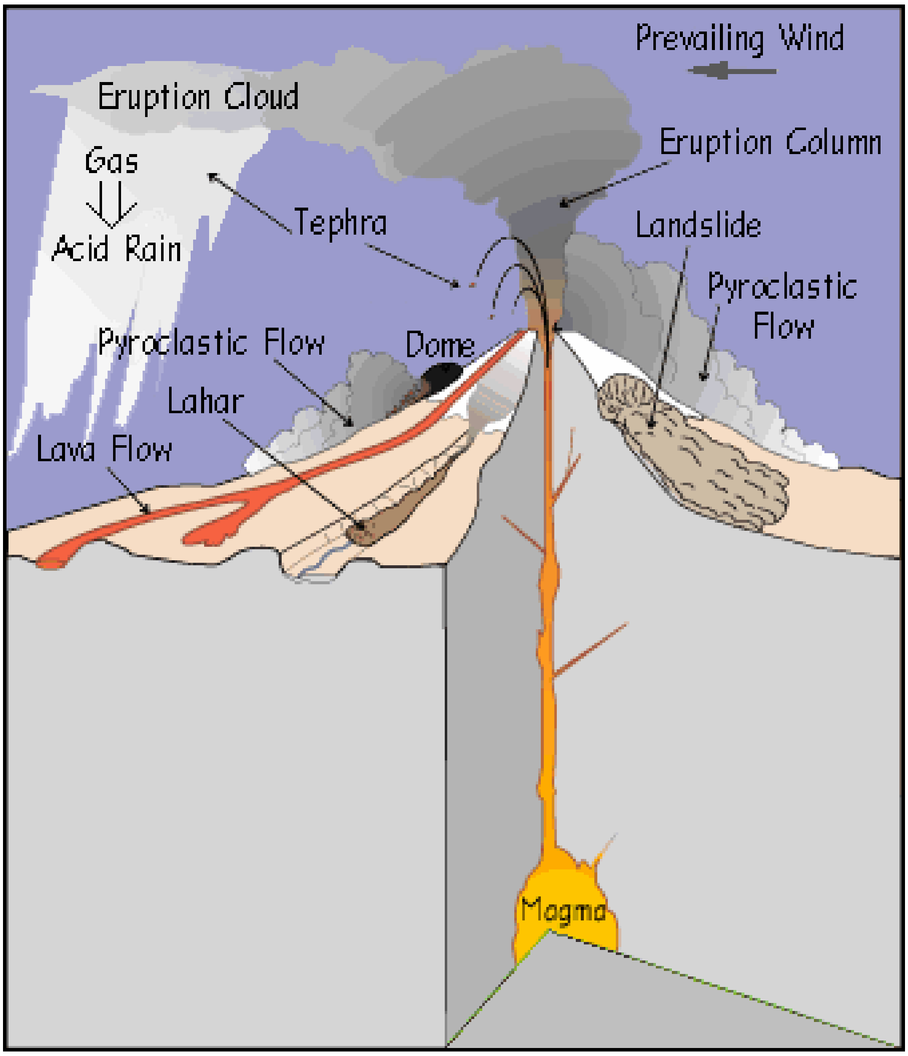

Fig. 1.2: Schematic diagram of volcanic hazards (USGS, 2002d)

Tephra Falls

Tephra is a general term for fragments of volcanic rock and lava regardless of size that are blasted into the air by explosions, or carried upward by hot gases during an eruption. Such fragments range in size from less than 2mm (ash) to several metres in diameter. Large-sized tephra (so-called volcanic bombs) typically fall back to the ground close to the volcano, but may be projected kilometres from the source. Progressively smaller fragments are carried away from the vent by wind. A large eruption cloud can produce impenetrable darkness and poses a significant threat to aircraft (Gourgaud et al., 1989). Volcanic ash, the smallest tephra fragments, can travel hundreds to thousands of kilometres downwind from a volcano. Accumulated ash falls can cause roofs to collapse and bury whole structures.

Lava Flows

Lava flows are streams of molten rock (temperatures ranging from 750-1200°C) that pour or ooze from an erupting vent. They destroy everything in their path, but usually move slow enough not to be a threat to human life. The speed of an advancing lava flow is primarily a function of the type of lava erupted and its viscosity, the ground slope over which it travels and the effusion rate at the vent, ranging from a few tens of m/h, up to 50km/h in extreme cases. The two most common types of lavas are the *aa* and *pahoehoe* lavas, both of which are Hawaiian terms. Aa lava is relatively viscous and is characterised by a rubble of broken lava blocks on its surface as it flows downslope. Pahoehoe lava flows are generally thinner and move more quickly, sometimes crusting over and creating lava tubes, which transport the lava even further from the source. Once cooled, pahoehoe flows form a smooth-to-wrinkled surface of solid rock.

Pyroclastic Flows

Pyroclastic flows (also known as *nuée ardentes*) are high-density mixtures of hot, dry rock fragments and hot gases that move away from the vent that erupted them at speeds which can exceed 200km/h. They are among the most potentially dangerous and destructive types of volcanic activity as they occur suddenly and progress very rapidly, and are capable of wiping out towns as far as 100km distant from the volcano (Murray et al., 2000).

Lahars

The Indonesian term *lahar* refers to a volcanic mudflow, a flowing mixture of water-saturated ash, mud and debris that moves downslope under the force of gravity. Lahars can cover distances of up to several tens of kilometres in a short time and originate in many ways. They can occur when heavy rains wash down loose ash or when an earthquake dislodges a steep slope of clay and rocks that have been weathered by volcanic gas vents and hot springs. They can also be generated when an eruption ejects a crater lake or rapidly melts the snow and ice on a volcano's high summit.

Earthquakes and Ground Deformation

Earthquakes can be defined as either tectonic or volcanic. Tectonic earthquakes are typically much larger in magnitude and are easily distinguished using seismic observations. Volcanic earthquakes reflect magma movements inside a volcano and provide a good indication of where and when an eruption may take place. As the magma moves towards the surface, it also causes ground deformation, which can be measured in order to gather additional information on impending eruptive activity. The damaging effects of volcanic earthquakes and associated ground deformation are very localised to the volcano.

Tsunamis

Tsunami is a Japanese name for a great sea wave produced by a submarine earthquake or volcanic eruption. It can reach open ocean travel rates of more than 800km/h and wave heights exceeding 30m can be experienced on the coast (Blong, 2000). Tsunamis were responsible for the deaths of approximately 36,000 people following the violent 1883 eruption of Krakatau Island in the Sunda Strait, Indonesia (Simkin & Siebert, 1994).

Gases

Magma contains dissolved gases that are released into the atmosphere during eruptions. Gases are also released from magma that either remains below ground (for example, as an intrusion) or is rising toward the surface. In such cases, gases may escape continuously into the atmosphere from the soil or volcanic vents. While the well-known smell of sulphur dioxide at active volcanoes is noxious, it usually does not pose a threat. However, the tragic example of the sudden release of carbon dioxide at Lake Nyos, Cameroon in 1986 showed that other gases can be lethal. The released carbon dioxide (a colourless, odourless gas that is heavier than air) accumulated into a cloud of an estimated one km^3 in volume and flowed down the valley below the crater, killing approximately 1700 people and 3000 head of cattle (Decker & Decker, 1997).

While a number of factors may influence the degree of hazard presented by the various forms of volcanic activity, the most important are the distance travelled from the volcano and the area covered, the velocity, the temperature, the length of warning and the frequency of occurrence (Blong, 1984). Pyroclastic flows, lahars and tephra falls are regarded as the most dangerous hazards. To a limited extent, lava flows can be redirected away from populated areas by constructing earth banks and reinforced concrete canals to steer their flow. Improved building standards can reduce the effects of earthquakes and accumulated ash on rooftops.

From the above summary it is evident that volcano hazards pose a significant threat to the ever-increasing population inhabiting areas around active volcanoes. In order to reduce the risk to human life and infrastructure stemming from volcanic activity, it is therefore necessary to monitor volcanoes in some way. Volcano monitoring systems can provide data that can be used by volcanologists and public health administrators to issue warnings in the event of ‘abnormal’ behaviour that may signal an imminent eruption, hence contributing to volcanic hazard mitigation and disaster risk management. The use of ground deformation measurements for this purpose will be described in section 2.2.

1.2 The Global Positioning System

According to Wooden (1985) “the NAVSTAR Global Positioning System (GPS) is an all-weather, space-based navigation system under development by the U.S. Department of Defense to satisfy the requirements for the military forces to precisely determine their position, velocity, and time in a common reference system, anywhere on or near the earth on a continuous basis.” GPS has been under development since 1973 and has been fully functional since the mid-1990s. It can be partitioned into three segments, the space segment, control segment and user segment. Technical details about GPS can be found in a large number of textbooks and reports. This section only presents a brief overview.

The *space segment* nominally consists of 24 satellites arranged in six orbital planes of approximately 20,200 km altitude above the earth's surface. Each plane is inclined about 55° to the equator and hosts four satellites (Fig. 1.3). The satellite orbits are almost circular and the orbital period is half a sidereal day (approximately 11 hours and 58 minutes in length). This design provides global coverage with at least four satellites simultaneously visible anywhere on earth at any given time. At present 27 GPS satellites are operational (USCG, 2003).

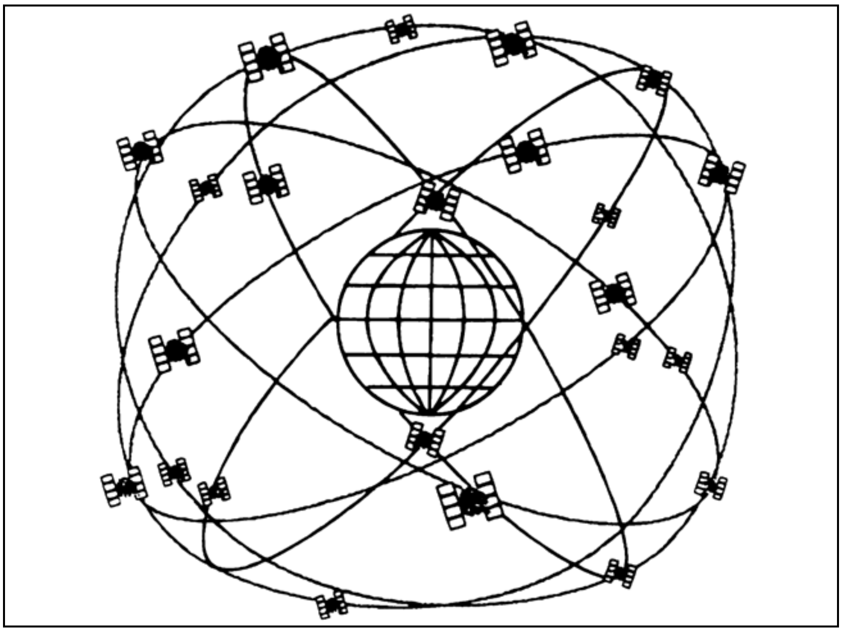

Fig. 1.3: Schematic view of the GPS satellite constellation (Parkinson & Spilker, 1996)

The satellites continuously transmit a signal on two L-band frequencies of the electromagnetic spectrum, namely L1 = 1575.42 MHz (corresponding to a wavelength of 19.05cm) and L2 = 1227.60 MHz (corresponding to a wavelength of 24.45cm). In addition, two codes are generated and modulated onto these carrier waves in order to produce the pseudorange signal. The restricted Y-code is modulated onto both frequencies, while the freely available C/A-code is only present on L1. The navigation message, containing information about the satellite orbits, satellite clock corrections and satellite status, is also modulated onto the carrier waves. Figure 1.4 shows the different GPS satellite signal components.

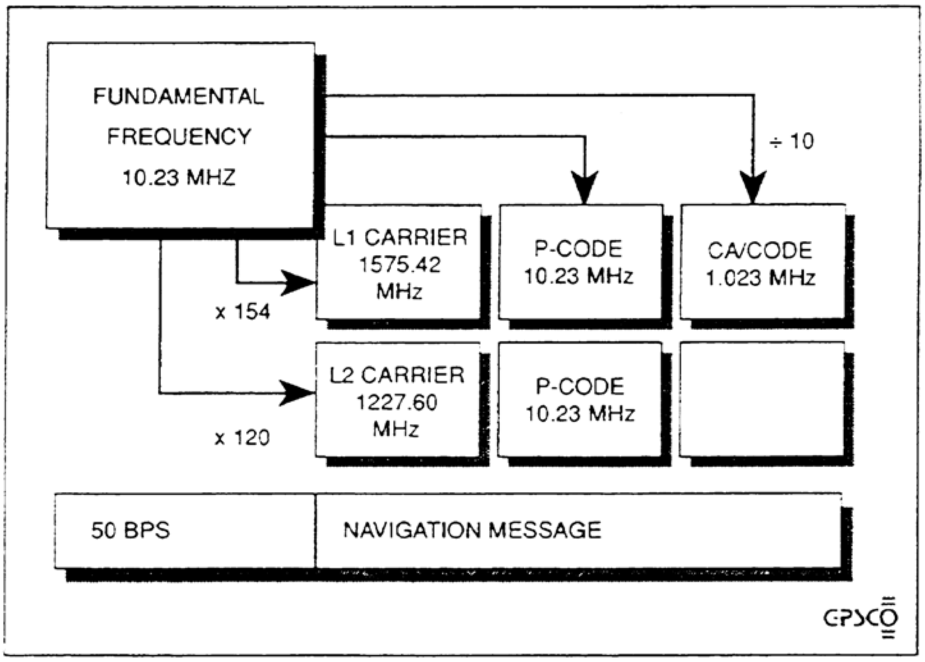

Fig. 1.4: GPS satellite signal components (Rizos, 1997)

The *control segment* comprises a network of five globally distributed monitor stations located in Hawaii, Colorado Springs, Ascension Island, Diego Garcia and Kwajalein (Fig. 1.5). The latter three are equipped with ground antennas for communication with the space segment via an S-band uplink. Colorado Springs also hosts the master control station (MCS), responsible for the overall supervision of the system. Here, GPS time is maintained by a set of atomic clocks, satellite clock corrections and ephemerides are computed from the data collected by the monitor stations, and, if necessary, actions such as satellite manoeuvering and signal encryption are initiated. Satellite orbits are expressed in the ECEF (earth-centred, earth-fixed) World Geodetic System 1984 (WGS84), and the navigation message is generated and uploaded to each satellite via the ground antennas. All stations are owned and operated by the U.S. Department of Defense. Several NIMA (National Imagery and Mapping Agency) ground stations also contribute tracking data to the MCS.

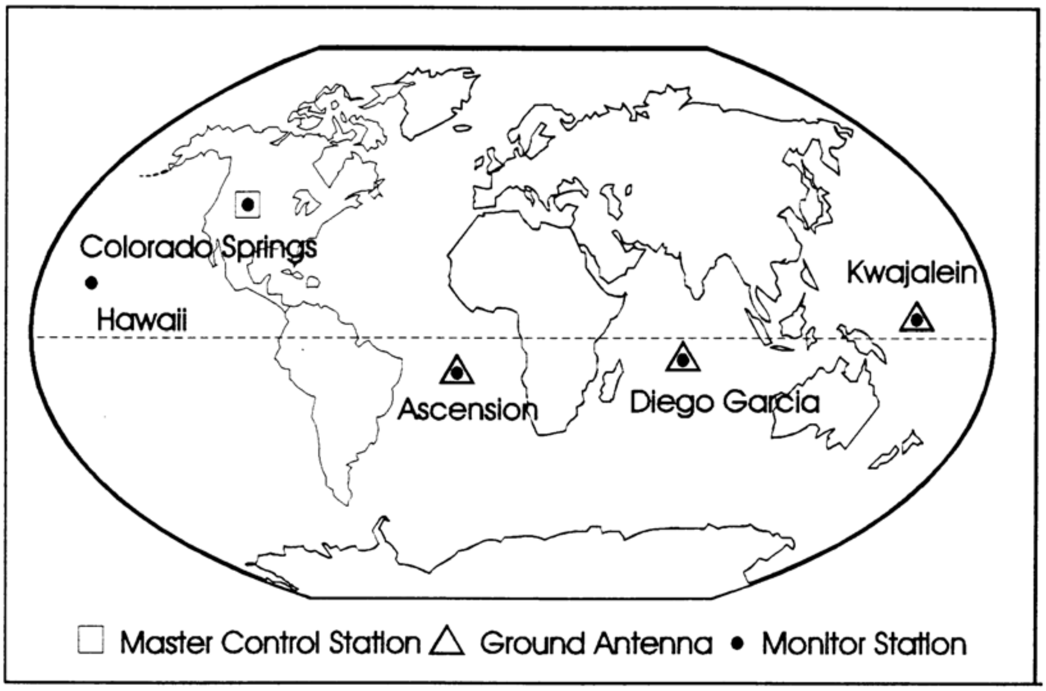

Fig. 1.5: GPS control segment

The *user segment* consists of the entire range of hardware, software and operational procedures available to collect and process GPS data by both military and civilian users. It also contains infrastructure such as civilian reference stations for differential GPS (DGPS) in order to increase the system's positioning accuracy. Although GPS was initially designed as a navigation system, nowadays a vast variety of surveying and geodetic applications have been able to utilise GPS due to advances in technology and processing procedures. These techniques make possible centimetre level accuracy using relatively low-cost equipment. A large number of reference books and monographs deal with the many different facets of GPS, both in theoretical and practical terms (see e.g. Hofmann-Wellenhof et al., 2001; Kleusberg & Teunissen, 1996; Leick, 1995; Parkinson & Spilker, 1996; Rizos, 1997; Seeber, 1993; Wells et al., 1987).

1.3 The GPS Measurements

There are two fundamental GPS measurements, namely the pseudorange observation and the carrier phase observation.

1.3.1 Pseudorange Observation

The pseudorange observable is the difference between the transmission time and the reception time of a particular satellite signal scaled by the speed of light. The receiver makes this measurement by replicating the code being generated by the satellite and determining the time offset required to make the incoming code synchronous with the code replica within the receiver. If the receiver and satellite clocks were synchronised, multiplication of the time offset (or travel time) with the speed of light yields the true range between the satellite and receiver. However, perfect synchronisation is not generally achieved. In addition, there are other errors and biases affecting the satellite signal as it propagates through the earth's atmosphere. The pseudorange observation equation can be written as (e.g. Langley, 1993):

$$PR = \rho + d\rho + c \cdot (d\delta_i - d\delta^j) + d_{ion} + d_{trop} + d_{mp}^{PR} + \varepsilon_{PR} \qquad (1\text{-}1)$$

where PR = pseudorange observation in units of metres

ρ = geometric range between receiver station and satellite

$d\rho$ = effect of satellite ephemeris error on a particular one-way observation

c = speed of light

$d\delta_i$ = receiver clock error

$d\delta^j$ = satellite clock error

d_{ion} = ionospheric delay

d_{trop} = tropospheric delay

d_{mp}^{PR} = pseudorange multipath effect

ε_{PR} = pseudorange observation noise for a particular one-way observation

The geometric range between receiver and satellite is expressed as:

$$\rho = \sqrt{(X^j - X_i)^2 + (Y^j - Y_i)^2 + (Z^j - Z_i)^2} \qquad (1\text{-}2)$$

where X^j, Y^j, Z^j = known satellite coordinates

X_i, Y_i, Z_i = receiver coordinates to be determined

Pseudorange measurements are generally used for navigation purposes. With the discontinuation of Selective Availability – the intentional degradation of the single point positioning accuracy – by order of the President of the United States at 04:00:00 UTC on 2 May 2000, the accuracy of the Standard Positioning Service increased from about 100m to less than 10m (Rizos & Satirapod, 2001). While this move was certainly welcomed by navigation users and outdoor enthusiasts, it did not have any effect on the surveying community.

1.3.2 Carrier Phase Observation

For precise applications, such as deformation monitoring and surveying, the carrier phase observable is used instead of the pseudorange. Applications in this area are generally termed *GPS surveying* or *GPS geodesy*. The carrier phase observable is a measure of the difference between the carrier signal generated by the receiver's internal oscillator and the carrier signal transmitted from a satellite. This observable is made up of an integer number of full cycles and an additional fractional part. Unfortunately a GPS receiver is not capable of distinguishing one cycle from another. It can only measure the fractional part and keep track of *changes* in the carrier phase. Hence, when a receiver first locks onto a satellite signal, the number of full cycles is initially unknown, or *ambiguous*. In order to convert the carrier phase observable into a range between the receiver and the satellite, this so-called *phase ambiguity* must be resolved or accounted for in some way (Wells et al., 1987). The carrier phase observation equation can be written as:

$$\phi = \rho + d\rho + c \cdot (d\delta_i - d\delta^j) + \lambda \cdot N - d_{ion} + d_{trop} + d_{mp}^{\phi} + \varepsilon_{\phi} \qquad (1\text{-}3)$$

where ϕ = carrier phase observation in units of metres

λ = wavelength of the carrier phase

N = integer ambiguity for a particular receiver-satellite pair

d_{mp}^{ϕ} = carrier phase multipath effect

ε_{ϕ} = carrier phase observation noise for a particular one-way observation

The remaining terms are the same as in equation (1-1). Note that the ionospheric delay for carrier phase observations has the same magnitude as for pseudorange measurements, but is of the opposite sign. In GPS processing, usually the *double-difference* observation, involving measurements from two receivers to two satellites, is formed (see sections 3.2 and 4.5). Ambiguity resolution is discussed in section 3.5.

1.4 Error Sources in GPS Positioning

Several errors impact GPS measurements and must be accounted for in order to achieve precise and reliable results.

1.4.1 Orbit Bias

The orbit bias is a satellite-dependent systematic error that can be interpreted as the 'wobbling' of a satellite along its orbit in space. Orbits are perturbed by such effects as the non-sphericity of the earth and the gravitational attraction of the Sun and Moon (gravitational effects of the other planets can be neglected). Non-gravitational effects such as solar radiation pressure, relativistic effects, solar winds and magnetic field forces also result in small perturbing accelerations on the satellite orbit.

The GPS monitor stations (within the system's control segment) track the satellites so that the MCS can use this data to generate the satellites' orbits (or ephemerides). The predicted orbits are then uploaded to the satellites and broadcast in the navigation message. These orbits are referred to as the *broadcast ephemerides*. However, in practice it is impossible to perfectly model the satellite orbits, and the difference between the predicted position of a satellite and its true position is the *satellite orbit bias*.

The International GPS Service (IGS) coordinates a global network of nearly 200 continuously operating GPS stations (see Fig. 2.3) in order to collect data for the generation of the *precise ephemerides*. The final orbits are available after 7 days and can offer considerable mitigation of the orbit bias for post-processing applications. Additionally, a range of predicted ephemerides is available for real-time applications (IGS, 2002a).

1.4.2 Clock Bias

As perfect synchronisation of the clocks with true GPS time can not be achieved in the satellites nor in the receivers, clock biases are introduced into the observations. The difference between the satellite clock time and GPS time is the *satellite clock bias*. Accordingly, the difference between the receiver clock time and GPS time is the *receiver clock bias*. While the GPS satellites are equipped with high quality cesium and rubidium atomic clocks, receivers typically use relatively inexpensive quartz oscillators whose performance characteristics are several orders of magnitude poorer. Hence, the receiver clock error is much larger than the satellite clock error. However, both biases can be eliminated by forming the double-differenced observable, as used for relative GPS positioning.

1.4.3 Ionospheric Delay

The ionosphere is that part of the earth's atmosphere located at a height of between 50–1000km above the surface. The effect of the ionosphere on the GPS signal travelling from the satellite to the receiver is a function of the Total Electron Content (TEC) along the signal path and the frequency of the signal. The TEC varies with time, season and geographic location, with the main influences on the signal propagation being the solar activity and the geomagnetic field. When propagating through the ionosphere the speed of the signal deviates from the speed of light, causing measured pseudoranges to be 'too long' compared to the geometric distance between satellite and receiver, while carrier phase observations are 'too short'. The ionospheric range error on L1 in the zenith direction can reach 30m or more, and near the horizon this effect is amplified by a factor of about three (Kleusberg & Teunissen, 1996).

The ionosphere is a dispersive medium for microwaves, i.e. the refractivity depends on the frequency of the propagating signal. Hence, measurements on both the L1 and L2 frequency can be used to account for the ionospheric effect on GPS observations by forming the so-called ionosphere-free linear combination of L1 and L2. In addition, global ionosphere maps generated from IGS data are available (AIUB, 2002). For short baselines the ionospheric effect is considered to be the same for both receivers, and therefore assumed to be eliminated by differencing the measurements taken at both receivers. However, recent studies have shown that this assumption is not always true, especially in periods of high solar activity (Janssen et al., 2001).

1.4.4 Tropospheric Delay

The troposphere is part of the lower atmosphere and stretches from the earth's surface to a height of approximately 50km, with the majority of the variability being in the first 10km (Spilker, 1996). It is a non-dispersive medium for microwaves, hence, unlike the ionosphere, its effect cannot be accounted for by a linear combination of observations on two frequencies. The tropospheric delay is dependent on temperature, atmospheric pressure and water vapour content. The type of terrain below the signal path can also have an effect. The resulting range delay varies from approximately 2m for satellites at the zenith to about 20m for satellites at 10° elevation (Leick, 1995; Seeber, 1993). The tropospheric effect can be divided into two components, the dry and the wet component. The dry component accounts for 90% of the effect and can be precisely modelled using surface measurements of temperature and pressure. However, due to the high variation in the water vapour it is very difficult to model the wet component, which contributes the remaining 10% and can play a significant part in the error budget for certain applications.

Several models based on a 'standard atmosphere' have been developed to try to account for the tropospheric delay. For example, the Hopfield model, Saastamoinen model and Black model are all routinely used in GPS processing (e.g. Mendes, 1999; Spilker, 1996). For short baselines, the tropospheric effect is considered to be the same for both receivers, and therefore assumed to be eliminated by differencing. However, for baselines involving a significant difference in receiver altitude, which is usually the case in GPS volcano deformation monitoring networks, this assumption is not realistic. Moreover, it has been suggested that an additional residual relative zenith delay parameter be estimated in such cases (e.g. Abidin et al., 1998; Dodson et al., 1996; Roberts & Rizos, 2001).

1.4.5 Multipath

Multipath occurs when a GPS signal arrives at a receiver's antenna via two or more different pathways due to reflections from nearby objects such as buildings, vehicles, trees, the ground or water surfaces (Fig. 1.6). Reflections at the satellite during signal transmission also contribute to the error, but these effects are considered to be negligible. The superposition of the delayed reflected signals and the direct line-of-sight signal leads to distortion of the received signal at the GPS antenna, and results in ranging errors of varying magnitude (Walker et al., 1998). Multipath is characterised by amplitude, time delay, phase and phase rate-of-change relative to the direct signal, and is dependent on satellite elevation and azimuth. Due to the higher risk of signal reflection, low elevation satellites are much more prone to be affected by multipath than satellites close to the station's zenith. Satellites located in a certain azimuth region might be more affected than others due to obstructive features in the antenna environment.

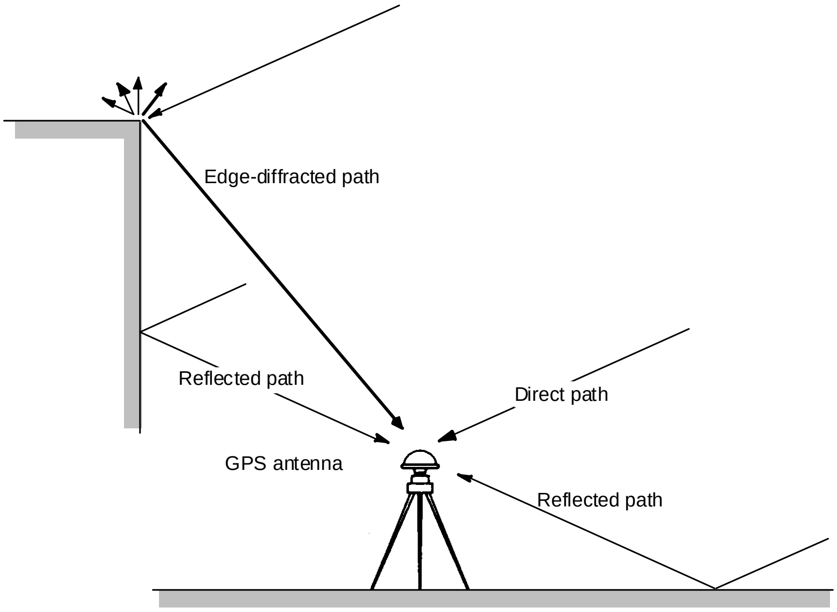

Fig. 1.6: The multipath environment around a GPS receiver

It is well known that the effect of multipath can be reduced by using choke ring antennas. Furthermore, the multipath disturbance has a periodic characteristic. If the antenna environment remains constant, the multipath situation will repeat itself every sidereal day (the sidereal day being about 236 seconds shorter than the solar day). This has led to the development of several techniques to account for the multipath signal in GPS observations (e.g. Comp & Axelrad, 1996; Han & Rizos, 1997; Hardwick & Liu, 1995; Ge et al., 2000a; Walker et al., 1998). In theory, carrier phase multipath does not exceed a quarter of the wavelength, which translates into a maximum range error of 4.8cm for the L1 carrier and 6.1cm for the L2 carrier (Georgiadou & Kleusberg, 1988; Leick, 1995). In general, multipath can be minimised by carefully choosing the GPS site location. However, cost considerations and the nature of certain applications, such as GPS deformation monitoring, where the deforming body itself can be a source of multipath, might prevent the user from observing in a multipath-free environment.

1.4.6 Antenna Phase Centre Offset and Variation

GPS measurements are referred to the electrical phase centre of the antenna, which is usually not identical to the physical antenna centre. The difference can be divided into an offset and a component which is a function of the direction of the incoming signal (e.g. Hofmann-Wellenhof et al., 2001). While the offset can be described by a constant, the antenna phase centre variation is dependent on satellite elevation and azimuth, as well as the strength of the incoming signal. Both offset and variation are different for L1 and L2. Usually, phase centre offset and variation are calibrated by the manufacturer. In addition, the U.S. National Geodetic Survey provides antenna phase centre models for various antennas (NGS, 2002). Single-differencing and high quality oscillators are used to determine the relative phase centre position and phase variations with respect to a Dorne-Margolin type T choke ring antenna as a reference (Mader & MacKay, 1996). These models can then be used to account for the effect during data processing. However, mixing antenna types in a GPS survey should be avoided if possible.

1.5 Motivation

As indicated in section 1.1, volcanoes pose a significant threat to many communities in the world, particularly in developing countries. Indonesia, for instance, leads the world in the number of historically active volcanoes (Simkin & Siebert, 2000). Of the nearly 240,000 recorded deaths caused by volcanic eruptions between 1600 and 1982, 67% occurred in Indonesia alone (Blong, 1984). An estimated 10% of Indonesia's population of over 200 million people live in close proximity to hazardous volcanoes. In total, the country is home to 129 historically active volcanoes, of which 60 are regularly monitored by the Volcanological Survey of Indonesia (VSI), the government department overseeing all volcano monitoring in Indonesia (Abidin & Tjetjep, 1996). Figure 1.7 shows the major volcanoes of Indonesia with recorded eruptions since the year 1900.

Fig. 1.7: Major volcanoes of Indonesia (SI, 2002)

One type of precursor to volcanic eruptions is the geodetic measurement of horizontal and vertical deformations of the volcano. The pattern and rate of surface movement can reveal the depth and rate of pressure increase within the underlying magma reservoir. The data obtained can contribute to volcanic hazard mitigation by providing timely ground deformation information to volcanologists.

The GPS technology has been recognised as an ideal tool for volcano deformation monitoring. It is particularly suited to monitor deformation on a *continuous* rather than *periodic* basis, thus giving more detailed information about the dynamics of the volcanic edifice. A permanent GPS network can be deployed in an inhospitable environment, utilising sophisticated telemetry equipment, to obtain continuous deformation measurements for online processing. However, for countries such as Indonesia, a low-cost approach is preferred. While the limited funds available in less developed countries restrict the number of GPS receivers that can be deployed, a large number of receivers is necessary in order to adequately monitor the volcano. In addition, the danger of losing part or all of the equipment during an eruption needs to be considered. A low-cost GPS-based volcano deformation monitoring system has been developed by the Satellite Navigation and Positioning (SNAP) group at The University of New South Wales (UNSW) in collaboration with the Department of Geodetic Engineering at the Institute of Technology Bandung (ITB) and the VSI (see Roberts, 2002).

However, all of Indonesia's volcanoes, and a large number of the world's volcanoes, are located in the equatorial region, an area where ionospheric disturbances have a significant impact on GPS measurements, effectively degrading the accuracy of baseline results. These effects are of concern particularly in times of maximum solar cycle activity, as experienced during the period this research has been conducted. Hence, the low-cost network of single-frequency GPS receivers on the volcano needs to be augmented by an outer framework of more sparsely distributed dual-frequency receivers. The dual-frequency receivers are used to mitigate residual biases so that this *mixed-mode* array system may deliver the sub-centimetre accuracies required for volcano deformation monitoring.

Although the main focus of this thesis is to further volcano deformation monitoring, the proposed strategy is also applicable to a wide range of other deformation monitoring tasks, such as the monitoring of tectonic faults, landslides, ground subsidence, open-cut mines, or engineering structures like dams, bridges and tall buildings.

1.6 Methodology

During the past few years a strategy has been developed for processing data collected by GPS networks consisting of a mixed set of single-frequency and dual-frequency receivers. The strategy is to deploy a few permanent, 'fiducial' GPS stations with dual-frequency, geodetic-grade receivers surrounding an 'inner' network of low-cost, single-frequency GPS receivers. Such a configuration offers considerable flexibility and cost savings for deformation monitoring applications, which require a dense spatial coverage of GPS stations, and where it is not possible, nor appropriate, to establish permanent GPS networks using dual-frequency instrumentation.

The basis of the processing methodology is to separate the dual-frequency, fiducial station data processing from the baseline processing involving the inner (single-frequency) receivers located in the deformation zone. The data processing for the former is carried out using a modified version of the Bernese software, to generate a file of 'corrections' (analogous to Wide Area DGPS correction models for the distance dependent biases – primarily due to atmospheric refraction). These 'corrections' are then applied to the double-differenced phase observations from the inner GPS receivers to improve the baseline accuracies (primarily through empirical modelling of the residual atmospheric biases that otherwise would be neglected).

The main residual atmospheric bias is the ionospheric delay. Accounting for this effect is particularly important for GPS deformation monitoring networks located in the equatorial region, where the ionosphere is most disturbed and variable (spatially and temporally). The impact of the ionosphere is most severe in periods of heightened solar sunspot activity, adversely affecting baseline accuracy for single-frequency instrumentation, even for comparatively short baselines.

A fiducial network was temporally established around Gunung Papandayan in Indonesia, the subject volcano in this thesis, to complement the low-cost volcano deformation monitoring system already installed. Algorithms were developed to integrate the 'corrections' obtained from the fiducial network into the baseline processing. An epoch-by-epoch solution in multi-baseline mode is preferred in order to detect ground deformation in near real-time. Special considerations for GPS receivers situated on the flanks of a volcano, such as the obstruction of the sky caused by the volcano itself, have to be made.

1.7 Outline of the Thesis

This thesis consists of six chapters and one Appendix.

Chapter 1 – *Introduction*. A brief description of volcanoes and their hazards is given, followed by an introduction to GPS. The fundamental GPS measurements and the error sources of GPS positioning are introduced. The factors motivating this research are summarised, an outline of the methodology is presented, and the contributions of this research are listed.

Chapter 2 – *Volcano Deformation Monitoring with GPS*. A brief history of volcano deformation monitoring using geodetic techniques is given, before the chapter focuses on the utilisation of GPS for this purpose. Permanent GPS networks are classified by type, and examples are given. The UNSW-designed GPS-based volcano deformation monitoring system is described. This single-frequency system is augmented with the addition of an outer dual-frequency network in order to form a *mixed-mode* volcano deformation monitoring system. Details of the system design, its deployment on Gunung Papandayan in Indonesia, and the data processing strategy are given.

Chapter 3 – *Optimising the Number of Double-Differenced Observations for GPS Networks in Support of Deformation Monitoring Applications*. For a number of applications the deforming body itself blocks out part of the sky, significantly reducing the number of GPS satellite signals received by the monitoring receivers. Considering the special conditions existent around a volcanic edifice, a method to optimise the number of double-differenced GPS observations by generating a set of independent double-differenced combinations is presented. Multi-baseline processing versus baseline-by-baseline processing, as well as ambiguity resolution techniques are discussed.

Chapter 4 – *Ionospheric Corrections to Improve GPS-Based Volcano Deformation Monitoring*. The ionosphere and its effects, being the primary error source on GPS signals, are characterised, with special consideration for the situation present in equatorial regions where high TEC values and severe scintillations occur. A mixed-mode GPS network processing approach is described, which accounts for the ionospheric effect by generating double-differenced ‘corrections’ from an outer dual-frequency network, and applying these ‘corrections’ to the inner single-frequency deformation monitoring network. Using several data sets collected at various geographical locations, and under different ionospheric conditions, the nature of these empirically-derived ‘correction terms’ is investigated.

Chapter 5 – *Data Processing and Analysis*. Data from several networks located in different parts of the world, including data collected on Gunung Papandayan, are analysed to show the benefits of the proposed mixed-mode GPS network processing strategy for deformation monitoring. Ionospheric ‘correction terms’ are generated using dual-frequency data, and then applied to the inner single-frequency network used for deformation monitoring. It is demonstrated how the resulting GPS baseline vectors can be used to detect ground displacements in real-time.

Chapter 6 – *Summary and Conclusions*. The final chapter of this thesis contains a summary of the research findings, conclusions and recommendations for future research.

Appendix – *The November 2002 Eruption at Gunung Papandayan*. A chronology of the November 2002 eruption and its effects on the GPS stations on the volcano is presented.

1.8 Contributions of this Research

The contributions of this research can be summarised as follows:

- A fiducial network has been designed and established to augment the single-frequency GPS volcano deformation monitoring system on Gunung Papandayan in Indonesia. The fiducial baseline lengths had to be carefully chosen in order to produce reliable ‘correction terms’, which are representative of the ionospheric conditions present within the network area, even during periods of maximum sunspot activity.

- The UNSW-designed baseline processing software has been modified in order to accommodate an epoch-by-epoch solution in multi-baseline mode, and to allow the ‘correction terms’ obtained from the dual-frequency network to be applied to the single-frequency data.

- A method to optimise the number of double-differenced observations for deformation monitoring applications, where the deforming body itself blocks out part of the sky for the GPS receivers, has been integrated into the data processing software, resulting in more reliable and precise baseline solutions.

- The nature of the empirically-derived double-differenced ‘correction terms’ has been investigated. A wide range of GPS data sets were processed, combining a variety of baseline lengths, different geographical locations, and different periods of solar activity, in order to analyse the ‘corrections’ obtained under varying conditions.

- Data from several GPS networks have been processed in order to illustrate the benefits of the proposed mixed-mode data processing strategy for deformation monitoring applications. The data sets were collected under solar maximum conditions in different geographical latitude regions, including Gunung Papandayan, and have varying fiducial baseline lengths.

Chapter 2

VOLCANO DEFORMATION MONITORING WITH GPS

2.1 Introduction

Volcanoes are an awesome display of Nature’s power. In addition, volcanic explosions are often very destructive events having a massive impact on the natural and human environment. In a world of ever-growing population, more and more people live in close proximity to an active volcano. While the volcanic soil is very fertile, volcanoes also pose a significant threat to human life. The disastrous impacts of the eruptions of Tambora, Indonesia in 1815 (92,000 fatalities), Krakatau, Indonesia in 1883 (36,417 fatalities), Mt. Pel■e on the Caribbean island of Martinique in 1902 (29,000 fatalities) and, more recently, Nevado del Ruiz, Colombia in 1985 (25,000 fatalities) have emphasised this fact in an impressive and sobering manner (McGuire, 1995). It is therefore necessary to closely monitor volcanoes in order to avoid such catastrophes triggered by an eruption. The successful prediction of the extremely explosive 1991 eruption of Mt. Pinatubo in the Philippines (the second largest eruption in the 20th century) saved many thousands of lives, as 60,000 people had been evacuated on the day prior to the eruption (Newhall & Punongbayan, 1996). However, each volcano is unique and has its own characteristics and behaviour. To really understand a volcano, the researcher has to essentially ‘marry’ the volcano (Abidin, 2000, personal communication). This humorous statement illustrates the need for long-term monitoring to study the varying ‘moods’ of these beautiful, but also hazardous, giants in order to detect as early as possible any deviations from their normal behaviour.

This chapter gives a brief overview of the techniques used for volcano deformation monitoring and then focuses on the utilisation of GPS for this purpose. Different types of permanent GPS networks are described and the UNSW-designed mixed-mode GPS-based volcano deformation monitoring system is introduced.

2.2 Volcano Deformation Monitoring

When and where will the volcano erupt? This is the essential question scientists concerned with volcano monitoring have to answer, as precisely as possible. Several different techniques – such as seismic, microgravitational, geomagnetic, geodetic, chemical, thermal, hydrologic, remote sensing and visual observations – can be applied to study volcanoes (Fig. 2.1).

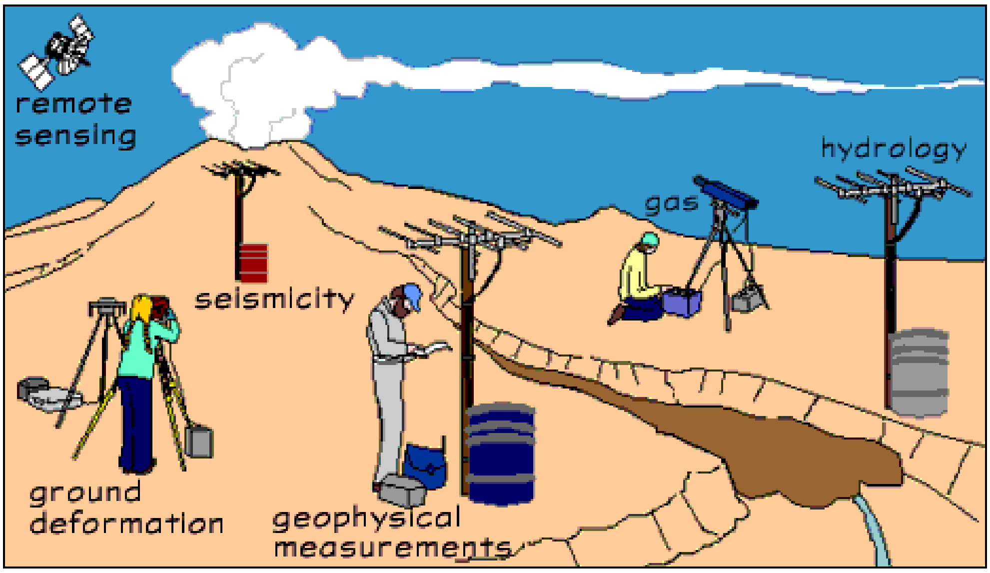

Fig. 2.1: Volcano monitoring techniques (USGS, 2002a)

Ground deformation due to volcanic magma intrusion is recognised as an important precursor of eruptive activity at a volcano. Before an eruption occurs, the ground surface generally expands due to the pressure increase within the shallow magma chamber caused by upward magmatic movements below the volcano. The trend is reversed after magma is released from the chamber causing deflation of the flanks of the volcano (Fig. 2.2). Furthermore, the pattern and rate of surface displacements reveal the depth and the rate of pressure increase within the subterranean magma chamber (Dvorak & Dzurisin, 1997), giving important information about the state of the volcano. As ground deformation tends to precede eruptions by periods of hours to months, geodetic monitoring is an effective tool for hazard mitigation. Ground deformation monitoring techniques for volcanic environments have developed from precise spirit levelling to electronic distance measuring (EDM) techniques, and more recently to the use of InSAR, and campaign-style or continuous GPS surveys.

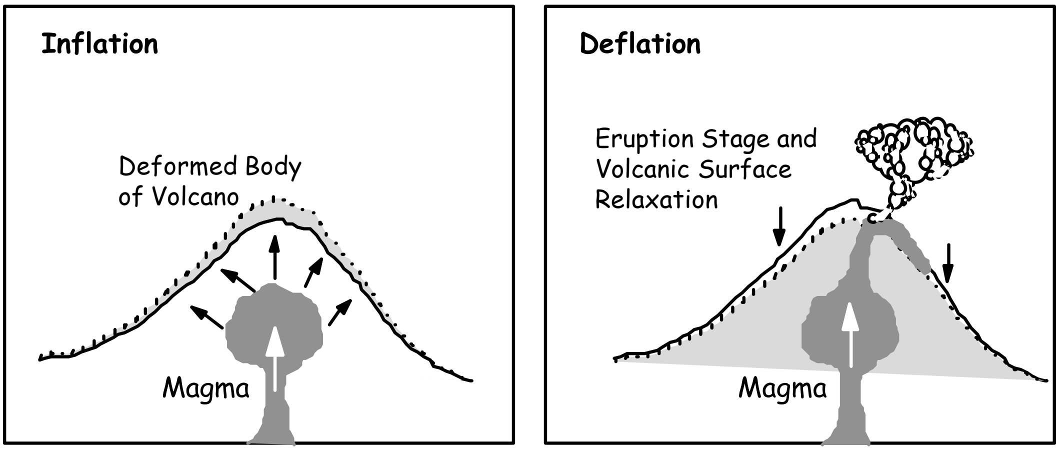

Fig. 2.2: Ground deformation caused by magmatic activity (Abidin, 1998)

Perhaps the first documented ground deformation associated with a volcanic event was the work reported by Omori (1914). His investigations indicated vertical ground displacements on the Mt. Usu volcano in Japan of up to 2 metres when conducting precise levelling surveys before and after the eruption of 1910. A 100-metre upheaval of the ground surface was also recorded close to the crater at the time of eruption.

Using elastic theory and data from several case studies, Mogi (1958) developed a mathematical model in order to determine the position and depth of a magma source based on ground deformation measurements and their locations. He assumed that the ground deformation is caused by a spherical source (magma chamber) located below a volcano edifice, which exerts hydrostatic pressure upward to the ground surface. Ibid (1958) proposed that the earth's crust behaves elastically at the time of eruption while, during the long period of deformation after the eruption, the crust behaves as a visco-elastic medium. This simple model has proven to be very effective and is still widely being used today to estimate the location of the magma source.

From the 1960s through to the 1980s, traditional surveying techniques were used for ground deformation monitoring. Generally these networks consisted of spirit levelling runs to detect vertical movements, and triangulation networks in order to determine horizontal displacements.

The introduction of electronic distance measuring (EDM) equipment enabled relatively long distances to be measured quickly and precisely. Suganda (1993) reports a 2m change of horizontal distance between points spanning the crater of the notoriously active Mt. Merapi in Indonesia from four campaigns of EDM measurements conducted between 1988 and 1992. At Mt. Unzen (Japan) EDM observations showed that the growing lava dome was expanding at a rate of 70-80cm per hour over a few days preceding the eruptive event of May 24, 1991 (GVN, 1991).

Combining several geodetic techniques further improved ground deformation monitoring. Bonasia & Pingue (1981) report on a system on Mt. Vesuvius in Italy comprising a levelling network, EDM measurements, tilt measurements, and the analysis of apparent zenith distances of the crater bottom from a fixed point located on the crater rim. Blick et al. (1989) describe a network combining angle measurements, EDM measurements and tilt measurements on Mt. Erebus in Antarctica. Even repeated steel tape measurements across cracks in the ground can provide valuable information, as reported by Swanson et al. (1983), who successfully used this technique to record episodes of accelerating growth of the Mount St. Helens lava dome between 1980 and 1982. These measurements, in conjunction with data gathered by other means, led to the prediction of 13 eruptions during this period. A comprehensive review of the various ground deformation monitoring techniques used by the staff of the Cascades Volcano Observatory for the period 1980-1990 can be found in Ewert & Swanson (1992).

With advances in GPS techniques in the 1980s it was quickly realised that GPS is well suited to monitor deformation caused by tectonic motion, ground subsidence and volcanic activity. The GPS techniques will be discussed further in section 2.3.

In recent years, interferometric synthetic aperture radar (InSAR) techniques have increasingly been used to map the topography of volcanoes and detect ground deformation. Using ERS-1 SAR images taken between 1992 and 1993, Briole et al. (1997) detected a deflation “moderate in size and amplitude” associated with the 1986-87 and 1989 lava flows on Mt. Etna, Italy. Around the vent of the New Trident volcano in Alaska, a 7-9cm uplift was observed over a 2-year period by Lu et al. (1997). Other case studies were reported by Rosen et al. (1996), Amelung et al. (2000) and Fujiwara et al. (2000). Due to the large area being covered by a single InSAR image (100km × 100km), its cost-effectiveness and ability to penetrate clouds the use of InSAR is certainly a beneficial option in complex and inaccessible terrain. However, dense vegetation and snow cover can preclude the use of InSAR as a volcano monitoring tool. Furthermore, these techniques rely on the repeat period of the satellite track (35 days in the case of ERS-1/2), which also influences the coherence of the images. Hence it is not possible to detect short-term deformation. Tobita et al. (2001) proposed a different technique using SAR amplitude images acquired from ascending and descending orbits in order to create a map of three-dimensional displacement vectors. The technique provides wide spatial coverage, delivers 3D displacement components, enables the estimation of displacement velocities and does not depend on coherence. During the 2000 Mt. Usu eruption in Japan, inflation was observed with both vertical and horizontal displacements exceeding 20m. The uplift and north-south spreading velocities were found to reach values of 3.3m/day and 2.7m/day respectively. However, this technique is less precise than InSAR and GPS, and not very sensitive to local deformation. Currently research is being undertaken in order to integrate the use of InSAR and GPS for deformation monitoring applications (e.g. Williams et al., 1998; Ge et al., 2000b; 2001; 2003; Ding et al., 2002).

Deformation monitoring techniques can be classified as being either *episodic* or *continuous* (Abidin, 1998). Episodic techniques include angle and distance measurements, levelling, InSAR and repeated GPS surveys. Instrumentation used for continuous monitoring includes tiltmeters, extensiometers, dilatometers and permanent GPS networks.

2.3 Volcano Deformation Monitoring Using GPS

GPS is well suited for monitoring volcanoes (or ground subsidence, landslide prone areas, dams, buildings, etc.) because GPS measurements can provide 3D positions at centimetre-level accuracy, unlike levelling which only produces height, or EDM which only measures distance. In addition, there is no requirement for intervisibility between stations within a GPS network. Measurements can be made independent of weather conditions, 24 hours a day and over relatively long distances. GPS has therefore many advantages over conventional geodetic techniques, considering that most of the world’s volcanoes reach high altitudes and are prone to frequent cloud cover. Furthermore, once a GPS network is installed, no human presence is needed at a potentially dangerous volcanic locale. By repeatedly measuring the same baseline vector to an accuracy commensurate to (and preferably much higher than) the expected baseline component changes due to deformation, the rate of change in the baseline components can be reliably determined (after several surveys).

Probably the first GPS survey to be carried out in a volcanic area was undertaken in Iceland during 1986 (Foulger et al., 1987). A little later, Sigmundsson et al. (1992) detected ground deformation associated with a fissure eruption at the Hekla volcano in Iceland. Marshall et al. (1997) observed ground inflation caused by dike opening at the Long Valley Caldera, California from five annual GPS campaigns between 1990 and 1994. Ground deformation caused by magma intrusion and lava discharge was detected and reported by Nishi et al. (1999) after a series of GPS campaigns were conducted on Mt. Unzen in Japan over 5 years. The study revealed ground inflation before the lava dome extrusion took place. This was followed by deflation, as the lava dome grew and created pyroclastic flows caused by frequent collapses of the lava dome. The detected ground deformation (inflation and deflation) was successfully explained by a pressure source located about 6km west of the active crater at a depth of 11km, determined using the Mogi model. At the Soufriere Hills volcano, Montserrat, a series of GPS campaigns conducted fortnightly over a period of one year revealed displacements radially symmetrical around the growing lava dome. It was concluded that the centre of pressure causing the observed ground deformation was within the dome itself rather than within a magma chamber at any significant depth beneath the volcano or within a large conduit leading to the surface (Shepherd et al., 1998). The Institute of Technology Bandung conducts regular campaigns on Gunung Guntur and Gunung Papandayan in West Java, Indonesia (Abidin et al., 1998; 2000). Local GPS campaigns are also used to monitor dome growth in conjunction with EDM distance measurements and precise levelling lines on Mt. Etna, Italy (Nunnari & Puglisi, 1994; Puglisi et al., 2001).

Numerous examples of GPS deformation monitoring networks for other applications, such as the monitoring of dams, bridges, tall buildings, etc., can be found in the literature (e.g. Duffy & Whitaker, 1999; Lovse et al., 1995; Stewart & Tsakiri, 2001; Watson & Coleman, 1998).

All of these surveys, however, are conducted in a campaign-style mode, i.e. short measurement surveys separated by long time periods, and therefore give no indication of the rate of ground movement between the campaigns. This might be suitable for quiescent volcanoes, but is certainly not sufficient for volcanoes exhibiting a higher degree of activity. Roberts (2002) summarised the disadvantages inherent in a campaign-style GPS survey approach for deformation monitoring as follows:

- Episodic surveys only provide a snapshot of the phenomenon, and are unlikely to catch an event such as an earthquake as it happens,
- stability of the monuments becomes an issue, as the geodynamic signal can be contaminated by systematic biases such as centring errors of a tripod, movement of marks due to changing local environmental conditions, or theft/vandalism of the marks themselves,
- antenna mixing introduces biases (particularly in the vertical component),
- the cost of planning and executing a GPS campaign can be the largest expense, not the cost of the instruments themselves,
- establishing in-country collaborators, and obtaining permission to work in these countries, is often time-consuming,
- equipment has to be shipped in and out of the country, and cleared in and out of customs,
- in-country observers, often inexperienced, have to be trained as GPS surveyors in intensive courses prior to a survey,
- in-country archiving of the data risks data loss in harsh environments, and
- processing of all of the data is often not completed satisfactorily until months after the data capture survey has been completed.

Most of these disadvantages can be overcome by adopting a *continuous* GPS deformation monitoring approach. The setting up of a continuous GPS infrastructure is cumbersome, but provides uninterrupted measurements of the displacement of volcano monitoring points. GPS is well suited to operate automatically in a remote environment powered by batteries and solar panels, with the logged data being transmitted to a central computing facility via a radio link.

One of the first continuous GPS networks was established in March 1988 on the Izu Peninsula in central Japan to support earthquake prediction research. Daily observations of this network led to the first GPS measurements of surface deformation as it occurred. Shimada et al. (1990) reported that, “We have, for the first time, used GPS fixed-point measurements to follow the evolution with time of the crustal movements; such measurements provide a continuous uninterrupted record of deformation.” Their results showed that the distance between two benchmarks 10km apart increased by 14.5cm during the seismic activity. This was attributed to the opening of a magma-filled fracture, which indeed fed a new eruption of the Teisha sea-floor volcano located off the coast 10 days later.

Since then several networks of continuously operating GPS receivers have been installed at volcanoes around the world, e.g. at the Long Valley Caldera, California (Dixon et al., 1997), Soufriere Hills volcano, Montserrat (Mattioli et al., 1998), and Kilauea volcano, Hawaii (Owen et al., 2000a; 2000b). Other continuous deformation monitoring applications include tectonic fault lines (Bock et al., 1997; Tsuji et al., 1995) and engineering structures such as tall buildings (Celebi & Sanli, 2002; Ogaja et al., 2001), bridges (Ashkenazi et al., 1997; Wong et al., 2001) and dams (Behr et al., 1998; Whitaker et al., 1998).

On a larger scale, permanent GPS networks can be utilised to detect global or regional tectonic plate motions and to serve as reference stations for geodetic control. Hence GPS networks can be categorised into large scale and small scale networks. Small scale networks can further be subdivided into static, kinematic and ‘low-cost’ networks (Roberts, 2002). These different *types* of continuous GPS networks are briefly discussed below.

2.3.1 Large Scale Permanent GPS Networks

Large scale permanent GPS networks cannot be used for volcano deformation monitoring. The spacing between receivers is too large and baseline results are normally obtained from 24-hour solutions, providing no information on any sub-diurnal effects. However, these networks carry out important tasks in a global and national context. Three examples, namely the IGS, GEONET and SCIGN networks, and their roles, are briefly described.

IGS Network

The International GPS Service (IGS) has coordinated the establishment of a *global* network of about 200 continuously operating dual-frequency GPS receivers (Fig. 2.3). This network is used to realise the International Terrestrial Reference Frame (ITRF), to which all GPS surveys can be connected. In addition, the IGS provides a range of products, such as GPS satellite ephemerides, earth rotation parameters, IGS tracking station coordinates and velocities, and GPS satellite and IGS tracking station clock information (IGS, 2002b). All this information is made available on their website, furthering scientific research, and aiding commercial GPS surveying.

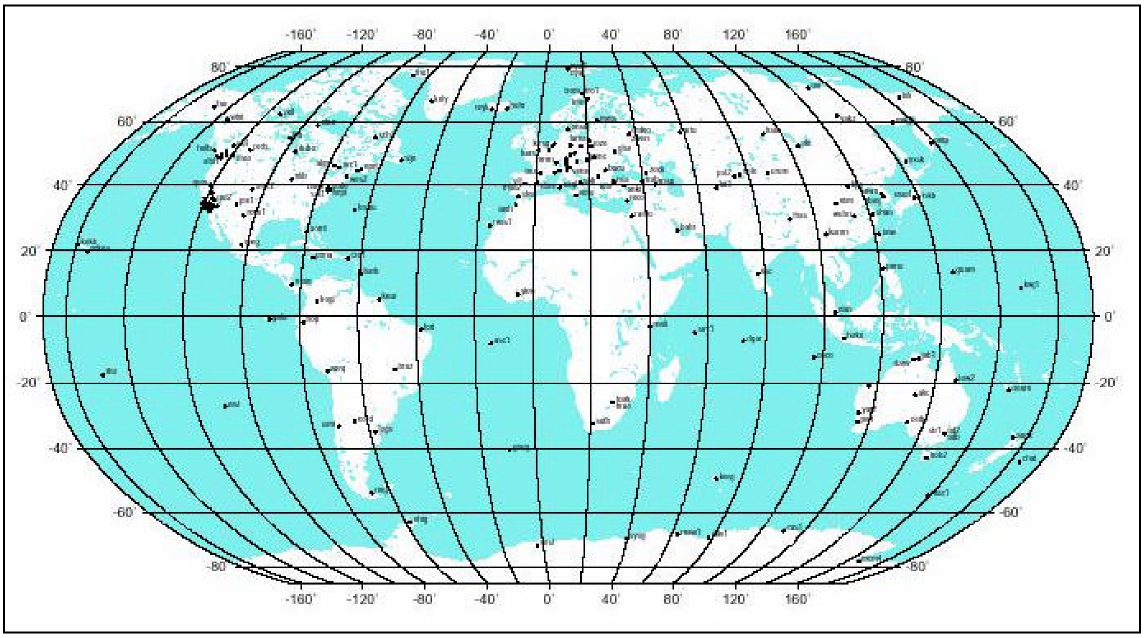

Fig. 2.3: The global IGS network (IGS, 2002b)

GEONET

Since 1994 Japan's Geographical Survey Institute (GSI) has operated the GPS Earth Observation Network (GEONET). The main purpose of this GPS array is to continuously monitor crustal deformation in order to study, and hopefully predict, earthquakes and volcanic events, as well as providing the basic geodetic control for Japan (GSI, 2002). It is the world's most dense permanent GPS network, spanning the entire country and consisting of almost 1000 GPS sites with an average spacing of about 30km (Miyazaki et al., 1997; 1998). The data collected at each station are transferred to GSI's data processing centre in Tsukuba via telephone lines. These data are processed with a cluster of workstations to yield the position of each station with an accuracy of a few centimetres or better, in a global reference frame (such as the ITRF). Daily variations of station position are monitored in order to detect any abnormal changes in estimated crustal strain that could indicate an impending earthquake or volcanic eruption. During the 1994 Hokkaido-Toho-Oki earthquake, horizontal displacements of up to 44cm were observed (Tsuji et al., 1995). Unfortunately no precursors were detected during the week preceding the event.

SCIGN

The Southern California Integrated GPS Network (SCIGN) was first established in 1990 for the purpose of continuously monitoring crustal deformation in California. Since July 2001 the network has consisted of 250 permanent GPS sites in and around the Los Angeles basin (Hudnut et al., 2001; SCIGN, 2002). Major participants in SCIGN include NASA/JPL, the U.S. Geological Survey (USGS), and the University of California San Diego, operating under the umbrella of the Southern California Earthquake Center (SCEC). GPS data are transmitted to a processing centre via telephone lines, archived and made available to the public via the internet. From 24-hour files of GPS data the coordinates of each receiver are computed to an accuracy of a few millimetres. During the 1992 Landers earthquake a maximum horizontal displacement of 48mm at a distance of 80km from the seismic rupture zone was observed (Bock et al., 1993).

The advantages of continuous GPS networks are manyfold. There is hardly any delay between surveys and coordinate results. No in-field archiving is necessary because the data is downloaded automatically and transferred to a central processing facility. Here, the data can be automatically screened, processed and archived. These networks require reliable power supply, assured communication links, and sophisticated hardware and software.

2.3.2 Small Scale Permanent GPS Networks

While large scale GPS networks can be used to detect crustal motion, smaller scale networks are necessary in order to monitor volcanoes or engineering structures such as bridges, dams or high-rise buildings. However, the development of an automatic GPS array for such small scale monitoring is an engineering and software challenge. A network of permanent GPS receivers must be deployed in an often inhospitable environment, in which they must operate reliably on a continuous basis. Power supply in remote locations becomes a big issue, with batteries and solar panels having to be used. The GPS observations must then be telemetered to a central computing facility where data processing occurs with minimum delay. Such *local* networks can be realised in different ways. Which system design is chosen usually depends on the expected amplitude and frequency of deformation, the terrain, available power sources and budget constraints.

2.3.2.1 Static Small Scale GPS Networks

A local network of continuously operating GPS receivers is well suited to monitor relatively small areas around a volcano. One of the first such networks was established by the U.S. Geological Survey (USGS) on the Augustine volcano, Alaska (Fig. 2.4). Three dual-frequency GPS receivers are used, and the baselines are measured on a weekly basis. The data are transmitted from the two remote stations on the flank and summit of the volcano to a base station for processing (USGS, 2002b).

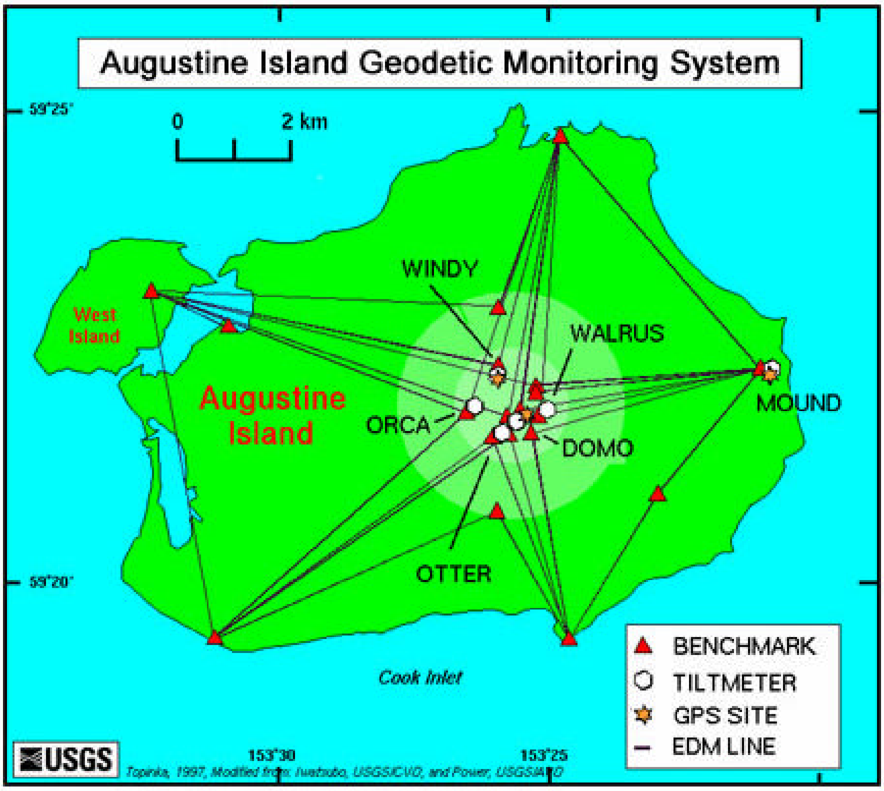

Fig. 2.4: Volcano deformation monitoring network on Augustine Island (USGS, 2002b)

The USGS also operates 16 continuous GPS sites as part of a ground deformation network to monitor the Kilauea, Mauna Loa and Mauna Kea volcanoes in Hawaii (USGS, 2002c). The network is coordinated by scientists of the Hawaiian Volcano Observatory (HVO), in collaboration with Stanford University. GPS data are sampled every 30 seconds and downloaded once a day to calculate one-day average positions. In addition, more than 100 other sites are surveyed intermittently during GPS campaigns. Figure 2.5 shows part of this network, the sites NUPM and KTPM spanning the east rift zone of Mauna Kilauea, about 6km from the Pu'u 'O'o vent. MLPM is located on the southeastern flank of Mauna Loa, while MKPM is located on the summit of Mauna Kea. During a brief eruptive episode of the Kilauea volcano that began on January 30, 1997, continuously recording GPS receivers measured significant ground deformation near the eruption site. As magma forced its way up into the rift beneath the Napau Crater, the two GPS sites located on either site of the east rift moved apart by 36cm during the activity, and continued to move apart at a slower rate after the activity stopped on January 31 (Fig. 2.6). The results clearly showed that the relatively small eruption was associated with a much larger volume of magma that intruded into the rift zone and remained below ground.

The eruption on Kilauea was preceded by 8 hours of rapid deflation of Kilauea's summit (Owen et al., 2000b).

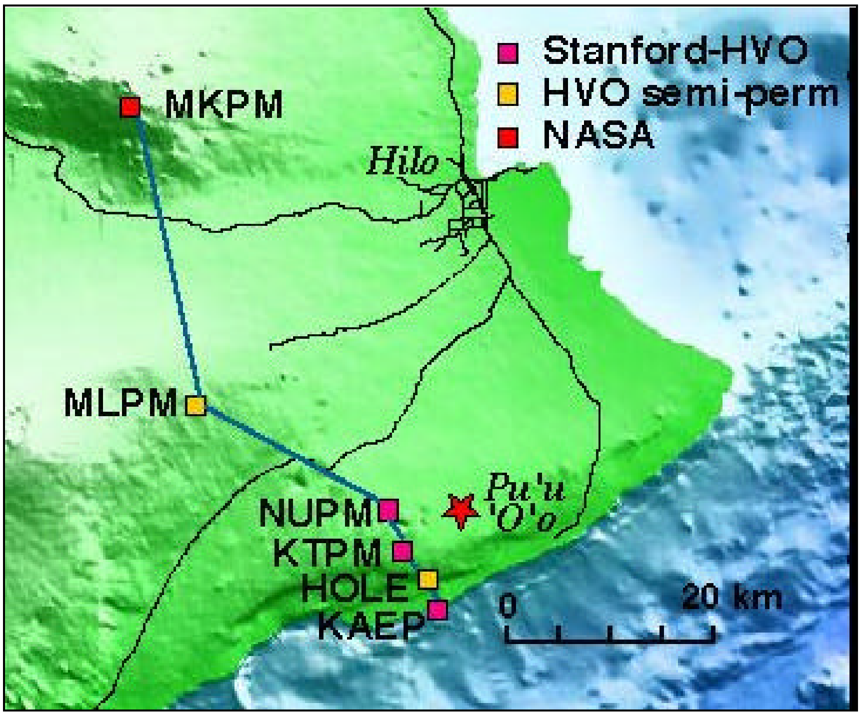

Fig. 2.5: Map showing the location of several GPS receivers on Hawaii (USGS, 2002c)

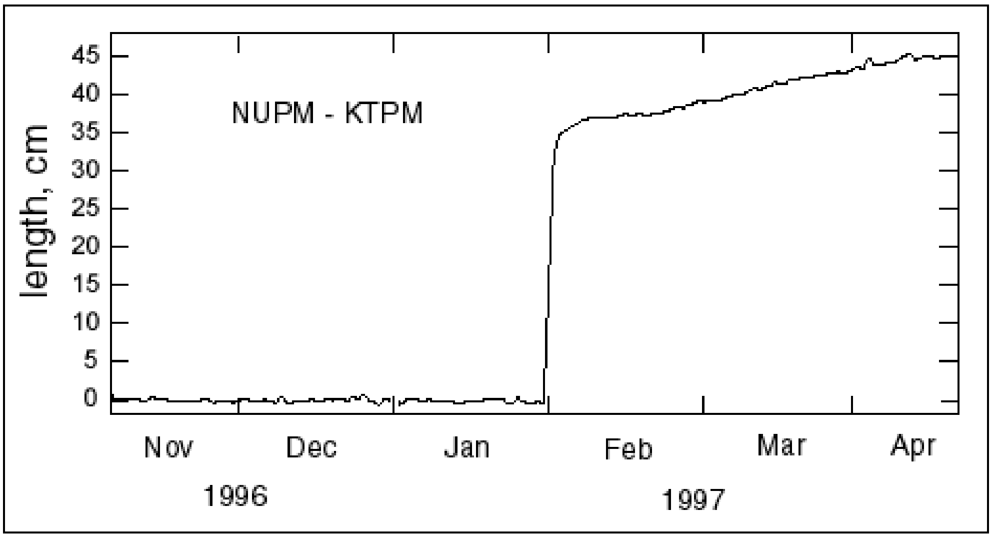

Fig. 2.6: Increase in distance between the sites NUPM and KTPM during the eruptive event of January 30, 1997 (USGS, 2002c)

A dense, continuous GPS network of about 20 sites was established to monitor ground deformation at the Iwate volcano in Japan. GPS data are collected at a sampling rate of

60 seconds and transferred to the computing facility at Tohoku University via phone line, cellular phone or radio link, depending on the site location. The data are analysed using the GAMIT software (King & Bock, 1995) and precise ephemerides to produce daily solutions. During a period of unrest in 1998, significant deformation of about 3-4cm horizontally and a 2cm uplift were observed (Miura et al., 2000). The horizontal displacements showed a radial pattern pointing outward from the western flank of the volcano and displacement rates increased especially in the east-west components. It was estimated that the source of deformation was initially dike intrusion caused by a tensile fault located 5km west of the summit at a depth of 3km. During the course of activity it then changed its nature to an isotropic pressure source according to the Mogi model, and migrated approximately 6km further westward. Displacements due to an M6.1 earthquake that occurred on September 3, 1998, about 10km southwest of the summit were also detected. A fault model of the earthquake was determined based on GPS data and showed good agreement with the results from seismological studies (Ibid, 2000). After the earthquake the volcano deformation ceased.

Recently a software package called Eolo has been developed in Italy, which permits the automatic management of data from a GPS deformation monitoring network (Amore et al., 2002). The software combines the treatment of raw data, their storage in a database, the calculation of the main strain parameters, and the visualisation of the results. Eolo takes into account a lot of the problems associated with the management of a deformation monitoring network. Missing data due to technical difficulties is dealt with, the constant operation of a reference station is not required, and the software is capable of contacting the supervisor by sending emails or SMS messages over the mobile telephone network whenever any anomaly in the analysed data is detected. The desired parameters, such as height variation, distance variation, dilateration and shear, can be visualised in several panels for easy interpretation. Eolo is in use on the island of Stromboli, Italy where a network of four continuous GPS receivers monitors the volcano by observing a 3-hour session daily.

A small scale deformation monitoring network implies a higher density of GPS stations, and therefore better resolution of the deformation pattern. However, these systems use expensive, dual-frequency GPS receivers, and this high expense can severely restrict the number of GPS stations that can be deployed. Usually daily baseline solutions are determined, although it is possible to process shorter sessions if the frequency of data transfer from the remote stations to the computing facility, and the processing software package that is used, allow this. At the Kilauea volcano, efforts have been made to upgrade the continuous GPS network, so that instead of the routinely generated 24-hour solutions, 15-minute position estimates can be computed in near real-time, based on a random walk parameterisation of ground displacement. Using this approach, smaller inflation events that had amplitudes as low as 1cm, with periods ranging from 6 hours to 2 days, were observed (Larson et al., 2001).

2.3.2.2 Kinematic Small Scale GPS Networks

The Real-Time Kinematic (RTK) GPS surveying technique typically requires two dual-frequency GPS receivers, connected by a radio data link. Carrier phase measurements are simultaneously observed at the reference or ‘base’ station and the (user) ‘rover’ station. The base station generates RTK messages and transmits these to the rover receiver. Using these corrections, the rover can determine its position to centimetre accuracy in *real-time*, making this an excellent option for some deformation monitoring applications. Several GPS manufacturers have developed RTK products, which can be used for deformation monitoring.

One such system was modified to specifically meet the requirements of a volcano deformation monitoring application, and has been deployed at the Rabaul volcano in Papua New Guinea (Lowry & MacLeod, 1997). It works essentially as a reverse RTK system by computing the position solutions at the rover and then transmitting these results back to the base for archiving. While this approach delivers real-time positions of the monitoring stations, the requirements for hardware, software, field computer and telemetry components are relatively high, making the equipment comparatively expensive. The volume of data transmission between the base and rover is doubled, which either limits the number of GPS sites in the network, or the sampling rate between epochs, as only one station at a time can transmit its data to the base.

Another example of a RTK system where the base station receives the computed positions of its roving receivers is the Furuno landslide monitoring system (Kondo & Cannon, 1995). It utilises 8-channel GPS receivers capable of outputting raw C/A code and carrier phase at a 0.5Hz data rate, and has been designed to facilitate up to 10 rover stations. The receivers communicate via a cable connection, which is also used to supply the system with power. This, however, limits the baseline lengths to a maximum of 1200m (typically only 800m) between any two receivers in the network. All data are collected at a central PC, where baseline vectors are determined in real-time with typical accuracies of 2cm. Due to the cable connection between GPS receivers, amongst other things, this system is unsuitable for volcano monitoring.

Kato et al. (2000) report on tests of a newly developed RTK system to detect tsunamis before they reach the coast. This system utilises dual-buoys consisting of a support-buoy and a sensor-buoy, both equipped with GPS antennas. The support-buoy is designed to move with the wind-waves and is equipped with two GPS receivers, a number of batteries, a wind generator and solar panels for power supply, and a communication device. It is anchored by tri-directional sinkers in order not to float away or rotate. The sensor-buoy is a spar-type buoy designed to be resistant to wind-wave motion and is connected to the support-buoy by the antenna cable and loosely tied to the supporting ropes to restrict its motions as little as possible. A reference station located on the shore complements the system. GPS data are processed in RTK mode onboard the support-buoy and the resulting positions are transmitted to the base station via a radio link. At the base facility the positions of the GPS sensors, which have an accuracy of a few centimetres, are monitored and archived. A test performed over nine days revealed that the buoy system successfully tracks the change of the sea-surface. Frequency analysis of the data after adding a real tsunami record to the observed RTK data suggests that the system is capable of detecting a tsunami. At present, however, no corrections for ionospheric or tropospheric effects can be applied, restricting the baseline lengths to about 10km. In order to detect tsunamis early enough to initiate warning procedures, the ‘tsunami-meter’ will have to be installed further from the coast.

An interesting, unique experiment was recently carried out in Japan, where earthquakes were simulated by controlled blasting of explosives (Turner, 2002). RTK GPS observations were used to study the effects on ground deformation, pipelines and bridge structures. In this RTK system raw code and carrier phase data are collected at a 10-20Hz sampling rate and transmitted via a radio link, from two base stations and up to ten rover stations, to a single computer that processes the data. Both single- and dual-frequency GPS receivers were tested in a laboratory environment and were found to deliver horizontal accuracies at the centimetre-level. The field tests in Japan demonstrated the versatility and robustness of the GPS monitoring package under severe weather conditions. Deployment of this system is planned on two landslide sites and two bridges in California.

Researchers in Germany developed the GPS-based Online Control and Alarm (GOCA) system, a software infrastructure that is designed to receive GPS baseline solutions from any combination of single- or dual-frequency GPS systems (K•lber et al., 2000). It can be set up as an early warning system to monitor engineering structures, landslide activity, earthquakes or volcanoes. Data from the base station is transmitted to the rover stations, where the baseline processing takes place. The estimated baseline vectors, along with their covariances and other information, are then transferred to the GOCA centre via radio modems. Here, a network adjustment is performed in order to detect any movements between observation epochs. The system is designed to handle both permanently and intermittently occupied rover stations, offering a high degree of flexibility. GOCA was successfully used to detect movements caused by filling and emptying the lock Uelzen I in Germany (Borchers & Heer, 2002). The lock, which is part of the Elbe-Seiten-Canal, has a length of 185m and overcomes a height difference of 23m. During operation (filling and emptying the lock) the walls of the lock expanded in the range of 25mm to both sides, and a typical operation period of one hour was clearly estimated by time series analysis.

A real-time monitoring software package, called 3-D Tracker, was developed by Condor Earth Technologies Inc. (Condor, 2000). It can process data from single- or dual-frequency GPS receivers, or a combination of both. Instead of raw GPS data from reference station(s) and rover station(s) being processed at the rover(s), all data are processed at a centralised station. After a period of initialisation, Kalman-filtered epoch-by-epoch solutions are provided by processing both double-differenced and triple-differenced data. The manufacturers claim mm-accuracy for this system.

RTK systems can provide real-time coordinates of rover stations at the computing facility and are certainly an attractive option for a range of deformation monitoring applications. However, such systems are comparatively expensive. On a volcano, most of the time deformational signals cannot be characterised as 'kinematic', except under extreme conditions just before an eruption. Since only positions are received and stored by the base facility, raw GPS data is not archived for the processing of longer observation sessions. This, however, may be very useful in order to analyse long-term displacements and to check the RTK solution in quiescent periods.

2.3.2.3 Low-Cost GPS Networks

The monitoring systems mentioned above are very costly because they require the use of high-quality, dual-frequency instrumentation. This is a significant constraint, especially as most of the world's active volcanoes are located in less developed countries, which cannot fund such systems for monitoring all potentially hazardous volcanoes. In recent years, however, low-cost options have been developed. Based on original equipment manufacturer (OEM) board sets, single-frequency GPS receivers are available at a fraction of the cost of standard dual-frequency receivers. They can be integrated into custom-built systems that output code and/or carrier phase measurements for baseline determination.

The lower cost of such systems means that it is possible to deploy a denser network, which in turn makes it feasible to map deformation on a finer scale. Such systems can fulfil all requirements needed for a deformation monitoring system, such as suitability for remote locations, power supply in the form of batteries and solar panels, transmission of data via radio links, and computerised control of data management and communications software. In addition, the lack of peripheral components to the GPS receiver and computer (e.g. displays, screens and hard disks) significantly reduces the power usage of the system. Hence, the size of the battery bank and the solar panels can be reduced, resulting in further cost savings.

The GPS volcano deformation monitoring system developed by the University NAVSTAR Consortium (UNAVCO) is an example of such a system. As described by

Meertens (1999), single-frequency GPS receivers continuously transmit carrier phase and pseudorange observations through a Time Delay Multiple Access (TDMA) radio data modem network to a central computing facility. Instead of sending logged data files, these ‘intelligent’ radios send GPS data epochs continuously according to pre-defined time slots. The data (collected at a 10-second sampling rate) can be processed at hourly or shorter intervals in order to provide station deformation estimates. The UNAVCO system was deployed at the Long Valley Caldera, California, in 1998 and on the Popocat■petl volcano near Mexico City in April 1999. The latter network comprises five remote stations located on the flanks of the volcano, including one just 300m below the summit (Fig. 2.7).

Fig. 2.7: L1 GPS station at a remote location on Popocat■petl volcano (UNAM, 2002)

Another low-cost, single-frequency system has been developed at The University of New South Wales (UNSW) and will be described in greater detail in the next section.

The commercially available Movement Monitoring System (MMS) has been developed by the University of Applied Sciences of Southern Switzerland and GEODEV (GEODEV, 2002). This system consists of a network of single-frequency GPS receivers which are connected to a base station via either a cable, cellular modem or a radio link. The system follows a repetitive sequence of measurement, communication and post-processing. Observation sessions are typically 15-30 minutes in length, and processing takes place at the base facility where the GPS data are also archived. The baseline results can be visualised using tables or graphs in relative or cummulative terms, and the software can automatically initiate the distribution of warning or alarm messages (e.g. via email or mobile phone) if the deformation exceeds a certain pre-set limit. The horizontal precision achievable for baselines up to 10km is claimed to be 7mm ± 1.5·(baseline length in km) (Knecht & Manetti, 2001). Although designed for monitoring buildings, dams, bridges and landslide sites, this system can also be utilised in a volcano environment.

Low-cost systems are more appropriate for developing countries like Indonesia. The use of custom-designed software means access to the source code for algorithm improvement. Due to the use of only one frequency, however, the ionospheric bias cannot be accounted for. In general, a single-frequency, carrier phase-tracking system is appropriate for small-scale continuous GPS networks if the baseline lengths are not longer than about 10 kilometres (a scale usually adopted for volcano deformation monitoring systems). This ‘rule-of-thumb’ implies that the differential ionospheric delay between the two receivers is assumed to be essentially zero, and therefore does not impact on the baseline result. Orbit bias over such short distances can also be ignored (Rizos, 1997). However, as outlined in section 2.5 and chapter 4, these assumptions do not always hold true, and a sparse outer network of dual-frequency receivers may be required to ensure high accuracy.

2.4 A Continuous Low-Cost GPS-Based Volcano Deformation Monitoring System in Indonesia

The Indonesian archipelago is home to 129 active volcanoes and 271 eruption points as a consequence of interactions and collisions among several continental plates, including the Australian plate (Abidin & Tjetjep, 1996). 20 million Indonesians, approximately 10% of the total population, live in areas under threat from volcanic eruptions.

A small scale, low-cost, continuous GPS volcano deformation monitoring system was designed by UNSW in collaboration with the Institute of Technology Bandung (ITB) and the Volcanological Survey of Indonesia (VSI). The general specifications of this system are (Roberts, 2002):

- Suitable for short baselines,
- remote stations powered by batteries and solar panels,
- remote stations designed for harsh environments,
- L1 OEM GPS boards controlled by PC or micro-controller,
- radio modems modular in design to allow for different range transmissions in different environments,
- in-house baseline processing software,
- centimetre accuracy from post-processed static baselines,
- designed for volcano monitoring in equatorial regions,
- suitable for operation in developing countries, and
- as inexpensive as possible.

The system has been deployed on Gunung Papandayan, which is located about 60km south-southeast of Bandung in West Java, Indonesia (Fig. 2.8). Papandayan is a complex stratovolcano with four large summit craters and a maximum elevation of 2665m above sea level. A very violent eruption occurred on August 11-12, 1772, resulting in the collapse of the summit portion of the mountain, which was ejected over 250km^2 surrounding the area, and the creation of the present horseshoe-shaped crater. A subsequent debris avalanche destroyed 40 villages, killing 2951 people (Kusumadinata, 1979; Kimberly et al., 1998). Although it later developed into a tourist destination, the volcano continued to be an eruptive threat with heightened activity observed in the 1920s, and several explosions of mud occurring until 1993 (VSI, 2002a). This was underlined recently with the spectacular November 11-20, 2002 eruption that dramatically changed the topography inside the old crater complex (see Appendix).

Fig. 2.8: Map of Java showing the location of Gunung Papandayan

Rizos et al. (2000) describe the four-station network of single-frequency GPS receivers installed on Gunung Papandayan. The network array consists of one base station situated at the VSI observatory and three ‘slave’ stations (Bukit Maung, Nangklak and Kawah) located approximately 8km away in the zone of deformation around the crater of the volcano (Fig. 2.9). Each station comprises five components: (1) GPS/PC module, (2) radio modem sub-system, (3) monument, (4) GPS antenna, and (5) power supply. These components are briefly described below.

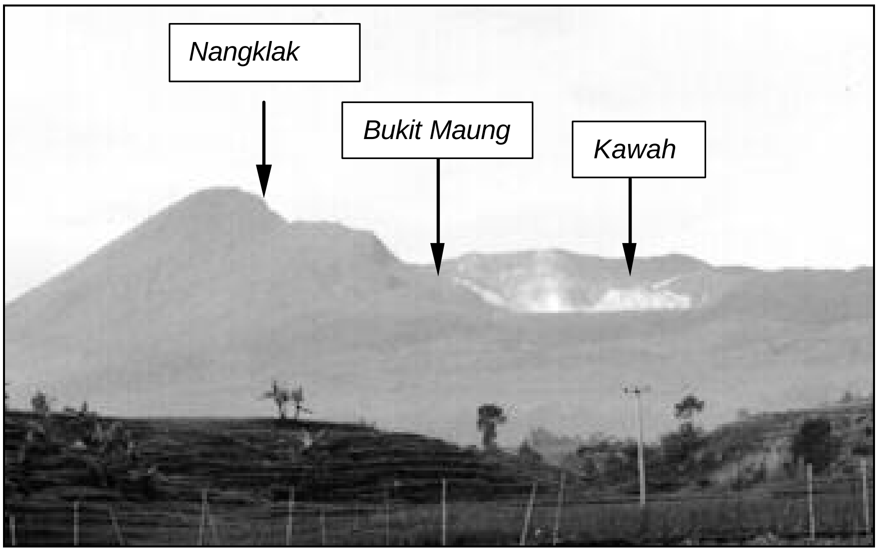

Fig. 2.9: Location of the three slave stations on Gunung Papandayan (Roberts, 2002)

GPS/PC Module

GPS/PC modules integrate a 12-channel, single-frequency, Canadian Marconi Company (CMC) Allstar GPS receiver board with an 8086 PC board, which controls data decoding, file management and communications. The slave station computers do not have a screen, keyboard or hard disk (memory storage is restricted to the RAM only), resulting in a significantly reduced power usage. At the base station a 133MHz Pentium computer board is utilised, as it collects data from all slave stations (and its own receiver), and runs the baseline processing software. GPS data is collected at a data rate of 15 seconds and logged hourly at all stations. The GPS/PC modules were custom-built by GPSat Systems Pty. Ltd., Melbourne, Australia.

Radio Modem Sub-System

The base station sequentially polls the three slave stations and downloads their binary data files via a VHF radio link on an hourly basis. Two frequencies (152.375 and 152.475 MHz) are used to transmit and receive data, whereby the ‘transmit’ frequency for the base station corresponds to the ‘receive’ frequency of the slaves, and vice versa. The base station is located at the VSI observatory at the foot of the volcano, about 8km away from the zone of deformation, and has a clear line-of-sight to the summit. VHF radios with directional Yagi antennas at all slave stations and an Omni dipole antenna at the base are used for data telemetry.

Monument

Berntsen 3D monuments (Berntsen, 2002) were emplaced and concreted in position at suitable locations. Issues such as skyview, site stability, line-of-sight for radio communications and avoidance of corrosive gases were important considerations for the location of the monuments. Additionally, the advice of experts from the Volcanological Survey of Indonesia was sought to locate the stations in order to most likely detect any deformation of the volcano. A fibreglass pole, connected to the monument by a screw thread and reinforced by concrete around the base, is used to mount a GPS antenna at all stations.

GPS Antenna

MicroPulse L1 lightweight survey GPS antennas are used at all stations. The U.S. National Geodetic Survey estimated the phase centre variation of these antennas, and the offset model has been incorporated into the GPS baseline processing software. In order to mitigate multipath disturbance, the antenna is mounted on a 1.5m high fibreglass pole. Fibreglass was chosen due to its resistance to the corrosive gases (which are constantly being emitted from the main crater).

Power Supply

At the remote slave stations 12V DC lead acid batteries are used to supply continuous power to the GPS/PC module, GPS antenna and radio modem. Solar panels recharge the batteries during daylight hours, and a solar regulator is used to ensure that the power output from the solar panel array is kept at 12V DC. The base station is powered by AC power backed up by a modified uninterruptable power supply (UPS) to guard against spikes, surges or extended blackouts, which are rather common in rural Indonesia.

Figure 2.10 shows the main hardware components of the slave station equipment: GPS/PC module, radio modem and single-frequency antenna. At the slave stations, the GPS/PC module, radio, solar regulator and battery are housed in a robust plastic drum locked onto a concrete pad to protect the equipment from the environmental elements and theft. Furthermore, PVC tubing surrounding the cables was used in order to give protection from damage by animals. The entire slave station setup is depicted in Figure 2.11, showing GPS antenna, solar panels, radio antenna and the plastic drum containing the remainder of the equipment at Nangklak. At Kawah, in addition, a barbed-wire fence was erected to guard the equipment against vandalism because this area is frequently visited by tourists. The base station setup can be seen in Figure 2.12.

Fig. 2.10: UNSW system equipment: GPS/PC module, radio modem, GPS antenna and cables

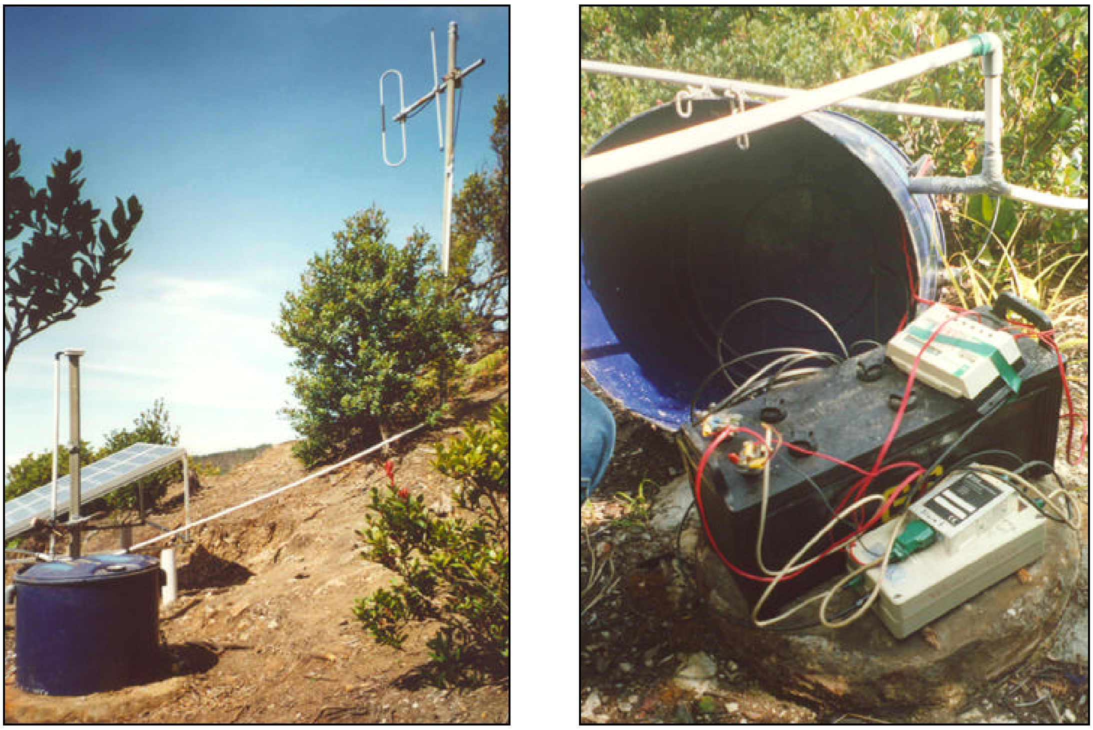

Fig. 2.11: Slave station setup on Gunung Papandayan (Nangklak): Solar panels, GPS antenna, plastic drum and radio antenna (left); battery, solar regulator, radio modem and GPS/PC module (right)

Fig. 2.12: Base station setup at the VSI observatory (Roberts, 2002)

Data is collected at a sampling rate of 15 seconds. All software to operate this GPS network has been developed at UNSW to ensure maximum design flexibility. Rudimentary software onboard the GPS/PC module controls the creation of a new data file every hour, which is stored in the RAM at the slave station in the receiver's binary proprietary format, and the radio transmission of the completed sessions to the base station. The communications software at the base station is more 'intelligent' than that at the slave stations. The base station controls the data download via the radio modems by polling each slave station in sequence on an hourly basis, downloading the latest file from its RAM. The binary data received from the slaves is then automatically converted to the Receiver INdependent EXchange (RINEX) format and stored on the hard disk at the base facility. Therefore 24 one-hour files are generated daily for each station, resulting in approximately 12MB of data per day, comprising 192 files. At present baselines are not automatically processed. Data must be manually downloaded from the hard disk at the base station and post-processed. This is a sub-optimal solution and it is intended to remedy this in the near future.

A detailed description of the UNSW-designed system (first installed in 1999), as well as a comprehensive guide for installation, operation and trouble shooting, can be found in Roberts (2002).

The aim was to limit the cost for one receiver station (including monuments and labour) to $US 3000 (Rizos et al., 1997a). The actual cost exceeded this target only by around $US 500, leaving the total cost for the entire four-station network below the cost of one state-of-the-art GPS receiver, which can cost of the order of $US 20,000 or more (Roberts, 2002).

2.5 A Mixed-Mode GPS Network for Volcano Deformation Monitoring

Low-cost GPS networks for deformation monitoring rely on the use of single-frequency GPS receivers. While these receivers are significantly cheaper than dual-frequency instrumentation, they cannot directly account for the ionospheric delay because they only make measurements on one frequency. For short baselines of up to 10km or so, it is generally assumed that the GPS signals propagate through essentially the same portion of the atmosphere and the biases therefore mostly cancel out when the double-differenced observable is formed. However, most of the world’s volcanoes are situated in the equatorial region, an area prone to highly disturbed ionospheric conditions. The resulting effects on the GPS signal are further amplified during the present solar sunspot maximum. Ionospheric disturbances have indeed corrupted baseline measurements over distances less than 10km on Mt. Papandayan, adversely affecting baseline repeatability (Janssen et al., 2001).

During the past few years a methodology has been developed for processing data collected by mixed sets of single-frequency and dual-frequency GPS receivers. For example, Hartinger & Brunner (2000) and Brunner et al. (2000) report on a system to monitor landslides in the Austrian Alps. The UNAVCO L1 system on the Popocatépetl volcano, mentioned in section 2.3.2.3, is expected to be extended by using two dual-frequency receivers to aid atmospheric modelling in the near future (Meertens, 1999).

In order to obtain centimetre-level accuracy for the system deployed on Gunung Papandayan, the single-frequency network has been augmented by the addition of an outer *fiducial* network of dual-frequency GPS receivers (Rizos et al., 1997b). As discussed in chapter 4, this dual-frequency network surrounding the deformation zone of the volcano is used to generate empirical ‘correction terms’, which are then applied to the inner single-frequency data during baseline processing. This *mixed-mode* GPS network approach can account for the ionospheric biases that would normally be neglected in a system using single-frequency instrumentation only.

As described by Han (1997), the fiducial network should ideally surround the inner single-frequency network. Figure 2.13 depicts the ideal network configuration where the triangles denote fiducial stations, while the dots indicate single-frequency receiver sites. The fiducial reference stations are to be situated outside the deformation zone of the volcano but within the local tectonic region. Their precise coordinates can be updated regularly by connection to the IGS network. Sites should have stable monumentation, a clear view of the sky and minimal multipath disturbance due to reflections from nearby structures. Security and power issues are significant and have to be addressed in order to enable long-term continuous operation of the fiducial network.

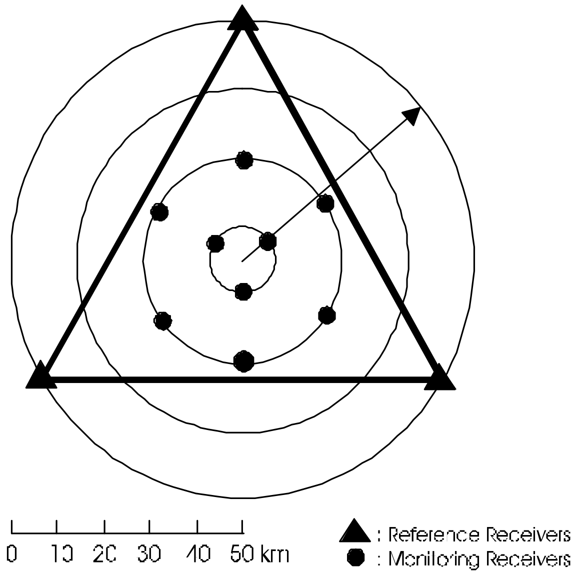

Fig. 2.13: Ideal network configuration of a mixed-mode GPS deformation monitoring network

Obviously this *mixed-mode* GPS network strategy is not restricted to volcano deformation monitoring, but can also be utilised for a wide range of other deformation monitoring applications. Moreover, existing dual-frequency networks can be cost-effectively densified by large numbers of single-frequency GPS receivers.

2.5.1 February/March 2000 Deployment

The fiducial network surrounding Gunung Papandayan was first deployed in February/March 2000. The selection of sites with (more or less) continuous AC power at secure locations in a rather remote part of West Java proved to be a big challenge. The initial network comprised three GPS stations located at the ITB in Bandung, the VSI observatory at Galunggung and the National Aeronautics and Space Agency (LAPAN) observatory in Pameungpeuk, forming a 72km-60km-85km triangle surrounding the deformation zone of the volcano. This configuration left the inner network close to the baseline Bandung-Pameungpeuk, but still well inside the fiducial triangle (Fig. 2.14). The figure also shows the altered fiducial network used during the July 2001 deployment (see next section).

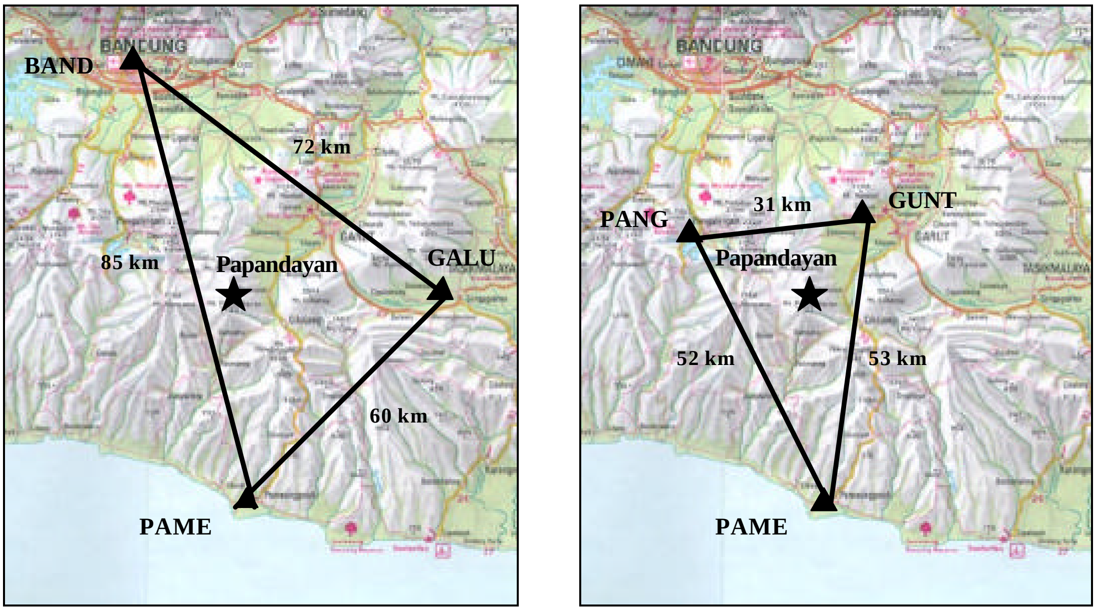

Fig. 2.14: Fiducial network for the Feb/Mar 2000 deployment (left) and the July 2001 deployment (right)

The equipment used at all fiducial stations comprised Leica CRS1000 dual-frequency GPS receivers equipped with choke ring antennas, a 120Ah/12V DC lead acid battery and a battery charger (Fig. 2.15). Reliable power supply always is a significant issue in GPS network design, and is particularly challenging in Indonesia. In order to guard against the rather common power outages of up to 6 hours (only the site in Bandung had continuous AC power during the entire campaign), the following configuration was used. An 'intelligent' battery charger connected to a 12V DC lead acid battery is plugged into mains power to continuously charge the battery whenever AC power is available. The charger automatically trickles the charge when the battery is approaching full charging capacity. The GPS receiver is connected to the battery, which continues to supply power in the event of a blackout. Spikes and surges in the AC power are absorbed by the battery charger, and the battery, and therefore do not affect the GPS receiver.

In general there are two types of batteries on the market, the so-called (wet) float/cranking batteries and (dry) deep cycle batteries. While the former are designed to provide large amounts of power over a short period of time (e.g. to start a car engine), the latter provide relatively low continuous power over a long period of time. Hence, a deep cycle battery would be preferable for the task of powering a GPS receiver. Nevertheless, a (wet) lead acid cranking battery is used due to its significantly lower cost and ready availability in Indonesia. (Note that the same applies for the single-frequency stations of the inner network.) The size of the battery was chosen to guarantee continuous power even during extended AC power failures. As the CRS1000 draws approximately 15 Watts at 12V, which translates into 1.25Ah, a 120Ah battery is sufficient to cover blackouts of up to three days.

Fig. 2.15: The author at the Galunggung site: GPS equipment comprising battery charger, battery and Leica CRS1000 GPS receiver

A GPS choke ring antenna consists of concentric rings of aluminium or brass mounted on a circular base surrounding a microstrip patch located flush with the plane of the rings (see Figures 2.16 and 2.17). This design has proven to be very effective in terms of multipath protection and phase centre stability. It is the standard antenna used by the IGS in their global GPS network, hence choke ring antennas were utilised at all fiducial network stations around Gunung Papandayan. In addition, antenna sites were carefully selected away from reflecting surfaces (as much as this was possible under the given circumstances) in order to further minimise the effects of multipath. Figure 2.16 depicts the construction of a wooden antenna platform at Galunggung with the help of a local carpenter. Note that these sites were only intended to be temporary, for demonstrating the 'proof-of-concept'. In the case of an actual installation for volcano monitoring purposes, the sites would be installed in a manner appropriate for long-term operation of permanent reference stations.

Fig. 2.16: Construction of a GPS antenna platform on the roof of the VSI observatory at Galunggung

Communication with the GPS receiver is established via a laptop computer, which can be used to download data files and check the status of the receiver while it is operating, but does not have to be continuously connected to the receiver. The Leica CRS1000 is equipped with 60MB of flash memory, so it can conveniently store data files (collected at a 15s data rate) for several weeks without the need for downloading. Eventually, however, the downloading process will be automated in order to make the GPS data available as quickly as possible to satisfy near real-time data processing.

Problems encountered during the first deployment of the fiducial network surrounding Gunung Papandayan were mainly concerned with the continuous supply of power. The battery chargers originally used proved to be unreliable and inadequate for recharging the batteries fast enough after a power outage. As a result, the battery went flat on a number of occasions, causing the survey to be interrupted. In addition, one battery charger was damaged by a power surge.

At Kawah, one of the single-frequency GPS sites on the volcano, strong winds destroyed one solar panel by tearing the entire solar panel frame from its concrete mounts. Fortunately, the second solar panel survived and could be reinstalled to supply power after a new frame had been built. (The power system for the slave stations had been over-engineered, so the operation of just one solar panel is sufficient to supply continuous power, given that there are not too many sun-free days.)

Any metal surfaces, such as the metal drums originally housing the equipment and the barbed-wire fence at Kawah, were severely affected by the sulphur gas from the volcano’s crater. However, all aluminium and fibreglass components, as well as all surfaces covered with electrical isolation tape, proved resistant to corrosion from the acidic gases. Furthermore, caustic soda placed inside the drums proved to be an effective means of negating the sulphur gas attack on the equipment.

The antenna cable and GPS antenna at Nangklak were found to be faulty and had to be replaced. The 30m antenna cable at the base station was unknowingly cut by farmers despite being housed in PVC tubing and was repaired on-site. Many other minor problems, such as blown fuses and some baud rate incompatibilities, were also experienced during the February/March 2000 deployment.

The PC boards used in the GPS/PC modules at the slave stations proved to be problematic because the amount of available flash-PROM (Programmable Read-Only Memory) and RAM (Random Access Memory) decreased over time, causing the survey to stop (see Roberts, 2002). This was later rectified by obtaining new flash-PROMs and modifying the software used to operate the slave stations. However, many of the hardware faults in the GPS/PC modules can be attributed to the low-performance PC used and the DOS operating system (an operating system not designed for real-time applications). Efforts are underway to change the hardware of the GPS/PC modules to a micro-controller-based system for increased reliability.

Unfortunately due to the many hardware and software problems encountered at the time of deployment, an extensive, continuous data set with all seven stations of the mixed-mode GPS network operating simultaneously could not be collected. Data processing of the outer network revealed that the fiducial baselines were too long to generate reliable 'corrections' under severe ionospheric conditions, such as those experienced in the equatorial region during a solar maximum (see section 4.6.4). As a result, the 'corrections' could not be applied to the single-frequency data set collected on the volcano. Data processing of the single-frequency network proved to be extremely difficult due to the unstable nature of the ionosphere at the time of observation, resulting in a very high noise level of the GPS data logged (Janssen et al., 2001).

2.5.2 July 2001 Deployment

Following modifications to the hardware and software the system was redeployed in July 2001. Two new fiducial sites were chosen in Pangalengan and at the VSI observatory at Guntur, effectively reducing baseline lengths to form a 31km-53km-52km triangle around Gunung Papandayan (Fig. 2.14).

The faulty battery chargers were replaced with higher quality battery chargers designed to operate under conditions of fluctuating voltages and AC mains frequencies. An output current of 14A ensures fast recharging, even if power is drawn from the battery while the charging is in progress. In addition, a power surge protector was introduced to guard the battery charger against spikes and surges in the AC power. Figure 2.17 shows the setup at Guntur, where a stable fence post was modified with a screw thread embedded in additional concrete in order to mount the GPS antenna. In Pangalengan the antenna was installed on the roof of an elevated building, using a stable, wooden platform similar to the one shown in Figure 2.16.

At the single-frequency GPS sites on the volcano, the metal drums originally used to house the equipment had been corroded beyond recognition during the two years they had been left on site since the first installation of the single-frequency system on the volcano in 1999. They were replaced with robust plastic drums (see Fig. 2.11), which are expected to resist sulphur gas attack while still being strong enough to protect the equipment from vandalism. Indeed, the slave station at Kawah was badly vandalised. A new solar panel frame was built in Australia and reinstalled. The radio antenna cable had been severed and needed to be repaired, and a new fence was erected.

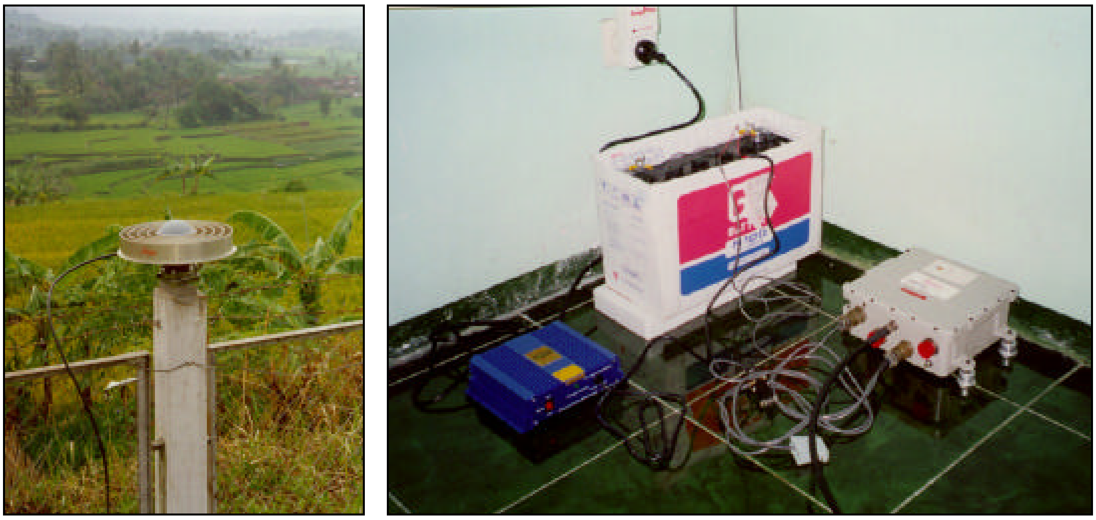

Fig. 2.17: Fiducial network: GPS antenna at Guntur (left) and GPS station equipment consisting of power surge protector, battery charger, battery and Leica CRS1000 GPS receiver (right)

Problems encountered during field-testing were few compared to the first deployment of the mixed-mode system in 2000. At the fiducial site in Pameungpeuk peculiar AC power conditions were experienced. Although the same site had been successfully occupied in the previous year, it was impossible to operate the GPS receiver while the battery was connected to the battery charger (and subsequently to AC power) because the entire setup became 'alive'. Attempts to negate the situation by ensuring sufficient isolation and earthing proved to be unsuccessful. In the end, a LAPAN observer was appointed to swap the used battery with a fully recharged one at the same time every day – a process that took no more than a couple of minutes, sacrificing only a few epochs of data. (The reader should be reminded that at this stage the UNSW-designed system was a 'proof-of-concept' system.)

Both the inner, single-frequency network and the fiducial, dual-frequency network operated well, and three weeks of continuous data were collected. Processing of the data unfortunately did not show any improvements when the empirical ‘corrections’ were applied. A discussion of the results is given in section 5.5.

2.5.3 Data Processing Strategy

Depending on the type of movement expected in a deformation monitoring application, different data processing strategies can be used. If ‘slow’ deformation at a constant rate is expected (e.g. tectonic plate movement or ground subsidence), the data is usually processed in static sessions of a few hours to a few days in length, assuming no movement during the session. This is generally done in post-processing mode, as the deformation does not pose an imminent threat to surrounding structures or the population inhabiting the area. In this case parameters describing precise satellite orbits and polar motion, which are generally not available in real-time, can be used to improve the quality of the solution. This procedure is typically used for processing large scale, global networks in order to detect plate motions where a comparison of several campaigns is usually sufficient to derive the average rate of tectonic motion. However, if the deformational signal is expected to take place over a short period of time (‘sudden’ deformation, e.g. caused by earthquakes) and/or varies with time (‘fast’ continuous deformation, e.g. long suspension bridges), the sampling interval must be increased accordingly. This suggests the use of continuous GPS networks, using short static sessions, or epoch-by-epoch solutions (resembling a kinematic processing strategy). If the deformation can cause failure of the deforming body (e.g. a collapsing dam or bridge, or an erupting volcano), a (near) real-time, epoch-by-epoch solution is desired in order to detect the deformation as soon as it occurs, so as to initiate warning and evacuation procedures.

In the case of volcano monitoring the deformation is expected to be of a mixed nature. During periods of quiescence the deformation will be slow (or not present at all), while increased activity will cause ground movements of increasing magnitude due to magma intrusion in the hours to days prior to an eruption. Hence, a near real-time, epoch-by-epoch solution is preferred in order to detect movements on the flanks of a volcano over a relatively short period of time. This can be interpreted as a ‘slow kinematic’ approach, where a static receiver moves slowly but continuously due to ground surface movement. In contrast to a true RTK system where only coordinate positions are stored and analysed, the raw GPS data is also being archived. Hence the raw data can be post-processed in longer observation sessions in order to detect long-term deformational signals and to periodically connect the sites to the ITRF through the IGS network. A fully automated system would then be able to 'switch' between epoch-by-epoch processing and hourly or daily solutions, depending on the nature of the deformation.

The baseline processing software developed at UNSW has been modified to enable epoch-by-epoch processing in multi-baseline mode. Routines to optimise the number of double-differenced observations used in the data processing (see chapter 3) and to implement the use of ionospheric 'corrections' (see chapter 4) have also been added.

2.5.4 Starting Coordinates

GPS stations designed for deformation monitoring must be referred to one (or more) fixed points that are assumed to be unaffected by the local ground displacement. The IGS network provides a global infrastructure of GPS coordinates in the ITRF with an accuracy at the sub-centimetre level, to which smaller networks can be connected (IGS, 2002b).

A regional GPS network used for deformation monitoring therefore needs accurate 'starting' coordinates. These can be obtained in a number of ways, listed in order of accuracy (Roberts, 2002):

1) Rigorously connect one or more or all of the monitoring stations to the IGS network in a global solution using long observation sessions and considering all geodetic effects,
2) rigorously connect one or more or all of the monitoring stations to a local part of the IGS network (i.e. 10 or less stations only) in a regional solution also using long observation sessions and considering all geodetic effects,
3) connect to the nearest IGS station and transfer the absolute coordinate to the reference station of the local network, or
4) compute a single point positioning solution of the base station of the local network independent of the IGS network.

The first three methods provide centimetre-level coordinates, while the last method should provide an absolute coordinate of approximately 5-10m accuracy. It should be noted that an *absolute* starting coordinate for a reference station in a deformation monitoring network at metre-level accuracy can still resolve centimetre-level *relative* coordinates *between* stations in the network. Nevertheless, it is desired to obtain absolute starting coordinates of the highest possible accuracy.

The absolute coordinate of a GPS reference station can be interpreted as a four-dimensional quantity, i.e. the position (X,Y,Z) at a certain time epoch. As the entire surface of the earth is in constant motion, global velocity vectors can be applied to all stations in the network to account for any secular crustal effects. This is especially important if the network straddles a tectonic plate boundary.

The ‘starting’ coordinates of the mixed-mode GPS network at Gunung Papandayan are obtained according to method (3), in a two-step process. First, the fiducial network stations established in February/March 2000 were connected to the nearest IGS station at Bakosurtanal (BAKO), whose coordinates are known with an accuracy of approximately 1cm (IGS, 2002b). Secondly, the derived coordinates for the fiducial sites were held fixed and the base station coordinates for the inner single-frequency network were computed.

Three 24-hour sessions of dual-frequency data collected at the fiducial GPS stations were used to connect all three fiducial sites independently to the IGS station at Bakosurtanal. The Bernese software (Rothacher & Mervart, 1996) was used to compute coordinate values using precise ephemerides and conventional long static baseline processing procedures. Three coordinate sets were obtained for each fiducial site and the mean was then computed. In a second step, these fiducial coordinates were held fixed and three baselines using 24 hours of single-frequency data were processed to determine the coordinates of the base station at Gunung Papandayan. The resulting three coordinate sets showed differences of up to 1m, possibly due to the high ionospheric activity at the time (baselines of up to 60km observed on L1 only). Using the Bernese software, from these three coordinate sets a mean value was generated, which could be claimed to have an accuracy of 1m or better. Table 2.1 lists the starting coordinates used for the single-frequency network on Gunung Papandayan.

Tab. 2.1: ITRF2000 starting coordinates for the single-frequency inner network on Gunung Papandayan

Station	X [m]	Y[m]	Z[m]
Base	-1933614.0131	6025645.7317	-802279.9143
Bukit Maung	-1928406.6847	6027755.3781	-806707.8448
Nangklak	-1927104.2280	6028391.0919	-807450.2857
Kawah	-1927737.2506	6028054.2288	-806646.1924

In 2001 a slightly different approach was used to obtain starting coordinates for the fiducial network sites. The AUSPOS Online GPS Processing Service (Geoscience Australia, 2002) is provided free of charge by Geoscience Australia and is able to process GPS data collected anywhere on earth. GPS data submitted via the internet are processed by connecting the user site to the three nearest IGS sites, providing coordinates at the centimetre-level for 24-hour data files. For each of the fiducial network stations seven 24-hour data files were used to obtain coordinates. From these seven coordinate solutions, a mean value was generated. For the sake of completeness, Table 2.2 lists the coordinates of all fiducial stations occupied during the campaigns at Gunung Papandayan. Note that the coordinates of the site occupied in successive years differ slightly because during reinstallation the antenna was not mounted in exactly the same position.

Data processing results and analyses using these coordinates are given in section 4.6.4 and chapter 5 of this thesis.

Tab. 2.2: ITRF2000 starting coordinates for the dual-frequency fiducial network at Gunung Papandayan

Year	Station	X [m]	Y[m]	Z[m]
2000	Bandung	-1915926.4768	6036457.8403	-759944.4172
	Galunggung	-1967112.5935	6013829.5148	-804979.3261

	Pameungpeuk	-1921225.3645	6022771.6076	-843402.2881
2001	Guntur	-1941161.3710	6024021.5960	-794042.8210
	Pameungpeuk	-1921225.4130	6022771.7460	-843402.3270
	Pangalengan	-1911887.9510	6034118.5770	-793233.9550

Augmenting the single-frequency system with a fiducial network of three expensive, dual-frequency GPS receivers may seem to contradict the aim of a low-cost system, but this mixed-mode approach is proposed in order to generate centimetre-level coordinate accuracies under solar maximum conditions, as were experienced during the period this research was conducted. In addition, if the fiducial sites are appropriately chosen, it is possible to use one fiducial network to simultaneously generate ‘corrections’ for a number of different volcanoes within the triangle. This is particularly useful in the case of Indonesia, where a large number of volcanoes are located in a comparatively small area. For instance, one fiducial network could service L1 deformation monitoring networks on Gunung Papandayan, Gunung Guntur and Gunung Galunggung. Furthermore, with the ever-increasing number of continuous dual-frequency networks being established around the world, these could provide a convenient backbone for densification with single-frequency GPS receivers.

The ideal GPS volcano deformation monitoring system simultaneously satisfies the criteria of high accuracy, low-cost, continuous measurements with real-time data access and full automation. However, in practice the realisation of such a system is usually a compromise due to many factors (e.g. logistics, funding, accessibility, magnitude and frequency of expected movements, data handling, power supply and communications).

Chapter 3

OPTIMISING THE NUMBER OF DOUBLE-DIFFERENCED OBSERVATIONS FOR GPS NETWORKS IN SUPPORT OF DEFORMATION MONITORING APPLICATIONS

3.1 Introduction

Deformation monitoring using GPS techniques is usually carried out by installing and operating a local network of GPS receivers located on and around the deforming body, e.g. the flanks of a volcano, or on a dam wall, bridge structure, etc. As mentioned in chapter 2, GPS networks for deformation monitoring can generally be observed in two ways, using either episodic campaigns or continuous measurements. Campaign-style surveys are conducted by reoccupying the same stations every few months or so to detect movements between campaigns. While these measurements have produced useful results (e.g. Abidin et al., 1998; Nishi et al., 1999; Shepherd et al., 1998), they give no indication of short-term ground movement in the long periods between the campaigns. Continuous GPS networks, however, can potentially monitor all ground deformation signals and thus give detailed information about the dynamics of the deforming body.

As described in section 2.5.3, different data processing strategies can be used depending on the type of deformation expected. If ‘slow’ deformation at a constant rate (with time) is expected (e.g. tectonic plate movement or ground subsidence), the data is usually processed in static sessions of a few hours to a few days in length. A comparison of several annually or quarterly conducted GPS campaigns is normally sufficient to derive the average rate of deformation in such cases. If the deformational signal is expected to occur over a short period of time (‘sudden’ deformation, e.g. caused by earthquakes) and/or varies with time (‘fast’ continuous deformation, e.g. long suspension bridges), the sampling interval needs to be increased to track these motions. If the deformation can cause failure of the deforming body (e.g. a collapsing dam or bridge, or an erupting volcano), a (near) real-time, epoch-by-epoch solution is desired in order to detect the deformation as soon as it occurs, and so as to initiate warning and evacuation procedures.

In the case of volcano deformation monitoring, the movements are expected to be of a mixed nature. While the deformation will be slow or even negligible during periods of quiescence, increased activity before an eruption will cause changing ground movement rates due to the expansion of the magma chamber below the volcano. A real-time, epoch-by-epoch solution is therefore preferable in order to detect movements on the flanks of a volcano with minimum delay. However, one has to keep in mind that a decreasing observation period increases the difficulty in resolving integer phase ambiguities. Hence, there is a trade-off between the length of the observation period and the difficulty in computing a reliable solution (see Roberts, 2002).

Multi-baseline processing strategies are preferred because all baselines are then computed together, taking into account the between-baseline correlations which arise from observing a GPS network simultaneously. Commercial software packages use a baseline-by-baseline processing approach, and therefore neglect these correlations (see section 3.4). Note, however, that some scientific software packages are able to use a different number of satellites for different baselines. GAMIT, for instance, uses all available double-differenced observations and accounts for this by using appropriate variances in the data processing (King & Bock, 1995). The Bernese software, on the other hand, scans all possible baselines first and then selects an independent set of double-differences, generally based on the shortest baselines (Rothacher & Mervart, 1996).

For the volcano deformation monitoring application there is a special challenge. The sides of the volcano will block out part of the sky, and therefore the network of receivers is not likely to track many satellites that are visible from all receivers simultaneously. Figure 3.1 shows the typical terrain consideration around a volcano. A GPS receiver on the summit would have a clear skyview but would be in great danger of being damaged by emission of gas and material, especially during periods of volcanic activity. Therefore the monitoring receivers are generally placed on the flanks of the volcano. If the usual base-station / base-satellite approach is used in the multi-baseline data processing, only the common satellites are considered, resulting in the total number of possible double-differences being comparatively low, hence a lot of valuable information can be lost. In the worst case, a solution may not be obtained if the number of common satellites tracked by all network receivers is reduced to less than four. In this chapter a method is described that considers satellites that are visible from a small number of GPS network stations only. Hence, the number of independent double-differenced observables can be maximised, which in turn would permit a more precise and reliable solution.

Fig. 3.1: Gunung Merapi, Indonesia

3.2 Generating an Independent Set of Double-Differences

When processing data from a local GPS network, double-differenced observables between pairs of receivers and pairs of satellites are used, rather than raw ‘one-way’ carrier phase measurements. The double-differences constructed from phase measurements made by two receivers m and n to two satellites i and j eliminate the two receiver clock biases and the two satellite clock biases (e.g. Hofmann-Wellenhof et al., 2001; Rizos, 1997):

$$\phi_{mn}^{ij} = \phi_n^j - \phi_n^i - \phi_m^j + \phi_m^i \tag{3-1}$$

ϕ_m^i denotes the ‘one-way’ carrier phase measurement between receiver m and satellite i.

In general, considering a network of r receivers tracking s satellites, the number of possible double-differences that can be formed is:

$$n_{DD} = \binom{s}{r} = \frac{s \cdot (s-1) \cdot (s-2) \cdot \ldots \cdot (s-r+1)}{1 \cdot 2 \cdot 3 \cdot \ldots \cdot r} \qquad (3\text{-}2)$$

However, only (r-1)·(s-1) of these double-differences are *linearly independent*. Hence any additional double-difference can be formed as a linear combination of the independent set of double-differences. These linearly dependent double-differences do not add any new information to the least squares data processing, and in fact artificially increase the redundancy, which is not desired. Usually the common satellites visible from all network GPS receivers are determined and a 'base station' and a 'base satellite' are selected to generate such an independent set of double-differenced observables.

Consider, for instance, two sites, both tracking the same seven satellites. If one of the receivers is selected as the 'base station' (say m = 1) and one of the satellites is selected as the 'base satellite' (say i = 1), six double-differenced observables ϕ_{12}^{1j} with j = 2, 3, …, 7 can be formed according to equation (3-1). However, this is not the only scheme available to obtain a set of independent double-differences. Another frequently used method is referred to as *sequential* double-differencing. Instead of using a 'base satellite' the satellites are sorted in ascending order and the double-differenced observable is formed between pairs of sequential satellites, in this example resulting in ϕ_{12}^{ij} with (i,j) = {(1,2), (2,3), …, (6,7)}. The situation becomes more complex when the network receivers each track some, but not all, of the satellites, as is likely in a local network around a volcano. The problem becomes apparent by expanding the previous example to three GPS network receivers each tracking some of the seven satellites, but with only three common satellites visible from all sites. If the usual base-station / base-satellite approach is used, only four double-differences can be formed in this case – not enough to obtain a coordinate solution for the two 'rover' sites. However, if satellites that are only visible by two of the three receivers were considered in the data processing, the number of double-differenced observables could be increased.

The data processing approach described here determines the receiver-to-satellite connections for each site of the network. A maximum set of independent double-differenced combinations is computed using vector space methods, and the geometric characterisations of Boolean matrices, as suggested by Saalfeld (1999). Hence, by using all the available information, the number of independent double-differenced observables can be optimised, permitting a more precise and reliable solution.

The Saalfeld (1999) algorithm uses a Boolean matrix of zeroes and ones to represent the receiver-to-satellite connections, where a 1 denotes that a certain satellite can be viewed by a certain network receiver. If this *connection matrix* is built so that the receivers are arranged in rows and the satellites are arranged in columns, an axis-parallel rectangle of 1s will represent a possible double-difference (Fig. 3.2).

	S_1	S_2	S_3	S_4	S_5	S_6	S_7	S_8	S_9
R_1	1	0	1	1	1	1	1	1	1
R_2	1	1	1	1	0	1	1	1	1
R_3	0	1	1	1	1	1	0	1	1
R_4	1	0	1	1	1	0	1	1	1
R_5	1	1	1	0	1	0	1	1	1
R_6	1	0	1	1	0	1	0	1	1

Fig. 3.2: Sample receiver-to-satellite connection matrix for 6 receivers and 9 satellites

For example, in Figure 3.2, a possible combination using receivers R_1 and R_2 and satellites S_3 and S_6 results in the double-differenced phase observable:

$$\phi_{12}^{36} = \phi_2^6 - \phi_2^3 - \phi_1^6 + \phi_1^3 \tag{3-3}$$

On the other hand, receivers R_1 and R_2 cannot form a double-difference with satellites S_2 and S_3. Some of the rectangles can be formed by appending or subtracting two other rectangles that share a common side. These newly formed rectangles correspond to linearly dependent double-differences. In Figure 3.2, the above mentioned double-difference can also be obtained by a linear combination of two other double-differences, e.g.

$$\phi_{12}^{36} = \phi_{12}^{34} + \phi_{12}^{46} \qquad \text{or} \qquad \phi_{12}^{36} = \phi_{12}^{16} - \phi_{12}^{13}\ . \tag{3-4}$$

The connection matrix is processed by rows, and within each row by columns. For each element containing a 1, the *submatrix* having this element in the lower-right corner is formed. Figure 3.3 shows the submatrix of connection matrix element a_{57}, which represents the connection between receiver R_5 and satellite S_7. The size of the submatrix is then reduced by removing all rows for which $a_{i7} = 0$ and all columns for which $a_{5j} = 0$, resulting in the *reduced submatrix* shown in Figure 3.4. The size of this submatrix is then further reduced by also removing the row corresponding to R_5 and the column referring to S_7. Thus, a matrix representing the possible upper-left corners of the rectangles having element a_{57} in their lower-right corner is created (Fig. 3.5). This matrix is referred to as the *upper-left corner matrix* and is used to identify the set of independent double-differences.

	S_1	S_2	S_3	S_4	S_5	S_6	S_7
R_1	1	0	1	1	1	1	1
R_2	1	1	1	1	0	1	1
R_3	0	1	1	1	1	1	0
R_4	1	0	1	1	1	0	1
R_5	1	1	1	0	1	0	1

Fig. 3.3: Submatrix of connection matrix element a_{57}

	S_1	S_2	S_3	S_5	S_7
R_1	1	0	1	1	1
R_2	1	1	1	0	1
R_4	1	0	1	1	1
R_5	1	1	1	1	1

Fig. 3.4: Reduced submatrix of connection matrix element a_{57}

	S_1	S_2	S_3	S_5
R_1	1	0	1	1
R_2	1	1	1	0
R_4	1	0	1	1

Fig. 3.5: Upper-left corner matrix of connection matrix element a_{57}

Two non-zero entries of the upper-left corner matrix are *path-connected* if there exists a sequence of 1s between them where successive elements are either in the same row or in the same column. The path-connected components in the upper-left corner matrix each consist of all the non-zero entries in a union of rows (or columns) of this matrix. Hence, whole rows either participate completely in the path-connected component or have no 1s intersecting the component. Two 1s in the upper-left corner matrix correspond to linear dependent double-differences if and only if they are in the same path-connected component. Hence, by finding all path-connected components of the upper-left corner matrix, and selecting a representative from each, the independent set of double-differences can be obtained. Note that this set no longer refers to just one base station and one specific base satellite.

In this example, Figure 3.5 contains only one path-connected component. If the upper-left most non-zero entry is selected as a representative, the resulting double-difference obtained here is ϕ_{15}^{17}. If the entire receiver-to-satellite connection matrix shown in Figure 3.2 is processed in such manner, the following set of 29 independent double-differences is generated:

$$\phi_{12}^{13},\ \phi_{12}^{14},\ \phi_{12}^{16},\ \phi_{12}^{17},\ \phi_{12}^{18},\ \phi_{12}^{19},\ \phi_{23}^{23},\ \phi_{13}^{34},\ \phi_{13}^{35},\ \phi_{13}^{36},\ \phi_{13}^{38},\ \phi_{13}^{39},\ \phi_{14}^{13},\ \phi_{34}^{14},$$
$$\phi_{14}^{15},\ \phi_{14}^{17},\ \phi_{14}^{18},\ \phi_{14}^{19},\ \phi_{25}^{12},\ \phi_{15}^{13},\ \phi_{15}^{17},\ \phi_{15}^{17},\ \phi_{15}^{18},\ \phi_{15}^{19},\ \phi_{16}^{13},\ \phi_{16}^{14},\ \phi_{16}^{16},\ \phi_{16}^{18},\ \phi_{16}^{19}.$$

Further details of the algorithm can be found in Saalfeld (1999).

3.3 Optimising the Double-Differencing Operator

The set of independent double-differences is used to construct the optimised double-differencing operator that transforms the one-way carrier phase measurements into independent double-differenced observables. This double-differencing operator will take into account all available information. If D denotes the double-differencing operator and Φ denotes the vector of one-way (satellite-to-receiver) carrier phase measurements, the vector of double-differences Φ_D is:

$$\Phi_{D} = D \cdot \Phi \tag{3-5}$$

In the example presented in Figure 3.2, assume a sub-network of three GPS receivers tracking seven satellites. The receiver-to-satellite connection matrix for this sub-network is shown in Figure 3.6.

	S_1	S_2	S_3	S_4	S_5	S_6	S_7
R_1	1	0	1	1	1	1	1
R_2	1	1	1	1	0	1	1
R_3	1	1	1	1	1	1	0

Fig. 3.6: Sample receiver-to-satellite connections for 3 receivers and 7 satellites

In commercial software, using the conventional data processing approach of one base station and one base satellite, only the common satellites are used to compute a solution. In this example, using R_1 as base station and S_1 as the base satellite, this approach results in six independent double-differences:

ϕ_{12}^{13}, ϕ_{12}^{14}, ϕ_{12}^{16}, ϕ_{13}^{13}, ϕ_{13}^{14}, and ϕ_{13}^{16}.

The resulting double-differencing operator D_{conv} has the form:

$$D_{conv} = \begin{bmatrix} 1 & -1 & 0 & 0 & -1 & 1 & 0 & 0 & 0 & 0 & 0 & 0 \\ 1 & 0 & -1 & 0 & -1 & 0 & 1 & 0 & 0 & 0 & 0 & 0 \\ 1 & 0 & 0 & -1 & -1 & 0 & 0 & 1 & 0 & 0 & 0 & 0 \\ 1 & -1 & 0 & 0 & 0 & 0 & 0 & 0 & -1 & 1 & 0 & 0 \\ 1 & 0 & -1 & 0 & 0 & 0 & 0 & 0 & -1 & 0 & 1 & 0 \\ 1 & 0 & 0 & -1 & 0 & 0 & 0 & 0 & -1 & 0 & 0 & 1 \end{bmatrix} \tag{3-6}$$

Each row corresponds to a double-difference, and each column represents a particular satellite (in this case S_1, S_3, S_4, and S_6). The first four columns are related to receiver R_1, while columns 5-8 and 9-12 refer to R_2 and R_3 respectively. The positions of the –1s, 0s and 1s within the matrix originate from the construction of a specific double-difference according to equation (3-1).

The alternative approach takes all available information into account resulting in nine double-differenced observables:

ϕ_{12}^{13}, ϕ_{12}^{14}, ϕ_{12}^{16}, ϕ_{12}^{17}, ϕ_{23}^{12}, ϕ_{13}^{13}, ϕ_{13}^{14}, ϕ_{13}^{15}, and ϕ_{13}^{16}.

The optimised double-differencing operator D_{opt} in this case is:

$$D_{opt} = \begin{bmatrix} 1 & 0 & -1 & 0 & 0 & 0 & 0 & -1 & 0 & 1 & 0 & 0 & 0 & 0 & 0 & 0 & 0 & 0 & 0 & 0 & 0 \\ 1 & 0 & 0 & -1 & 0 & 0 & 0 & -1 & 0 & 0 & 1 & 0 & 0 & 0 & 0 & 0 & 0 & 0 & 0 & 0 & 0 \\ 1 & 0 & 0 & 0 & 0 & -1 & 0 & -1 & 0 & 0 & 0 & 0 & 1 & 0 & 0 & 0 & 0 & 0 & 0 & 0 & 0 \\ 1 & 0 & 0 & 0 & 0 & 0 & -1 & -1 & 0 & 0 & 0 & 0 & 0 & 1 & 0 & 0 & 0 & 0 & 0 & 0 & 0 \\ 0 & 0 & 0 & 0 & 0 & 0 & 0 & 1 & -1 & 0 & 0 & 0 & 0 & 0 & -1 & 1 & 0 & 0 & 0 & 0 & 0 \\ 1 & 0 & -1 & 0 & 0 & 0 & 0 & 0 & 0 & 0 & 0 & 0 & 0 & 0 & -1 & 0 & 1 & 0 & 0 & 0 & 0 \\ 1 & 0 & 0 & -1 & 0 & 0 & 0 & 0 & 0 & 0 & 0 & 0 & 0 & 0 & -1 & 0 & 0 & 1 & 0 & 0 & 0 \\ 1 & 0 & 0 & 0 & -1 & 0 & 0 & 0 & 0 & 0 & 0 & 0 & 0 & 0 & -1 & 0 & 0 & 0 & 1 & 0 & 0 \\ 1 & 0 & 0 & 0 & 0 & -1 & 0 & 0 & 0 & 0 & 0 & 0 & 0 & 0 & -1 & 0 & 0 & 0 & 0 & 1 & 0 \end{bmatrix} \quad (3\text{-}7)$$

Obviously the optimised double-differencing operator matrix is of larger dimension than the conventional operator matrix because it considers all seven satellites in view across the network. The first seven columns relate these satellites to R_1, while columns 8-14 and 15-21 refer to R_2 and R_3 respectively.

Using a double-differencing operator in the multi-baseline data processing is one of the most efficient means of taking into account the between-baseline correlations (Craymer & Beck, 1992). This is discussed further in the next section.

3.4 Multi-Baseline Processing versus Baseline-By-Baseline Processing

Data collected by a network of GPS receivers can be processed essentially in two ways: (a) the multi-baseline mode, or (b) the single-baseline mode. Only the multi-baseline approach is rigorously correct because between-baseline correlations introduced by observing the baselines simultaneously are considered. However, most available commercial software are only capable of processing data in the single-baseline mode.

In the baseline-by-baseline approach, the data processing is done in two steps. First the single baseline solution vectors are obtained (neglecting the between-baseline correlations). These are then used as input for the second step, the network adjustment used to derive the final station coordinates. Normally a set of independent baseline solutions is selected for the network adjustment. Consider, for example, a network of four GPS sites denoted A, B, C and D. One possible set of independent baselines is AB, BC and CD; another consists of the baselines AB, AC and AD. However, the final coordinate results will be different, depending on which set of independent baselines is chosen. Hence the coordinate solution is not unique. Usually the shortest baselines are selected in order to reduce the impact of the unmodelled atmospheric biases.

Han & Rizos (1995) describe a methodology for obtaining more reliable results by processing all possible baselines in the single-baseline mode. In the subsequent network adjustment the baselines' co-factor matrices are scaled by r/2 (r being the number of network receivers) to account for the fact that all baselines are processed. However, this procedure is suitable only for exactly simultaneous sessions, i.e. all receivers commencing and stopping data collection at the same time. Moreover, the assumption of identical design matrices for all sites is only valid for small networks with baseline lengths of up to 20km. Ibid (1995) state that if outliers are present in the double-differenced data and are deleted during a baseline solution, the data for the same time interval should also be deleted for all other baseline determinations. This will lead to 'good' data (collected on baselines not affected by outliers) being discarded in the processing.

In multi-baseline mode the data processing is performed in one step. A double-differencing operator is formed for the whole network, resulting in a fully populated co-factor matrix that accounts for the between-baseline correlations. Also a stochastic model for double-differences is used. Applying the error-propagation law, the resulting co-factor matrix C_M is obtained by:

$$C_M = D_M \cdot C_\phi \cdot D_M{}^T \tag{3-8}$$

C_ϕ denotes the variance-covariance matrix of the raw carrier phase observations and D_M denotes the double-differencing operator. C_ϕ is a diagonal block matrix containing the a priori variances of the phase observations. The co-factor matrix C_M is fully populated, and the resulting coordinates are the same no matter which set of independent double-differences is selected.

The situation can be illustrated by referring to the earlier example. In a network of four GPS receivers A, B, C and D, three independent baselines AB, AC and AD can be formed with A being selected as the reference site. Let all receivers track the same four satellites and assume, for the sake of simplicity, the same variance σ^2 for all carrier phase observations from the receivers to the satellites. The variance-covariance matrix

$$C_\phi = \mathrm{diag}\,(\sigma^2) \tag{3-9}$$

has the dimension [r·s, r·s], r being the number of receivers and s denoting the number of satellites. In the baseline-by-baseline approach the three baselines are computed one after the other, resulting in a C_ϕ of dimension [8, 8]. Following equation (3-8), the co-factor matrices C_S for the single-baseline mode can be derived:

$$C_S{}^{AB} = C_S{}^{AC} = C_S{}^{AD} = \begin{bmatrix} 4s^2 & 2s^2 & 2s^2 \\ 2s^2 & 4s^2 & 2s^2 \\ 2s^2 & 2s^2 & 4s^2 \end{bmatrix} \tag{3-10}$$

Due to the assumptions made above, C_S is identical for the three baselines. In multi-baseline mode the baselines are processed together resulting in the co-factor matrix C_M:

$$C_M = \begin{bmatrix} C_S{}^{AB} & C_{AC}^{AB} & C_{AD}^{AB} \\ C_{AC}^{AB} & C_S{}^{AC} & C_{AD}^{AC} \\ C_{AD}^{AB} & C_{AD}^{AC} & C_S{}^{AD} \end{bmatrix} \tag{3-11a}$$

where

$$C_{AC}^{AB} = C_{AD}^{AB} = C_{AD}^{AC} = \begin{bmatrix} 2s^2 & s^2 & s^2 \\ s^2 & 2s^2 & s^2 \\ s^2 & s^2 & 2s^2 \end{bmatrix} \tag{3-11b}$$

The matrix C_{AC}^{AB} describes the correlation between the baselines AB and AC, which is neglected in the baseline-by-baseline solution. The matrices C_{AD}^{AB} and C_{AD}^{AC} have a similar structure. Figure 3.7 shows the general structure of the block matrix C_M for a network of four receivers. Note that all the correlations would be set to zero in single-baseline processing.

Baseline 1	Correlation 1-2	Correlation 1-3
Correlation 1-2	Baseline 2	Correlation 2-3
Correlation 1-3	Correlation 2-3	Baseline 3

Fig. 3.7: Structure of the resulting co-factor matrix C_M in multi-baseline mode

The effect of these correlations on GPS network computation was investigated by Santos et al. (1997). It was shown that by taking the between-baseline correlations into account, improved baseline results and more realistic precisions of the estimated baseline components can be obtained.

3.5 Ambiguity Resolution

In order to detect deformational signals over a short period of time, it is desired to compute a solution with minimum delay. Ideally, a coordinate set should be available each measurement epoch, effectively operating in a ‘kinematic’ mode of positioning. However, due to the nature of the carrier phase observations, the initially unknown integer ambiguities have to be resolved first. This process becomes increasingly difficult with decreasing observation session length, and is therefore a considerable challenge for single-epoch solutions unless the process is somehow aided. (Note that cycle slips do not have to be considered in an epoch-by-epoch solution such as this.)

Single-epoch solutions are desirable for deformation monitoring of hazardous structures such as volcanoes because they potentially produce near-real-time information about GPS baseline changes. Appropriate analysis of the time series of coordinate solutions enables authorities to put into effect plans that mitigate the impact of an eruption. Moreover, short-term movements can be picked up and used to better understand the dynamics of the deforming body. Solutions produced every few hours, or on a daily basis, will not be able to provide such detailed information. However, decreasing the observation period causes difficulties in ‘fixing’ the ambiguities to integer values. As the initial carrier phase ambiguity is constant as long as the receiver maintains lock on the satellite, the probability of its correct determination will increase with changing satellite geometry over time. Hence, ambiguity resolution can prove to be extremely difficult for single-epoch solutions, if no a priori information is available.

The basic approach to determining the integer ambiguities is to use the relatively noisy pseudorange measurements to define a search volume, which is assumed to contain the correct set of integer ambiguities. All possible integer ambiguity combinations are then tested to determine the best set, the test criterion often being the ambiguity set that minimises the sum of the squared double-differenced carrier phase residuals. A ratio test is performed between the sum of the squared carrier phase residuals of the 'best' and 'second best' sets, and if the ratio exceeds a certain threshold, then the 'best' set is accepted for fixing the carrier phase ambiguities. Han & Rizos (1996c) have identified six classes of ambiguity resolution (AR) techniques:

- AR using special operational modes, such as 'antenna swap' initialisation, re-occupation procedures, 'stop & go' and relative positioning of a single receiver (Remondi, 1988; Han & Rizos, 1996a).
- AR through a search in the 'Observation Domain', using pseudorange and carrier phase data based on linear combinations of the L1 and L2 carrier phase (with longer wavelength), and/or linear combinations of the L1 and L2 P-code pseudorange (with lower noise) (Han & Rizos, 1996c).
- AR through a search in the 'Coordinate Domain', such as in the case of the Ambiguity Function Method (AFM) (Remondi, 1989), which requires the use of accurate initial coordinates.
- AR through a search in the 'Estimated Ambiguity Domain' by first estimating the ambiguities as real-valued parameters, and then determining the likeliest integer ambiguities in a least squares estimation process. Examples include the Fast Ambiguity Resolution Approach (FARA) (Frei & Beutler, 1990), the Least Squares Ambiguity Search Technique (LSAST) (Hatch, 1990), the Cholesky Decomposition Method (Euler & Landau, 1992), the Fast Ambiguity Search Filter (FASF) (Chen, 1993) and the Least-squares Ambiguity Decorrelation Adjustment (LAMBDA) (Teunissen, 1995).
- The 'Ambiguity Recovery' technique, where the ambiguity search procedure is based on cycle slip estimation techniques (Han, 1995).
- The 'Integrated Method', which combines the techniques mentioned above, possibly with the addition of other physical sensors such as an Inertial Navigation System (INS), to aid ambiguity resolution (Abidin, 1993; Han & Rizos, 1996b).

Which AR technique is to be used generally depends on the application. The observation mode (e.g. static or kinematic positioning), the length of the observed baselines, the duration of the observation session and the processing mode (e.g. real-time processing or post-processing) all play a role in defining the optimal AR technique. In this case the AR search in the 'Estimated Ambiguity Domain' is adopted in a simplified form. First real-valued ambiguities are determined, which are then simply 'rounded-off' to integers in a second step. This is feasible if the real-valued ambiguity estimates are close to integer values, which is likely to be the case if accurate initial coordinates are available.

It is possible to use high accuracy initial coordinates (± 5cm) in order to aid the resolution of the carrier phase ambiguities on an epoch-by-epoch basis. The initial coordinates are typically obtained from the previous epoch's solution and can provide additional information for the parameter estimation. Hence they are introduced into the least squares process as fictitious 'observations' with their variance-covariance matrix (see equation 3-17). This procedure is suitable for the type of motion expected to occur on an active volcano. While, in times of increased activity, the ground deformation may be rather large, it will occur in a continuous manner. The volcano will not show any sudden 'jumps' between successive measurement epochs (generally 15 or 30 seconds apart).

The variance-covariance matrix C_{ϕ} used in the data processing contains a priori information about the precision of the observations. It can be used to increase the weight of 'good' observations in comparison to 'bad' observations (the weight matrix being the inverse of the variance-covariance matrix). This is particularly important if different types of geodetic measurements (e.g. GPS and spirit levelling or EDM) are combined in a least squares adjustment. For GPS networks it is often assumed that all observations taken between the network sites and the orbiting satellites are independent and of equal quality, resulting in the same diagonal matrix of equal variances for each GPS receiver (equation 3-9). In this case, however, a specific variance-covariance matrix C_{ϕ_i} is computed for each receiver i based on the elevation of the observed satellites, rather than assuming that the conditions at all network sites are the same. Hence, the resulting variance-covariance matrix C_ϕ for the whole network is a diagonal block matrix consisting of *different* C_{ϕ_i} matrices (r and s denoting the number of receivers and satellites, respectively):

$$C_\phi = \begin{bmatrix} C_{\phi_1} & 0 & \cdots & 0 \\ 0 & C_{\phi_2} & \cdots & 0 \\ \vdots & \vdots & \ddots & \vdots \\ 0 & 0 & \cdots & C_{\phi_r} \end{bmatrix} \tag{3-12a}$$

where

$$C_{\phi_i} = \begin{bmatrix} (\sigma_i^1)^2 & 0 & \cdots & 0 \\ 0 & (\sigma_i^2)^2 & \cdots & 0 \\ \vdots & \vdots & \ddots & \vdots \\ 0 & 0 & \cdots & (\sigma_i^s)^2 \end{bmatrix} \tag{3-12b}$$

It is well known that most of the residual unmodelled biases are dependent on the satellite elevation. An exponential function can be used to represent the standard deviation of the one-way L1 observations for satellite j (Han, 1997):

$$\sigma^j = s \cdot \left(a_0 + a_1 \cdot \exp(-E^j / E_0) \right) \tag{3-13}$$

where σ^j is the standard deviation of the L1 observations for satellite j with elevation angle E^j. The s represents a scale factor. The values for a_0, a_1 and E_0 are approximated by constants, which can be empirically determined. Table 3.1 shows the values for L1 carrier phase observations, obtained by Ibid (1997), which are used in the UNSW-designed baseline processing software. The corresponding values for pseudorange observations are also given.

Tab. 3.1: Standard deviation of one-way L1 observations

	a_0 [m]	a_1 [m]	E_0 [°]
Carrier phase observations	0.003	0.026	20
Pseudorange observations	0.070	0.600	20

In the usual least squares procedure the unknown parameter correction vector δX is determined using the equations (e.g. Harvey, 1994; Koch, 1999):

$$V = A \cdot \delta X_0 - L \tag{3-14}$$

$$\delta X = (A^T P A)^{-1} A^T P L \tag{3-15}$$

where V = error vector
A = design matrix
δX_0 = vector of initial coordinates
L = observation vector
P = weight matrix

The root mean square is:

$$RMS = \sqrt{\frac{V^T P V}{n - u}} \tag{3-16}$$

where n = number of observations
u = number of unknowns

If the initial coordinates X_0 are introduced as 'observations' with their variance-covariance matrix D_X, which is equivalent to the Bayesian least squares approach (see Koch, 1990), the equations are as follows (Kleusberg & Teunissen, 1996; Vaniček & Krakiwsky, 1986):

$$\delta X = (A^T P A + D_X{}^{-1})^{-1} A^T P L \tag{3-17}$$

$$RMS = \sqrt{\frac{V^T P V + \delta X^T D_X{}^{-1} \delta X}{(n + u) - u}} = \sqrt{\frac{V^T P V + \delta X^T D_X{}^{-1} \delta X}{n}} \tag{3-18}$$

3.6 Numerical Example

Data collected from a network of six GPS receivers in Sydney, Australia, with baseline lengths ranging from 2.0 to 2.7km were used to test the data processing procedure. Figure 3.8 shows the location of the network sites, which were carefully chosen to ensure a clear skyview. A 2-hour session was observed on October 12, 1999 using Leica CRS1000 receivers, equipped with choke ring antennas to minimise the effect of multipath. The sampling rate was set to 30 seconds, with a satellite elevation mask angle of 15°.

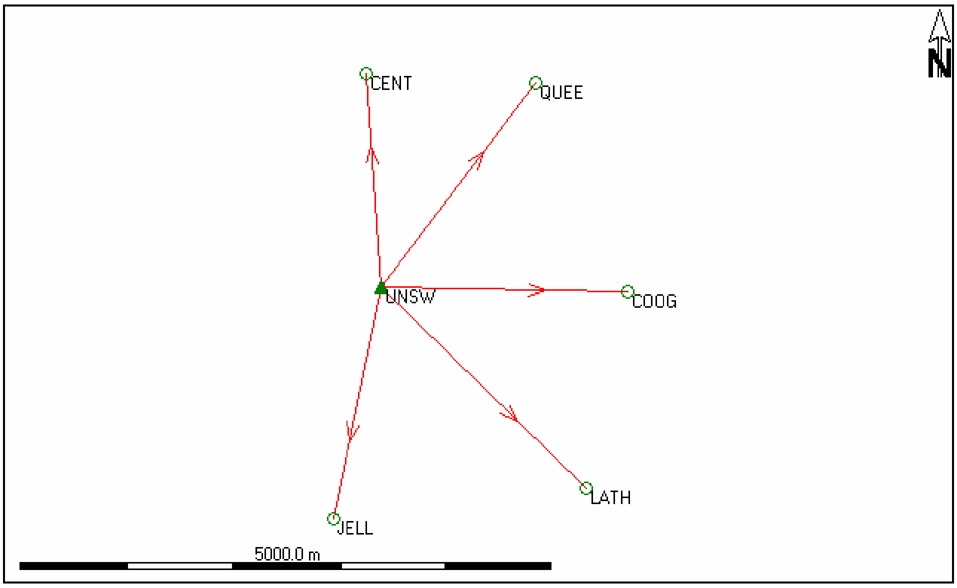

Fig. 3.8: GPS test network at UNSW

The coordinate results obtained from the processing of the 2-hour session were used as the 'true' coordinates against which the single-epoch solutions were compared. The data set was then altered by manually editing data at the network stations. At each site a different azimuth band of 40° pointing towards the centre of the network, with satellite elevations of less than 50°, was blocked out in order to simulate the situation around a volcano. The results of the epoch-by-epoch solution using conventional double-differencing and the proposed approach were compared.

Using the proposed approach, the number of double-differenced observables at each epoch was increased by an average of 9.8 observables, with a maximum difference between the approaches being 20 observations (Fig. 3.9). The minimum number of independent double-differenced observables required to obtain a solution for a network of six sites is 15. For certain epochs no solution could be obtained using the conventional approach because the number of common satellites tracked by all network receivers dropped to three, resulting in only 10 double-differenced observables. However, using the proposed double-differencing approach satisfactory solutions could be obtained for these epochs.

Figure 3.9 also shows the root mean square of the double-differenced residuals. While the RMS for the proposed method is often slightly higher than for the common method, it shows less variation. The standard deviation of the root mean square was reduced by 34%, from 0.1232m to 0.0811m.

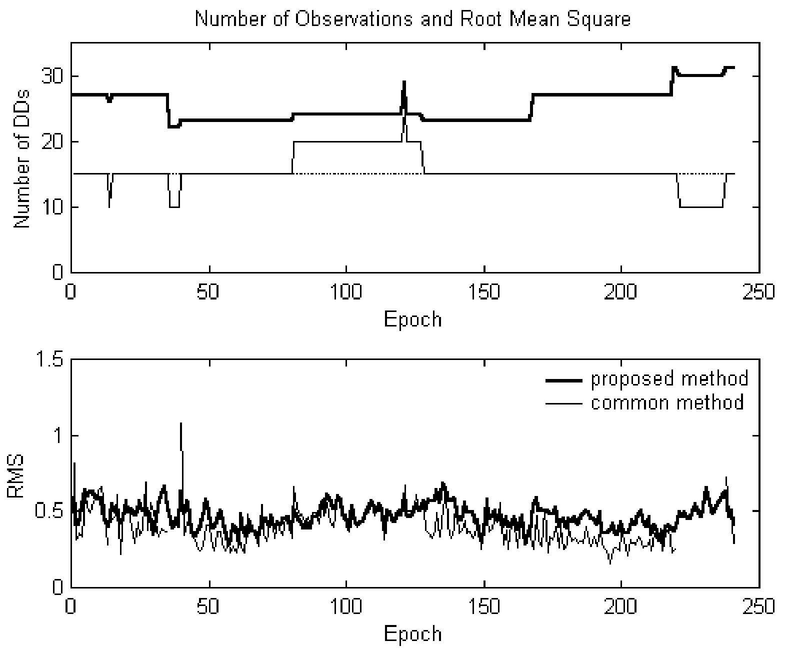

Fig. 3.9: Number of double-differenced observations and RMS of epoch-by-epoch solutions

The coordinates obtained by both data processing approaches were compared against the ‘true’ coordinate values. Figures 3.10a-e show the resulting coordinate differences. Note that the gaps in the curves representing the ‘common satellite method’ are caused by an insufficient number of double-differenced observables for those epochs. It can be seen that the proposed method increases the quality of the results. The coordinate variations obtained using the proposed method are also smaller. This can be verified from the standard deviations of the X-, Y- and Z-components shown in Figures 3.11a-e.

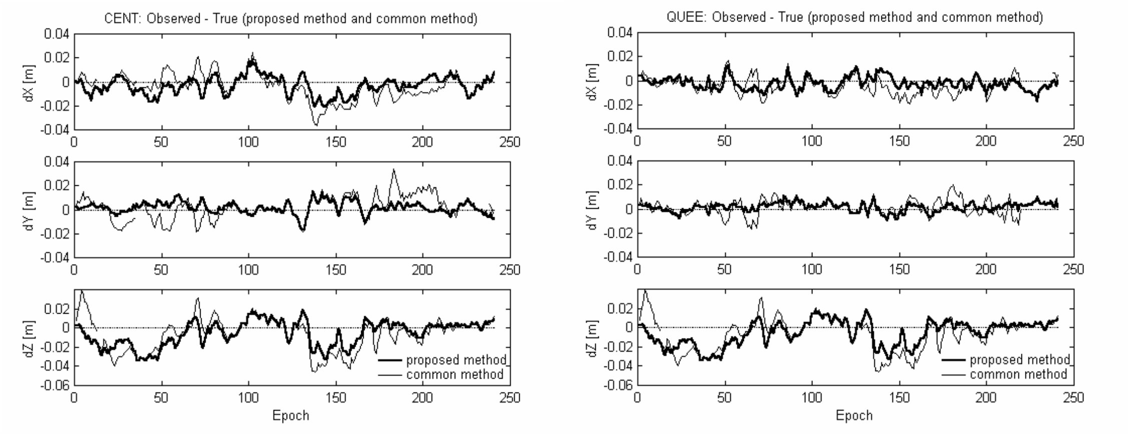

Fig. 3.10a+b: Solution coordinates compared to ‘truth’ (left: CENT, right: QUEE)

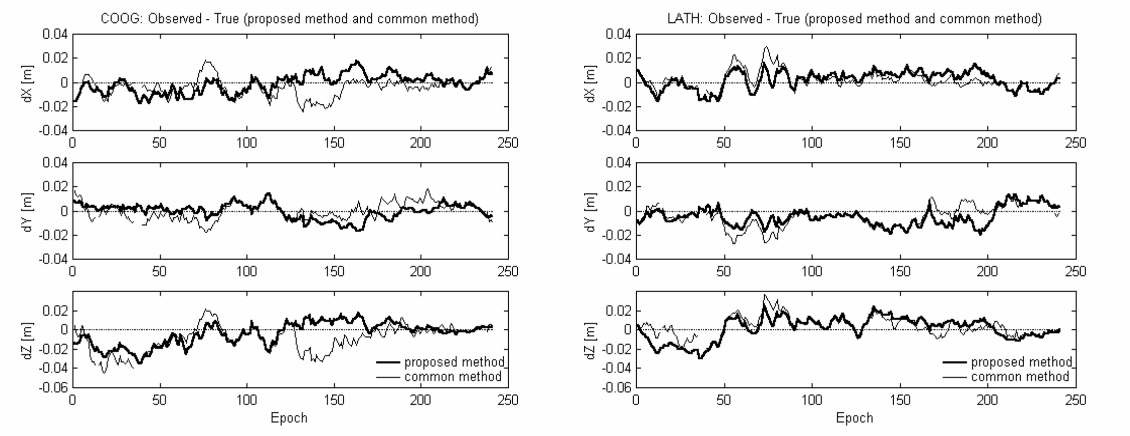

Fig. 3.10c+d: Solution coordinates compared to ‘truth’ (left: COOG, right: LATH)

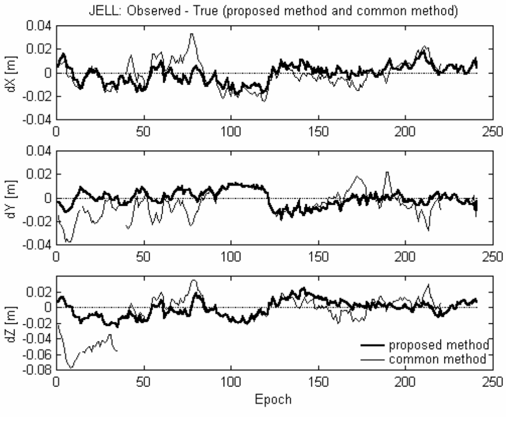

Fig. 3.10e: Solution coordinates compared to ‘truth’ (JELL)

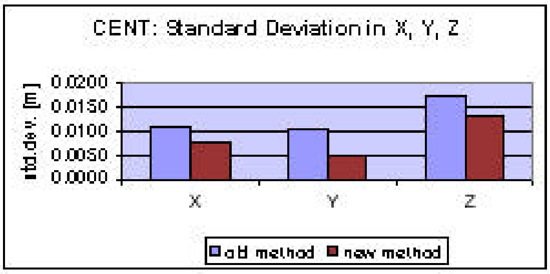

Fig. 3.11a: Standard deviations (CENT)

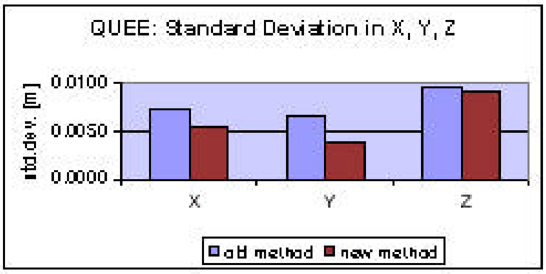

Fig. 3.11b: Standard deviations (QUEE)

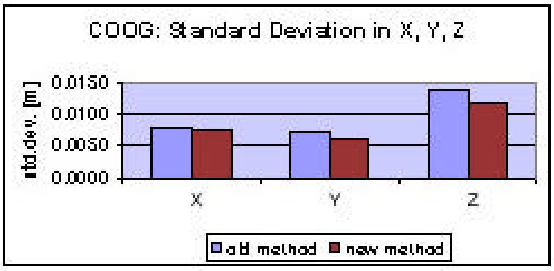

Fig. 3.11c: Standard deviations (COOG)

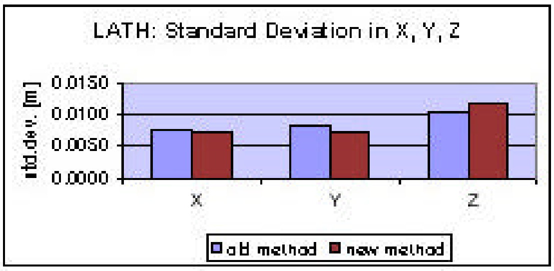

Fig. 3.11d: Standard deviations (LATH)

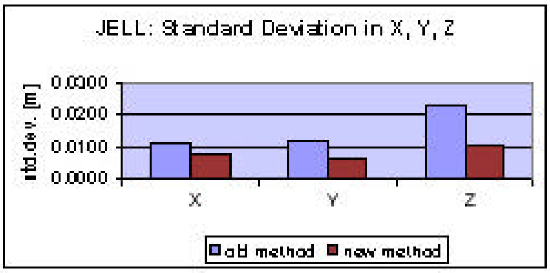

Fig. 3.11e: Standard deviations (JELL)

The reason for obtaining better coordinate results with the proposed method in spite of slightly higher RMS (or standard deviation) values of the double-differenced residuals (see Fig. 3.9) lies in the increased number of observations. If σ^2_{obs} denotes the variance of a single observation and n is the number of observations, then the variance of the mean σ^2_m is defined as:

$$\sigma^2_m = \frac{\sigma^2_{obs}}{n} \tag{3-19}$$

Assuming, for example, $\sigma_{obs} = 0.4$ and $n = 16$ yields $\sigma_m = 0.10$, while a slightly higher standard deviation σ_{obs} of 0.5 with a larger number of double-differenced observations $n = 36$ results in $\sigma_m = 0.08$.

3.7 Concluding Remarks

A number of GPS deformation monitoring applications have to deal with the problem of the deforming body itself blocking out part of the sky, thereby effectively reducing the number of satellites that can be tracked by the monitoring GPS receivers. This chapter has described a method to optimise the number of double-differenced GPS observations by generating a set of independent double-differenced combinations using vector space methods, and the geometric characterisations of Boolean matrices, based on the algorithm by Saalfeld (1999).

A numerical example has demonstrated that the proposed data processing methodology does indeed improve the coordinate results. The number of double-differenced observables available to compute a solution is maximised by using all available information, thereby improving the quality of the results. A solution can be obtained even if less than four common satellites can be tracked simultaneously at all network sites. Hence the problem of the deforming body obstructing part of the sky, reducing the effectiveness of certain deformation monitoring applications, can be overcome using this data processing approach.

The benefits of processing a GPS network in multi-baseline mode as opposed to baseline-by-baseline processing, as well as the appropriate ambiguity resolution technique to be used for monitoring applications, have been discussed.

Chapter 4

IONOSPHERIC CORRECTIONS TO IMPROVE GPS-BASED VOLCANO DEFORMATION MONITORING

4.1 Introduction

The ionosphere is part of the earth’s upper atmosphere and located at a height of between 50-1000km above the surface. Its high spatial and temporal variability has a significant effect on GPS signals travelling from the satellites to the receivers. Moreover, the condition of the ionosphere is strongly related to the 11-year solar cycle. Hence, in a local deformation monitoring network the ionospheric effect has to be accounted for, even for short baselines, and especially in equatorial regions.

This chapter describes the ionosphere and its effects on the GPS signals. A procedure to adjust single-frequency GPS observations for the ionospheric delay effects using empirical corrections derived from a dual-frequency network of reference receivers is described. The nature of these correction terms is investigated by analysing GPS data collected over baselines of varying length, in different geographical locations, and at different periods of sunspot activity (and hence varying ionospheric conditions).

4.2 Sunspot Number and the Solar Cycle

Sunspots are the physical expression of complex magneto-dynamical processes within the Sun and are seen as dark areas on the solar disk that wax and wane (NASA, 2002). Sunspots are darker than their surrounding area because they are cooler than the average temperature of the solar surface, and can therefore easily be observed. The pattern of sunspots on the Sun varies on timescales from a few hours to many years. An index called the *sunspot number* was introduced approximately 300 years ago and has since continued to be used to quantify the abundance of spots.

The sunspot number (here denoted SSN) is defined as (IPS, 2002):

$$SSN = K\,(10 \cdot G + I) \tag{4-1}$$

where G is the number of sunspot groups visible on the Sun; I is the total number of individual spots; and K is an instrumental factor to take into account differences between observers and observatories.

In this context it is necessary to clarify a few terms associated with solar activity. As explained in Knight (2000), sudden increases in the intensity of solar radiation associated with sunspot activity are known as *solar flares*. *Solar winds* are particles charged with high energy that are emitted from the Sun. *Coronal holes* are low density regions of the solar corona that are associated with these solar winds. *Geomagnetic storms* are large variations in the strength and direction of the earth’s magnetic field caused by eruptions on the Sun that eject a mixture of electrons, protons and ions into the solar wind.

The solar cycle has an average length of 11 years. However, cycles vary considerably in length from as short as 9 years up to almost 14 years (IPS, 2002). Due to its large day-to-day variability the sunspot number is usually averaged over a month. If smoothed over a 13-month period, the SSN effectively charts the progress of the solar cycle. The daily and monthly averages exhibit considerable variation with respect to the smoothed curve due to bursts of rapid solar region growth often associated with events like solar flares. Figure 4.1 shows the monthly sunspot numbers for the entire historical record (top) and for the most recent solar cycle 23 (bottom). The sunspot data are freely available on the internet (NASA, 2002; IPS, 2002). In the bottom graph the high-frequency curve depicts the observed monthly sunspot number, while the low-frequency curve shows the smoothed (solid line) and predicted (dashed line) monthly values. The most recent solar maximum occurred in 2000; however, the ionospheric activity remains high for several years after the solar maximum.

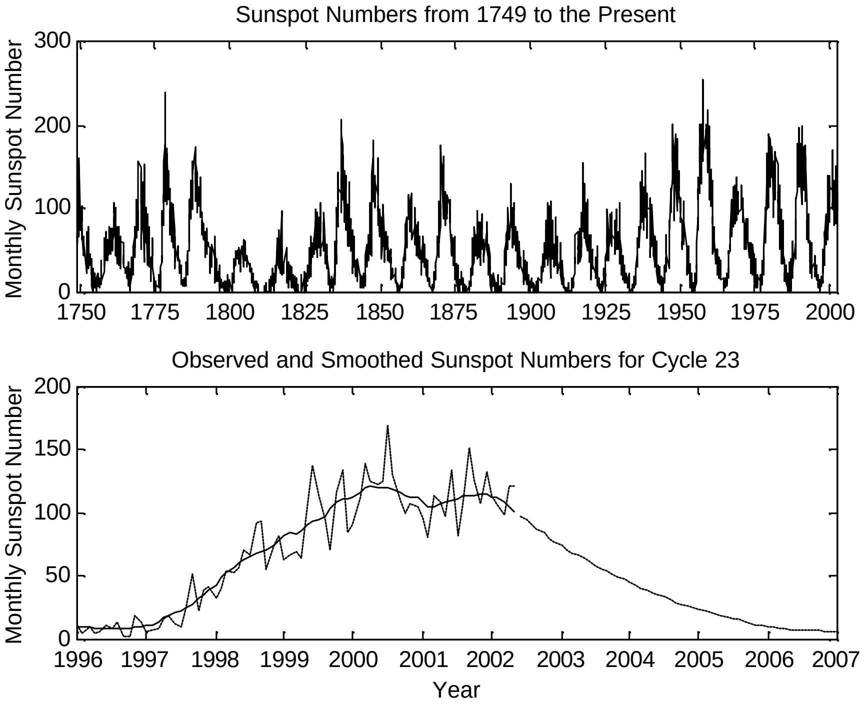

Fig. 4.1: Sunspot numbers from 1749 until the present (top) and for the current cycle 23 (bottom)

4.3 The Ionosphere

The ionosphere is a band of the atmosphere located approximately 50-1000km above the earth’s surface, thinning into the plasmasphere (or protonosphere) and eventually into the interplanetary plasma at greater heights. Most of the ionosphere is electrically neutral, but ionisation results when solar radiation strikes the ionosphere. The upper atmosphere then becomes an electrical conductor, which supports the flow of electric currents, and hence affects the propagation of radio waves. The condition of the ionosphere is strongly related to the 11-year solar cycle (see previous section).

The ionosphere is traditionally divided into several regions (D, E and F) and layers, on the basis of the level of ionisation within a region (Anderson & Fuller-Rowell, 1999; Goodman & Aarons, 1990). Figure 4.2 shows the ionospheric layers and the principle ions that compose each region; the electron density is also included (in units of electrons/cm^3). The F2 layer is particularly important for GPS because here the electron concentrations reach their highest values. The effect of the ionosphere on GPS signals travelling from the satellites to the receivers is dependent on the electron content along the signal path and the frequency of the signal (Seeber, 1993). Other factors influencing the ionospheric refraction are geographic location, the period in the solar cycle and time of day.

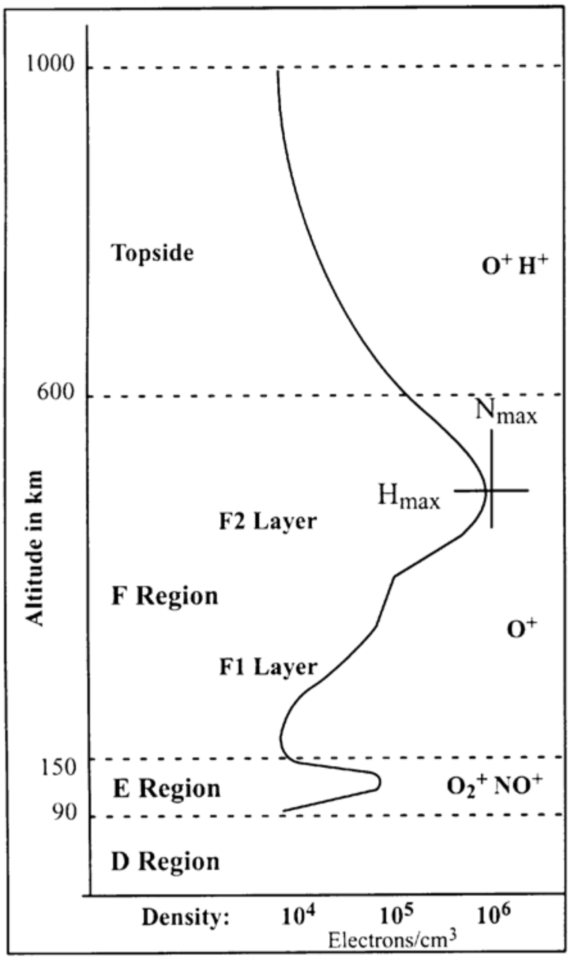

Fig. 4.2: Regions and layers of the ionosphere, their predominant ion populations and electron density (Anderson & Fuller-Rowell, 1999)

The propagation speed v of a signal is related to the refractive index n according to (e.g. Hofmann-Wellenhof et al., 2001; Rizos, 1997):

$$v = \frac{c}{n} \tag{4-2}$$

where c is the speed of electromagnetic radiation in a vacuum. Note that the refractive index is dimensionless.

Seeber (1993) gives a useful approximate expression for the refraction coefficient n_p for carrier phase observations:

$$n_p = 1 - 40.3 \cdot \frac{n_e}{f^2} \tag{4-3}$$

where n_e = electron density integrated along the signal propagation path [electrons/m^3]
f = carrier frequency [MHz]

Note that the coefficient 40.3 contains several constant parameters including their dimensions. The refraction coefficient for the pseudorange measurement n_g is of the same size but opposite sign:

$$n_g = 1 + 40.3 \cdot \frac{n_e}{f^2} \tag{4-4}$$

This indicates that measured pseudoranges are ‘too long’ compared to the geometric distance between satellite and receiver, while carrier phase observations are ‘too short’. The terms *group delay* and *phase advance* are also used in this context (Kleusberg & Teunissen, 1996). Note that n_g is expressed as a group index (a wave group generated by superposition of different waves of different frequencies), as opposed to the phase index n_p of a particular wave with constant wavelength. Note also that the electron density n_e must be known in order to determine the refraction indices.

Integrating the electron density along the signal path results in the widely used TEC measure (Total Electron Content), expressed in TEC units (TECU), with 1 TECU corresponding to 10^{16} free electrons per m^2. TEC is highly variable on both a temporal and spatial basis. However, the dominant variability is diurnal. TEC is a function of many variables, including long and short term fluctuations in solar radiation, magnetic activity, season, time of day, user location and viewing direction (Klobuchar, 1987). Generally, the equivalent vertical TEC (VTEC) is determined by dividing the slant TEC by the secant of the zenith angle at a mean ionospheric height (usually between 350 and 400km) in order to permit convenient comparison between different data sets. Typical daytime values of VTEC for mid-latitude sites are of the order of 10^{18} electrons/m^2 with corresponding nighttime values of 10^{17} electrons/m^2. However, these values can be exceeded by a factor of two or more, especially in near-equatorial regions (Kleusberg & Teunissen, 1996). Values of TEC from 10^{16} to 10^{19} electrons/m^2 represent the extremes observed in the earth's ionosphere (Klobuchar, 1996).

The ionosphere is a dispersive medium for microwaves, i.e. the refractivity depends on the frequency of the propagating signal. Hence, measurements on both the L1 and L2 frequencies can be used to account for the ionospheric effect on GPS observations (see section 4.4).

The ionosphere is most active in a band extending up to approximately 20° on either side of the geomagnetic equator (Fig. 4.3). This is also one of the two regions where small-scale ionospheric disturbances (*scintillations*) mainly occur. The other being the high-latitude (auroral) regions close to the poles.

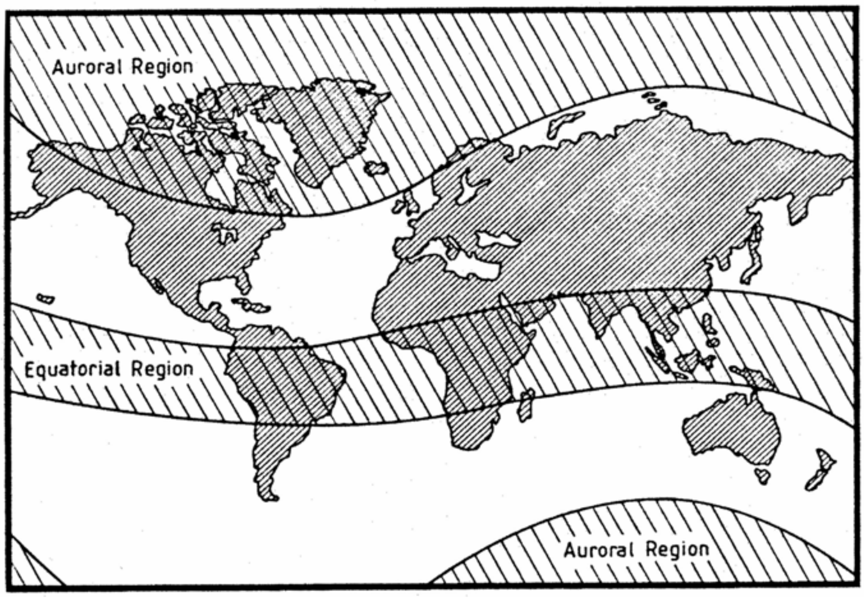

Fig. 4.3: Regions of the world with high ionospheric activity (Seeber, 1993)

Scintillations are short-term variations in the amplitude and phase of radio signals travelling through the ionosphere. While auroral and polar scintillations are mainly the result of geomagnetic storms that are associated with solar flares and coronal holes, in the equatorial region scintillations are caused by irregularities in the F-layer of the ionosphere following the passage of the 'evening terminator', the boundary that divides day from night (Knight, 2000). They generally occur between approximately one hour after sunset until midnight (Klobuchar, 1996) and should have disappeared by 3am local time (IPS, 2002). Figure 4.4 illustrates the L-band ionospheric scintillation fading depths for solar minumum and maximum conditions. Note that the main anomaly region located at ±15° of the geomagnetic equator experiences the deepest signal fades of up to 20dB below the mean signal level. Less intense fading is experienced at the geomagnetic equator and in regions surrounding the main anomaly region.

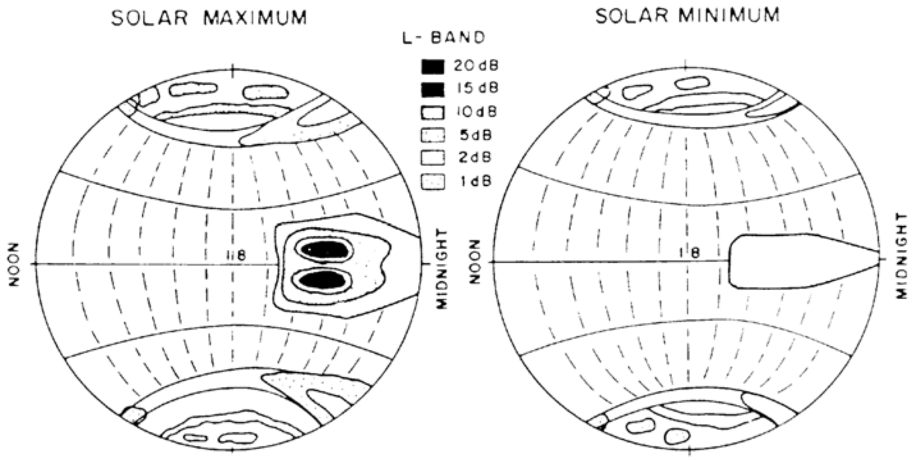

Fig. 4.4: Ionospheric scintillation during high and low solar activity
(Goodman & Aarons, 1990)

The occurrence of scintillations also varies with the seasons. Between April and August they are less severe in the American, African and Indian longitude regions, but are at a maximum in the Pacific region, while the situation is reversed from September to March (Seeber, 1993). Using data collected at a site located very close to the geomagnetic equator in Peru over three and a half years from January 1997, Doherty et al. (2000) studied the seasonal dependence of scintillation activity in the equatorial region. Their study revealed virtually no trace of scintillations in the months between June and August, while peak occurrence could be observed in the equinox seasons. A clear increase in scintillation effects with increasing sunspot activity (approaching a solar maximum) was also apparent.

High-latitude scintillations are strongly dependent on geomagnetic activity levels, but can occur in all seasons and are not limited to the local nighttime hours (Essex et al., 2001; Doherty et al., 2000). In mid-latitudes scintillations are rarely observed, but Medium-Scale Travelling Ionospheric Disturbances (MSTIDs) occur frequently, mainly in the daytime in the winter months, during periods of high solar activity, with a maximum around local noon (Wanninger, 1999). In all regions, however, increased solar activity amplifies scintillation frequency and intensity. Numerous researchers have investigated the nature of the scintillations and their impact on GPS observations. The results of these studies can readily be found in the literature (e.g. Dodson et al., 2001; Fedrizzi et al., 2001; Fu et al., 1999; Knight et al., 1999; Nichols et al., 1999).

The effect of the ionosphere on GPS coordinate solutions can be very severe, even on short baselines. Wanninger (1993) reports that single-frequency data from a 10km baseline located in southern Brazil, which was processed in data blocks of one hour, showed coordinate errors of 1cm (or 1ppm of the baseline length) before sunrise, of up to 5cm (5ppm) during the daylight hours, and more than 30cm (30ppm) between sunset and midnight.

With the removal of Selective Availability in May 2000, the ionosphere is now the largest individual systematic error in the GPS error budget, accounting for as much as 80% or more (Kunches & Klobuchar, 2001). The ionospheric range error on L1 in the zenith direction can reach 30m or more, and near the horizon this effect is amplified by a factor of about three (Kleusberg & Teunissen, 1996).

4.4 Ionospheric Corrections for Dual-Frequency Users

Due to the dispersive nature of the ionosphere, a linear combination of the L1 and L2 measurements can be formed to correct for the ionospheric delay. In the case of pseudorange measurements, the ionospheric bias can be estimated and subsequentially removed from the L1 measurements by forming the linear combination (Kleusberg & Teunissen, 1996):

$$d_{ion} = \frac{f_2^{\,2}}{f_2^{\,2} - f_1^{\,2}} \cdot [P_1 - P_2] \tag{4-5}$$

where f_1 and f_2 are the L1 and L2 carrier frequencies respectively, and P_1 and P_2 are the L1 and L2 pseudorange measurements.

Similarly, carrier phase measurements can be corrected using:

$$d_{ion} = \frac{f_2^{\,2}}{f_2^{\,2} - f_1^{\,2}} \cdot \left[(\lambda_1 N_1 - \lambda_2 N_2) - (\phi_1 - \phi_2) \right] \qquad (4\text{-}6)$$

where ϕ_1 and ϕ_2 are the L1 and L2 carrier phase measurements (in units of length) respectively, λ_1 and λ_2 are the L1 and L2 carrier wavelengths, and N_1 and N_2 are the L1 and L2 interger cycle ambiguities. The absolute values of N_1 and N_2 cannot be determined, but they remain constant for continuous observations without cycle slips. Hence the variation in the ionospheric delay, also called the differential ionospheric delay, can be obtained.

The ionospheric effect on carrier phase observations can be eliminated by forming the so-called L3 or *ionosphere-free* linear combination (e.g. Leick, 1995; Hofmann-Wellenhof et al., 2001; Rizos, 1997):

$$\phi_3 = \frac{f_1^{\,2}}{f_1^{\,2} - f_2^{\,2}} \cdot \phi_1 - \frac{f_1 f_2}{f_1^{\,2} - f_2^{\,2}} \cdot \phi_2 \qquad (4\text{-}7)$$

For double-differenced observables, the above equation can be written as (Rizos, 1997):

$$\nabla\Delta\phi_{1,\,iono-free} = \nabla\Delta\rho + \frac{f_1^{\,2}}{f_1^{\,2} - f_2^{\,2}} \cdot \nabla\Delta N_1 - \frac{f_1 f_2}{f_1^{\,2} - f_2^{\,2}} \cdot \nabla\Delta N_2 \qquad (4\text{-}8)$$

Similarly, a pseudorange L3 linear combination can also be formed (Ibid, 1997). However, measurements on both frequencies are obviously needed to determine these corrections.

The Center for Orbit Determination in Europe (CODE), located at the University of Berne in Switzerland, generates daily global ionosphere maps (GIMs) based on data collected at global IGS sites. Schaer et al. (1996) describe the procedure as follows. The geometry-free linear combination of double-differenced carrier phase observations made by the IGS network are processed to extract the global TEC information. Data are processed with a 3-minute observation rate using an elevation cut-off angle of 20°. The global TEC distribution is represented over 24 hours by spherical harmonics up to degree

8 in a geographical reference frame, which is rotating with the mean Sun. A spherical ionospheric shell at a height of 400km above the earth's mean surface is adopted. Figure 4.5 shows an example of a global ionosphere map. While the TEC values range from 2-12 at a latitude of 45°N, they show much larger variations of between 2-34 at the equator. Also note the steep gradients in TEC just after sunset (90° sun-fixed longitude) and around midnight (180° sun-fixed longitude) in the equatorial region.

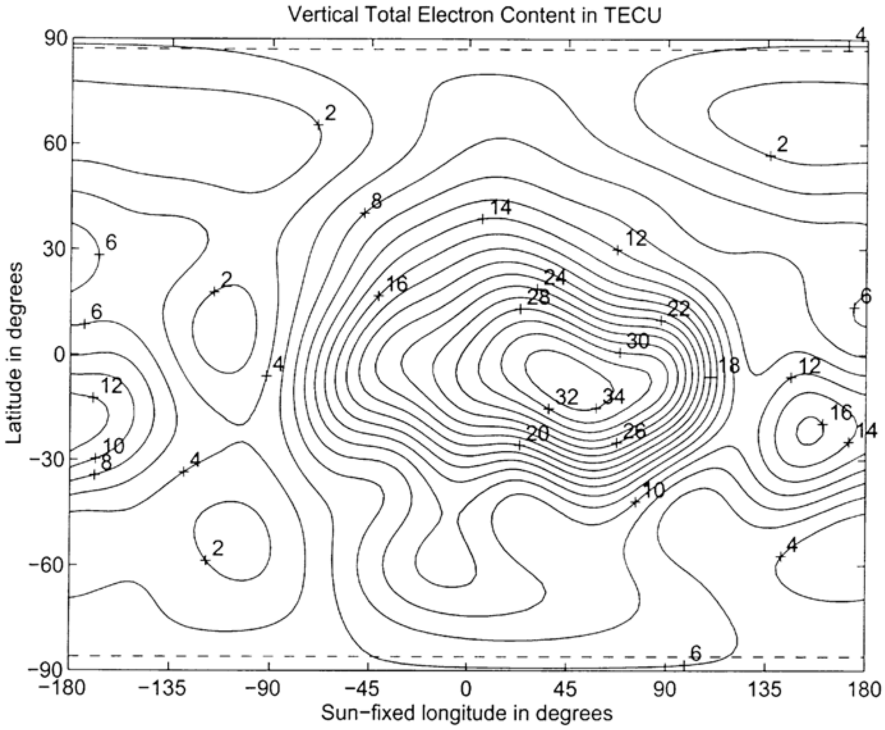

Fig. 4.5: Global Ionosphere Map (GIM) for day 073, 1996 (Schaer et al., 1996)

These maps are available on the internet (AIUB, 2002). However, being global maps, they are not very effective in modelling the ionospheric conditions in local GPS networks for short observation periods. Moreover, even though there are a large number of IGS sites, they are unevenly distributed, with most of the GPS stations being situated in the mid-latitude region of the northern hemisphere. The smaller number of GPS receivers in the equatorial region and the southern hemisphere, and consequently the reduced number of available TEC measurements, results in the ionospheric modelling to be less accurate for these regions.

4.5 A Mixed-Mode GPS Network Processing Approach to Account for the Ionospheric Effect

In general it is assumed that short baselines (say up to 10km in length) are not severely affected by ionospheric and tropospheric delays, as the GPS signals propagate through essentially the same portion of the atmosphere. Hence the bias effects will be very similar at either end of the baseline, and therefore effectively cancel in between-receiver data differencing, which is part of the double-differencing process. However, the geographical location in the equatorial region, and the significant height differences of 1400m between single-frequency receivers on an Indonesian volcano, make such assumptions questionable, even for short baselines.

While data from dual-frequency GPS receivers can account for the ionospheric delay directly (by the appropriate linear combination of measurements made on both frequencies – section 4.4), data from single-frequency receivers cannot be corrected in this way. Single-frequency GPS data processing can use a simple ionosphere model transmitted within the navigation message to account for about 50% RMS of the ionospheric range delay (see Klobuchar, 1987, for details of the model). However, this is not sufficient for volcano deformation monitoring applications where the objective is to detect movements of a few centimetres or less. Moreover, it cannot model the highly variable (in location and magnitude) TEC behaviour in equatorial regions, where most of the world's volcanoes are located.

In order to optimise the single-frequency volcano deformation monitoring system described in chapter 2, a network of three dual-frequency GPS receivers surrounding the deformation zone has been proposed. In this *mixed-mode* GPS network approach, the dual-frequency receivers would be used to generate 'correction terms', which can then be applied to the single-frequency observations to account for the ionospheric biases. Over the last few years several methods have been developed to generate ionospheric corrections based on a network of reference stations (e.g. Camargo et al., 2000; Chen et al., 2000; Odijk et al., 2000; Rocken et al., 2000; Yuan & Ou, 2001).

As described in Han (1997), such a *fiducial* network should ideally surround the inner single-frequency network (see Fig. 2.13). The fiducial reference stations operate continuously in order to determine a regional ionosphere model on an epoch-by-epoch and satellite-by-satellite basis, as proposed by Wanninger (1995). A single layer ionospheric model at a height of typically 350km is used, where it is assumed that the entire ionospheric layer is compressed into an infinitesimally thin surface (Fig. 4.6). In the case of a relatively small fiducial network, with baseline lengths of no more than 80km, the slant ionospheric delay measured at the reference stations can be considered to be in the zenith direction. The variation in the ionospheric delay across the network is also assumed to be linear. It should be noted that this assumption may not be valid in periods of increased solar activity due to the highly variable (in space and time) scintillation effects.

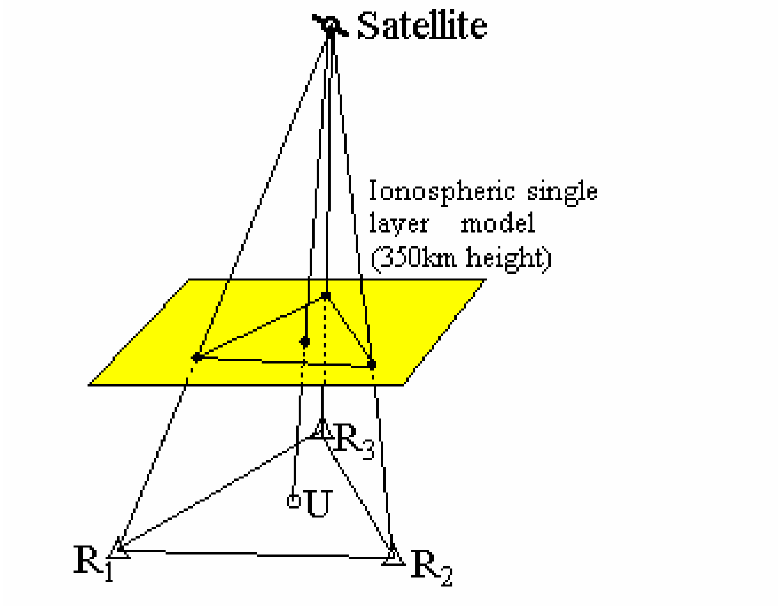

Fig. 4.6: Differential model of the ionospheric delay (Han & Rizos, 1996d)

At every epoch the ionospheric delay for the L1 signal can be determined relative to the reference receiver and the reference satellite (Han & Rizos, 1996d):

$$I_i^j(k) = \frac{f_2^2}{f_1^2 - f_2^2} \cdot \left(\left(\Delta\nabla\phi_{L1}^{j,i}(k) - \lambda_1 \cdot \Delta\nabla N_{L1}^{j,i} \right) - \left(\Delta\nabla\phi_{L2}^{j,i}(k) - \lambda_2 \cdot \Delta\nabla N_{L2}^{j,i} \right) \right) \tag{4-9}$$

where $\Delta\nabla\phi_{L1}^{j,i}(k)$, $\Delta\nabla\phi_{L2}^{j,i}(k)$ are the double-differenced observables of the L1 and L2 carrier phase (in units of metres) relative to the reference receiver and the reference satellite. Note that for a rising satellite, no ionospheric corrections can be applied until the ambiguities for that satellite have been resolved.

The ionospheric delay can then be expressed as:

$$I_i^j(k) = x_i \cdot a_N^j(k) + y_i \cdot a_E^j(k) \tag{4-10}$$

where $a_N^j(k)$ and $a_E^j(k)$ represent the north and east slope components for satellite j relative to the reference satellite and the reference station at epoch k. The slope parameters are unique to each satellite/receiver pair and change over time as the satellites move across the sky. The parameters x_i and y_i refer to the relative location of the reference station i.

This correction approach linearly interpolates the TEC across a surface and approximates the ionospheric delay at any point within the fiducial triangle. However, it cannot entirely account for scintillation effects, which can be highly localised.

The ionospheric correction method described above is part of the linear combination model proposed by Han & Rizos (1996d) and Han (1997). This model can account for orbit bias and ionospheric delay, as well as mitigate tropospheric delay, multipath and measurement noise across the network. Thus, data from the fiducial GPS reference station network can be used to derive empirical corrections to the double-differenced carrier phase data formed between the stations of the inner network. The procedure was investigated by Chen (2001) and Chen et al. (2001a), and is described in this section.

4.5.1 Single-Differenced Model

The single-differenced carrier phase observation can be written as (Han, 1997):

$$\Delta\phi = \Delta\rho + \Delta d\rho - c \cdot \Delta dT + \lambda \cdot \Delta N - \Delta d_{ion} + \Delta d_{trop} + \Delta d_{mp}^{\phi} + \varepsilon_{\Delta\phi} \tag{4-11}$$

where Δ = single-difference operator (difference between user and reference receiver)

ϕ = carrier phase observation in units of metres

ρ = distance between receiver station and satellite

$d\rho$ = effect of satellite ephemeris error on a particular receiver-satellite range
c = speed of light
dT = receiver clock error with respect to GPS time
λ = wavelength of the carrier phase
N = integer ambiguity for a particular satellite-receiver phase measurement
d_{ion} = ionospheric delay
d_{trop} = tropospheric delay
d^{ϕ}_{mp} = multipath effect on the carrier phase measurement
$\varepsilon_{\Delta\phi}$ = carrier phase observation noise in the one-way observation

If more than one reference station is available, several single-differenced carrier phase observables can be obtained between the user receiver and the reference receivers. In order to account for the distance dependent biases (orbit error, ionospheric delay and tropospheric delay) in equation (4-11), weights are introduced. These weights are inversely proportional to the baseline lengths and are used to average out the different distances between the user and the reference stations. This idea was suggested by Wu (1994) and Han & Rizos (1996d). In the case of a fiducial network consisting of three reference stations, a set of parameters α_i can be determined such that the following conditions are satisfied:

$$\sum_{i=1}^{3} \alpha_i \cdot \left(\vec{X}_u - \vec{X}_i\right) = 0 \qquad (4\text{-}12)$$

where $\vec{X}_u$ and $\vec{X}_i$ are the coordinate vectors of the user receiver and reference receiver in the Gaussian plane coordinate system respectively, and α_i is the weight for reference station i.

To average out the different distances between the user receiver and the reference receivers, the sum of the weights is required to be equal to 1:

$$\sum_{i=1}^{3} \alpha_i = 1 \qquad (4\text{-}13)$$

In order to minimise the standard deviation of the linear combination of single-differenced observations, another constraint should be added:

$$\sum_{i=1}^{3} \alpha_i^2 = \min \tag{4-14}$$

The linear combination of the single-differenced observables can now be written as:

$$\begin{aligned} \sum_{i=1}^{3} \alpha_i \cdot \Delta\phi_i = {} & \sum_{i=1}^{3} \alpha_i \cdot \Delta\rho_i + \sum_{i=1}^{3} \alpha_i \cdot \Delta d\rho_i - c \cdot \sum_{i=1}^{3} \alpha_i \cdot \Delta dT_i + \lambda \cdot \sum_{i=1}^{3} \alpha_i \cdot \Delta N_i \\ & - \sum_{i=1}^{3} \alpha_i \cdot \Delta d_{ion,i} + \sum_{i=1}^{3} \alpha_i \cdot \Delta d_{trop,i} + \sum_{i=1}^{3} \alpha_i \cdot \Delta d_{mp,i}^{\phi} + \varepsilon_{\sum_{i=1}^{3} \alpha_i \cdot \Delta\phi_i} \end{aligned} \tag{4-15}$$

Orbit Bias

According to equation (4-12), the orbit bias term has been shown to be:

$$\sum_{i=1}^{3} \alpha_i \cdot \Delta d\rho_i \approx 0 \tag{4-16}$$

Ionospheric Delay

The ionospheric delay can be expressed as:

$$\sum_{i=1}^{3} \alpha_i \cdot \Delta d_{ion,i} = d_{ion,u} - d_{ion,3} - \begin{bmatrix} \alpha_1 & \alpha_2 \end{bmatrix} \cdot \begin{bmatrix} d_{ion,1} - d_{ion,3} \\ d_{ion,2} - d_{ion,3} \end{bmatrix} \tag{4-17}$$

If the ionospheric delay at the user station can be correctly interpolated from the delays determined at the reference stations, this term will be very close to zero. With increasing distance between the reference stations, however, the residual bias will become larger due to errors in the ionospheric delay interpolation.

Tropospheric Delay

If the tropospheric delay can be interpolated from the residual tropospheric delay at the reference stations, the tropospheric delay can be represented as:

$$\sum_{i=1}^{3} \alpha_i \cdot \Delta d_{trop,i} = d_{trop,u} - d_{trop,3} - \begin{bmatrix} x_u & y_u \end{bmatrix} \cdot \begin{bmatrix} x_1 & y_1 \\ x_2 & y_2 \end{bmatrix}^{-1} \cdot \begin{bmatrix} d_{trop,1} - d_{trop,3} \\ d_{trop,2} - d_{trop,3} \end{bmatrix} \qquad (4\text{-}18)$$

where (x_1, y_1), (x_2, y_2) and (x_u, y_u) are the coordinates of the reference and user receivers relative to reference station 3 in the Gaussian plane coordinate system. How close this term is to zero depends on the spatial correlation characteristics of the tropospheric delay. The residual tropospheric delay is largely influenced by the wet component of the troposphere, which is highly variable with height, time and geographic location. It can be expected that the tropospheric delay will be mitigated to some extent, but its effectiveness is an unknown function of the distance between the GPS receivers. For local networks, however, it can be assumed that the term is very close to zero.

Multipath

The carrier phase multipath effect can be expressed as:

$$\sum_{i=1}^{3} \alpha_i \cdot \Delta d^{\phi}_{mp,i} = d^{\phi}_{mp,u} - \sum_{i=1}^{3} \alpha_i \cdot d^{\phi}_{mp,i} \qquad (4\text{-}19)$$

The second term on the right side of equation (4-19) is the weighted mean of the multipath values at the three reference receivers for this satellite. Due to the random nature of multipath at different receivers, the weighted mean value will be reduced if all α_i ($i = 1, 2, 3$) are positive and less than 1, although the weight α_i is not derived from its standard deviation. On the other hand, the multipath at the user receiver will become a high-frequency bias, and will be assumed to be close to random noise (Zhang & Schwarz, 1996). Therefore, the multipath term can be assumed to have been significantly reduced and will consequently be ignored in the functional model.

Observation Noise

The standard deviation of the one-way carrier phase observation can be approximated as a function of the elevation angle. If all GPS network receivers are located within a region of about 100km radius, the elevation of a satellite is approximately the same. If σ_j denotes the standard deviation of a one-way carrier phase observation, the standard deviation of the linear combination of single-differenced observations can be represented as:

$$\sigma_{\sum\limits_{i=1}^{3}\alpha_i\cdot\Delta\phi_i} = \sqrt{1+\alpha_1{}^2+\alpha_2{}^2+\alpha_3{}^2}\cdot\sigma_j \tag{4-20}$$

In comparison to the standard deviation of the single-differenced carrier phase observation $\sqrt{2}\cdot\sigma_j$, the standard deviation will become smaller if the user receiver is located inside the triangle formed by the reference stations. Hence, the overall noise across the network will be reduced.

The single-differenced functional model for the linear combination (equation 4-15) can now be written in a simplified form:

$$\sum_{i=1}^{3}\alpha_i\cdot\Delta\phi_i = \sum_{i=1}^{3}\alpha_i\cdot\Delta\rho_i - c\cdot\sum_{i=1}^{3}\alpha_i\cdot\Delta dT_i + \lambda\cdot\sum_{i=1}^{3}\alpha_i\cdot\Delta N_i + \varepsilon_{\sum\limits_{i=1}^{3}\alpha_i\cdot\Delta\phi_i} \tag{4-21}$$

Considering a user receiver u and the relation (Han, 1997):

$$\begin{aligned}\sum_{i=1}^{3}\alpha_i\cdot\Delta\phi_i &= (\phi_u-\phi_3)-\left[\alpha_1\cdot(\phi_1-\phi_2)+\alpha_2\cdot(\phi_2-\phi_3)\right]\\ &= \Delta\phi_{u,3}-\left[\alpha_1\cdot\Delta\phi_{1,3}+\alpha_2\cdot\Delta\phi_{2,3}\right]\end{aligned} \tag{4-22}$$

equation (4-21) can be expressed as:

$$\begin{aligned}\Delta\phi_{u,3}-\left[\alpha_1\cdot\Delta\phi_{1,3}+\alpha_2\cdot\Delta\phi_{2,3}\right] &= \Delta\rho_{u,3}-\left[\alpha_1\cdot\Delta\rho_{1,3}+\alpha_2\cdot\Delta\rho_{2,3}\right]-c\cdot\sum_{i=1}^{3}\alpha_i\cdot\Delta dT_i\\ &\quad+\lambda\cdot\Delta N_{u,3}-\left[\alpha_1\cdot\Delta N_{1,3}+\alpha_2\cdot\Delta N_{2,3}\right]+\varepsilon_{\sum\limits_{i=1}^{3}\alpha_i\cdot\Delta\phi_i}\end{aligned} \tag{4-23}$$

4.5.2 Double-Differenced Model

The double-differenced carrier phase observable can be written as (Chen et al., 1999):

$$\nabla\Delta\phi = \nabla\Delta\rho + \nabla\Delta d\rho + \lambda \cdot \nabla\Delta N - \nabla\Delta d_{ion} + \nabla\Delta d_{trop} + \nabla\Delta d_{mp}^{\phi} + \varepsilon_{\nabla\Delta\phi} \qquad (4\text{-}24)$$

where $\nabla\Delta$ denotes the double-differencing operator. Note that the receiver clock error term present in the single-differenced observable cancels by forming the between-satellite differences.

Based on the discussion in the last section and considering equation (4-23), the double-differenced observation model can also be represented as:

$$\begin{aligned}\nabla\Delta\phi_{u,3} - \left[\alpha_1 \cdot \nabla\Delta\phi_{1,3} + \alpha_2 \cdot \nabla\Delta\phi_{2,3}\right] &= \nabla\Delta\rho_{u,3} - \left[\alpha_1 \cdot \nabla\Delta\rho_{1,3} + \alpha_2 \cdot \nabla\Delta\rho_{2,3}\right] \\ &+ \lambda \cdot \nabla\Delta N_{u,3} - \left[\alpha_1 \cdot \nabla\Delta N_{1,3} + \alpha_2 \cdot \nabla\Delta N_{2,3}\right] + \varepsilon_{\sum_{i=1}^{3} \alpha_i \cdot \nabla\Delta\phi_i}\end{aligned} \qquad (4\text{-}25)$$

Residual vectors can be formed from the double-differenced observations between reference stations 1 & 3 and 2 & 3:

$$V_{1,3} = \nabla\Delta\phi_{1,3} - \nabla\Delta N_{1,3} - \nabla\Delta\rho_{1,3} \qquad (4\text{-}26a)$$

$$V_{2,3} = \nabla\Delta\phi_{2,3} - \nabla\Delta N_{2,3} - \nabla\Delta\rho_{2,3} \qquad (4\text{-}26b)$$

The double-differenced observable can then be written as:

$$\nabla\Delta\phi_{u,3} - \left[\alpha_1 \cdot V_{1,3} + \alpha_2 \cdot V_{2,3}\right] = \nabla\Delta\rho_{u,3} + \lambda \cdot \nabla\Delta N_{u,3} + \varepsilon_{\sum_{i=1}^{3} \alpha_i \cdot \nabla\Delta\phi_i} \qquad (4\text{-}27)$$

After the initialisation of the reference stations, the integer ambiguities are known, and together with the known coordinates the correction vectors $V_{1,3}$ and $V_{2,3}$ can be determined. The correction term $\left[\alpha_1 \cdot V_{1,3} + \alpha_2 \cdot V_{2,3}\right]$ can now be obtained and applied to the user receiver data.

4.5.3 Extended Model for Multiple User Receivers

The model described above can be extended to account for two or more user receivers situated within the fiducial network of reference receivers. This will be the case in a mixed-mode GPS-based volcano deformation monitoring network, comprising three dual-frequency reference receivers surrounding the single-frequency receivers located in the deformation zone on the volcano. Figure 4.7 depicts such a scenario, triangles and dots denoting GPS reference sites and user sites respectively.

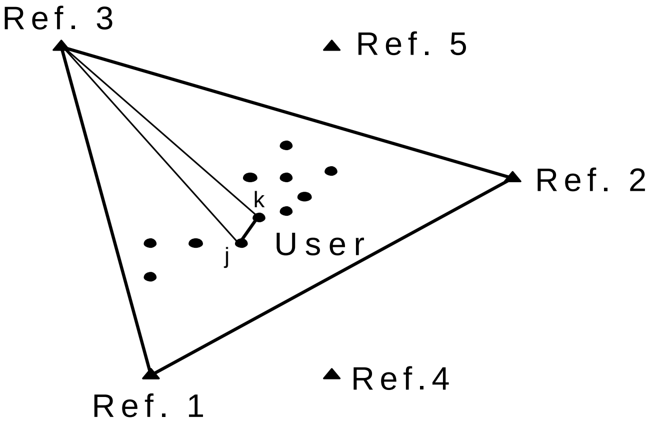

Fig. 4.7: Mixed-mode GPS network of fiducial reference receivers surrounding several user receivers

Consider two user stations j and k. According to equation (4-27), the double-differenced carrier phase observables can then be written as:

$$\nabla\Delta\phi_{j,3} - \left[\alpha_1^j \cdot V_{1,3} + \alpha_2^j \cdot V_{2,3}\right] = \nabla\Delta\rho_{j,3} + \lambda \cdot \nabla\Delta N_{j,3} + \varepsilon_{\sum_{j=1}^{3} \alpha_j \cdot \nabla\Delta\phi_j} \qquad (4\text{-}28)$$

$$\nabla\Delta\phi_{k,3} - \left[\alpha_1^k \cdot V_{1,3} + \alpha_2^k \cdot V_{2,3}\right] = \nabla\Delta\rho_{k,3} + \lambda \cdot \nabla\Delta N_{k,3} + \varepsilon_{\sum_{k=1}^{3} \alpha_k \cdot \nabla\Delta\phi_k} \qquad (4\text{-}29)$$

Forming the linear combination between the two user stations j and k yields:

$$\nabla\Delta\phi_{k,j} - \left[\alpha_1^{k,j} \cdot V_{1,3} + \alpha_2^{k,j} \cdot V_{2,3}\right] = \nabla\Delta\rho_{k,j} + \lambda \cdot \nabla\Delta N_{k,j} + \varepsilon_{k,j} \qquad (4\text{-}30)$$

where $\alpha_i^{k,j}$ (i = 1, 2) is the difference in the α_i value for user stations k and j. $\left[\alpha_1^{k,j} \cdot V_{1,3} + \alpha_2^{k,j} \cdot V_{2,3}\right]$ is the 'correction term' for the inner baseline between these user receivers.

The advantage of equation (4-30) over equation (4-27) is the possibility of accommodating more than one user receiver operating simultaneously within the fiducial network of reference receivers. By forming the double-differenced observables between the inner (single-frequency) receivers, and using the residual vectors generated from the fiducial reference stations, the inner stations' coordinates can be determined without the need to directly use any GPS reference station observations at all.

The procedure of generating these 'correction terms' for a mixed-mode GPS-based volcano deformation monitoring network can be summarised as follows. Consider a network of three fiducial reference stations equipped with dual-frequency GPS receivers surrounding an inner network of several single-frequency receivers (see Figures 2.13 and 4.7). Holding the coordinates of one fiducial site fixed, the baselines to the other two reference receivers are processed and corrections are obtained for both fiducial baselines. These are then scaled (with the help of the α values) according to the position of the inner receivers inside the fiducial triangle to generate double-differenced 'correction terms' for the inner baselines.

4.6 Analysis of the Empirically-Derived Correction Terms

The nature of the empirically-derived double-differenced 'correction terms' is investigated in this section. A range of GPS data sets were processed, incorporating a variety of baseline lengths, different geographical locations and different periods of sunspot activity (and hence varying ionospheric conditions).

4.6.1 The L4 Linear Combination

In order to comment on the severity of the ionospheric delay under various conditions the difference between the L1 and L2 correction terms is formed. This linear combination eliminates the tropospheric effect, which is assumed to be the same for both frequencies. As opposed to the L1 corrections, the remaining L1-L2 correction terms represent only the ionosphere and the negligible orbit bias (very small due to the use of precise ephemerides in this case), if the multipath effect can be ignored.

According to equation (4-24), the double-differenced observable can be written as:

$$\nabla\Delta\phi = \nabla\Delta\rho + \nabla\Delta d\rho + \lambda \cdot \nabla\Delta N - \nabla\Delta d_{ion} + \nabla\Delta d_{trop} + \nabla\Delta d_{mp}^{\varphi} + \varepsilon_{\nabla\Delta\phi}$$

Neglecting orbit bias, multipath and observation noise, the following equations can be obtained for L1 and L2:

$$\nabla\Delta\phi_{L1} = \nabla\Delta\rho - \nabla\Delta d_{ion} + \nabla\Delta d_{trop} + \lambda_{L1} \cdot \nabla\Delta N_{L1} \tag{4-31}$$

$$\nabla\Delta\phi_{L2} = \nabla\Delta\rho - \frac{f_1^{\,2}}{f_2^{\,2}} \nabla\Delta d_{ion} + \nabla\Delta d_{trop} + \lambda_{L2} \cdot \nabla\Delta N_{L2} \tag{4-32}$$

Forming the difference between the L1 and L2 correction terms gives:

$$\begin{aligned} \nabla\Delta\phi_{L1-L2} &= -\nabla\Delta d_{ion} + \lambda_{L1} \cdot \nabla\Delta N_{L1} + \frac{f_1^{\,2}}{f_2^{\,2}} \nabla\Delta d_{ion} - \lambda_{L2} \cdot \nabla\Delta N_{L2} \\ &= \left(-1 + \frac{f_1^{\,2}}{f_2^{\,2}} \right) \cdot \nabla\Delta d_{ion} + \lambda_{L1} \cdot \nabla\Delta N_{L1} - \lambda_{L2} \cdot \nabla\Delta N_{L2} \end{aligned} \tag{4-33}$$

Substituting the frequencies f_1 = 1575.42 MHz and f_2 = 1227.60 MHz for L1 and L2 yields:

$$\nabla\Delta\phi_{L1-L2} = 0.647 \cdot \nabla\Delta d_{ion} + \lambda_{L1} \cdot \nabla\Delta N_{L1} - \lambda_{L2} \cdot \nabla\Delta N_{L2} \tag{4-34}$$

The second and third terms on the right side of the equation are constants. Hence, under the assumptions made above, this so-called L4 linear combination represents entirely the ionospheric effect. However, the L4 corrections are muted by a factor of 0.647 and of opposite sign in comparison to the L1 corrections. The L4 observable is independent of receiver and satellite clocks and contains no receiver-satellite range term, hence it is also known as the *geometry-free* observable. While investigating the nature of the empirical

L1 correction terms, the L4 linear combination provides useful information about the magnitude of the ionospheric effect.

4.6.2 Analysis of Field Data Collected at Mid-Latitudes

In order to understand the nature of the double-differenced correction terms, two data sets collected in the mid-latitude region were analysed. Data for different baseline lengths were collected in Japan during a 24-hour observation period on January 2, 1997, and on March 7, 2000. While the solar activity was rather low in January 1997, it was approaching a maximum during March 2000.

In order to investigate the ionospheric effect on baselines of different lengths, under different solar activity conditions, seven baselines with lengths ranging from 26km to 101km were analysed. The GPS stations belong to the Hokkaido network, which is part of Japan’s GEONET (GPS Earth Observation Network), and are equipped with dual-frequency GPS receivers. The data were processed with a modified version of the Bernese software package to generate the empirical corrections. (In order to draw conclusions relevant to the volcano application, the following analysis is only concerned with the L1 correction terms.)

Figures 4.8 and 4.9 show the double-differenced L1 correction terms obtained for different baseline lengths for the 1997 and 2000 data sets respectively. A clear increase in ionospheric activity between the data sets is evident (see also Table 4.1 for a list of relevant parameters). Furthermore, it can be seen that ionospheric activity is mainly a daytime phenomenon in mid-latitude regions.

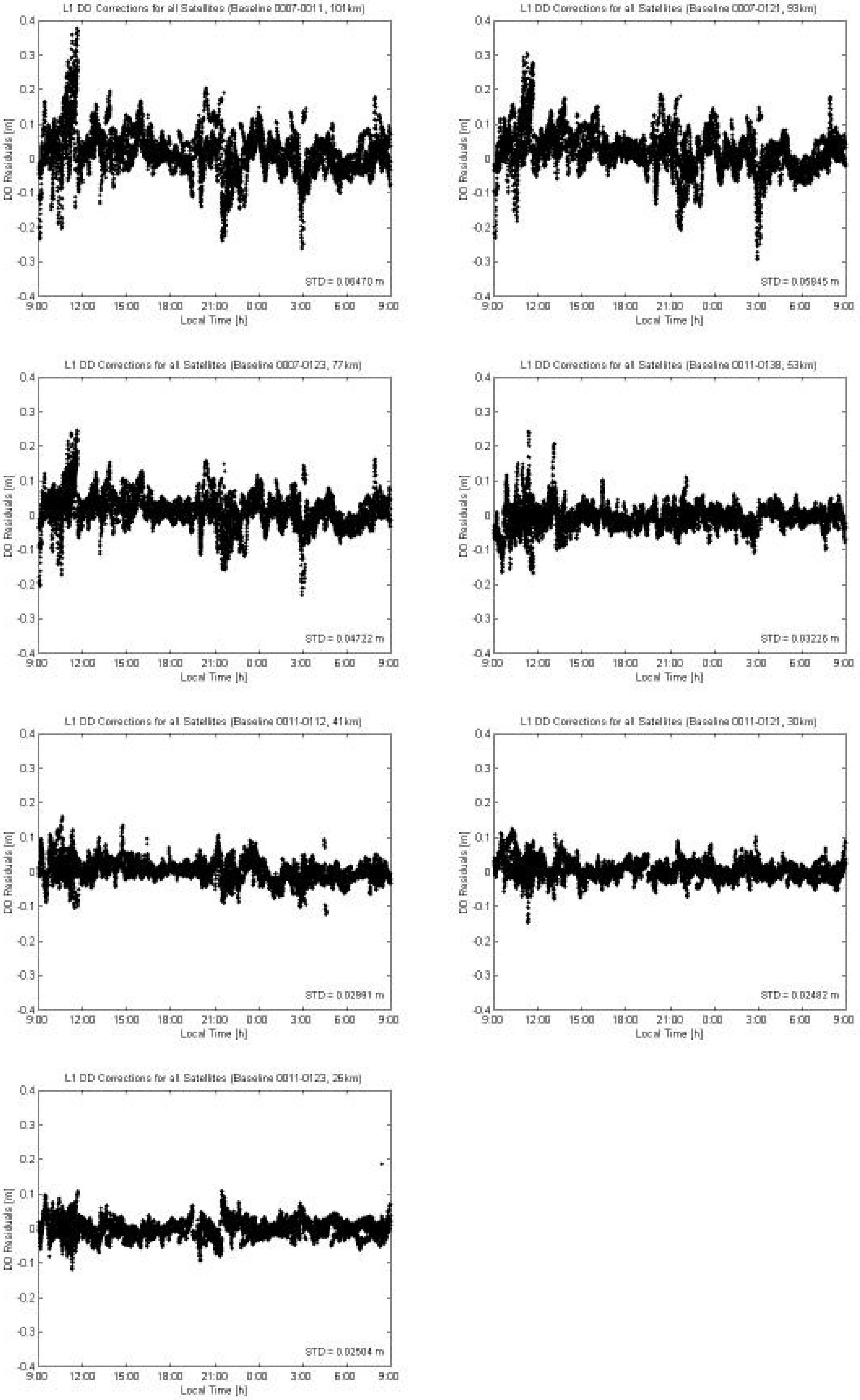

Fig. 4.8: L1 double-differenced correction terms for different baseline lengths

(2 January 1997)

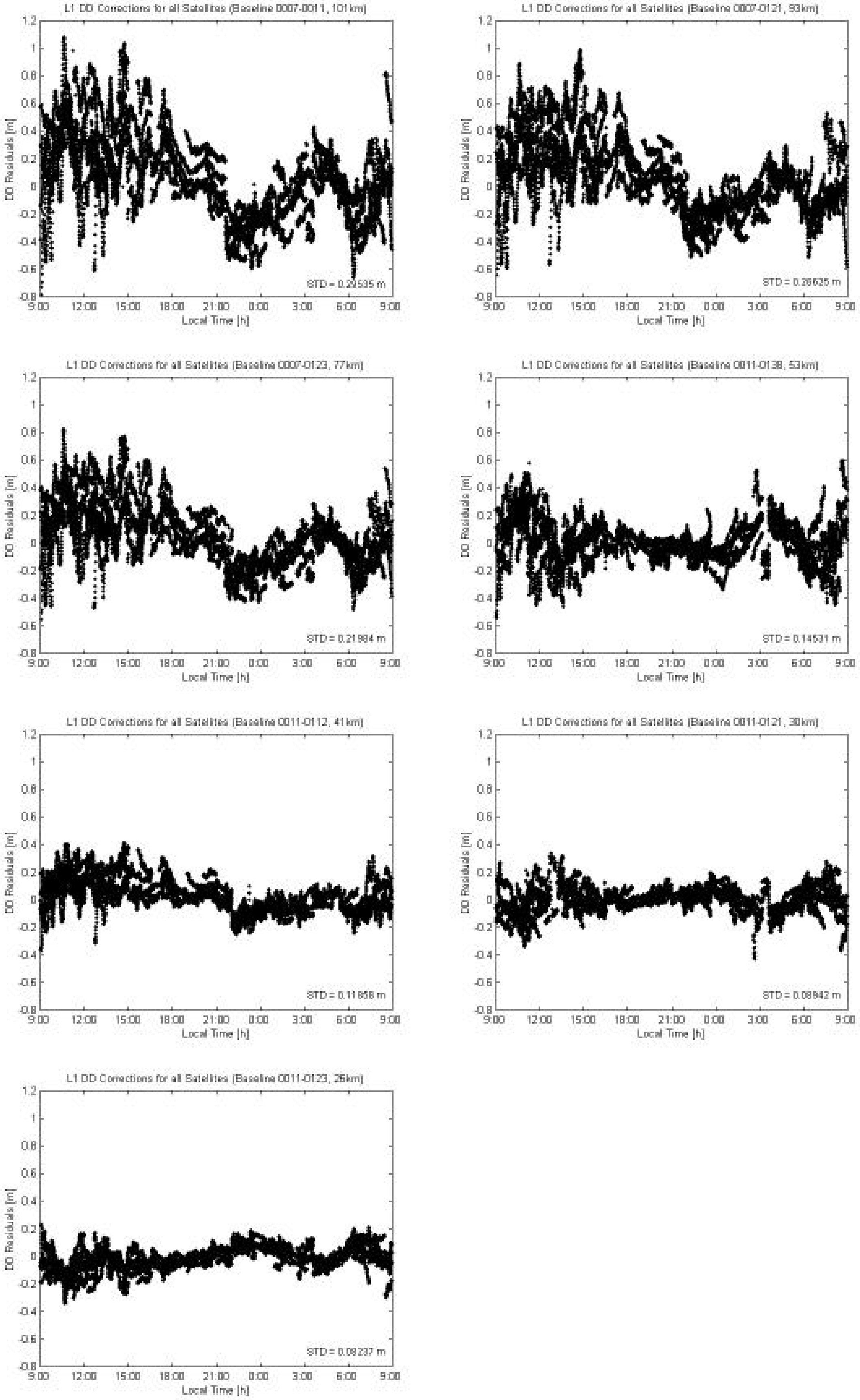

Fig. 4.9: L1 double-differenced correction terms for different baseline lengths (7 March 2000)

Figure 4.10 shows the standard deviation of the double-differenced L1 correction terms for different baseline lengths in January 1997 and March 2000. The effect of the increased ionospheric activity due to the solar maximum period in the year 2000 is obvious. It can be seen that the standard deviation increases more or less linearly with increasing baseline length, confirming the findings by Odijk (2000) and showing that the correct assumptions have been made. Under solar maximum conditions this trend is much more pronounced.

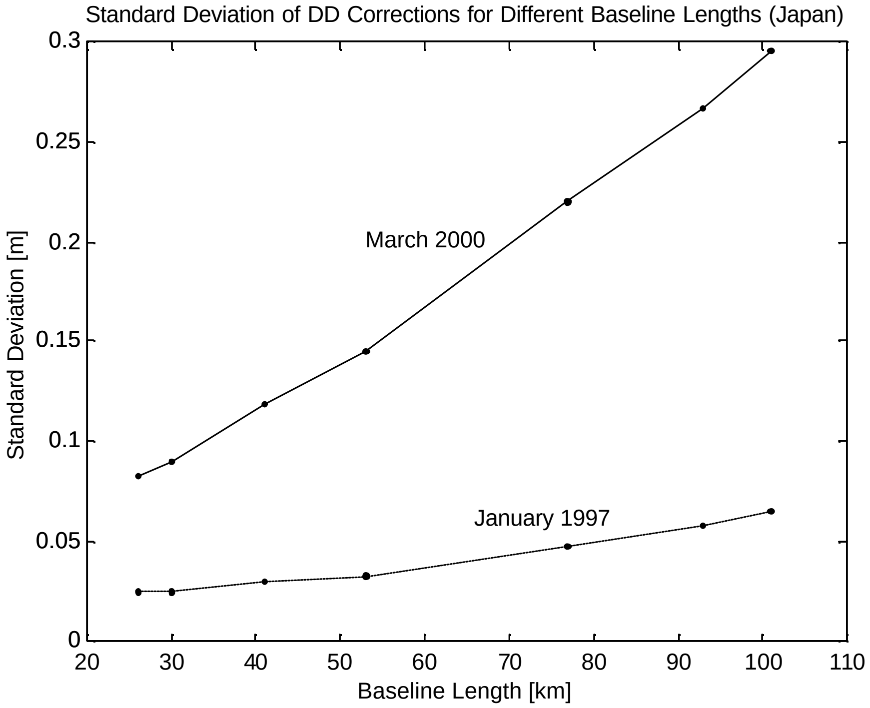

Fig. 4.10: Standard deviation of double-differenced correction terms for different baseline lengths under low (1997) and high (2000) solar activity conditions

Figure 4.11 shows the minimum and maximum correction values obtained for different baseline lengths over a period of 24 hours. It can be seen that the magnitude of the correction terms for longer baselines increases rather rapidly during solar maximum conditions. This suggests that long baselines between reference stations would not be capable of generating reliable corrections under these conditions. However, the magnitude of these biases is not entirely a function of distance, hence it is difficult to predict what should be the dimensions of the reference station network that would reliably model these distance-dependent biases.

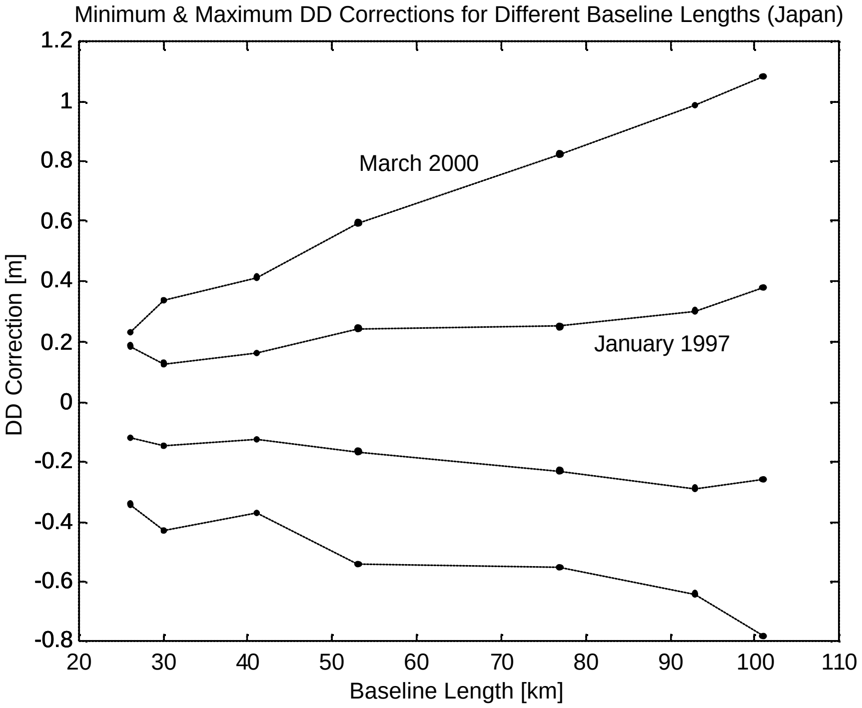

Fig. 4.11: Minimum and maximum double-differenced correction terms obtained for different baseline lengths

For comparison purposes, Figure 4.12 shows the double-differenced L1 corrections for a 77km baseline over 24 hours in January 1997, and then again in March 2000. While the ionosphere remains calm, not showing much change during the 24-hour observation period in 1997, the effect of the increased ionospheric activity in 2000 can clearly be seen. Here, the diurnal variability of the ionosphere in mid-latitudes can easily be discerned. As expected, the ionosphere is most active during daylight hours between 8am and 6pm local time, and calms down after dark. Between the years 1997 and 2000 the standard deviation increased by a factor of 4.6. The magnitude of the correction terms only range from –0.232m to 0.248m in 1997, while they vary from –0.555m to 0.824m in 2000.

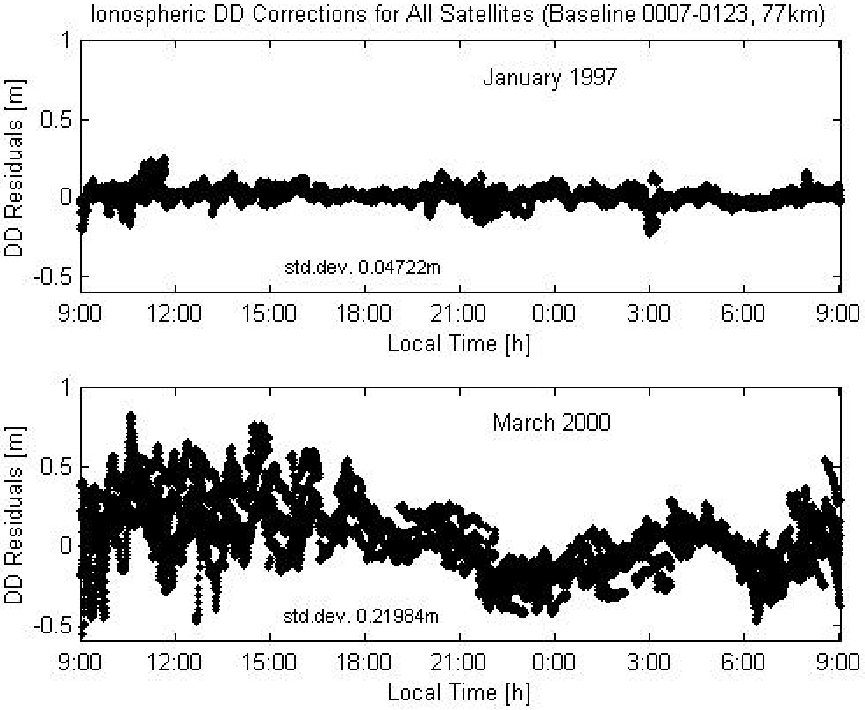

Fig. 4.12: Double-differenced corrections for a 77km baseline over 24 hours under different solar activity conditions

In order to further study the effects of the ionosphere, the L4 correction terms were formed. As mentioned earlier, the L4 corrections represent entirely the ionospheric effect, while the L1 corrections also include the tropospheric delay. Table 4.1 shows several parameters characterising both the L1 and L4 correction terms obtained for each baseline, i.e. the minimum, maximum and mean correction terms, their standard deviation (STD) and the number of double-differences involved. Figures 4.13 and 4.14 show the L4 correction terms for each 24-hour span, the sign having been reversed to enable easy comparison. It is evident that the L4 correction terms show the same signature as the L1 corrections (see Figures 4.8 and 4.9) for both data sets. This indicates that the ionosphere is indeed the dominant systematic error in the double-differenced residuals. It also confirms that multipath is not a significant effect in these data sets. The difference in magnitude of the corrections for a period of low solar activity (1997) as opposed to a solar maximum period (2000) is clearly visible.

Tab. 4.1: Correction terms for different baseline lengths

Baseline	D [km]	min [m]	max [m]	mean [m]	STD [m]	#DD
Japan 02.01.1997 (L1)						
0011-0123	26	-0.11903	0.18583	0.00003	0.02504	13795
0011-0121	30	-0.14631	0.12638	0.00480	0.02482	13828
0011-0112	41	-0.12282	0.16038	0.00275	0.02991	13732
0011-0138	53	-0.16833	0.24263	-0.00681	0.03226	13848
0007-0123	77	-0.23173	0.24761	0.01435	0.04722	13784
0007-0121	93	-0.29142	0.30538	0.01998	0.05845	13783
0007-0011	101	-0.26170	0.37799	0.01722	0.06470	13902
Japan 02.01.1997 (L4 = L1-L2)						
0011-0123	26	-0.07773	0.08481	-0.00114	0.01705	13795
0011-0121	30	-0.09202	0.10501	0.00262	0.01712	13827
0011-0112	41	-0.09529	0.12280	0.00354	0.02151	13731
0011-0138	53	-0.11983	0.15890	-0.00324	0.02180	13848
0007-0123	77	-0.15542	0.18877	0.01004	0.03230	13784
0007-0121	93	-0.19970	0.20975	0.01392	0.03962	13781
0007-0011	101	-0.18324	0.27219	0.01338	0.04119	13901
Japan 07.03.2000 (L1)						
0011-0123	26	-0.33989	0.23406	-0.01376	0.08237	15067
0011-0121	30	-0.43000	0.33577	-0.00042	0.08942	14595
0011-0112	41	-0.36978	0.41469	0.02554	0.11858	15055
0011-0138	53	-0.54182	0.59514	0.00610	0.14531	15097
0007-0123	77	-0.55529	0.82423	0.04445	0.21984	15033
0007-0121	93	-0.64220	0.98978	0.05911	0.26625	15016
0007-0011	101	-0.77948	1.08251	0.05582	0.29535	15246
Japan 07.03.2000 (L4 = L1-L2)						
0011-0123	26	-0.21892	0.19969	-0.01075	0.04733	15067
0011-0121	30	-0.28134	0.20743	-0.00182	0.05525	14595
0011-0112	41	-0.21345	0.28141	0.01713	0.07505	15055
0011-0138	53	-0.31408	0.38284	0.00245	0.08926	15097
0007-0123	77	-0.34374	0.53256	0.02866	0.13806	15033
0007-0121	93	-0.40431	0.66483	0.03898	0.16861	15016
0007-0011	101	-0.50554	0.68613	0.03846	0.17769	15246

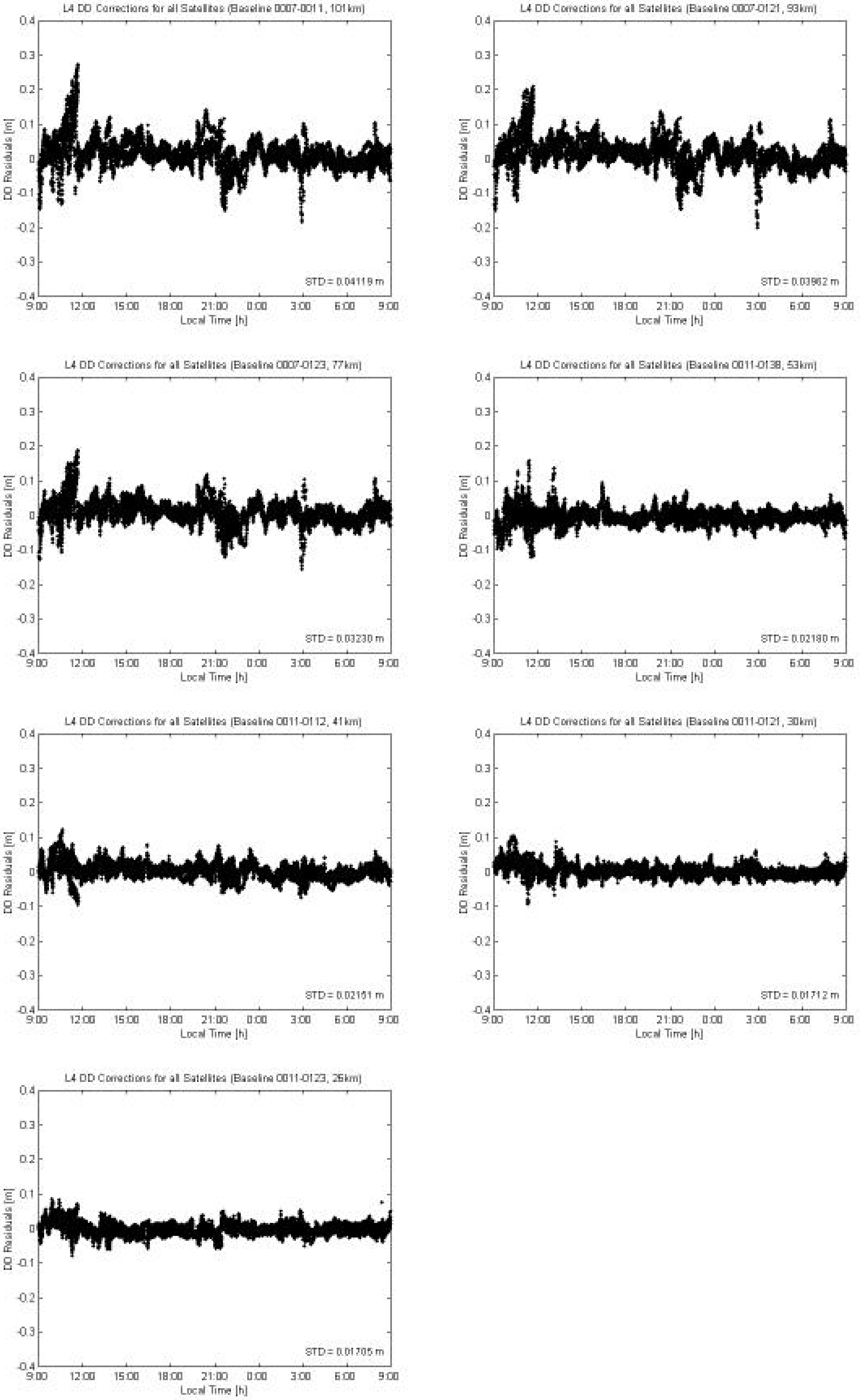

Fig. 4.13: L4 double-differenced correction terms for different baseline lengths

(2 January 1997)

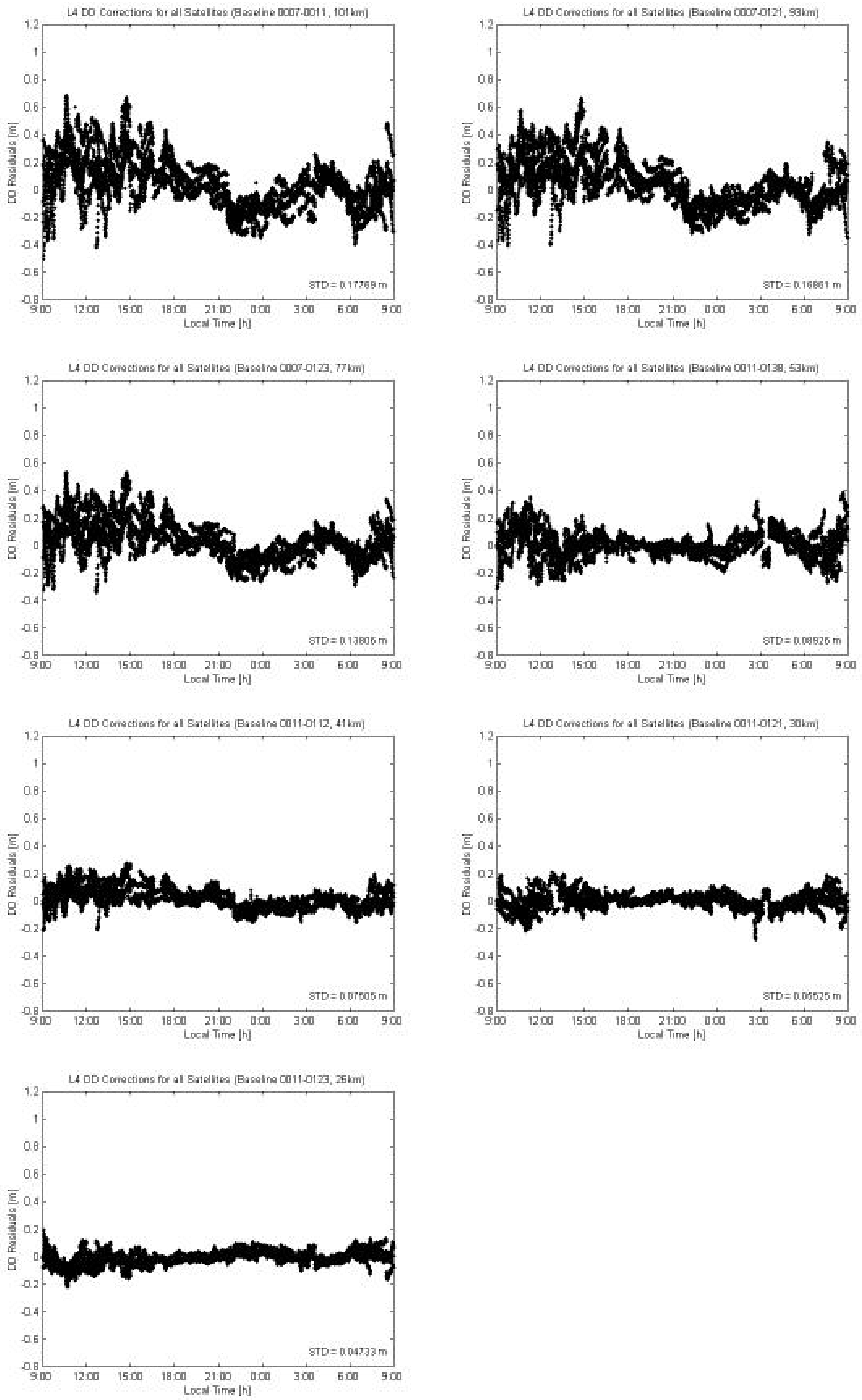

Fig. 4.14: L4 double-differenced correction terms for different baseline lengths (7 March 2000)

Figure 4.15 gives an indication of how much more severe the ionospheric conditions were in 2000 relative to those in 1997. The 'box and whisker' plots show the median, 10th, 25th, 75th and 90th percentiles as vertical boxes with error bars. The ends of the box refer to the 25th and 75th percentiles (i.e. showing the range of the middle half of the data), while the whiskers extend to the 10th and 90th percentiles (i.e. indicating the distribution of 80% of the data). For the sake of completeness a plot referring to the L1 corrections (still including the tropospheric effect) is also shown.

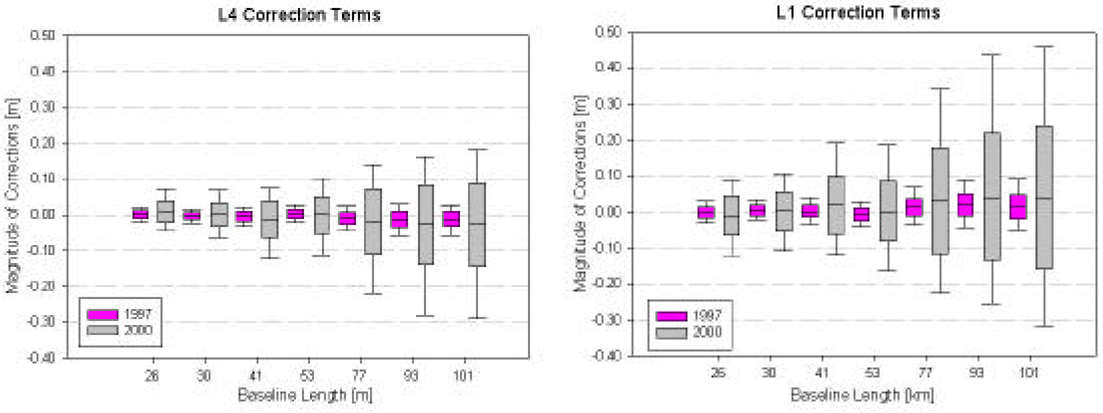

Fig. 4.15: Increase in the ionospheric effect for different baseline lengths between 1997 and 2000: L4 corrections (left) and L1 corrections (right)

This figure confirms that the severity of the ionospheric effect increased significantly. It also confirms that the correction terms become less reliable for longer baseline lengths. Table 4.2 tries to quantify the increase of the ionospheric conditions from 1997 to 2000. The minimum, maximum, mean and STD values of the two data sets (see Table 4.1) were compared and expressed as percentages. Some of the mean values had opposite signs and were therefore left out of the analysis.

Analysis of the L4 correction terms shows that the minimum and maximum values of the corrections increased by a factor of about 2.5, while the standard deviation increased by a factor of approximately 3.8 on average. The increase of the standard deviation shows a dependency on the baseline length, reaching a maximum factor of 4.3 for the 101km baseline. This was expected, and is in line with the trend depicted in Figures 4.10, 4.11 and 4.15. The L1 corrections give slightly higher factors.

Tab. 4.2: Percentage increase of the ionospheric effect between the 1997 and 2000 data sets in Japan

Japan	L4 correction terms				L1 correction terms			
	Min (97-00)	Max (97-00)	Mean (97-00)	STD (97-00)	Min (97-00)	Max (97-00)	Mean (97-00)	STD (97-00)
26 km	282 %	235 %	943 %	278 %	286 %	126 %	-	329 %
30 km	306 %	198 %	-	323 %	294 %	266 %	-	360 %
41 km	224 %	229 %	484 %	349 %	301 %	259 %	929 %	396 %
53 km	262 %	241 %	-	409 %	322 %	245 %	-	450 %
77 km	221 %	282 %	285 %	427 %	240 %	333 %	310 %	466 %
93 km	202 %	317 %	280 %	426 %	220 %	324 %	296 %	456 %
101 km	276 %	252 %	287 %	431 %	298 %	286 %	324 %	456 %
mean	**253 %**	**251 %**	**-**	**378 %**	**280 %**	**263 %**	**-**	**416 %**

However, it should be stressed that these values can only be interpreted as an indication of how much more severe the ionospheric effect is during a solar maximum period compared to a period of low solar activity. Although the 1997 and 2000 data sets were collected in the same season, it is apparent that a 24-hour observation period is not enough to draw general conclusions. The high variability of the ionosphere in time and space makes it extremely difficult to derive a meaningful ‘rule-of-thumb’. (Many more data sets from different parts of the globe with longer observation periods need to be investigated in order to do this. However, this goes beyond the scope of this thesis.)

4.6.3 Analysis of Field Data Collected in Different Geographical Regions

The effect of the ionospheric layer on a certain baseline length as a function of geographical location was investigated. The magnitudes of the double-differenced correction terms for a 30km baseline located in mid-latitudes (Japan) and in the equatorial region (Singapore) were compared. The data were collected under solar maximum conditions on March 7, 2000, and the results are shown in Figure 4.16. The more severe ionospheric delay effects in the equatorial region are obvious. In Singapore the magnitude of the minimum and maximum corrections are –0.610m and 0.681m, respectively, with a standard deviation of 0.170m, while in Japan the values only range from –0.430m to 0.336m with a standard deviation of 0.089m. The standard deviation has doubled while the minimum and maximum values have increased by a factor of approximately 2.

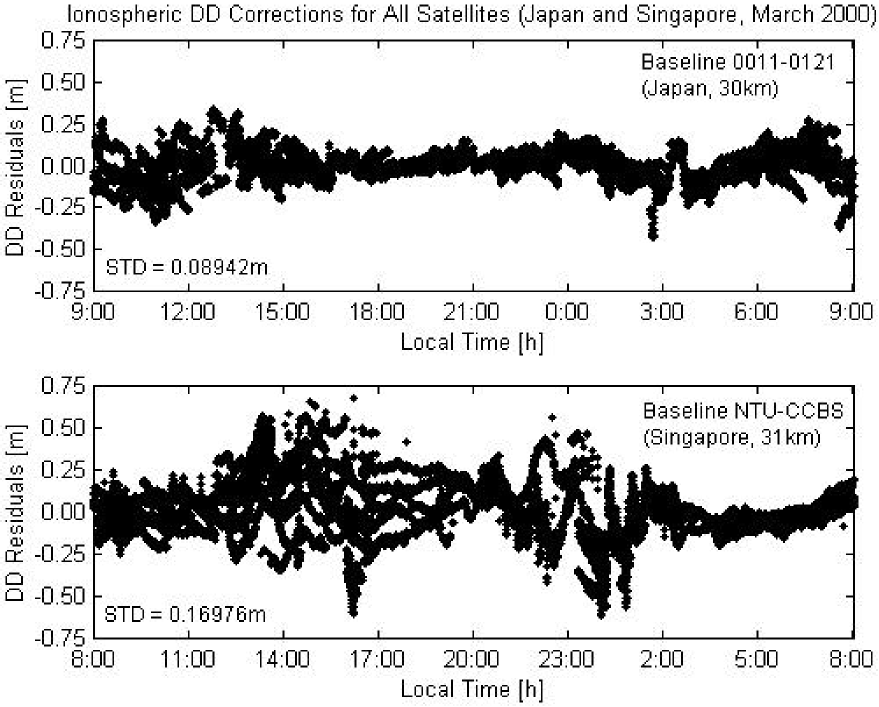

Fig. 4.16: Double-differenced L1 corrections for a 30km baseline over 24 hours in different geographical regions (mid-latitude region and equatorial region)

In addition, it can be seen that the ionospheric effect is mainly a daytime phenomenon in mid-latitudes. However, the graph shows that there is also a lot of ionospheric activity between local noon and sunset in Singapore. This is contrary to the expectation that most of the ionospheric activity occurs between sunset and midnight in equatorial regions, and might be due to intensified small-scale disturbances in the ionosphere during a period of increased solar activity. Furthermore, it can be identified as the primary diurnal maximum of the *equatorial anomaly*, also known as the 'fountain effect' (high electron concentration observed on either side of the geomagnetic equator at magnetic latitudes of around 10-20°). Huang & Cheng (1991) state that the daily equatorial anomaly generally begins to develop at around 9-10am local time, reaching its primary maximum development at 2-3pm local time. In periods of solar maximum conditions, however, the anomaly is prone to peak after sunset, and gradients in TEC are considerably larger at this secondary diurnal maximum (Skone, 2000). Horizontal gradients of up to $30 \cdot 10^{16}$ el/m^2 (30 TECU) have been observed in the equatorial region under solar maximum conditions

(Wanninger, 1993). The equatorial anomaly, as well as the additional ionospheric disturbances present around midnight in the equatorial region (Fig. 4.16), can also be clearly seen in the GIM shown in Figure 4.5.

L4 correction terms were also obtained for both baselines and are shown in Figure 4.17. The plots of the L1 and L4 corrections show the same signature, indicating that the ionosphere is indeed the main systematic error in the double-differenced residuals. Table 4.3 lists the minimum, maximum and mean corrections, their standard deviation and the number of double-differences involved for both the L1 corrections and the L4 corrections, while Table 4.4 shows the increase of ionospheric activity in terms of percentage in both cases. An increase of the ionospheric effect by a factor of about 2 is apparent. This trend is also visible in Figure 4.18.

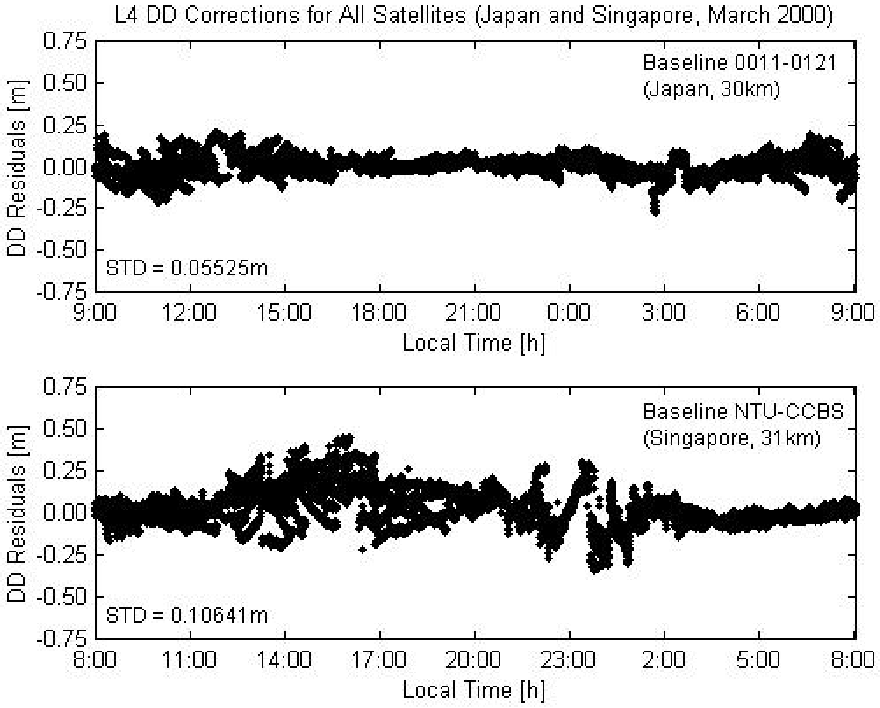

Fig. 4.17: Double-differenced L4 corrections for a 30km baseline over 24 hours in different geographical regions (mid-latitude region and equatorial region)

Tab. 4.3: Correction terms for baselines in different geographic regions

Baseline	D [km]	min [m]	max [m]	mean [m]	STD [m]	#DD
L1 corrections 07.03.2000						
0011-0121	30	-0.43000	0.33577	-0.00042	0.08942	14595
NTU-CCBS	31	-0.60977	0.68101	0.02467	0.16976	16082
L4 corrections 07.03.2000						
0011-0121	30	-0.28134	0.20743	-0.00182	0.05525	14595
NTU-CCBS	31	-0.34159	0.44913	0.03153	0.10641	13257

Tab. 4.4: Increase of the ionospheric effect for a 30km baseline in the equatorial region in comparison to mid-latitudes (March 2000)

L4 correction terms				L1 correction terms			
Min	Max	Mean	STD	Min	Max	Mean	STD
121 %	217 %	(1732 %)	193 %	142 %	203 %	(5874 %)	190 %

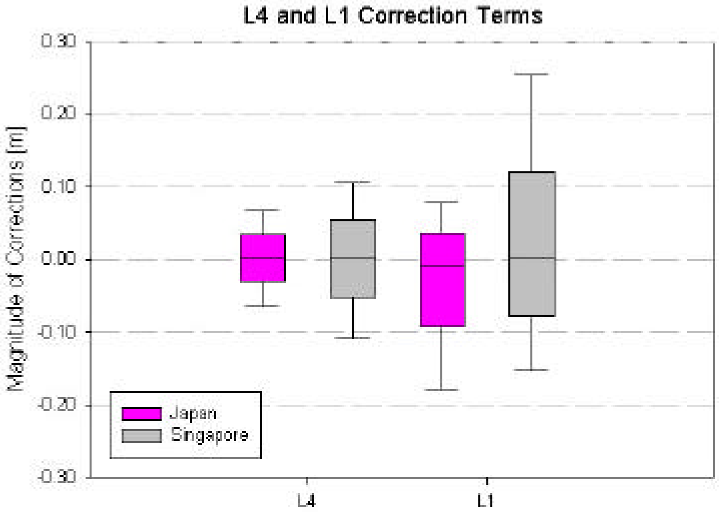

Fig. 4.18: Ionospheric corrections in the mid-latitude region (Japan) and the equatorial region (Singapore): L4 corrections (left) and L1 corrections (right)

However, this statement is based on one 24-hour data set only, hence it can only give an indication of how much more severe the ionosphere is in equatorial regions compared to mid-latitude regions. Because the ionosphere is highly variable, a large amount of global data would have to be analysed in order to draw general conclusions.

4.6.4 Analysis of Field Data Collected at the Mt. Papandayan Volcano in 2000 & 2001

In early 2000 first testing of the mixed-mode GPS-based volcano deformation monitoring system took place on Gunung Papandayan in West Java, Indonesia (see Figure 2.14). Due to its close proximity to the geomagnetic equator, the ionospheric activity at the Mt. Papandayan volcano was expected to be much higher than in a mid-latitude region like Japan. Furthermore, in comparison to the data collected in Singapore, the correction terms were expected to be larger due to the much longer baseline lengths of the network surrounding Gunung Papandayan and the more pronounced effects of the equatorial anomaly in this area.

Figure 4.19 shows the double-differenced correction terms generated by the three fiducial baselines BAND-PAME (85km), BAND-GALU (72km) and GALU-PAME (60km) over 24 hours on March 7, 2000. It can be seen that the correction terms for the two baselines BAND-PAME and BAND-GALU, which were supposed to generate the corrections to be used in the data processing, are very large. The magnitude of the correction terms range from –5.556m to 4.597m (BAND-PAME) and from –2.976m to 2.830m (BAND-GALU), with standard deviations of 1.025m and 0.719m respectively. The correction terms for the third baseline range from -1.563m to 1.504m with a standard deviation of 0.377m. This confirms the hypothesis that the reliable generation of correction terms under such a scenario requires shorter baselines within the reference station network. However, it is not possible to predict a priori what the optimal (i.e. largest) spacing is. Unfortunately, an empirical process for testing reference station geometry will be necessary, employed on a case-by-case basis.

It can be seen that the maximum ionospheric effects occur between local sunset and midnight, which is as expected. However, there is also a lot of activity between 3pm and sunset. As mentioned before, this can be explained by intensified disturbances in the ionosphere caused by increased solar sunspot activity and the primary peak of the equatorial anomaly. From Figure 4.5 it is clear that this network is located in a region exposed to the greatest changes in the ionospheric conditions. Due to the high magnitude of the correction terms and the lack of a more continuous data set, the corrections could not be reliably applied to the single-frequency data set.

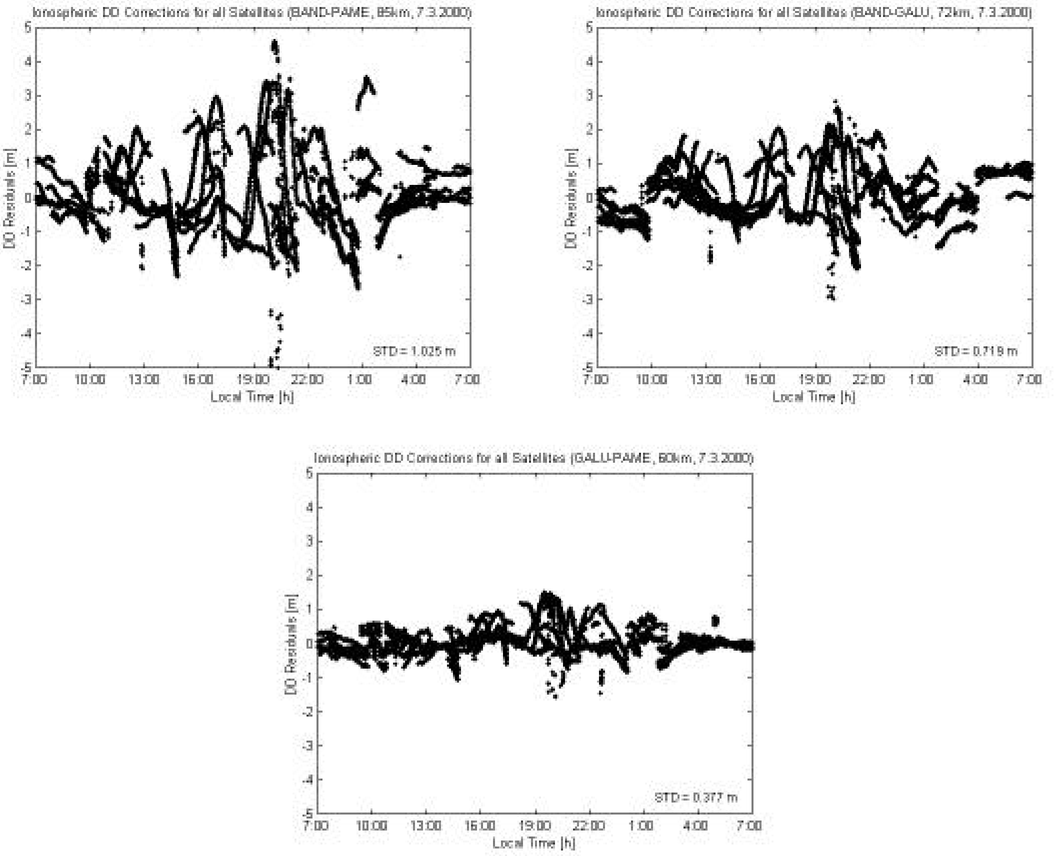

Fig. 4.19: Double-differenced L1 corrections for the fiducial baselines at Mt. Papandayan, Indonesia, over 24 hours on 7 March 2000

In mid 2001 further tests were carried out on the volcano under similar ionospheric conditions. As illustrated in Figure 2.14, the fiducial baseline lengths were reduced to 53km (GUNT-PAME) and 31km (GUNT-PANG). Figure 4.20 shows the L1 correction terms obtained for these baselines for 24-hour observation periods on four consecutive days (11-14 July 2001). The highly variable nature of the ionosphere is evident over the 4-day period studied. It is hardly possible to make out a distinct trend repeating on a daily basis. Compared to Figure 4.19 the 2001 correction terms are certainly more ‘realistic’ than the values obtained in 2000. The corrections obtained for the shorter baseline seem to faithfully represent the ionospheric conditions. This is supported by the information in Table 4.5, which lists the minimum, maximum and mean L1 corrections, their standard deviation and the number of double-differences involved for both fiducial baselines on four successive days. The standard deviation for the 31km baseline varies between 0.095m and 0.139m with the most extreme minimum and maximum corrections being -0.866m and 0.750m respectively on the fourth day. However, the results generated by the baseline GUNT-PAME indicate that a baseline length of 53km is still too long to generate reliable correction terms in the equatorial region under solar maximum conditions. As apparent in other data sets referred to earlier, high ionospheric activity is evident between local noon and sunset, which is in contrast to the expectations for this latitude band.

Tab. 4.5: Double-differenced L1 corrections for fiducial baselines
at Gunung Papandayan (2001)

Baseline	D [km]	min [m]	max [m]	mean [m]	STD [m]	#DD
Papandayan 11.7.2001 (DOY 192)						
GUNT-PAME	53	-1.5359	2.2233	0.0890	0.49083	31276
GUNT-PANG	31	-0.4612	0.6421	-0.0346	0.09519	35279
Papandayan 12.7.2001 (DOY 193)						
GUNT-PAME	53	-1.3066	1.3956	0.0691	0.27276	29408
GUNT-PANG	31	-0.5300	0.5295	-0.0289	0.11550	33273
Papandayan 13.7.2001 (DOY 194)						
GUNT-PAME	53	-1.7840	1.7787	0.0608	0.51468	29821
GUNT-PANG	31	-0.7234	0.3420	-0.0673	0.13933	33425
Papandayan 14.7.2001 (DOY 195)						
GUNT-PAME	53	-1.4751	1.3123	-0.0011	0.21523	30006
GUNT-PANG	31	-0.8661	0.7500	-0.0021	0.13215	34312

The empirical correction terms obtained from the fiducial network around Gunung Papandayan in 2001 were applied to the single-frequency deformation monitoring network located on the volcano. The results are presented in section 5.5.

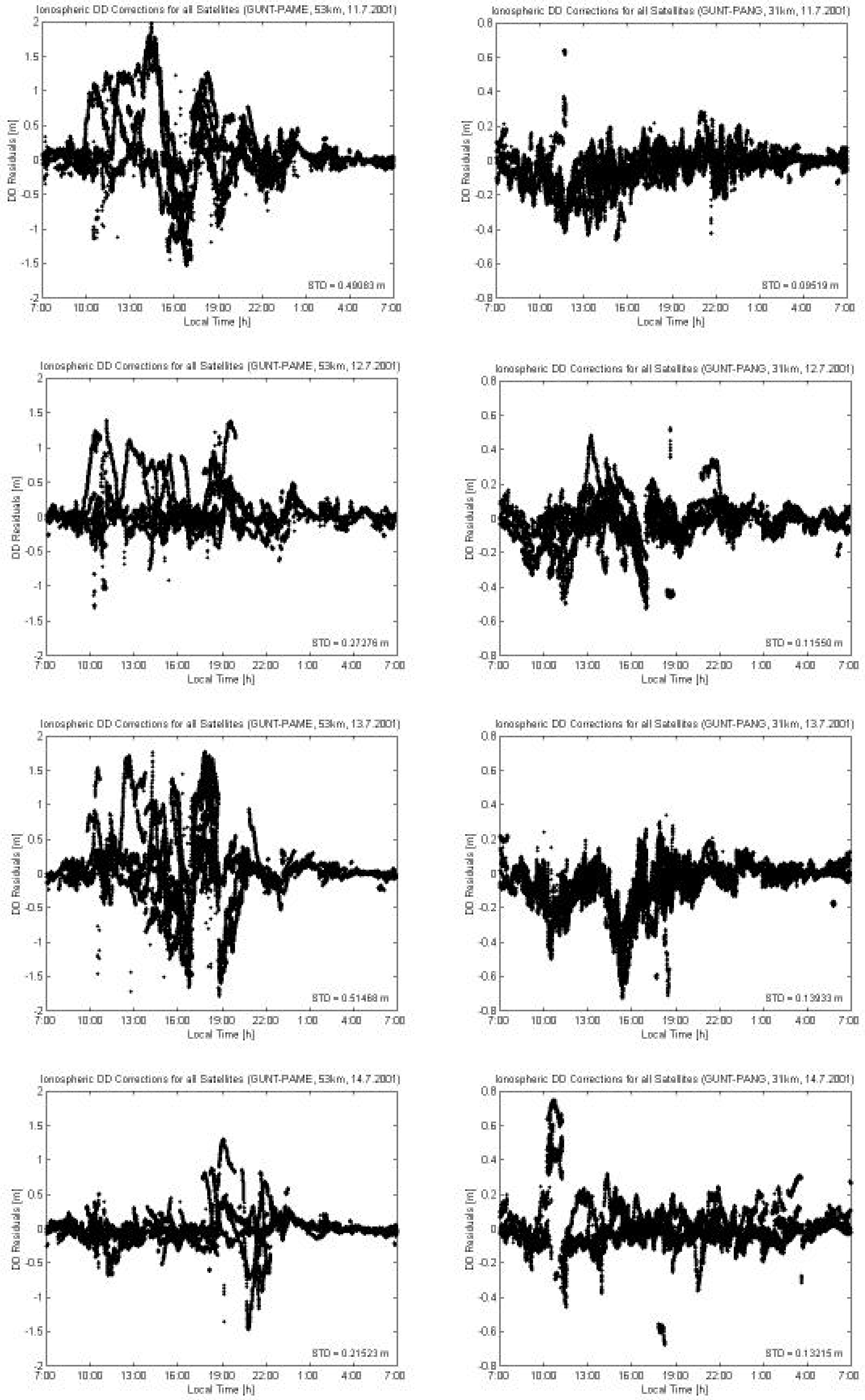

Fig. 4.20: Double-differenced L1 corrections for the fiducial baselines at Mt. Papandayan, Indonesia, on four successive days (11-14 July 2001)

4.7 Concluding Remarks

In this chapter the ionosphere and its effects on the GPS signal has been discussed. A procedure that could, in principle, be used to correct single-frequency GPS observations using empirical corrections derived from a network of dual-frequency reference receivers has been described.

A range of data sets were processed in order to investigate the nature of the empirically-derived double-differenced ‘correction terms’. The GPS data were analysed at a variety of baseline lengths, in different geographical locations and at different periods of sunspot activity (and hence varying ionospheric conditions). The following conclusions can be drawn:

- A large increase in solar activity (and hence ionospheric disturbance) is evident between the 1997 and 2000 data sets. GPS data processing in solar maximum periods is more difficult and a full correction model is necessary.
- The ionosphere is the dominant systematic error present in the ‘correction terms’.
- The standard deviation of the double-differenced ‘correction terms’ increases linearly with increasing baseline length, confirming that the correct model has been used. The rate of increase is much more severe under solar maximum conditions.
- During solar sunspot cycle maximum conditions the magnitude of the ‘correction terms’ for longer baselines in the mid-latitudes reaches several cycles. This indicates that longer baselines might not be able to generate reliable corrections under these conditions.
- Increased ionospheric activity during the daytime in mid-latitudes, and after sunset in the equatorial region, is evident. As expected, the ionospheric delay effects for sites at the equator are much larger compared to mid-latitude sites.
- The distances between the fiducial stations around the Mt. Papandayan volcano should be further reduced so as to generate reliable corrections during solar maximum conditions. Fiducial baseline lengths of below 30km seem to be necessary in order to account for the extreme ionospheric disturbances in this area. However, the optimal spacing will have to be determined empirically.

Chapter 5

DATA PROCESSING AND ANALYSIS

5.1 Introduction

This chapter presents results of the data processing strategies described in chapters 3 and 4, utilising various data sets located in different geographical locations. Sections 5.2, 5.3 and 5.4 validate the strategies described in the previous two chapters, while section 5.5 then focuses on the application at Mt. Papandayan volcano. Data were collected under solar maximum conditions. The Baseline software developed at UNSW was used to process the inner (single-frequency) network in multi-baseline mode, on an epoch-by-epoch basis, after the double-differenced correction terms obtained from the fiducial network were applied. As described in chapter 3, the Baseline software also utilises a procedure to optimise the number of double-differenced observables that are generated during data processing (Janssen, 2001).

Selected GPS coordinate time series were also processed with the UNSW-developed Real-Time System Monitor (RTSM) software in order to indicate how the baseline results could be used to detect movements of the deforming body.

5.2 SCIGN 2000

Data from the Southern California Integrated GPS Network (SCIGN) (Hudnut et al., 2001; SCIGN, 2002) were used to investigate the performance of the mixed-mode network configuration in the mid-latitude region. The geomagnetic equator is south of the geographical equator at these longitudes (see Fig. 4.3). Figure 5.1 shows the location of the GPS sites, which are all equipped with dual-frequency receivers. The part of the network used in these studies consisted of an outer network of three sites (FXHS, FMTP, QHTP) surrounding an inner network of three sites (CSN1, OAT2, CMP9). The outer sites were used as fiducial GPS reference stations, indicated by triangles in Figure 5.1, while the inner sites (indicated by circles) simulated single-frequency receiver stations (by ignoring the observations made on L2). The data were collected under solar maximum conditions, using an observation rate of 30s, on three consecutive days 8-10 August 2000 (DOY 221-223).

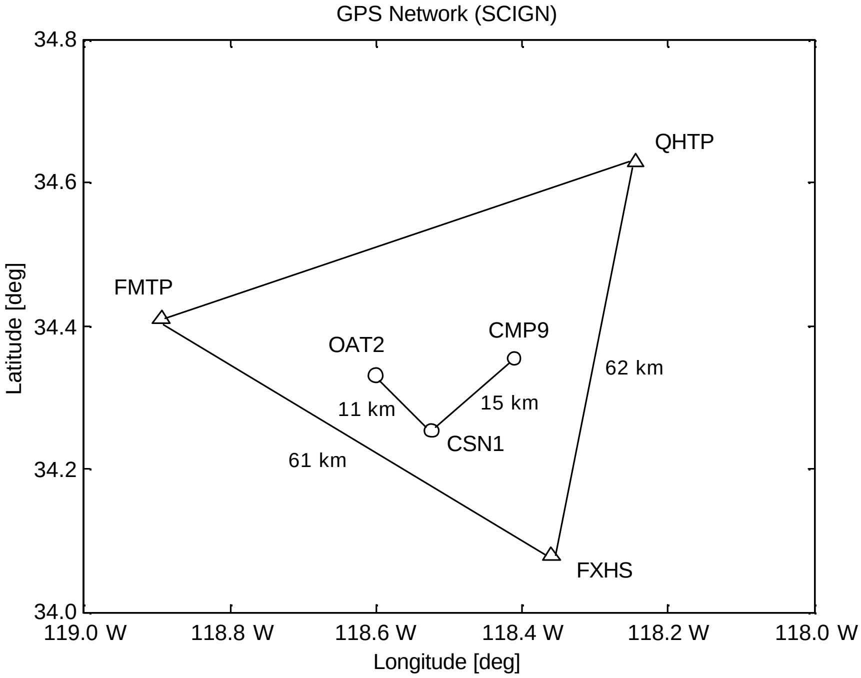

Fig. 5.1: Part of the GPS network in Southern California (SCIGN)

The ITRF coordinates of the GPS network stations are given in Table 5.1.

Tab. 5.1: ITRF2000 coordinates of the GPS network stations of SCIGN

Site	FXHS	FMTP	QHTP
X [m]	-2511943.6388	-2545459.7204	-2486712.3456
Y [m]	-4653606.7722	-4612207.1586	-4629002.0822
Z [m]	3553873.9778	3584252.1200	3604537.5090
Latitude (N)	34° 04’ 50.1730’’	34° 24’ 35.5071’’	34° 37’ 43.2475’’
Longitude (W)	118° 21’ 34.1088’’	118° 53’ 38.9045’’	118° 14’ 41.3211’’
Height [m]	33.319	362.805	863.039

Site	CSN1	OAT2	CMP9
X [m]	-2520225.8551	-2524553.6438	-2508505.9552
Y [m]	-4637082.4402	-4630094.2566	-4637175.0256
Z [m]	3569875.3624	3577352.1138	3579499.8619
Latitude (N)	34° 15’ 12.7752’’	34° 19’ 47.6064’’	34° 21’ 11.4434’’
Longitude (W)	118° 31’ 25.7116’’	118° 36’ 04.9555’’	118° 24’ 41.1177’’
Height [m]	261.443	1112.587	1138.042

These coordinates were obtained using the Scripps Coordinate Update Tool (SCOUT) provided by the Scripps Orbit and Permanent Array Center (SOPAC) (SOPAC, 2002). This service computes the coordinates of a GPS receiver (whose data are submitted to the website) by using the three closest located SCIGN reference sites and precise GPS ephemerides. The coordinates in Table 5.1 were obtained by taking the mean of five 24-hour solutions on successive days (average baseline length 6-18km). The inner network sites were chosen to simulate conditions present in a GPS-based volcano deformation monitoring network, e.g. where significant height differences between the base station on the foot of the volcano and the monitoring 'slave' stations on the flanks of the volcano typically occur.

5.2.1 Ionospheric Corrections for the Fiducial Baselines

By processing the dual-frequency data with a modified version of the Bernese software, ionospheric L1 correction terms were determined for four baselines on three successive days. The baselines FXHS-FMTP (61km) and FXHS-QHTP (62km) were used as fiducial reference baselines. For comparison, corrections were also obtained for the inner baselines CSN1-OAT2 (11km) and CSN1-CMP9 (15km) using observations made on both frequencies. Table 5.2 lists several parameters that characterise the correction terms, i.e. the minimum, maximum and mean corrections, their standard deviations and the number of double-differences involved. Figures 5.2, 5.4 and 5.6 show the double-differenced corrections obtained for the fiducial baselines on L1 for three consecutive 24-hour observation sessions, while Figures 5.3, 5.5 and 5.7 show the corrections obtained for the inner baselines.

It can be seen that ionospheric activity in mid-latitudes is a daytime phenomenon with most of the ionospheric activity occurring between local sunrise and sunset. The moderate day-to-day variability can be recognised and the ionosphere was a little less active on day 222 compared to days 221 and 223. The correction terms for both fiducial baselines show a similar pattern, indicating that the ionospheric conditions have been rather homogeneous across the network during the period of observation. The magnitude of the corrections for the fiducial baselines reaches a few cycles, indicating that the ionospheric effect is significant. Due to the shorter baseline lengths, the corrections for the inner baselines are smaller than those obtained for the fiducial baselines.

Tab. 5.2: Double-differenced L1 corrections for different baselines

Baseline	D [km]	min [m]	max [m]	mean [m]	STD [m]	#DD
SCIGN 8.8.2000 (L1)						
FXHS-FMTP	61	-0.47601	0.57315	0.00893	0.13664	15747
FXHS-QHTP	62	-0.76940	0.68799	0.00452	0.16120	15722
CSN1-OAT2	11	-0.14378	0.12188	0.00043	0.03173	15884
CSN1-OAT2*	11	-0.09892	0.11910	0.00169	0.02619	15613
CSN1-CMP9	15	-1.25630	0.83254	0.00547	0.05508	15206
CSN1-CMP9*	15	-0.17262	0.11415	-0.00013	0.03622	15613
SCIGN 9.8.2000 (L1)						
FXHS-FMTP	61	-0.52535	0.46483	-0.00341	0.13336	14303
FXHS-QHTP	62	-0.44155	0.43618	-0.00032	0.12339	14254
CSN1-OAT2	11	-0.11631	0.10590	0.00489	0.02884	14337
CSN1-OAT2*	11	-0.10111	0.07784	-0.00047	0.02399	14182
CSN1-CMP9	15	-0.36008	0.48812	0.00401	0.04750	13868
CSN1-CMP9*	15	-0.10325	0.09635	0.00045	0.02937	14182
SCIGN 10.8.2000 (L1)						
FXHS-FMTP	61	-0.63624	0.88364	0.00338	0.15906	15181
FXHS-QHTP	62	-0.85886	0.74558	-0.01725	0.14455	15120
CSN1-OAT2	11	-0.53362	0.37751	-0.00137	0.03578	15271
CSN1-OAT2*	11	-0.12634	0.13803	-0.00019	0.02767	15044
CSN1-CMP9	15	-1.12856	0.83593	-0.00229	0.06732	14669
CSN1-CMP9*	15	-0.18709	0.12648	-0.00507	0.03771	15044
* calculated using α values						

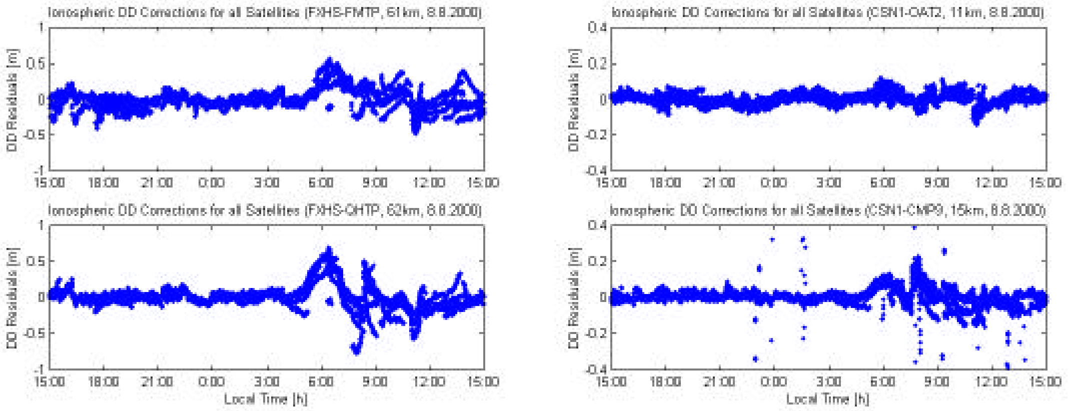

Fig. 5.2+5.3: Double-differenced L1 corrections for fiducial (left) and inner (right) baselines (DOY 221)

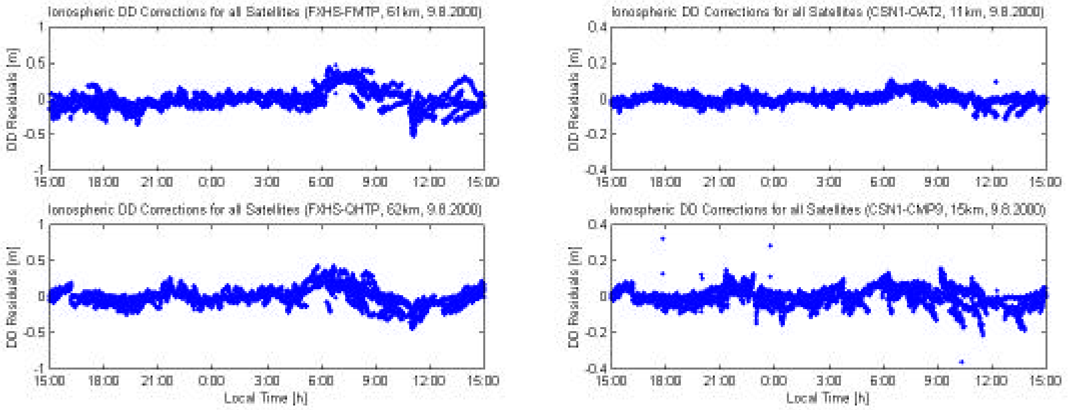

Fig. 5.4+5.5: Double-differenced L1 corrections for fiducial (left) and inner (right) baselines (DOY 222)

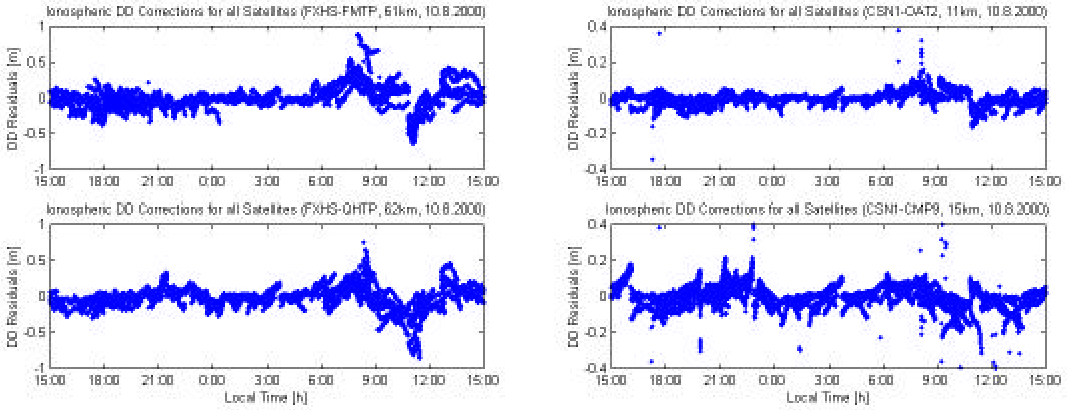

Fig. 5.6+5.7: Double-differenced L1 corrections for fiducial (left) and inner (right) baselines (DOY 223)

5.2.2 Ionospheric Corrections for the Inner Baselines

According to equations (4-12) to (4-14), the α values were derived in order to relate the position of the inner network sites to the fiducial baselines. Table 5.3 lists the α values obtained for the inner GPS sites, α_1 and α_2 indicating the values corresponding to the fiducial baselines FXHS-FMTP and FXHS-QHTP respectively.

Tab. 5.3: α values obtained for the inner GPS network stations

Site	α_1	α_2
CSN1	0.332228	0.115962
OAT2	0.487210	0.162147
CMP9	0.180552	0.388863

The L1 correction terms for the inner baselines can then be determined by forming the linear combination, from equation (4-30). In order to form this linear combination the correction files have been modified to ensure they have the same number of double-differenced correction terms, with matching receiver-satellite pairs, for both fiducial baselines. Hence, the double-differenced correction terms for the inner baselines could be derived in two different ways. Firstly, as described in the previous section, the corrections were determined directly using dual-frequency data and the modified Bernese software (Figures 5.3, 5.5 and 5.7). Secondly, they were obtained indirectly by forming a linear combination of the corrections for the fiducial baselines using the α values (Figures 5.8-5.10). Several parameters characterising these correction terms are listed in Table 5.2 (indicated by asterisks). It can be seen that the results are very similar. The corrections generated using the proposed method are a little smoother and do not show 'outliers' as in the case of the directly determined correction terms. They certainly model the dominant characteristics of the correction terms very well. This indicates that the proposed procedure does indeed compute reliable correction terms for the inner baselines.

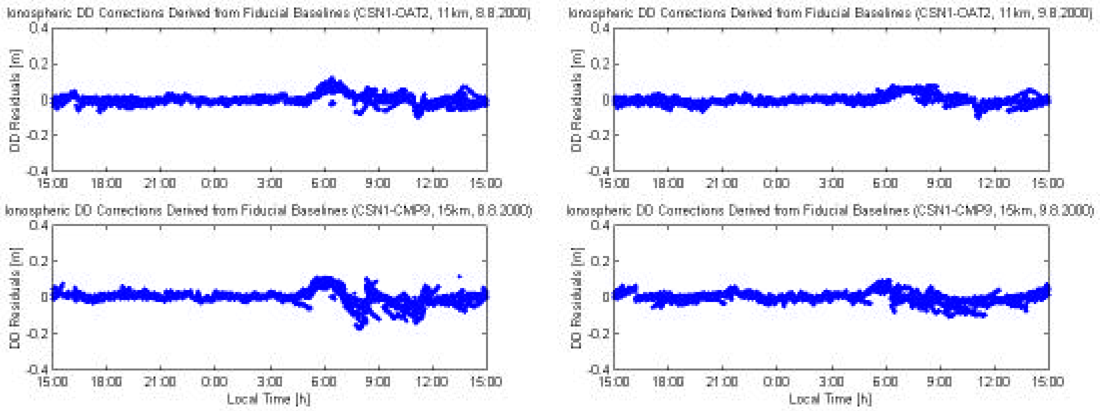

Fig. 5.8+5.9: Double-differenced L1 corrections for inner baselines obtained using α values (DOY 221+222)

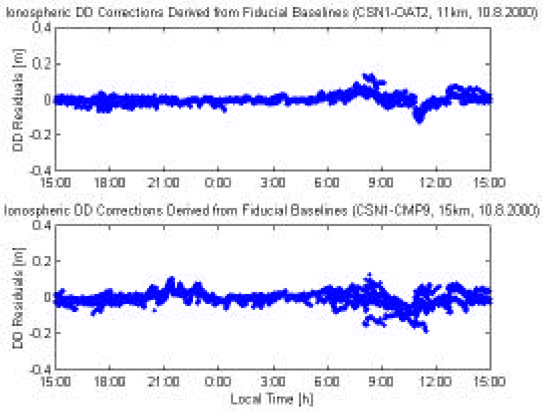

Fig. 5.10: Double-differenced L1 corrections for inner baselines obtained using α values (DOY 223)

5.2.3 Baseline Results

The Baseline software developed at UNSW is used to process the inner baselines in single-frequency mode, with and without using the empirically-derived ionospheric correction terms. For these investigations it can be assumed that no ground deformation has taken place during the period of observation. Hence, the baseline repeatability gives an indication of the accuracy that can be achieved with the proposed data processing strategy. Figure 5.11 shows the results obtained for the inner baselines using the Baseline software without applying ionospheric corrections on day 221, while Figure 5.12 shows the results obtained by applying the ionospheric corrections. Figures 5.13-5.14 and 5.15-5.16 present the results obtained for the following two days respectively. The graphs show the Easting, Northing and Height components over a 24-hour period, each dot representing a single-epoch solution. The standard deviation of each component is also given. In both cases the Saastamoinen model was used to account for the tropospheric bias, as recommended by Mendes (1999).

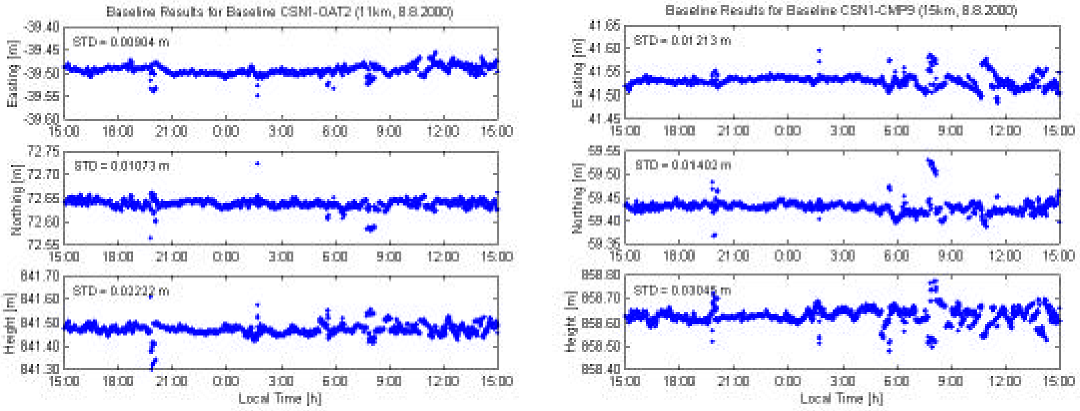

Fig. 5.11: Results for inner baselines not using ionospheric corrections (DOY 221)

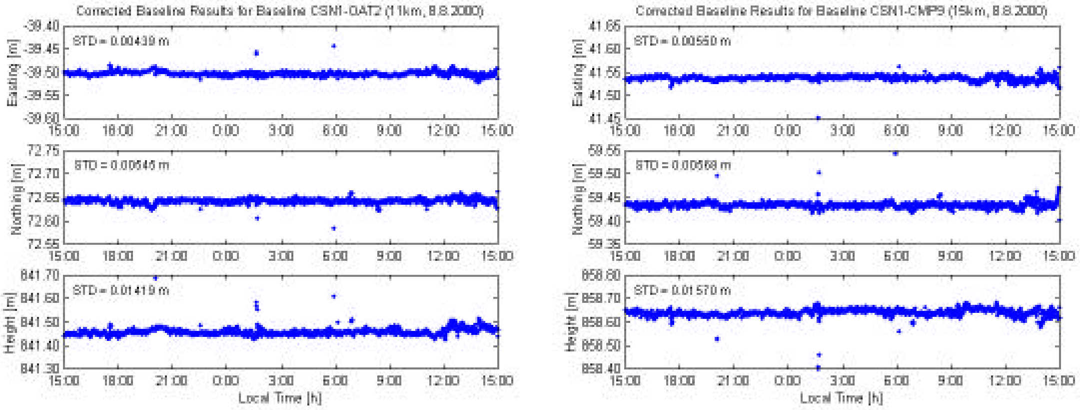

Fig. 5.12: Results for inner baselines applying ionospheric corrections (DOY 221)

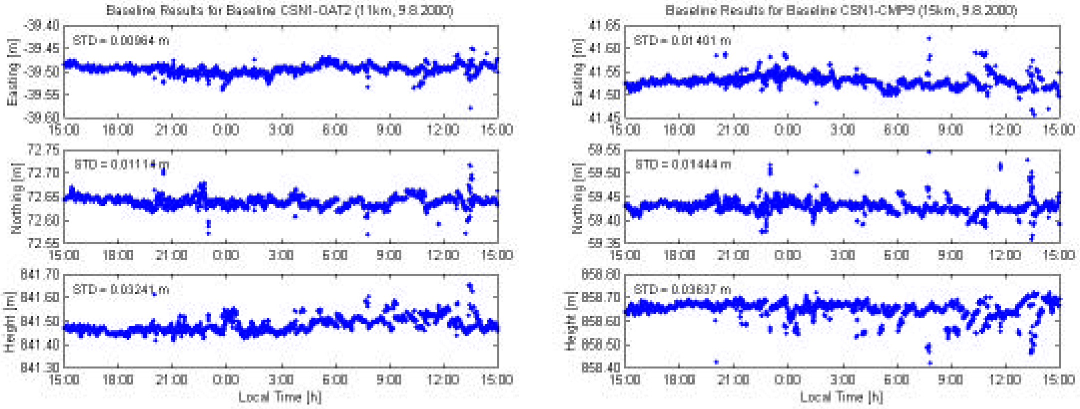

Fig. 5.13: Results for inner baselines not using ionospheric corrections (DOY 222)

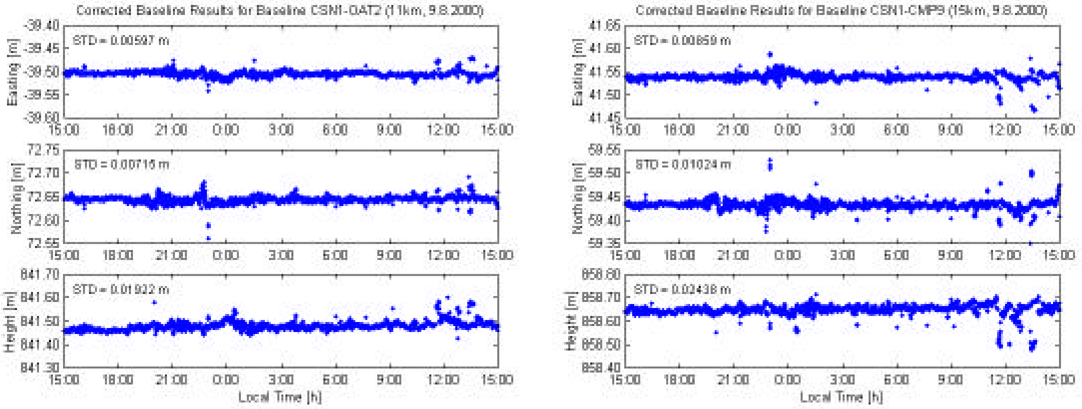

Fig. 5.14: Results for inner baselines applying ionospheric corrections (DOY 222)

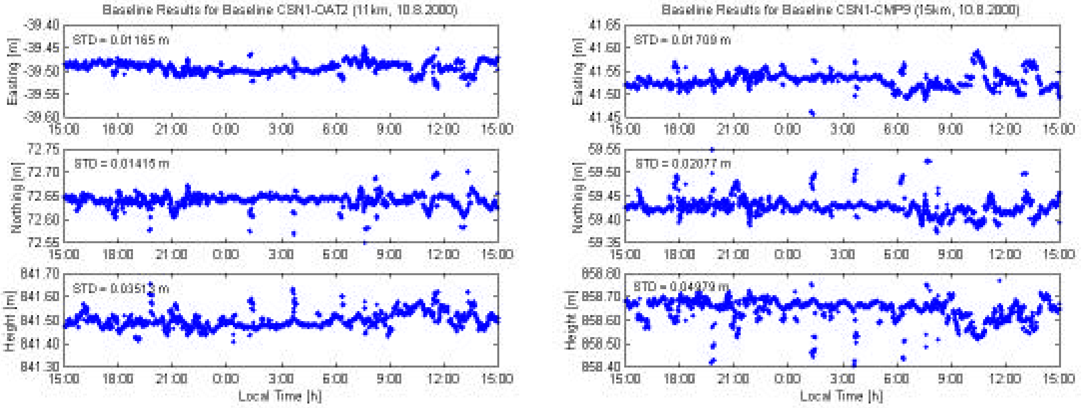

Fig. 5.15: Results for inner baselines not using ionospheric corrections (DOY 223)

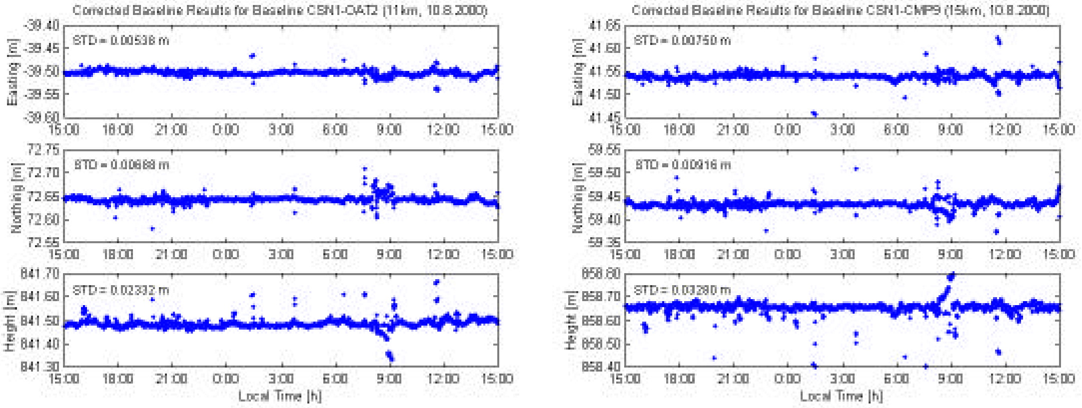

Fig. 5.16: Results for inner baselines applying ionospheric corrections (DOY 223)

Table 5.4 lists the standard deviations (STD) of the results obtained for the inner baselines using the two different processing strategies (not applying corrections versus applying corrections) on three successive days. Comparing Figures 5.11-5.16, and taking note of the information in Table 5.4, it is evident that the baseline results are improved significantly by applying the correction terms. On average, the standard deviation of the baseline results has been reduced by almost 50% for the horizontal components and almost 40% for the vertical component (Table 5.5). Using the proposed processing strategy, standard deviations of less than 1cm horizontally and 1.5-3cm vertically have been achieved for single-epoch baseline solutions (Table 5.4).

For baselines involving a significant difference in station altitude, as for example in GPS volcano deformation monitoring networks, the accuracy could be further improved by estimating an additional residual relative zenith delay parameter to account for the residual tropospheric bias. Abidin et al. (1998), Roberts (2002), and others, claim that global troposphere models alone are not sufficient in such cases, and the relative tropospheric delay should be estimated.

Tab. 5.4: Standard deviations of the inner baseline components on days 221-223 in [m]

	Day 221, no corr.	Day 221, corr.	Day 222, no corr.	Day 222, corr.	Day 223, no corr.	Day 223, corr.
Baseline CSN1-OAT2						
STD Easting [m]	0.00904	0.00439	0.00964	0.00597	0.01165	0.00538
STD Northing [m]	0.01073	0.00545	0.01114	0.00715	0.01415	0.00688
STD Height [m]	0.02222	0.01419	0.03241	0.01922	0.03513	0.02332
Baseline CSN1-CMP9						
STD Easting [m]	0.01213	0.00550	0.01401	0.00859	0.01709	0.00750
STD Northing [m]	0.01402	0.00568	0.01444	0.01024	0.02077	0.00916
STD Height [m]	0.03045	0.01570	0.03637	0.02438	0.04979	0.03280

Tab. 5.5: Average improvement in the STD for both baselines on days 221-223

Baseline	DOY	Easting [%]	Northing [%]	Height [%]
CSN1-OAT2 (11km)	221	51.4	49.2	36.1
	222	38.1	35.8	40.7
	223	53.8	51.4	33.6
CSN1-CMP9 (15km)	221	54.7	59.5	48.4
	222	38.7	29.1	33.0
	223	56.1	55.9	34.1
Average [%]		49	47	38

5.2.4 Summary

The procedure, described in chapters 3 and 4, to process a mixed-mode GPS network for deformation monitoring applications has been tested using data collected in the mid-latitude region. Single-frequency GPS observations have been enhanced using empirical corrections obtained from a fiducial network of dual-frequency reference stations surrounding the inner single-frequency network. This method accounts for the ionospheric bias that otherwise would have been neglected if using single-frequency data alone. Data from the SCIGN network have been used to simulate such a network configuration.

The ionosphere has been shown to have a significant effect on GPS baseline results. This effect should not be neglected if it is necessary to detect deformational signals with single-frequency instrumentation at a high-accuracy level, even for short baselines in mid-latitudes, experiencing rather homogeneous ionospheric conditions across the network.

The double-differenced correction terms for the inner baselines were derived in two ways: directly using dual-frequency data and indirectly using the modelling approach. It was shown that the correction generation algorithm successfully models the correction terms for the inner (single-frequency) baselines.

The single-frequency baseline repeatability has clearly been improved by applying the empirical correction terms. The standard deviation of the baseline results has been reduced by almost 50% for the horizontal components and almost 40% for the vertical component. Standard deviations of less than 1cm horizontally and 1.5-3cm vertically have been achieved for single-epoch baseline solutions. The strategy for processing a mixed-mode GPS network has proven to be a cost-effective and accurate tool for deformation monitoring, suitable for a variety of applications.

5.3 Hong Kong 2000

In an extension of the studies described in section 5.2, data from the Hong Kong GPS Active Network (Chen et al., 2001b) were used to investigate the performance of the proposed network configuration in low-latitude regions. Figure 5.17 shows the location of the GPS sites, which are all equipped with dual-frequency receivers. The test network consists of an outer network of three sites (HKKY, HKFN, HKSL) surrounding two inner sites (HKKT, HKLT). The outer sites were used as fiducial GPS reference stations, indicated by triangles in Figure 5.17, while the inner sites (indicated by circles) simulated single-frequency receiver stations (by ignoring the observations made on L2). The inner sites were connected to the fiducial site HKKY to form the inner (single-frequency) baselines. Note that HKLT is located just outside the fiducial triangle, which should normally be avoided. However, this does not have any effect on the processing in this case, as HKKY-HKFN and HKKY-HKSL were used as fiducial baselines. The data were collected under solar maximum conditions, using an observation rate of 30s, on three consecutive days 11-13 October 2000 (DOY 285-287).

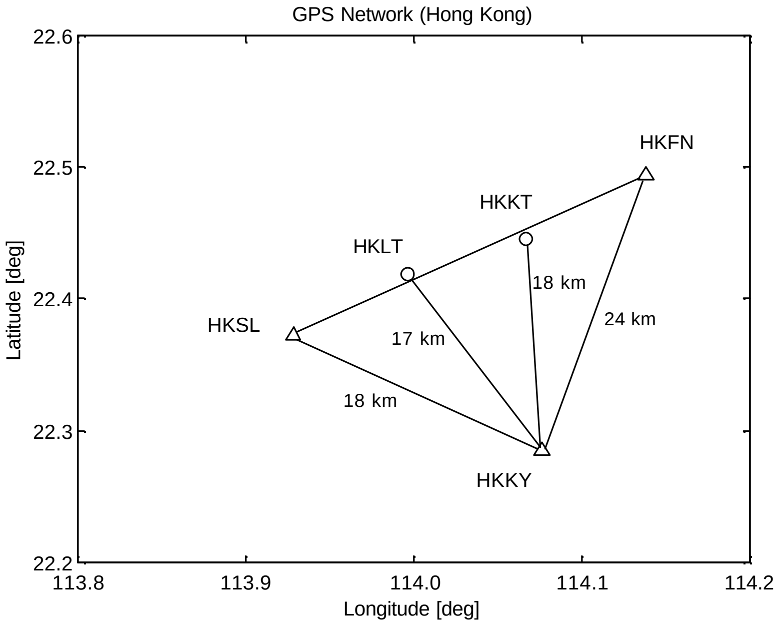

Fig. 5.17: Hong Kong GPS Active Network

The ITRF2000 coordinates of the GPS network stations are listed in Table 5.6. These coordinates were taken from a global solution of a survey campaign spanning several days, generated by A/Prof. P. Morgan at the University of Canberra (Morgan, 2002, personal communication).

Tab. 5.6: ITRF2000 coordinates of the GPS network stations located in Hong Kong

Site	HKKY	HKFN	HKSL
X [m]	-2408850.4252	-2411012.9507	-2393382.4714
Y [m]	5391042.1855	5380268.2082	5393861.1238
Z [m]	2403591.9360	2425129.0592	2412592.3735
Latitude (N)	22° 17’ 02.6499’’	22° 29’ 40.8696’’	22° 22’ 19.2165’’
Longitude (E)	114° 04’ 34.5651’’	114° 08’ 17.4086’’	113° 55’ 40.7355’’
Height [m]	113.975	41.173	95.261

Site	HKKT	HKLT
X [m]	-2405143.9578	-2399062.7955
Y [m]	5385195.1903	5389237.7987
Z [m]	2420032.5128	2417327.0294
Latitude (N)	22° 26’ 41.6614’’	22° 25’ 05.2822’’
Longitude (E)	114° 03’ 59.6371’’	113° 59’ 47.8470’’
Height [m]	34.532	125.897

5.3.1 Ionospheric Corrections for the Fiducial Baselines

Processing the dual-frequency data with a modified version of the Bernese software, ionospheric L1 correction terms were determined for four baselines on three successive days. The baselines HKKY-HKFN (24km) and HKKY-HKSL (18km) were used as fiducial reference baselines. For comparison, corrections were also obtained for the inner baselines HKKY-HKKT (18km) and HKKY-HKLT (17km) using observations made on both frequencies. Table 5.7 lists several parameters that characterise the correction terms, i.e. the minimum, maximum and mean corrections, their standard deviations and the number of double-differences involved. Figures 5.18, 5.20 and 5.22 show the double-differenced corrections obtained for the fiducial baselines on L1 for three consecutive 24-hour observation sessions, while Figures 5.19, 5.21 and 5.23 show the corrections obtained for the inner baselines.

It can be seen that, as expected, ionospheric activity in the equatorial region is at its peak between sunset and 2am local time. However, a lot of activity is also evident during daylight hours. As discussed in section 4.6.3, this can be explained by intensified small-scale disturbances in the ionosphere and the primary diurnal maximum of the equatorial anomaly. Figures 4.3 and 4.4 place Hong Kong in a region of severe ionospheric activity. The ionosphere was a little less active on day 287 compared to the two preceding days.

The correction terms for all baselines show a similar pattern, but also reveal a distinct gradient for the ionospheric conditions. The magnitude of the ionospheric effect increases in the general direction from the southwest to the northeast, as indicated by the minimum and maximum correction terms and their standard deviations in Table 5.7. Note that the baselines considered are of approximately the same length, ranging from 17-24 km. The magnitude of the correction terms reaches values of more than two metres in some cases, which is rather surprising for such short baselines, and initially raised questions concerning the reliability of the corrections (see section 4.6). However, the results presented below prove that the corrections obtained here are indeed capable of improving baseline accuracy. Clearly, the ionospheric activity was extremely severe during the period of observation, therefore significantly affecting GPS measurements.

Tab. 5.7: Double-differenced L1 corrections for different baselines

Baseline	D [km]	min [m]	max [m]	mean [m]	STD [m]	#DD
HK 11.10.2000 (L1)						
HKKY-HKFN	24	-1.71213	2.48976	-0.00822	0.42431	15336
HKKY-HKSL	18	-1.50008	2.05149	-0.04926	0.20338	15324
HKKY-HKKT	18	-0.94597	1.55869	-0.03585	0.32135	15457
HKKY-HKKT*	18	-0.95862	1.54679	-0.02357	0.31403	14980
HKKY-HKLT	17	-0.82337	0.88664	-0.04275	0.26003	13765
HKKY-HKLT*	17	-0.81494	1.59456	-0.03768	0.26240	14980
HK 12.10.2000 (L1)						
HKKY-HKFN	24	-2.22837	1.75940	-0.07406	0.35523	15340
HKKY-HKSL	18	-2.05571	1.70337	-0.07584	0.23511	15303
HKKY-HKKT	18	-1.13888	2.27508	-0.05846	0.33285	15381
HKKY-HKKT*	18	-1.17069	1.11037	-0.07131	0.27568	15054
HKKY-HKLT	17	-1.77687	0.98961	-0.08573	0.25912	13335
HKKY-HKLT*	17	-1.59388	1.21132	-0.07871	0.25588	15054
HK 13.10.2000 (L1)						
HKKY-HKFN	24	-1.02140	1.21435	0.00573	0.32181	16237
HKKY-HKSL	18	-0.57189	0.56004	-0.03961	0.18332	16127
HKKY-HKKT	18	-0.80377	0.88314	-0.00920	0.25847	16262
HKKY-HKKT*	18	-0.80317	0.88367	-0.00973	0.25514	16024
HKKY-HKLT	17	-0.70827	0.70789	-0.02482	0.23419	15638
HKKY-HKLT*	17	-0.69860	0.69954	-0.02541	0.22962	16024
* calculated using α values						

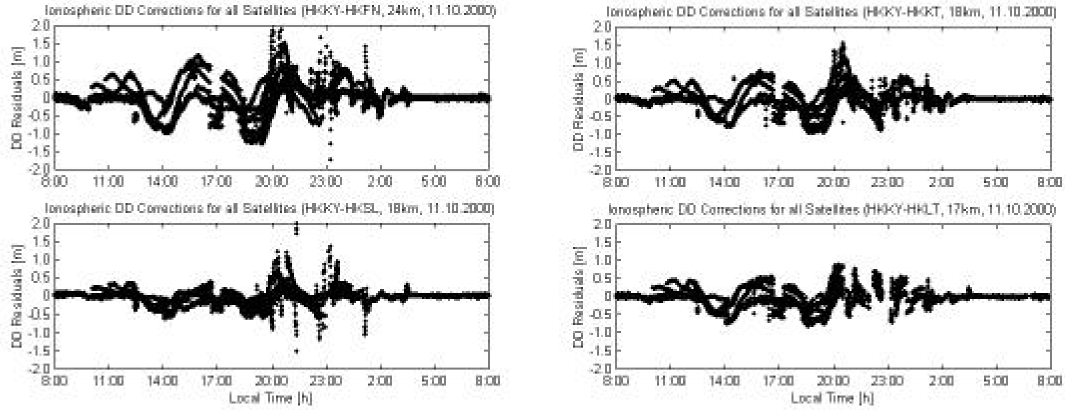

Fig. 5.18+5.19: Double-differenced L1 corrections for fiducial (left) and inner (right) baselines (DOY 285)

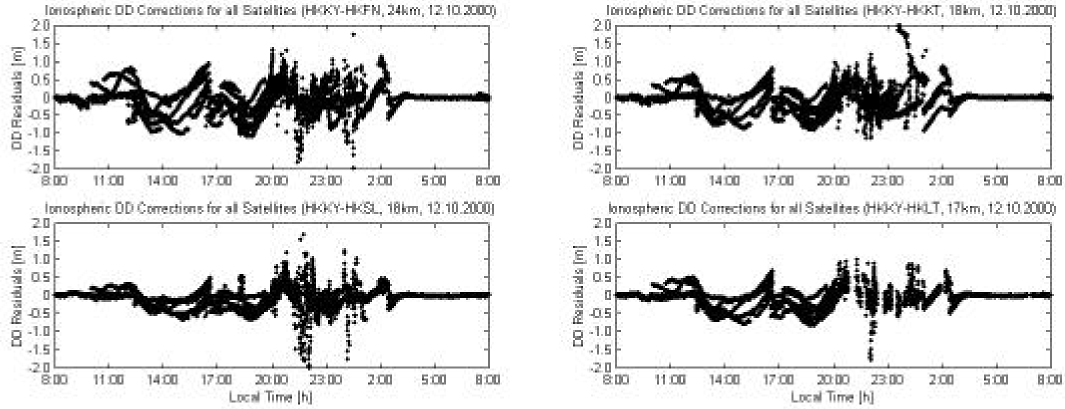

Fig. 5.20+5.21: Double-differenced L1 corrections for fiducial (left) and inner (right) baselines (DOY 286)

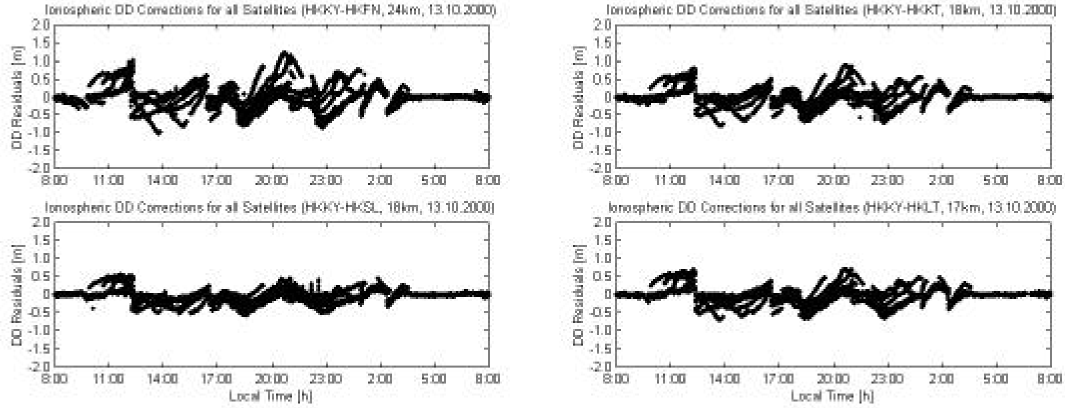

Fig. 5.22+5.23: Double-differenced L1 corrections for fiducial (left) and inner (right) baselines (DOY 287)

5.3.2 Ionospheric Corrections for the Inner Baselines

Using equations (4-12) to (4-14), the α values were derived in order to relate the position of the inner network sites to the fiducial baselines. Table 5.8 lists the α values obtained for the inner GPS sites, α_1 and α_2 indicating the values corresponding to the fiducial baselines HKKY-HKFN and HKKY-HKSL respectively.

Tab. 5.8: α values obtained for the inner GPS network stations

Site	α_1	α_2
HKKT	0.627043	0.327184
HKLT	0.351097	0.683660

In this case the relation between these α values and the network geometry can easily be recognised. The inner sites HKKT and HKLT are both close to the line HKSL-HKFN. Even more so, the distances HKSL-HKLT, HKLT-HKKT and HKKT-HKFN are all about equal (8.7km, 7.8km and 9.2km respectively). For HKKT, the weights $\alpha_1 \approx 0.63$ and $\alpha_2 \approx 0.33$ have been obtained, showing that this site is closer to the baseline HKKY-HKFN (or HKFN) while it is approximately double this distance from the second fiducial baseline (or HKSL). Due to the inverted geometry, values of $\alpha_1 \approx 0.35$ and $\alpha_2 \approx 0.68$ have been obtained for HKLT.

The L1 correction terms for the inner baselines can be determined by forming the linear combination using equation (4-27). In order to form this linear combination the correction files have been modified to ensure they have the same number of double-differenced correction terms, with matching receiver-satellite pairs, for both fiducial baselines. Hence, the double-differenced correction terms for the inner baselines could be derived in two ways. Firstly, as described in the previous section, the corrections were determined directly using dual-frequency data and the modified Bernese software (Figures 5.19, 5.21 and 5.23). Secondly, they were obtained indirectly by forming a linear combination of the corrections for the fiducial baselines using the α values (Figures 5.24-5.26). Several parameters characterising these correction terms are listed in Table 5.7 (indicated by asterisks). It can be seen that the results are very similar, and hence model the condition of the ionosphere very well. This again indicates that the proposed procedure indeed generates reliable correction terms for the inner baselines.

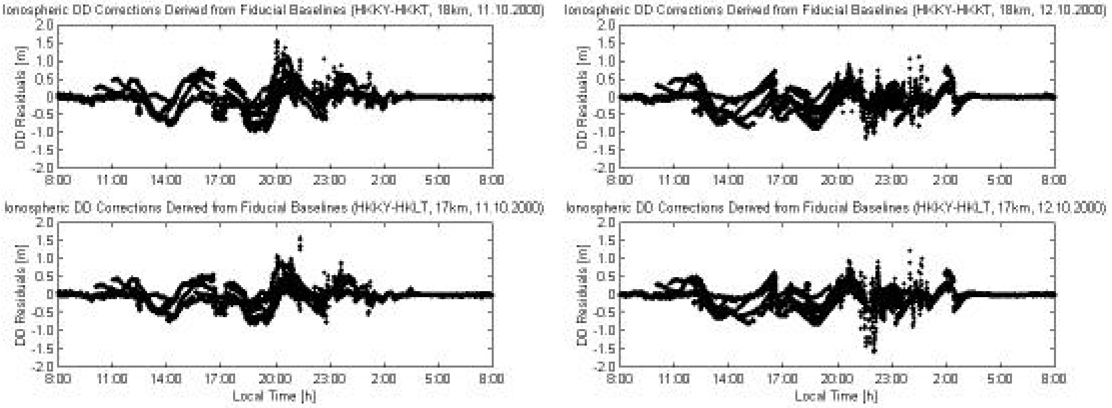

Fig. 5.24+5.25: Double-differenced L1 corrections for inner baselines obtained using α values (DOY 285+286)

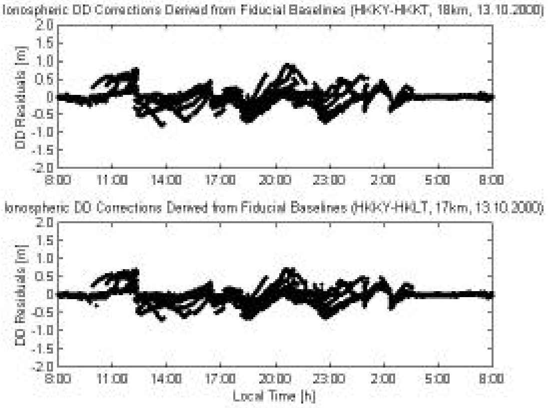

Fig. 5.26: Double-differenced L1 corrections for inner baselines obtained using α values (DOY 287)

5.3.3 Baseline Results

The Baseline software is again used to process the inner baselines in single-frequency mode, with and without using ionospheric correction terms. It was assumed that no ground deformation had taken place during the period of observation. Figure 5.27 shows the results obtained for the inner baselines using the Baseline software without applying ionospheric corrections on day 285, while Figure 5.28 shows the results obtained by applying the ionospheric corrections. Figures 5.29-5.30 and 5.31-5.32 present the results obtained for the following two days respectively. The graphs show the Easting, Northing and Height components over a 24-hour period, each dot representing a single-epoch solution. In both cases the Saastamoinen model was used to account for the tropospheric bias, as recommended by Mendes (1999).

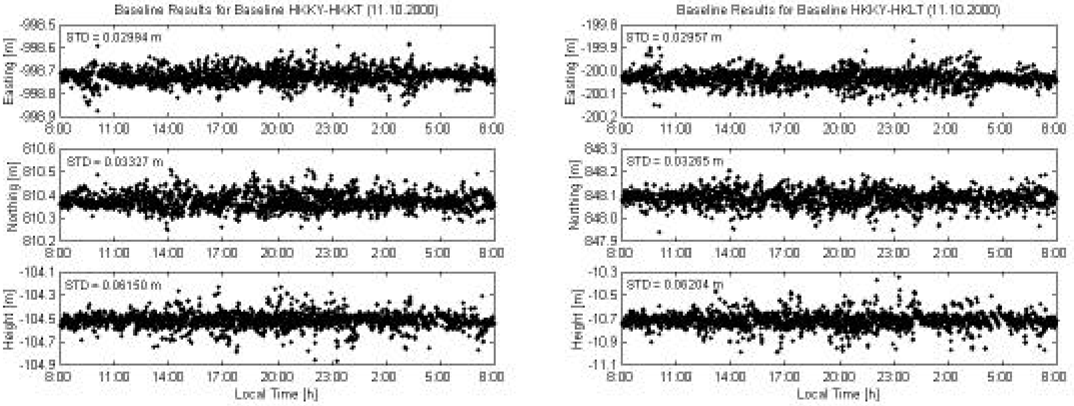

Fig. 5.27: Results for inner baselines not using ionospheric corrections (DOY 285)

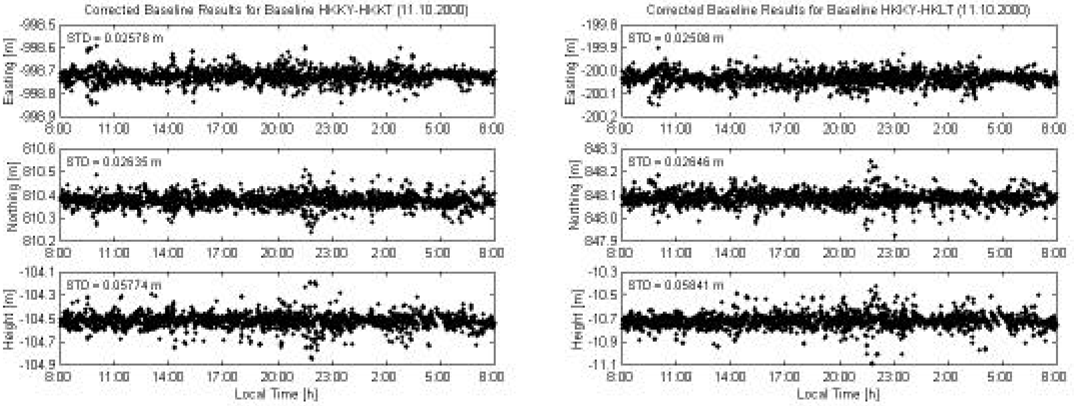

Fig. 5.28: Results for inner baselines applying ionospheric corrections (DOY 285)

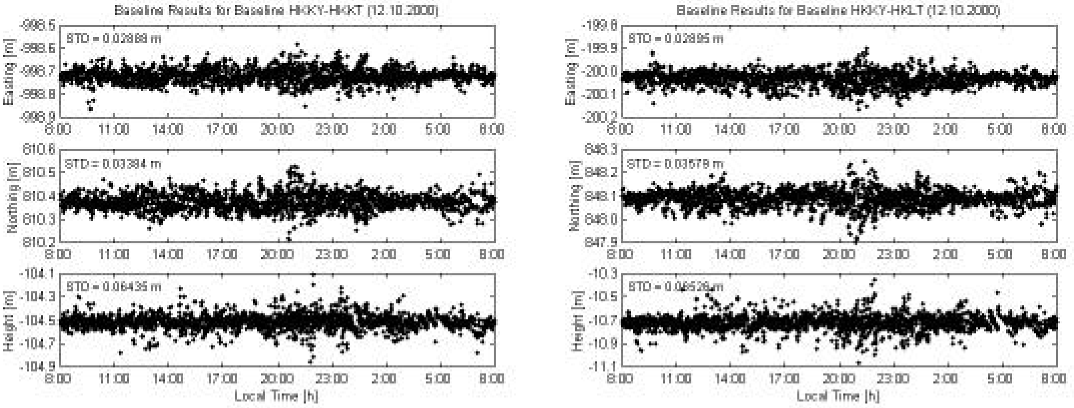

Fig. 5.29: Results for inner baselines not using ionospheric corrections (DOY 286)

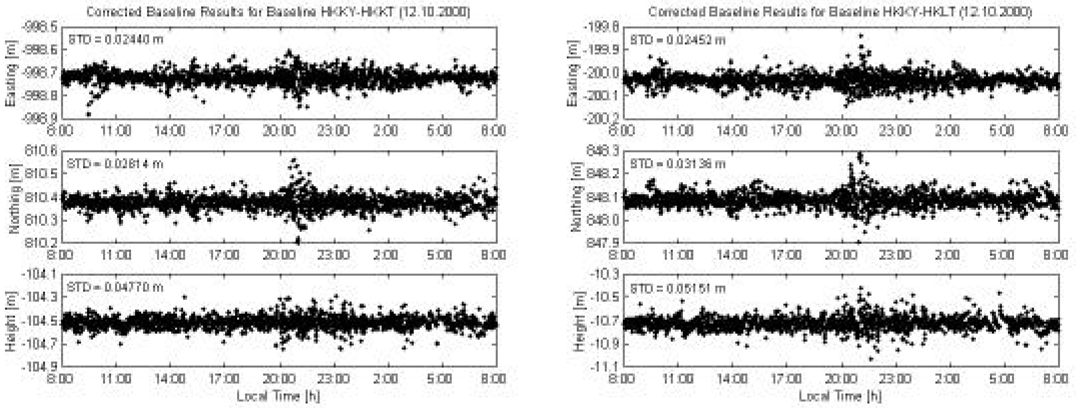

Fig. 5.30: Results for inner baselines applying ionospheric corrections (DOY 286)

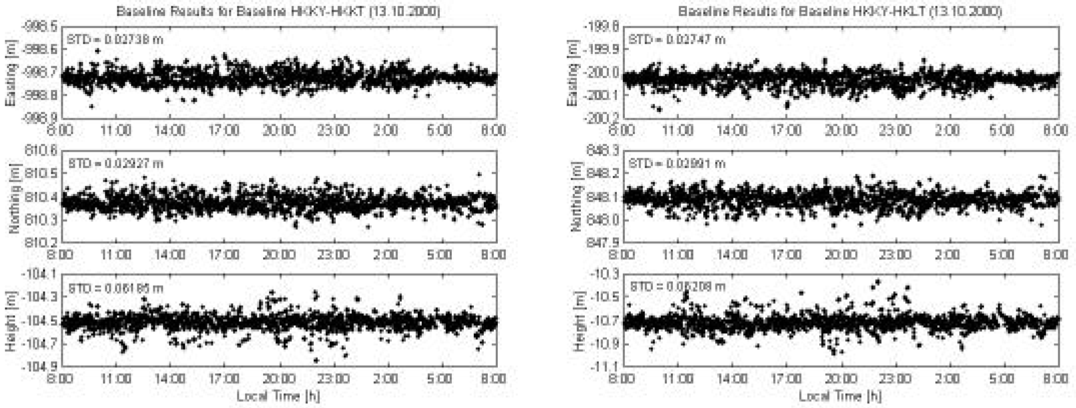

Fig. 5.31: Results for inner baselines not using ionospheric corrections (DOY 287)

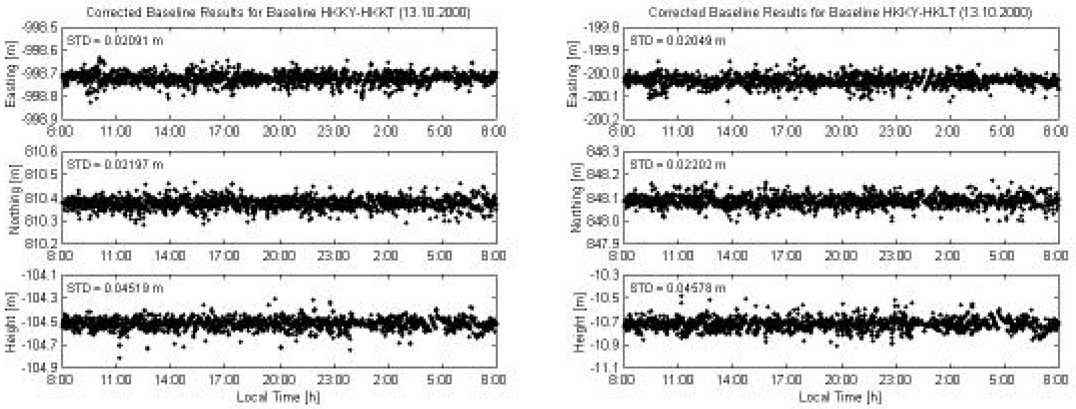

Fig. 5.32: Results for inner baselines applying ionospheric corrections (DOY 287)

Table 5.9 lists the standard deviations (STD) of the results obtained for the inner baselines using the two different processing methods (not applying corrections versus applying corrections) on three successive days. Although a comparison of Figures 5.27-

5.32 does not clearly show this, indeed the baseline results are improved by applying the correction terms (as indicated by Table 5.9). On average, the standard deviation of the baseline results has been reduced by about 20% in all three components (Table 5.10). The biggest improvement (of approximately 25%) was achieved on day 287, the day with comparatively calm ionospheric conditions. This indicates that extreme ionospheric conditions, such as those experienced in the equatorial anomaly region during solar cycle maximum periods, can reduce the efficiency of the proposed method. This is most likely due to short-term effects that cannot be modelled adequately. When applying the correction terms, the standard deviations still reach values of 2.0-3.5cm for the horizontal components and 4.5-6.5cm for the height component – values too large to permit reliable detection of ground deformation at the centimetre level. Unfortunately the promising results obtained at mid-latitudes (see section 5.2) could not be repeated for this network, situated as it is in the equatorial region, even though the fiducial baseline lengths in this network were much shorter compared to SCIGN.

Tab. 5.9: Standard deviations of the inner baseline components on days 285-287 in [m]

	Day 285, no corr.	Day 285, corr.	Day 286, no corr.	Day 286, corr.	Day 287, no corr.	Day 287, corr.
Baseline HKKY-HKKT						
STD Easting [m]	0.02994	0.02578	0.02888	0.02440	0.02738	0.02091
STD Northing [m]	0.03327	0.02635	0.03384	0.02814	0.02927	0.02197
STD Height [m]	0.06150	0.05774	0.06435	0.04770	0.06185	0.04519
Baseline HKKY-HKLT						
STD Easting [m]	0.02957	0.02508	0.02895	0.02452	0.02747	0.02049
STD Northing [m]	0.03265	0.02646	0.03579	0.03136	0.02991	0.02202
STD Height [m]	0.06204	0.05841	0.06526	0.05151	0.06208	0.04578

Tab. 5.10: Average improvement in the STD for both baselines on days 285-287

Baseline	DOY	Easting [%]	Northing [%]	Height [%]
HKKY-HKKT (18km)	285	13.9	20.8	6.1
	286	15.5	16.8	25.9
	287	23.6	24.9	26.9
HKKY-HKLT (17km)	285	15.2	19.0	5.9
	286	15.3	12.4	21.1
	287	25.4	26.4	26.3
Average [%]		18	20	19

5.3.4 Summary

The results obtained for the Hong Kong GPS network show that very large ionospheric correction terms (of the order of several cycles) are still able to improve the accuracy of the baseline solutions. Hence they do model the ionospheric conditions (at least to some extent). However, due to the severity of the ionospheric conditions, the fiducial baselines have to be comparatively short in order to ensure this. A distinct gradient in the ionospheric conditions has been detected with increasing ionospheric effects in the general direction from the southwest to the northeast of the GPS network. The single-frequency baseline repeatability has been improved by applying the empirical correction terms. The standard deviation of the baseline results has been reduced by approximately 20% in all three components. However, the findings also indicate that extreme ionospheric conditions, such as those experienced in close proximity to the geomagnetic equator during solar cycle maximum periods, can reduce the efficiency of the proposed method.

5.4 Malaysia / Singapore 2001

In order to investigate the performance of the proposed network configuration for a network situated in the centre of the equatorial region, data from a network comprising sites in Malaysia and Singapore were analysed. Figure 5.33 shows the location of the GPS sites, which are all equipped with dual-frequency receivers. The test network consists of an outer network of three sites (LOYA, DOP2, TSDL) surrounding one inner site (SEMB). The outer sites were used as fiducial GPS reference stations, indicated by triangles in Figure 5.33, while the inner site (indicated by a circle) was used as a single-frequency receiver station (by ignoring the observations made on L2). The inner site was connected to the fiducial site LOYA to form the inner baseline. The data were collected under solar maximum conditions, using an observation rate of 30s, on three consecutive days 9-11 October 2001 (DOY 282-284).

The ITRF2000 coordinates of the GPS network stations are listed in Table 5.11. These coordinates were taken from a global solution of a survey campaign spanning several days, generated by A/Prof. P. Morgan at the University of Canberra (Morgan, 2002, personal communication).

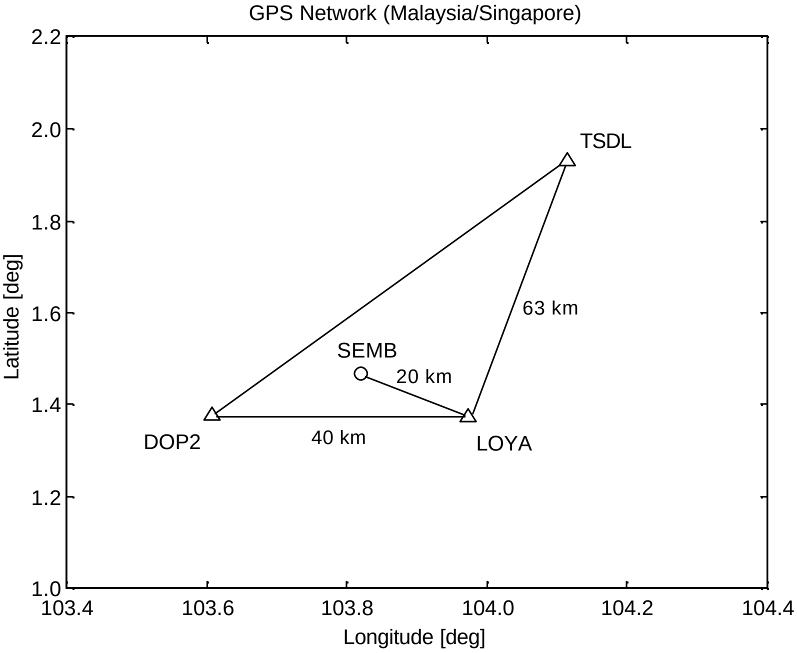

Fig. 5.33: GPS network in Malaysia / Singapore

Tab. 5.11: ITRF2000 coordinates of the GPS network stations located in Malaysia / Singapore

Site	DOP2	LOYA
X [m]	-1500246.3392	-1539521.7224
Y [m]	6197397.9982	6187727.2632
Z [m]	152195.8442	151766.4896
Latitude (N)	1° 22’ 35.4814’’	1° 22’ 21.5306’’
Longitude (E)	103° 36’ 29.4909’’	103° 58’ 17.9294’’
Height [m]	91.650	51.153

Site	TSDL	SEMB
X [m]	-1554345.1155	-1523020.9337
Y [m]	6182152.4267	6191514.2528
Z [m]	213246.3325	162500.1192
Latitude (N)	1° 55’ 43.9978’’	1° 28’ 11.1081’’
Longitude (E)	104° 06’ 46.9408’’	103° 49’ 10.3457’’
Height [m]	11.464	30.900

5.4.1 Ionospheric Corrections for the Fiducial Baselines

As before, processing the dual-frequency data with a modified version of the Bernese software permitted ionospheric L1 correction terms to be determined for the three baselines on three successive days. The baselines LOYA-DOP2 (40km) and LOYA-TSDL (63km) were used as fiducial reference baselines. For comparison purposes, corrections were also obtained for the inner baseline LOYA-SEMB (20km) using observations made on both frequencies. As in the previous studies, Table 5.12 lists several parameters characterising the correction terms. Figures 5.34, 5.36 and 5.38 show the double-differenced corrections obtained for the fiducial baselines on L1 for three consecutive 24-hour observation sessions, while Figures 5.35, 5.37 and 5.39 show the corrections obtained for the inner baseline.

It can be seen that, as expected, ionospheric activity in the equatorial region is at its peak between sunset and 2am local time. The ionosphere was a little less active on day 283 compared to the other two days. The correction terms for all baselines show a similar pattern, but the magnitude of the correction terms reaches values of more than three metres in some cases! In addition, the corrections obtained for the inner baseline show large disturbances after 8pm local time, indicating severe ionospheric activity.

Tab. 5.12: Double-differenced L1 corrections for different baselines

Baseline	D [km]	min [m]	max [m]	mean [m]	STD [m]	#DD
Malaysia 9.10.2001 (L1)						
LOYA-DOP2	40	-3.23465	4.35245	0.19770	0.49512	16542
LOYA-TSDL	63	-2.74020	2.81592	0.28752	0.66578	16075
LOYA-SEMB	20	-4.16128	3.25775	-0.00094	0.37967	15810
LOYA-SEMB*	20	-1.64747	2.17213	0.13607	0.28752	15083
Malaysia 10.10.2001 (L1)						
LOYA-DOP2	40	-1.93588	2.45310	0.10724	0.38426	18318
LOYA-TSDL	63	-1.36700	2.31962	0.17131	0.53219	17671
LOYA-SEMB	20	-0.98025	1.49007	0.00706	0.16113	17110
LOYA-SEMB*	20	-1.03280	1.19043	0.08102	0.24261	17204
Malaysia 11.10.2001 (L1)						
LOYA-DOP2	40	-2.61689	3.82900	0.22161	0.55332	16666
LOYA-TSDL	63	-3.11448	2.73885	0.26741	0.62588	16160
LOYA-SEMB	20	-2.73022	1.87323	-0.01700	0.29432	15795
LOYA-SEMB*	20	-1.43918	1.72888	0.15298	0.31031	15172
* calculated using α values						

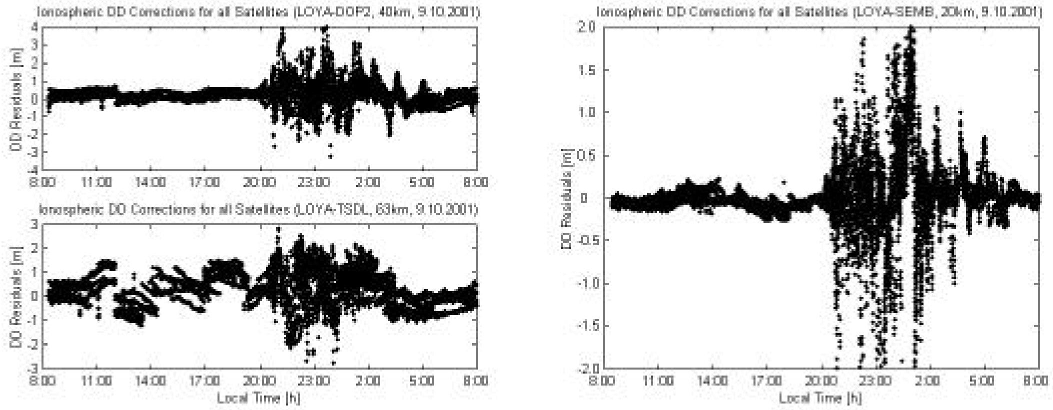

Fig. 5.34+5.35: Double-differenced L1 corrections for fiducial (left) and inner (right) baselines (DOY 282)

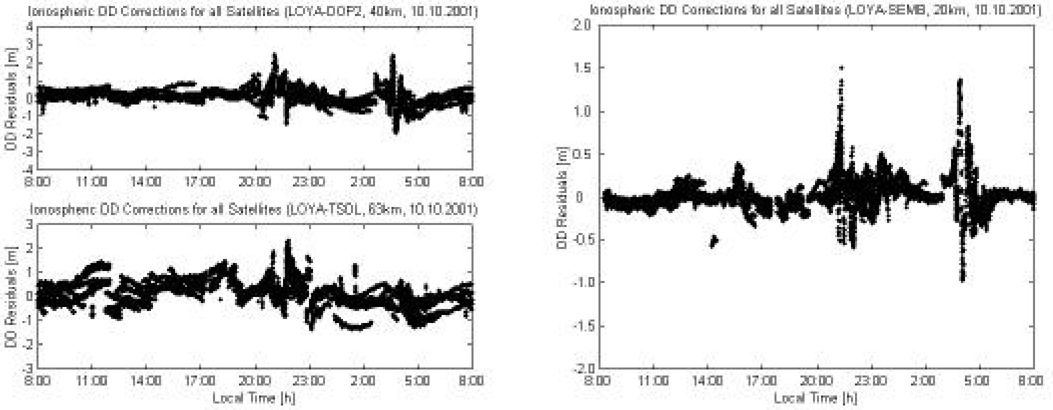

Fig. 5.36+5.37: Double-differenced L1 corrections for fiducial (left) and inner (right) baselines (DOY 283)

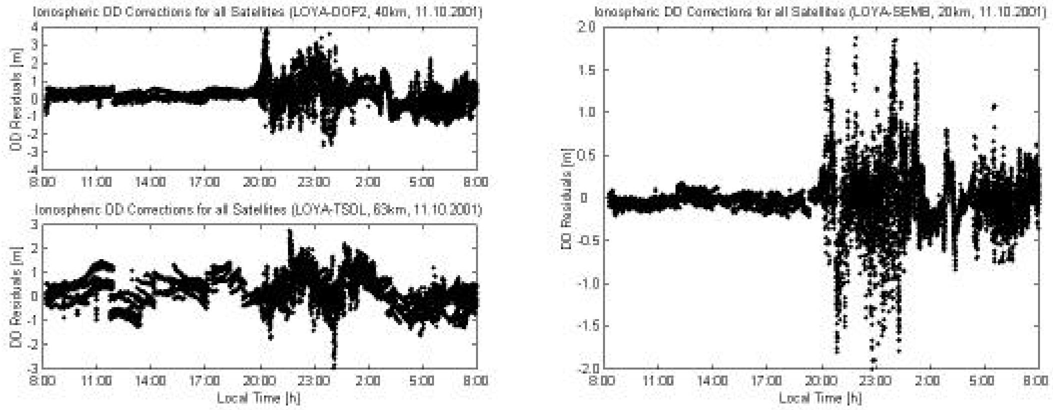

Fig. 5.38+5.39: Double-differenced L1 corrections for fiducial (left) and inner (right) baselines (DOY 284)

5.4.2 Ionospheric Corrections for the Inner Baseline

The position of the inner GPS site in relation to the fiducial baselines is expressed by the α values (equations (4-12)-(4-14)), which were found to be $\alpha_1 = 0.485100$ and $\alpha_2 = 0.171194$, corresponding to the fiducial baselines LOYA-DOP2 and LOYA-TSDL respectively.

The L1 correction terms for the inner baseline can then be determined by forming the linear combination using equation (4-27). In order to form this linear combination, the correction files have been modified to ensure that they contain the same number of double-differenced correction terms, with matching receiver-satellite pairs, for both fiducial baselines. As before, the double-differenced correction terms for the inner baseline could be derived in two ways. Firstly, as described in the previous section, the corrections were determined directly using dual-frequency data and the modified Bernese software (Figures 5.35, 5.37 and 5.39). Secondly, they were obtained indirectly by forming a linear combination of the corrections for the fiducial baselines using the α values (Figures 5.40-5.42). Several parameters characterising these correction terms are listed in Table 5.12 (indicated by asterisks). The graphs show a similar pattern, but the corrections generated using the α values are a little noisier. This indicates that unmodelled atmospheric biases are still present, which is likely to affect baseline results.

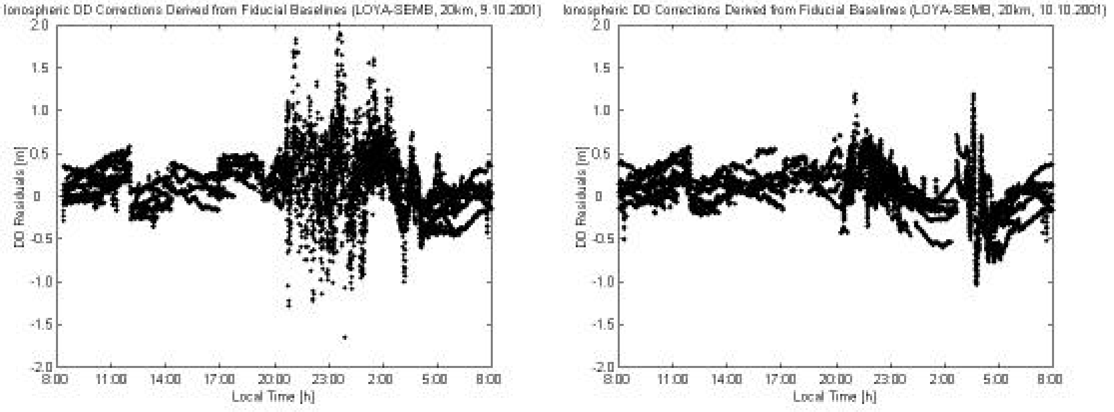

Fig. 5.40+5.41: Double-differenced L1 corrections for the inner baseline obtained using α values (DOY 282+283)

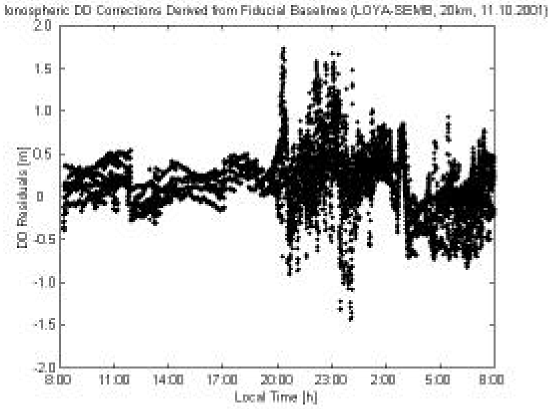

Fig. 5.42: Double-differenced L1 corrections for the inner baseline obtained using α values (DOY 284)

5.4.3 Baseline Results

The Baseline software was again used to process the inner baseline in single-frequency mode, with and without using ionospheric correction terms. It was assumed that no ground deformation had taken place during the period of observation. Figures 5.43-5.45 show the results obtained for the inner baseline using the Baseline software without applying ionospheric corrections (left), and after applying the ionospheric corrections (right). The graphs show the Easting, Northing and Height components over a 24-hour period on three successive days, each dot representing a single-epoch solution. In both cases the Saastamoinen model was used to account for the tropospheric bias, as recommended by Mendes (1999).

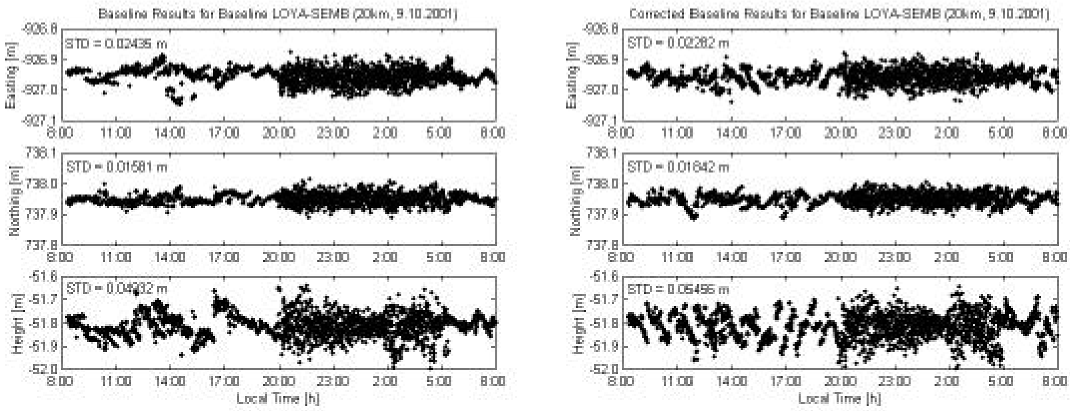

Fig. 5.43: Results for inner baseline not applying (left) and applying (right) corrections (DOY 282)

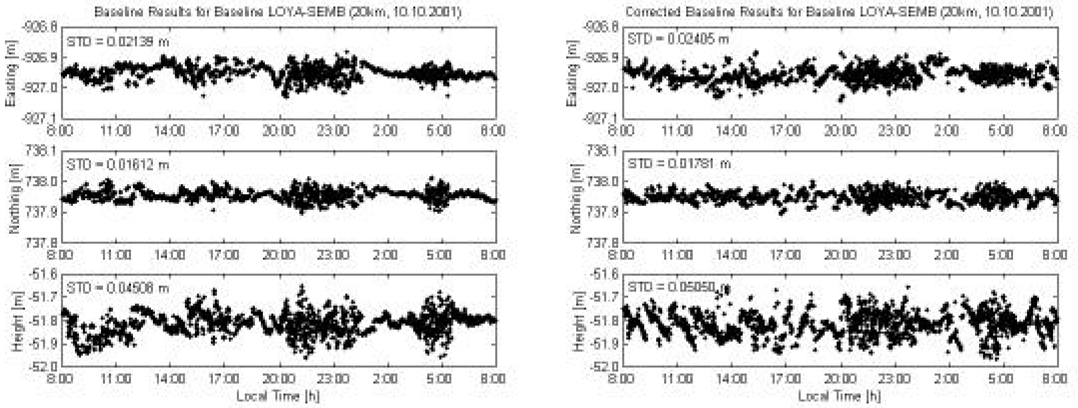

Fig. 5.44: Results for inner baseline not applying (left) and applying (right) corrections (DOY 283)

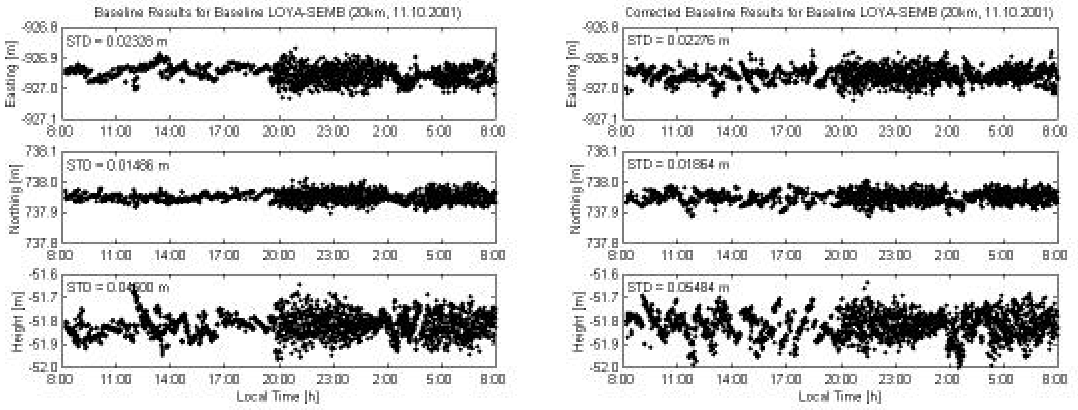

Fig. 5.45: Results for inner baseline not applying (left) and applying (right) corrections (DOY 284)

Table 5.13 lists the standard deviations (STD) of the results obtained for the inner baseline using the two different processing methods (not applying corrections versus applying corrections) on three successive days. This table and Figures 5.43-5.45 clearly show that the corrections do not improve the quality of the baseline results. In most cases the standard deviations are actually slightly increased when correction terms are used in the baseline processing. This result is rather disappointing and can be explained by the extremely variable ionospheric conditions that were experienced, which cannot be modelled properly in this case. However, it is interesting to note that the standard deviations reach values of 1.5-2.4cm for the horizontal components and 4.5-5.5cm for the height component. In spite of the slightly longer inner baseline and the significantly longer fiducial baseline lengths compared to the Hong Kong network, these values are actually better (lower). Nevertheless it seems that the performance of the proposed network processing strategy degrades with decreasing geographic latitude of the GPS network.

Tab. 5.13: Standard deviations of the inner baseline components on days 282-284 in [m]

	Day 282, no corr.	Day 282, corr.	Day 283, no corr.	Day 283, corr.	Day 284, no corr.	Day 284, corr.
Baseline LOYA-SEMB						
STD Easting [m]	0.02435	0.02282	0.02139	0.02405	0.02328	0.02276
STD Northing [m]	0.01581	0.01842	0.01612	0.01781	0.01486	0.01864
STD Height [m]	0.04932	0.05456	0.04508	0.05050	0.04600	0.05484

5.4.4 Summary

Similar to the Hong Kong network studies, the magnitudes of the correction terms were found to be very large for the Malaysia-Singapore network. The single-frequency baseline repeatability could not be improved by applying the empirical correction terms. It seems that the performance of the proposed network processing strategy degrades with decreasing geographic latitude of the GPS network, which is most likely due to the extreme short-term variations in the ionosphere in the equatorial region during a solar maximum.

It is worth noting that a large number of drop-outs on L2 occurred in the raw RINEX data for the fiducial sites DOP2 and TSDL. This indicates the presence of high scintillation effects causing loss-of-lock on L2. Furthermore, it reduces the number of double-differenced corrections that can be formed from the dual-frequency data, which in turn increases the number of double-differences that cannot be corrected in the single-frequency data processing (because the correction is missing). This partly explains the disappointing performance of the proposed processing strategy in this network.

5.5 Papandayan 2001

During July 2001 data were collected from the mixed-mode GPS-based volcano deformation monitoring system on Gunung Papandayan in West Java, Indonesia. Figure 5.46 shows the location of the GPS sites. The fiducial stations GUNT, PAME and PANG are denoted by triangles, while the inner single-frequency sites (BASE, BUKI, NANG, KAWA) are indicated by circles. The data were collected under solar maximum conditions, using an observation rate of 15 seconds, on four consecutive days 11-14 July 2001 (DOY 192-195). The Cartesian ITRF2000 coordinates of the GPS network sites are given in Tables 2.1 and 2.2 (see section 2.5.4).

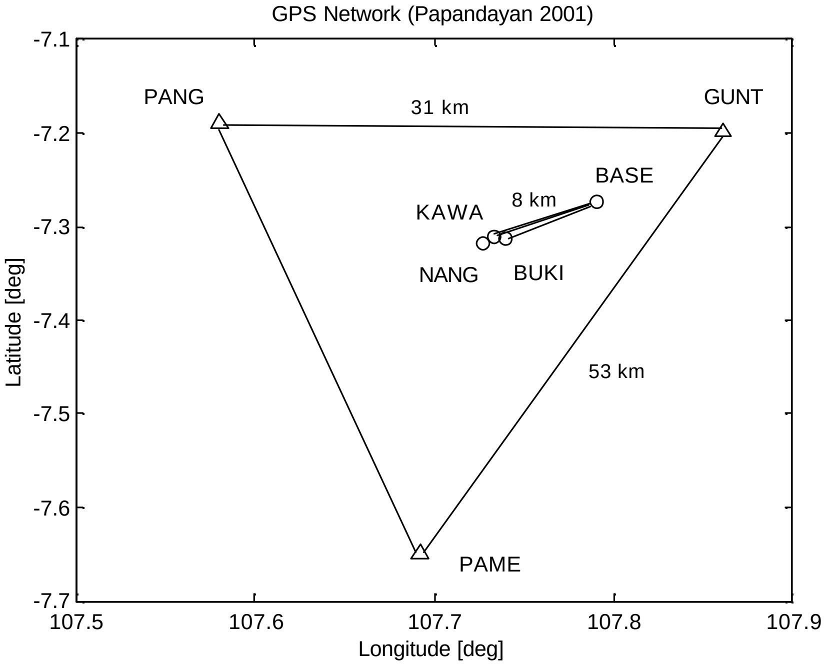

Fig. 5.46: Mixed-mode GPS network on Gunung Papandayan 2001

5.5.1 Ionospheric Corrections for the Fiducial Baselines

In order to check the quality of the fiducial stations, data collected on 28 successive days between July 5 and August 1, 2001, (DOY 186-213) were processed using the GAMIT software package (King & Bock, 1995), generating global 24-hour solutions. Figures 5.47-5.49 show the resulting Northing, Easting and Height components for the three sites, and their standard deviations, over the period considered (the horizontal axis indicating the day of year).

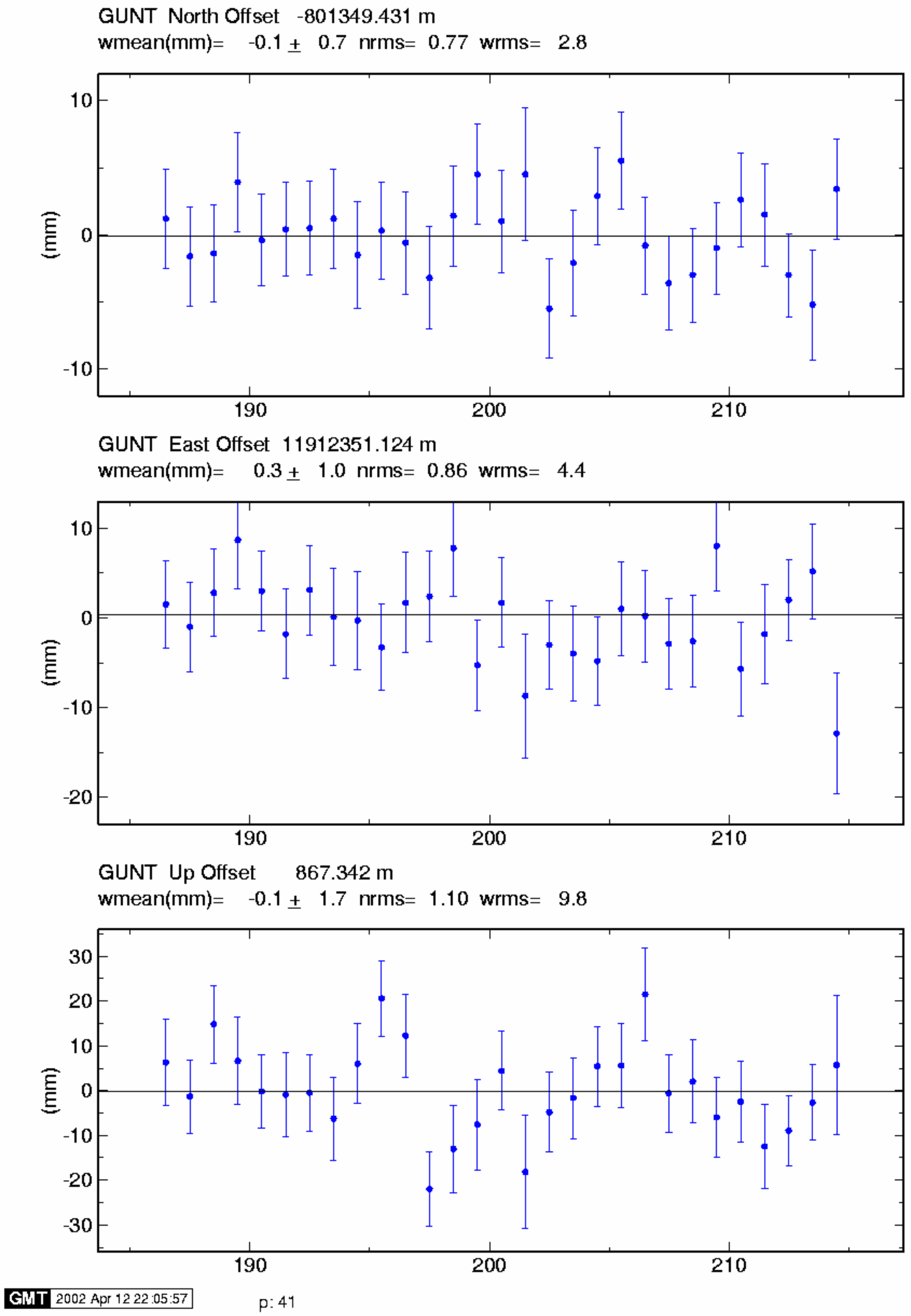

Fig. 5.47: Position time series of GUNT on 29 consecutive days (DOY 186-214)

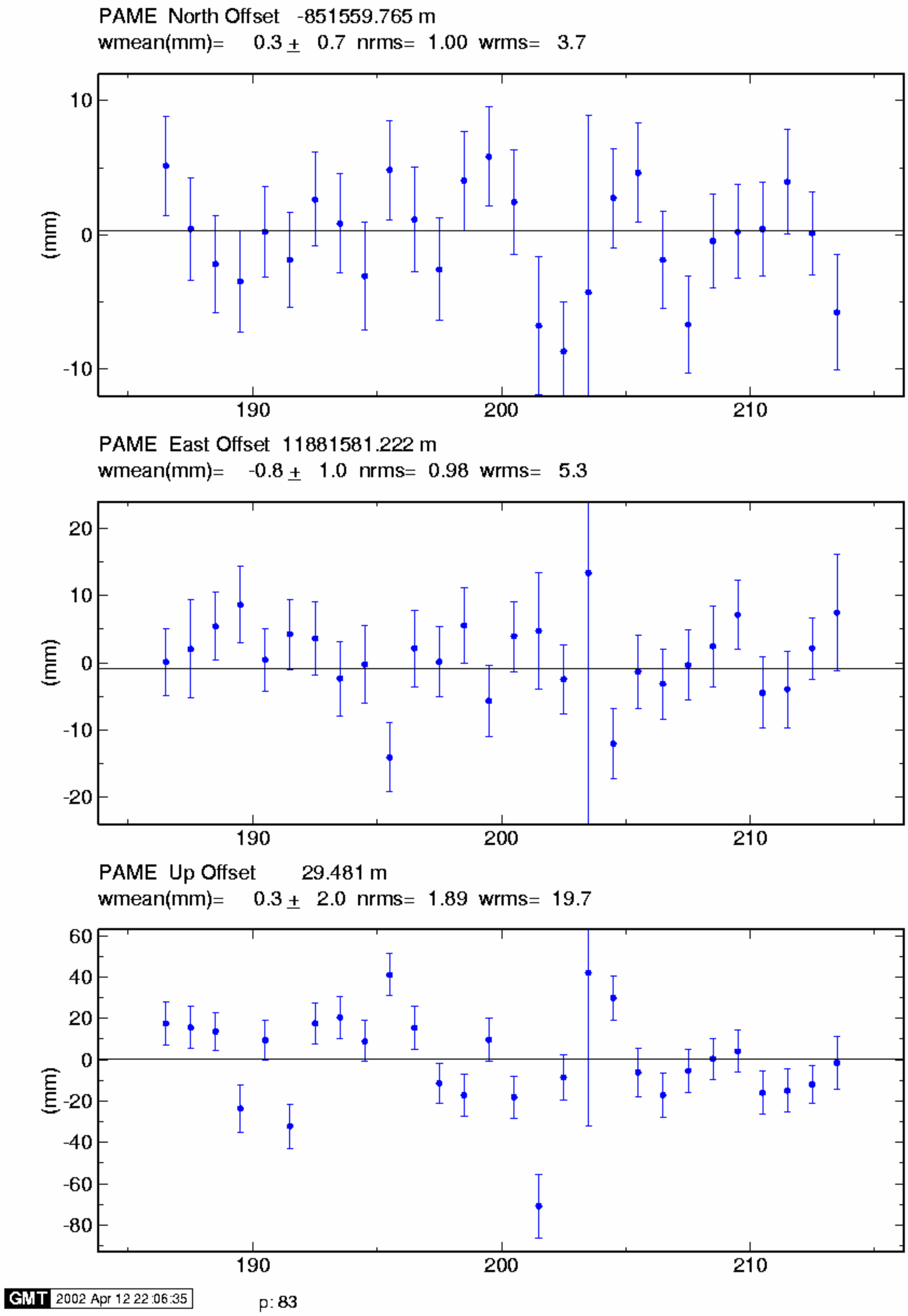

Fig. 5.48: Position time series of PAME on 28 consecutive days (DOY 186-213)

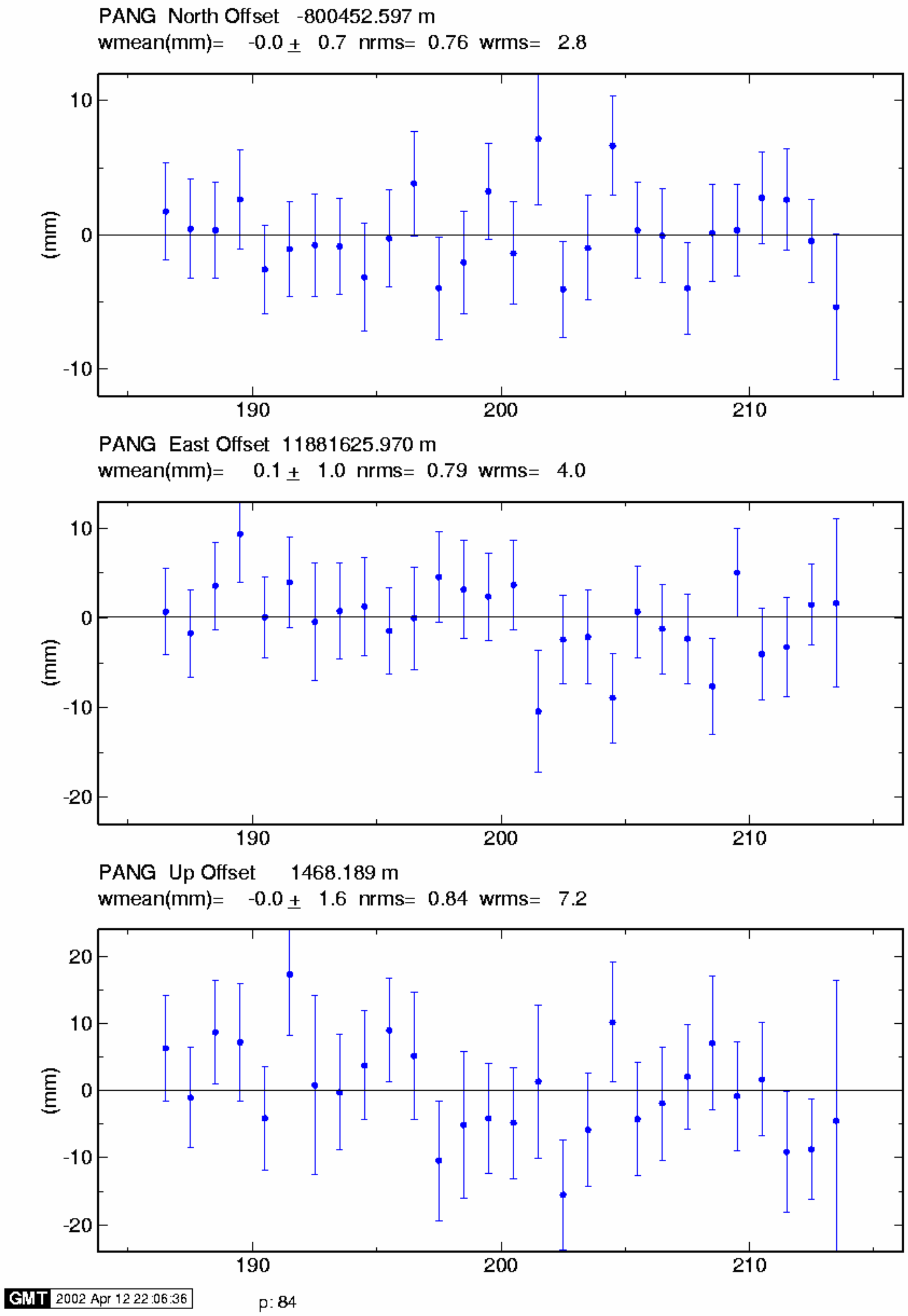

Fig. 5.49: Position time series of PANG on 28 consecutive days (DOY 186-213)

It can be seen that the repeatability of the horizontal coordinate components is at the sub-centimetre level, while the vertical component exhibits a larger variation. This illustrates the high quality of the dual-frequency data. However, it is evident that the quality of PAME is slightly inferior to the other two fiducial sites, as indicated by comparatively larger coordinate variations, especially in the height component. Clearly, a problem occurred at PAME on day 203, resulting in a very large uncertainty of the solution. Another example of obvious degradation in GPS data quality can be found at PANG on day 213.

Processing the dual-frequency GPS data with a modified version of the Bernese software allowed ionospheric L1 correction terms to be determined for the two fiducial baselines GUNT-PAME (53km) and GUNT-PANG (31km) on four successive days (DOY 192-195). The corrections have already been analysed in section 4.6.4 (see Figure 4.19 and Table 4.5).

It is obvious that the ionosphere is highly variable, resulting in correction terms of up to 2m in magnitude for the longer baseline. A lot of activity is evident during daytime hours, which is probably a result of a relatively high primary diurnal maximum for the equatorial anomaly, as discussed in section 4.6.3.

5.5.2 Baseline Results

Following the procedure outlined in chapter 4, the α values were derived using equations (4-12) to (4-14). Table 5.14 lists the α values obtained for the inner GPS sites, α_1 and α_2 indicating the values corresponding to the fiducial baselines GUNT-PAME and GUNT-PANG respectively.

Tab. 5.14: α values obtained for the inner GPS network stations

Site	α_1	α_2
Base (BASE)	0.168344	0.146958
Bukit Maung (BUKI)	0.257577	0.274309
Nangklak (NANG)	0.272469	0.311687
Kawah (KAWA)	0.256577	0.298450

Baseline processing was then carried out, with and without applying the empirically derived correction terms. In both cases the Saastamoinen model was used to account for the tropospheric bias, as recommended by Mendes (1999).

Figures 5.50-5.53 show the results obtained for the three inner baselines without applying ionospheric corrections (left), and the results obtained by applying the corrections (right) on four consecutive days. The graphs show the Easting, Northing and Height components over a 24-hour period, each dot representing a single-epoch solution.

Table 5.15 lists the standard deviations of the results obtained for the inner baselines using the two different processing methods (not applying corrections versus applying corrections). Clearly, the corrections do not improve the results when applied in the data processing. The standard deviations cannot be reduced below 3.1-5.0cm for the horizontal components and 7.0-8.0cm for the vertical component.

Tab. 5.15: Standard deviations of the inner baseline components on days 192-195 in [m]

	BASE-BUKI, no corr.	BASE-BUKI, corr.	BASE-NANG, no corr.	BASE-NANG, corr.	BASE-KAWA, no corr.	BASE-KAWA, corr.
DOY 192						
STD Easting [m]	0.04658	0.04610	0.04449	0.04467	0.04183	0.04796
STD Northing [m]	0.03791	0.03996	0.03420	0.03409	0.03039	0.03270
STD Height [m]	0.08198	0.07911	0.07950	0.07965	0.07122	0.07077
DOY 193						
STD Easting [m]	0.05059	0.04917	0.04796	0.04673	0.04783	0.05026
STD Northing [m]	0.03636	0.03703	0.03513	0.03357	0.03107	0.03154
STD Height [m]	0.08356	0.07987	0.08044	0.08049	0.07829	0.07945
DOY 194						
STD Easting [m]	0.04635	0.04924	0.04677	0.04811	0.04487	0.04910
STD Northing [m]	0.03889	0.04065	0.03706	0.03693	0.03218	0.03176
STD Height [m]	0.08283	0.07764	0.08220	0.07713	0.07639	0.07390
DOY 195						
STD Easting [m]	0.04951	0.04860	0.04266	0.04345	0.04807	0.04795
STD Northing [m]	0.03556	0.03610	0.03356	0.03265	0.03124	0.03128
STD Height [m]	0.07875	0.07811	0.07853	0.08005	0.07859	0.07408

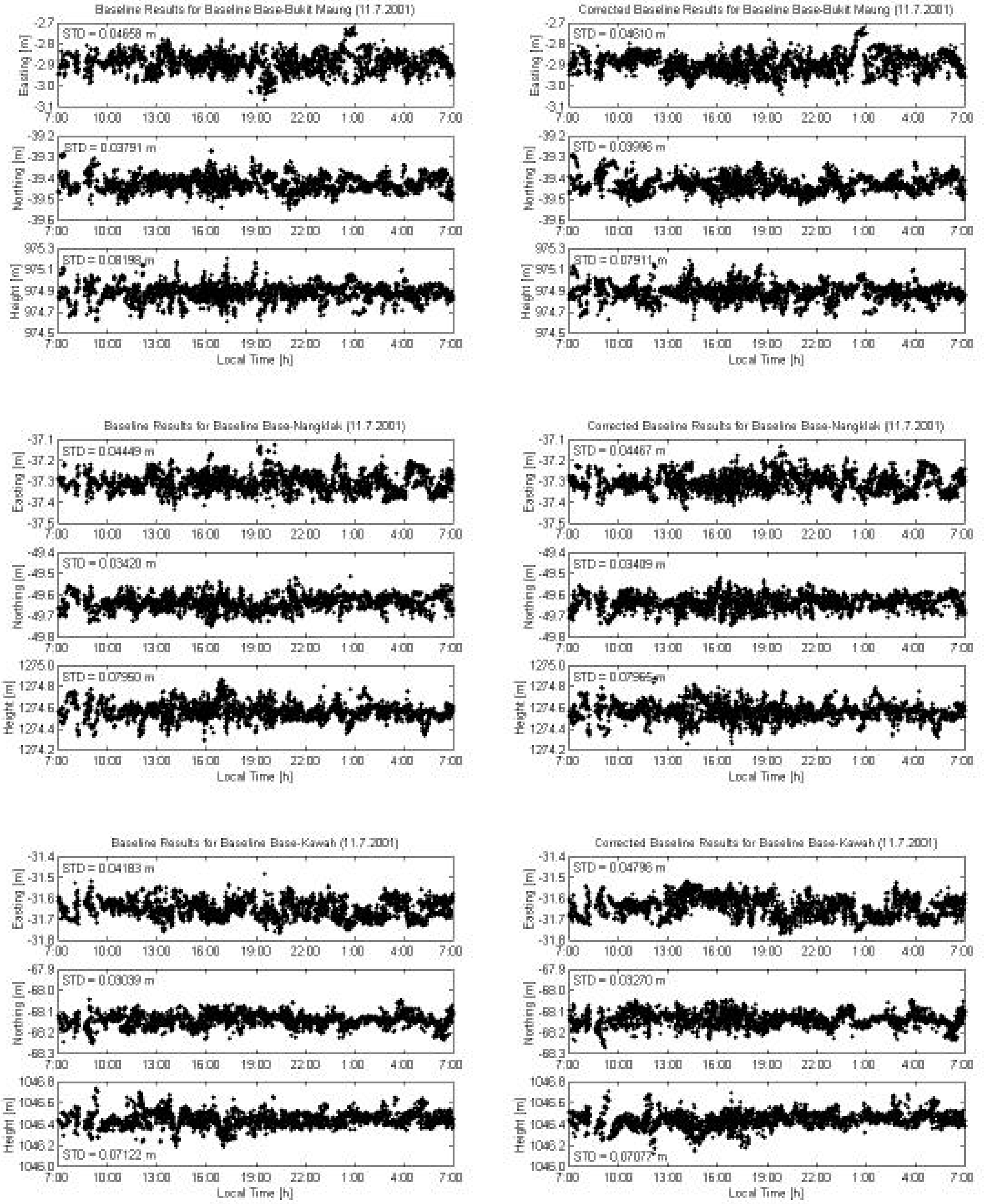

Fig. 5.50: Results for inner baselines not applying (left) and applying (right) corrections (DOY 192)

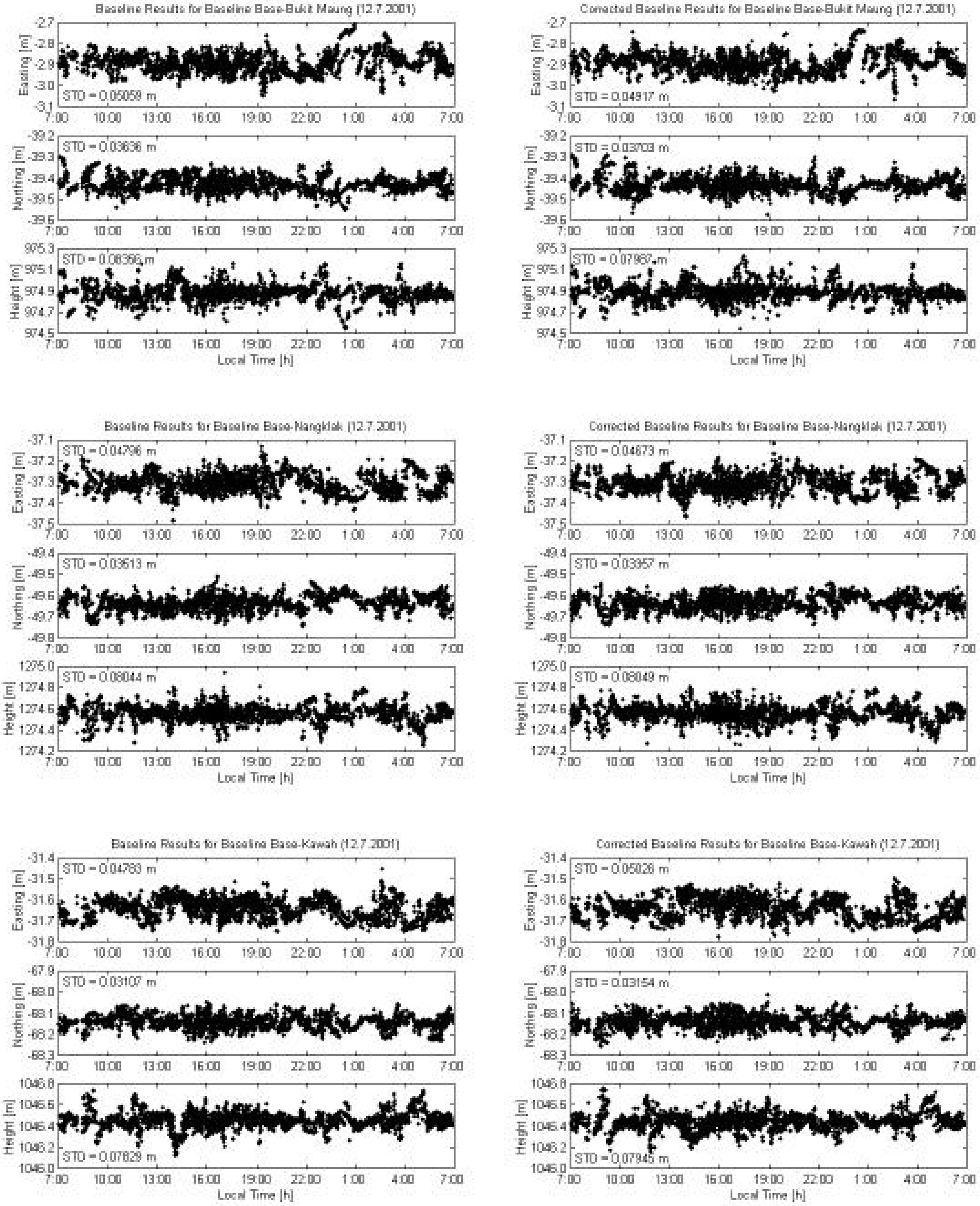

Fig. 5.51: Results for inner baselines not applying (left) and applying (right) corrections (DOY 193)

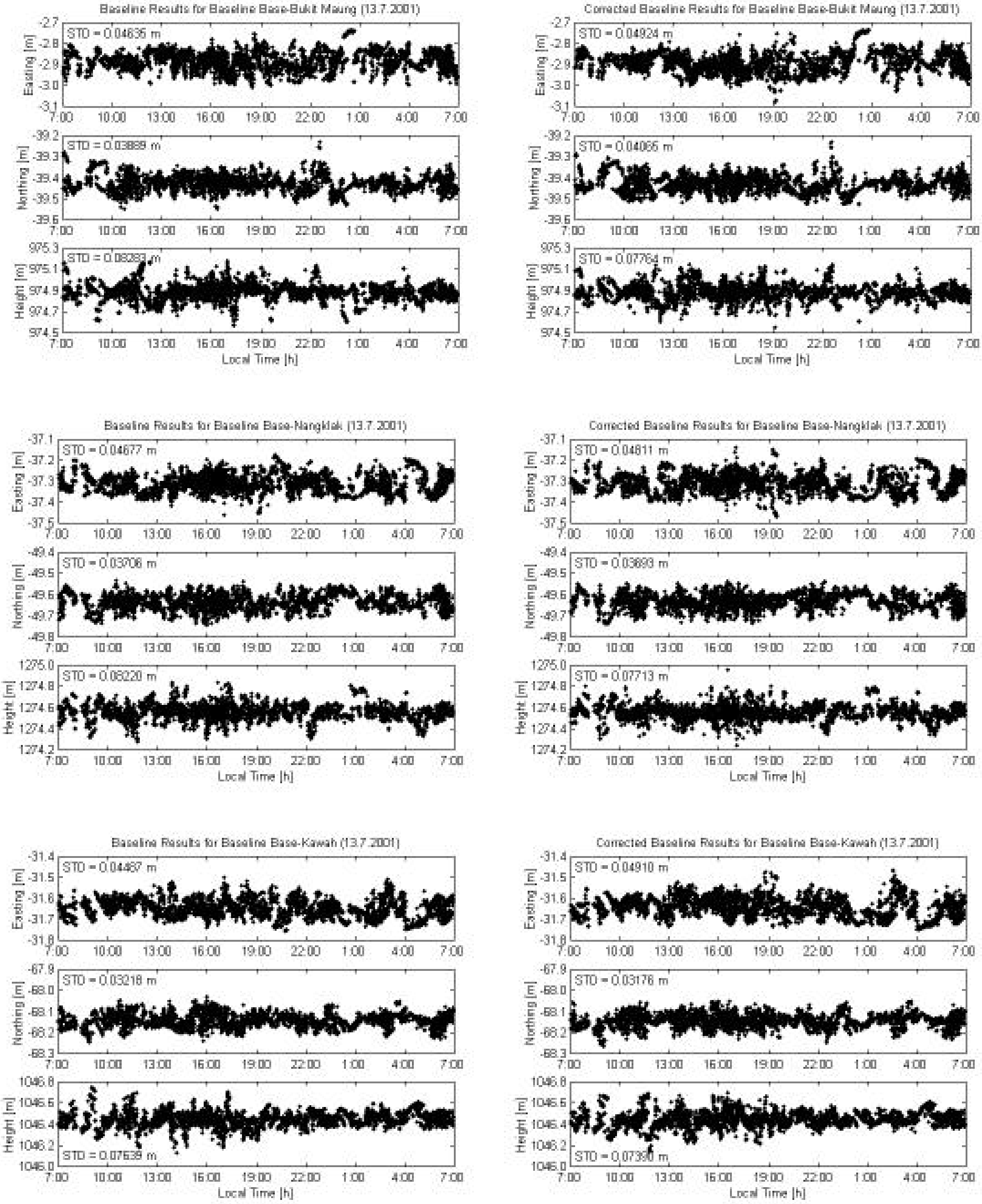

Fig. 5.52: Results for inner baselines not applying (left) and applying (right) corrections (DOY 194)

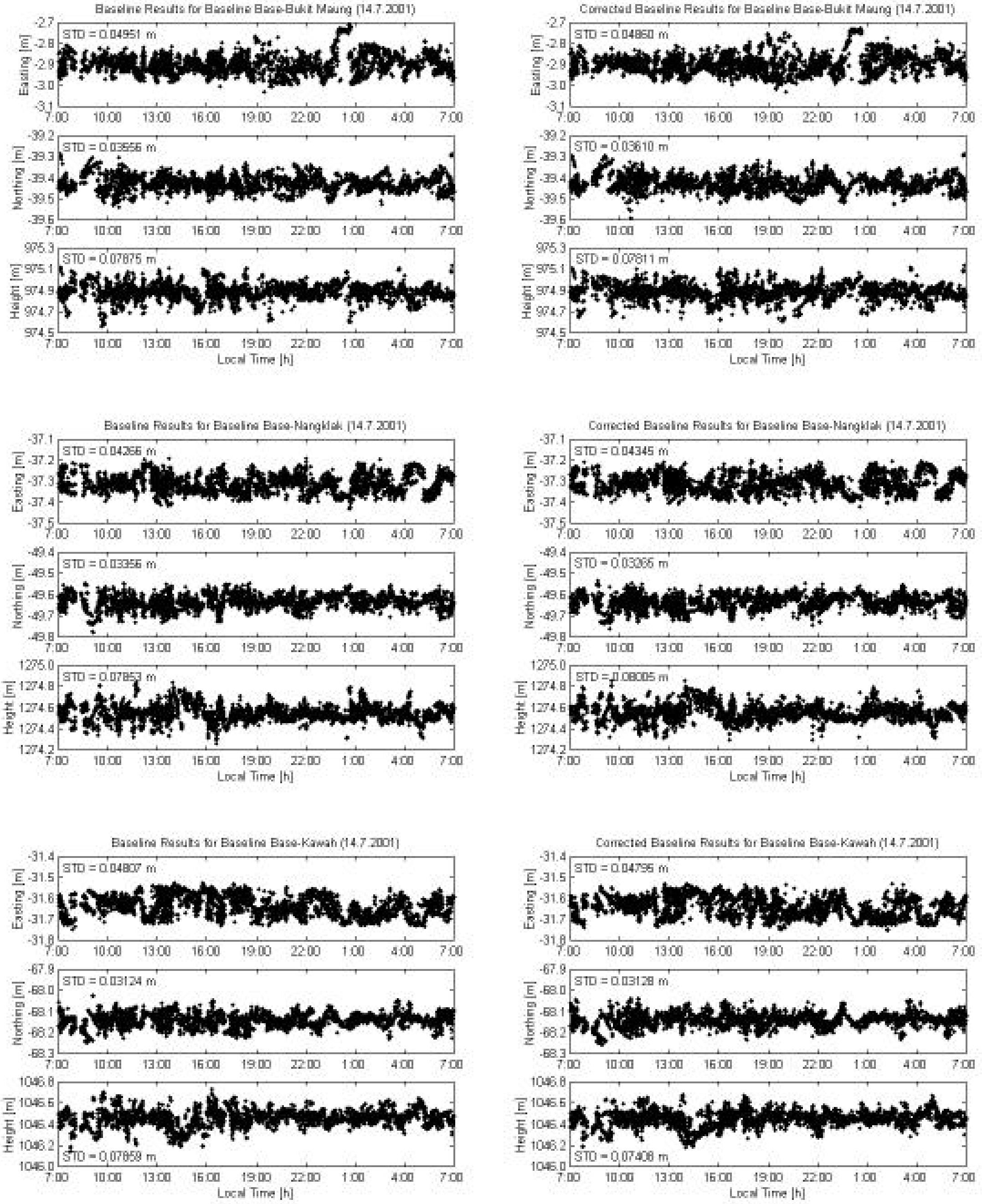

Fig. 5.53: Results for inner baselines not applying (left) and applying (right) corrections (DOY 195)

5.5.3 Summary

The results from Gunung Papandayan are disappointing, but are consistent with the trend of decreasing performance of the proposed mixed-mode data processing strategy the closer the GPS network is situated to the geomagnetic equator. Even for short baselines of the order of 8km in length, the fiducial network with baseline lengths of 31km and 53km cannot improve the single-frequency GPS results under solar maximum conditions, when applied on an epoch-by-epoch basis. The standard deviations of the baseline results could not be reduced below 3.1-5.0cm in the horizontal components and 7.0-8.0cm in the vertical component – values too large to detect ground deformation at the centimetre-accuracy level. The data were screened for multipath signals using the adaptive filter method developed by Ge et al. (2000a), but no multipath was detected.

5.6 Detection of Abnormal Deformation

A reliable deformation monitoring system has to ensure that ground displacements can be detected as soon as possible. Analysis of GPS coordinate time series using deformation monitoring software can detect variations from the usual deformation pattern that might, for example, indicate an imminent volcanic eruption. In such a case, the authorities can issue warnings to the population likely to be affected by the event and hazard mitigation procedures can be initiated. The software should be able to run automatically and to distinguish between the true deformational signal and any abnormal behaviour.

In order to demonstrate how the GPS baseline results, for example obtained in this chapter, can be used to detect deformation, selected coordinate time series have been processed with the UNSW-developed Real-Time System Monitor (RTSM) software (Ogaja, 2002a; 2002b). This software can analyse continuous data streams in real-time, and compare the results with specified criteria in order to detect deformation signals, as well as to characterise the behaviour of the monitoring system itself. Functions for online analysis check the consistency between multiple monitoring GPS receivers, detect abnormal observations as quickly as possible, and either provide clues on the possible cause (e.g. GPS sensor faults), or simply issue an alert if a pre-defined limit is exceeded.

RTSM utilises the cumulative sum (cusum) technique, an algorithm to detect small but persistent changes in the mean and/or the standard deviation of a time series (e.g. Basseville & Nikiforov, 1993; Hinkley, 1971; Mertikas, 2001; Page, 1954; 1957). The Easting, Northing and Height components of the rover receivers (e.g. located on the deforming body) are used as input parameters. Between-receiver residuals are then determined and used to generate cusums. The cusum essentially tests shifts in the mean of the residuals. RTSM is also capable of fast and online feedback, identifying when an abrupt shift occurs and estimating the magnitude of the shift. Hence the cusum algorithm is an ideal tool for controlling the performance of continuous GPS deformation monitoring networks.

Figure 5.54 shows the RTSM time series plots panel for the GPS coordinate time series obtained from the SCIGN network after applying ionospheric corrections on day 221 (see section 5.2.3). RTSM is currently designed to accommodate three GPS stations but the network considered here contains only two monitoring stations. Therefore, while the graphs for Rover 1 show the data referring to the baseline CSN1-OAT2, the graphs labelled Rover 2 and Rover 3 both show the data obtained for the baseline CSN1-CMP9. The limits for the Easting, Northing and Height components are calculated in real-time using the running mean, and are also shown. The windows in view correspond to one hour of data and can be changed to accommodate a different number of epochs if desired. The legend on the right shows the differences from the running mean for the current epoch in units of centimetres.

A graphic interpretation of the cumulative sum is given in the upper right corner of Figure 5.54. The graph shows the cusums for the three baselines connecting the three rovers to each other and their pre-set limit. In this case the cusums for the baselines are very similar and appear to be one single curve. If the curves belonging to the two baselines involving a certain rover exceed the cusum limit at the same time, a GPS sensor fault or abnormal deformation can be attributed to this receiver. The sensor flag, shown in the upper left corner of the panel, corresponding to this receiver will then be set to red. In addition, a warning message will appear on the screen whenever the pre-set limit is exceeded. Obviously, due to the nature of the data collected, no deformation has been detected in this case.

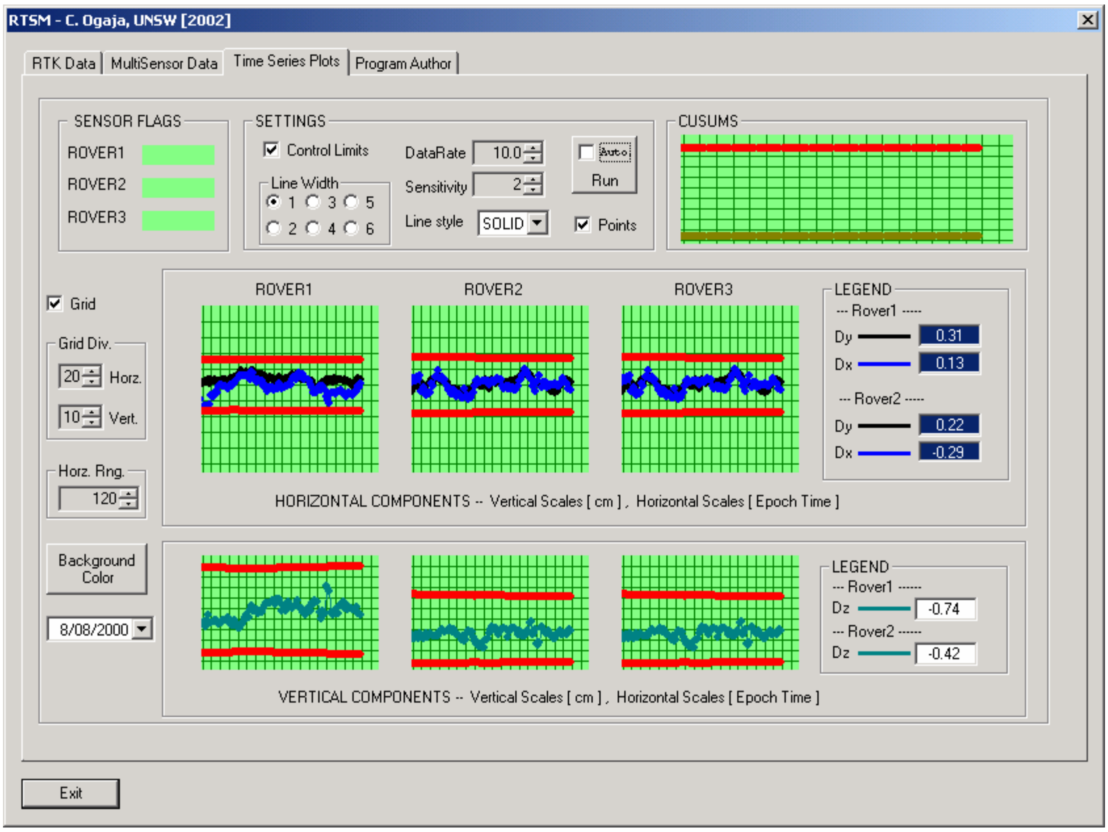

RTSM - C. Ogaja, UNSW [2002]

☑ Control Limits
Line Width ● 1 ○ 3 ○ 5 ○ 2 ○ 4 ○ 6
DataRate 10.0
Sensitivity 2
Line style SOLID
☐ Auto
☑ Points

☑ Grid
Grid Div. 20 Horz. 10 Vert.
Horz. Rng. 120
8/08/2000

LEGEND
--- Rover1 -----
Dy 0.31
Dx 0.13
--- Rover2 -----
Dy 0.22
Dx -0.29

HORIZONTAL COMPONENTS -- Vertical Scales [cm] , Horizontal Scales [Epoch Time]

LEGEND
--- Rover1 -----
Dz -0.74
--- Rover2 -----
Dz -0.42

VERTICAL COMPONENTS -- Vertical Scales [cm] , Horizontal Scales [Epoch Time]

Fig. 5.54: RTSM panel displaying time series plots for the SCIGN data (DOY 221)

In a similar manner, the coordinate time series obtained for the data collected on Gunung Papandayan after applying ionospheric corrections on day 192 is depicted in Figure 5.55. The graphs for Rover 1, 2 and 3 refer to the baselines between the base and the slave stations Bukit Maung, Nangklak and Kawah respectively (see section 5.5.2). The windows in view correspond to one hour of data. It is evident that the cusum chart shows more variation compared to the SCIGN data set and the curves belonging to the three baselines connecting the slaves are clearly visible. If the pre-set limits had not been increased to account for the large coordinate variations, several false alarms would have been issued. The large magnitude of the coordinate solution uncertainty precluded the detection of any small-scale deformation that might have occurred on the volcano.

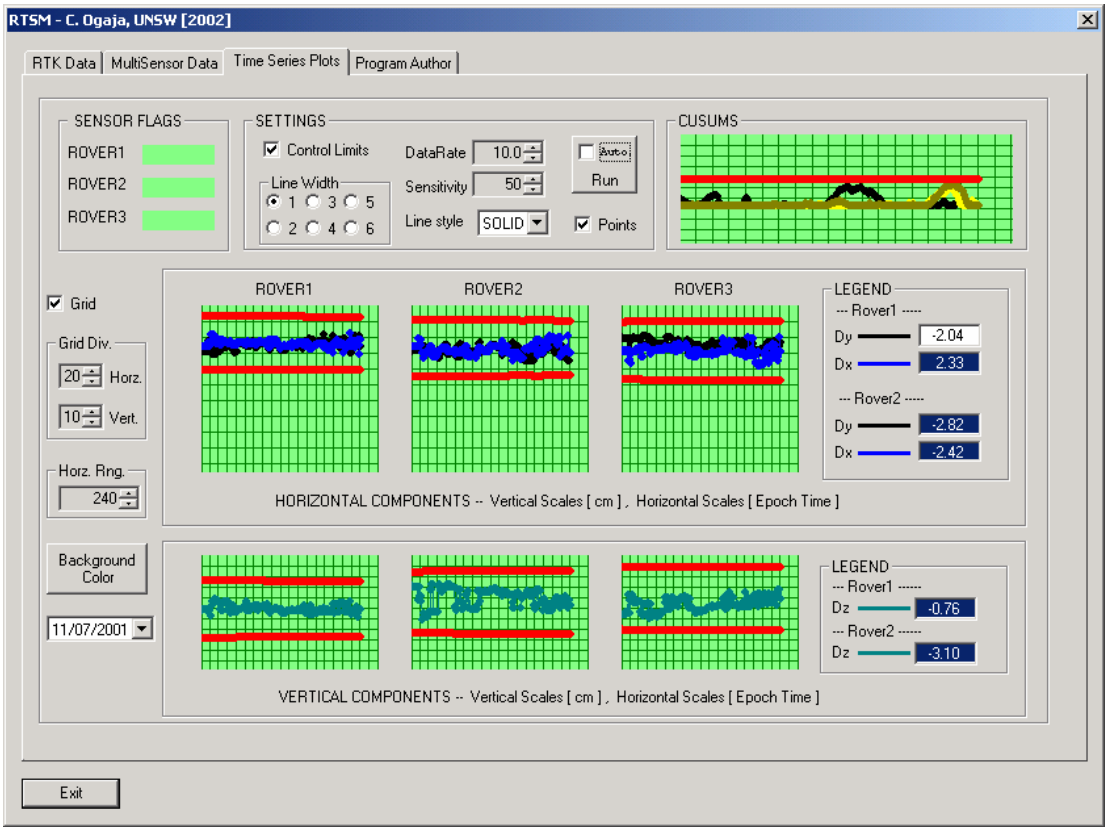

☑ Control Limits

Line Width: ● 1 ○ 3 ○ 5 ○ 2 ○ 4 ○ 6

DataRate 10.0

Sensitivity 50

Line style SOLID

☐ Auto

☑ Points

☑ Grid

Grid Div.: 20 Horz., 10 Vert.

Horz. Rng. 240

11/07/2001

--- Rover1 -----
Dy -2.04
Dx 2.33
--- Rover2 -----
Dy -2.82
Dx -2.42

--- Rover1 -----
Dz -0.76
--- Rover2 -----
Dz -3.10

Fig. 5.55: RTSM panel displaying time series plots for the Papandayan data (DOY 192)

5.7 Concluding Remarks

Data from several GPS networks have been used to show the feasibility of using the proposed data processing strategy for a mixed-mode GPS deformation monitoring network. The data were collected under solar maximum conditions at several different geographical locations.

The results have highlighted that the ionosphere has a significant impact on GPS baseline repeatability. It was shown that the correction generation algorithm can successfully model the ionospheric delay (at least to some extent).

In the mid-latitude region, single-frequency baseline repeatability has clearly been improved by applying the empirically-derived correction terms. The standard deviation of the GPS baseline results has been reduced by almost 50%. Standard deviations of less than 1cm horizontally and 1.5-3cm vertically have been achieved for single-epoch baseline solutions.

Unfortunately these promising results could not be repeated for GPS networks situated in the equatorial region. The empirical correction terms tend to be very large (of the order of several cycles), even for comparatively short (17-24 km) fiducial baselines, indicating severe ionospheric disturbances in close proximity to the geomagnetic equator during solar maximum periods. A data set collected in Hong Kong showed about 20% improvement in the standard deviation of all three components when corrections were applied. However, the standard deviation of the baseline components for single-epoch baseline solutions could not be reduced below the few-centimetre level. At Gunung Papandayan the single-frequency GPS baseline results could not be improved by applying the empirical corrections on an epoch-by-epoch basis, in spite of relatively short fiducial baselines of 31km and 53km in length.

It is evident that the performance of the proposed processing strategy degrades with decreasing geomagnetic latitude. This is most likely due to extreme short-term variations in the ionosphere that cannot be modelled adequately during periods of maximum sunspot activity using a sparse fiducial network. Nevertheless, it has been shown that a mixed-mode GPS network can be a cost-effective tool for deformation monitoring if it is not subject to extreme ionospheric conditions.

The UNSW-developed Real-Time System Monitor (RTSM) software has been used to demonstrate how the GPS baseline results obtained by such a GPS-based deformation monitoring system can be used to detect ground displacements in real-time. Obviously, due to the nature of the data sets used in this study, deformation was not experienced. The magnitude of the coordinate solution uncertainty at Gunung Papandayan precluded the detection of any small-scale deformation that might have occurred on the volcano. However, the continuous mixed-mode GPS network approach described in this thesis has been shown to have the potential to detect ground deformation as it occurs, thereby contributing to hazard mitigation.

Chapter 6

SUMMARY AND CONCLUSIONS

6.1 Summary

Ground deformation of a volcano is considered a sure indicator of impending eruptive activity. GPS is ideally suited for detecting and monitoring such deformation. A network of continuously operating single-frequency GPS receivers located on a volcano can be a cost-effective option to assist hazard mitigation. However, due to the use of only one frequency, the ionospheric delay cannot be accounted for, resulting in degraded baseline accuracies. This is of concern particularly in the equatorial region during times of maximum solar activity, as the ionosphere is highly disturbed and variable (spatially and temporally). In order to detect ground displacements at the centimetre-level under these conditions, the effect of the ionosphere on the GPS signal has to be properly considered, even for short baselines of less than 10km in length.

In this thesis, a *mixed-mode* GPS network approach has been suggested, in order to enhance the existing continuous low-cost GPS-based volcano deformation monitoring system on Gunung Papandayan in West Java, Indonesia. A sparse fiducial network of geodetic-quality dual-frequency GPS receivers surrounding the deformation zone is used to generate empirical 'correction terms' that attempt to model the regional ionospheric conditions in the area. These corrections are then applied to the single-frequency data during baseline processing to improve the accuracy of the results. This approach offers considerable cost savings for deformation monitoring applications, which require a dense spatial coverage of GPS stations, and where it is not feasible to establish permanent GPS networks using expensive dual-frequency instrumentation.

Due to the close proximity of active volcanoes in Indonesia, such a fiducial network could be established to encompass more than one active volcano, and therefore provide 'correction terms' for several single-frequency volcano networks. For example, the Papandayan, Guntur and Galunggung volcanoes in West Java could be combined in such a way. Furthermore, the ever-increasing number of permanent dual-frequency GPS networks established around the world could provide such a fiducial network at virtually no extra cost.

The fiducial ‘correction terms’ are generated using a modified version of the Bernese GPS processing software. Algorithms were developed to integrate these corrections into the UNSW-developed baseline processing software used to process the inner single-frequency network, and to generate epoch-by-epoch solutions in multi-baseline mode. Special considerations for GPS receivers located on the flanks of the volcano, such as the obstruction of the sky caused by the volcano itself, were taken into account.

Although this thesis mainly focuses on volcano deformation monitoring, the methodology can be utilised for a variety of monitoring applications, such as for tectonic fault lines, landslides, land subsidence, open-cut mines, dams, bridges, high-rise buildings, etc.

6.1.1 Deployment of a Mixed-Mode GPS Network at Gunung Papandayan

The single-frequency GPS volcano deformation monitoring system on Gunung Papandayan in Indonesia was augmented with a fiducial network of dual-frequency receivers in order to model the ionospheric conditions across the area. During the deployment several hardware and software problems had to be overcome, a major issue being the continuous supply of power. The fiducial baseline lengths had to be adjusted in order to account for the severe ionospheric conditions present in close proximity to the geomagnetic equator during a solar maximum period.

6.1.2 Optimising the Number of Double-Differenced Observations

Commercially available GPS processing software packages are only capable of baseline-by-baseline processing, neglecting the correlations that arise when a network of GPS receivers is operated simultaneously. If the data are processed in multi-baseline mode, however, all baselines are processed together, enabling more precise deformation monitoring. In the case of volcano deformation monitoring the ground displacements are expected to be complex. In periods of quiescence the deformation will be slow or even negligible, while increased volcanic activity will cause movements of increasing rate due to the expansion of the subterranean magma chamber. Hence, a near real-time, epoch-by-epoch solution is preferred in order to detect movements of the flanks of a volcano as quickly as possible.

For a number of GPS deformation monitoring applications the deforming body itself blocks out part of the sky, thereby significantly reducing the number of satellites being tracked by the monitoring receivers. If the usual base station / base satellite approach is used in the multi-baseline data processing, only the satellites common to all network sites are used in the solution. This can result in a relatively low number of double-differenced observables, and the loss of valuable information. Considering the special conditions around a volcanic edifice, a method to optimise the number of double-differenced GPS observations by generating a set of independent double-differenced combinations was implemented. This method considers satellites visible by a small number of network stations only, making use of vector space methods and the geometric characterisations of Boolean matrices, based on the algorithm by Saalfeld (1999).

A numerical example using data collected in a 6-station test network in Sydney demonstrated that the proposed data processing strategy significantly improved GPS baseline results. The number of double-differenced observables available to compute a solution was maximised by using all available information, therefore enhancing the quality of the results. The number of double-differenced observables at each epoch was increased by an average of about 10, and a solution could be obtained even if less than four common satellites were received simultaneously at all network stations. The standard deviation of the root mean square could be reduced by 34%, implying an improved quality of the baseline components.

6.1.3 Investigation of the Empirically-Derived Correction Terms

A fiducial network of dual-frequency GPS receivers surrounding the deformation zone is used to generate 'correction terms' in order to model the regional ionosphere in the area. Han & Rizos (1996d) and Han (1997) have proposed a linear combination model, which can account for orbit bias and ionospheric delay, as well as mitigate tropospheric delay, multipath and measurement noise across the GPS network. Using this model, empirical corrections can be derived, and then applied to the double-differenced carrier phase data formed between the stations of the inner single-frequency network. The double-differenced 'correction terms' are generated using a modified version of the Bernese GPS processing software.

In order to investigate the nature of the empirically-derived corrections a range of data sets were processed. The GPS data analysed were collected over a variety of baseline lengths, at different geographical locations, and in different periods of sunspot activity (and therefore varying ionospheric conditions).

A large increase in ionospheric activity between the years 1997 and 2000 (the most recent solar maximum) was evident. The differences in the diurnal behaviour of the ionosphere in mid-latitudes and the equatorial region were obvious, and the ionosphere was identified as the main systematic error present in the double-differenced residuals. It was found that the standard deviation of the double-differenced 'correction terms' increases linearly with increasing baseline length, the rate of increase being much more severe under solar maximum conditions.

In periods of heightened solar activity the magnitude of the corrections for longer baselines in the mid-latitude region reached a few cycles, indicating that longer baselines may not be able to generate reliable 'correction terms' under these conditions. This is particularly of concern for GPS networks located in close proximity to the geomagnetic equator, as the effects of the ionospheric delay at GPS sites in the equatorial region are much larger compared to those at mid-latitude sites. It is therefore necessary to carefully choose the baseline lengths of the fiducial network in order to produce corrections that reliably model the condition of the ionosphere present in the area. However, the magnitude of these biases is not entirely a function of distance, hence it is difficult to predict what should be the ideal dimensions of the reference station network. This has to be investigated on a case-by-case basis.

6.1.4 Mixed-Mode GPS Network Processing

Increased ionospheric activity during a solar maximum period, especially in the equatorial region, precludes high-quality GPS deformation monitoring results using single-frequency instrumentation only. The addition of a sparse, external network of geodetic-grade dual-frequency receivers to create a mixed-mode GPS network can, in principle, provide empirical corrections in order to model the regional ionosphere.

In order to test the feasibility of the proposed methodology of processing a mixed-mode GPS network for deformation monitoring applications, data from several GPS networks were processed. These networks were located at different geomagnetic latitudes and the data were collected under solar maximum conditions.

The significant effect of the ionosphere on GPS baseline repeatability was evident in the data analyses. It was shown that the correction generation algorithm can successfully model the ionospheric delay (at least to some extent) if the fiducial baseline lengths are not ‘too long’.

In the mid-latitude region, single-frequency baseline repeatability was clearly improved by applying the ‘correction terms’, which were generated by the fiducial dual-frequency network surrounding the deformation zone. The standard deviation of the GPS baseline results was reduced by almost 50% for the horizontal components and almost 40% for the height component. For single-epoch baseline solutions, standard deviations of less than 1cm horizontally and 1.5-3cm vertically were achieved.

Unfortunately these promising results could not be repeated for GPS networks situated in the equatorial region. Here, the empirical ‘correction terms’ were found to be very large (of the order of several cycles), even for comparatively short (17-24 km) fiducial baselines. This is indicative of severe ionospheric disturbances in close proximity to the geomagnetic equator during solar maximum periods. A data set collected in Hong Kong showed about 20% improvement in the standard deviation of all three components when corrections were applied. However, the standard deviation of the baseline components for single-epoch baseline solutions could not be reduced below the few-centimetre-level. Closer to the geomagnetic equator, at Gunung Papandayan, the single-frequency GPS baseline results could not be improved at all by applying the empirical corrections on an epoch-by-epoch basis, in spite of relatively short fiducial baselines of 31km and 53km in length.

It is concluded that the performance of the proposed processing strategy degrades with decreasing geomagnetic latitude. This is most likely due to extreme short-term variations in the ionosphere that cannot be modelled adequately during periods of maximum sunspot activity by just a few reference stations. Nevertheless, it has been shown that a mixed-mode GPS network can be a cost-effective tool for deformation monitoring if it is not subject to extreme ionospheric conditions, such as those experienced in close proximity to the geomagnetic equator during a solar maximum.

The optimal size of the fiducial network is dependent on whether the distance-dependent biases (mainly the ionospheric delay) can be realistically modelled with the proposed network configuration. This means that the size of the fiducial reference station network has to be carefully chosen, on a case-by-case basis, depending on the geographic location of the GPS receivers and the solar activity present in the area. While fiducial baseline lengths of several tens of kilometres are feasible for GPS deformation monitoring networks situated in the mid-latitude region, baselines have to be significantly shorter in the equatorial region in order to produce reliable ‘correction terms’ under solar maximum conditions. Obviously, the severity of the ionospheric effects on GPS baseline processing will be reduced with decreasing solar activity, which will reach its lowest level during the minimum period of the 11-year Solar Cycle.

The more complex ionospheric conditions present in close proximity to the geomagnetic equator require a more detailed model. For example, the interpolation of the ionospheric delay may have to be changed from the current linear process to a more complex interpolation procedure in order to account for intense small-scale disturbances. An increase in the number of reference stations might also appear to be of benefit in order to model the ionosphere in more detail. However, using data collected in the mid-latitude region, a study by Chen (2001) has found that baseline results did not improve by increasing the number of surrounding reference stations from three through to six. A reference station situated in the centre of the fiducial triangle could improve the modelling of the ionosphere. However, depending on the structure to be monitored, it may be very difficult to achieve this in practice because such a central reference station is required to be located outside the area of deformation. At Gunung Papandayan, an additional reference station could be installed next to the single-frequency base station at the foot of the volcano.

6.1.5 Real-Time Monitoring and Visualisation of Baseline Results

It was demonstrated how the baseline results obtained by the mixed-mode GPS-based deformation monitoring system can be used to detect ground displacements in real-time. The UNSW-developed Real-Time System Monitor (RTSM) software was utilised for this purpose. RTSM checks the quality of the GPS data and graphically presents the coordinate time series results, triggering an alarm whenever the detected deformation exceeds a pre-set limit.

As expected, significant deformation was not experienced in the data sets used in this study. The magnitude of the coordinate solution uncertainty at Gunung Papandayan precluded the detection of any small-scale deformation that might have occurred on the volcano. However, in appropriate circumstances, the continuous mixed-mode GPS network approach described in this thesis has the potential to detect ground deformation as it occurs, thereby contributing to hazard mitigation.

6.2 Suggestions and Recommendations for Future Research

The mixed-mode GPS network approach for deformation monitoring applications investigated in this thesis comprises an inner single-frequency network surrounded by an outer dual-frequency network, which is used to map the ionospheric conditions in the region and to generate corrections to account for these effects.

In this study the ionospheric ‘correction terms’ were generated in post-processing mode and applied to the single-frequency network in order to investigate the performance of the proposed data processing methodology. In the case of a long-term deployment of such a GPS-based deformation monitoring system, however, a near real-time solution is desired. Automatic baseline processing of the single-frequency network, with the addition of network-generated corrections, can be implemented. The GPS baseline results can then be automatically analysed in order to detect deformational signals and to present the results in an easy-to-understand manner, e.g. using the RTSM software. It is important to ensure that non-geodesists can understand and use this information for assessment of the hazards presented by a volcano (or any other deforming body that is being monitored) with minimum delay.

In order to move towards a ‘true’ real-time deformation monitoring system, the radio telemetry system used to transfer the GPS data from the slave stations to the base station can be improved. If the radios are set to an asynchronous mode and a unique address is assigned to each radio, data from all slave stations can be sent continuously and sorted by the base. This allows a larger number of slave stations in the network, because the radio polling methodology currently in use restricts the number of slaves on the deforming body. The ionospheric corrections should be transferred to the base facility in an RTK-like fashion to enable data processing without delay. Eventually this can result in an intelligent (volcano) deformation monitoring system that is able to switch between the processing of, say, hourly static sessions in quiescent periods and processing in RTK-mode if increased volcanic activity is observed.

The GPS/PC modules used for the single-frequency slave stations of the mixed-mode system on Gunung Papandayan use the DOS operating system. As DOS is not designed for real-time applications, the software must be carefully written to avoid problems with memory allocation. In order to remedy this disadvantage, subsequent versions of the GPS slave stations will utilise micro-controllers integrated with GPS OEM boards. This is expected to enhance reliability and to result in a more robust system.

A combination of GPS data with observations from GLONASS and Galileo satellites in the future can improve the volume of observations and the satellite geometry. Subsequently the reliability of the baseline results can be enhanced, especially for applications where the deforming body itself blocks out part of the sky. Obviously, the challenge lies in combining observations from different satellite systems and their respective ‘correction terms’ in order to generate one baseline solution. Pseudolites can also be used in this regard. However, for some applications it may be difficult to install them at stable locations above the monitoring receivers, as the pseudolite position needs to be free from displacements. Moreover, the distance of the pseudolite from the monitoring receivers has to be selected carefully in order to avoid in-band interference with the GPS signals.

REFERENCES

Abidin, H.Z. (1993): *Computational and Geometrical Aspects of On-The-Fly Ambiguity Resolution*, PhD Dissertation, Dept. of Surveying Engineering Tech. Rept. No. 164, University of New Brunswick, Fredericton, New Brunswick, Canada, 314pp.

Abidin, H.Z. (1998): *Monitoring the Volcano Deformation Using Repeated GPS Surveys: Experiences and Plans*, Proc. Int. Workshop on Advances in GPS Deformation Monitoring, Perth, Australia, 24-25 September, paper 18, 27pp.

Abidin, H.Z. and W.S. Tjetjep (1996): *GPS-Based Volcano Deformation Monitoring in Indonesia*, GIS Asia Pacific, 2(5), 30-33.

Abidin, H.Z., I. Meilano, O.K. Suganda, M.A. Kusuma, D. Muhardi, O. Yolanda, B. Setyadji, R. Sukhyar, J. Kahar and T. Tanaka (1998): *Monitoring the Deformation of Guntur Volcano Using Repeated GPS Survey Method*, Proc. XXI Int. Congress of FIG, Commission 5: Positioning and Measurements, Brighton, UK, 19-25 July, 153-169.

Abidin, H.Z., D. Darmawan, O.K. Suganda, M.A. Kusuma, I. Meilano, F. Anthony, M. Gamal and A.D. Wirakusumah (2000): *Studying the Deformation of Papandayan Volcano, Indonesia, Using Repeated GPS Survey Method*, Poster pres. at the International Association of Volcanology and Chemistry of the Earth's Interior (IAVCEI) General Assembly, Bali, Indonesia, 18-22 July.

AIUB (2002): Astronomic Institute of the University of Berne website: http://www.cx.unibe.ch/aiub/ionosphere.html.

Amelung, F., S. Jonsson, H. Zebker and P. Segall (2000): *Widespread Uplift and 'Trapdoor' Faulting on Galapagos Volcanoes Observed with Radar Interferometry*, Nature, 407, 993-996.

Amore, M., A. Bonaccorso, F. Ferrari and M. Mattia (2002): *Eolo: Software for the Automatic On-line Treatment and Analysis of GPS Data for Environmental Monitoring,* Computers & Geosciences, 28, 271-280.

Anderson, D. and T. Fuller-Rowell (1999): *Space Environment Topics: The Ionosphere*, SE-14, Space Environment Center, Boulder, Colorado, http://www.sec.noaa.gov/ Education/.

Ashkenazi, V., A.H. Dodson, T. Moore and G.W. Roberts (1997): *Monitoring the Movements of Bridges by GPS,* Proc. ION GPS-92, Kansas City, Missouri, 16-19 September, 1165-1172.

Basseville, M. and V. Nikiforov (1993): *Detection of Abrupt Changes – Theory and Applications*, Prentice Hall, New Jersey, 441pp.

Behr, J.A., K.W. Hudnut and N.E. King (1998): *Monitoring Structural Deformation at Pacoima Dam, California Using Continuous GPS*, Proc. ION GPS-98, Nashville, Tennessee, 15-18 September, 59-68.

Berntsen (2002): Berntsen International Inc. website: http://www.berntsen.com/.

Blick, G.H., P.M. Otway and B.J. Scott (1989*): Deformation Monitoring of Mt. Erebus, Antarctica, 1980-1985,* in: Latter, J.H. (Ed.): *Volcanic Hazards: Assessment and Monitoring*, Springer-Verlag, Berlin-New York, 554-560.

Blong, R.J. (1984): *Volcanic Hazards: A Sourcebook on the Effects of Eruptions*, Academic Press, Australia, 424pp.

Blong, R. (2000): *Volcanic Hazards and Risk Management,* in: Sigurdsson, H. (Ed.): *Encyclopedia of Volcanoes,* Academic Press, 1215-1227.

Bock, Y., D.C. Agnew, P. Fang, J.F. Genrich, B.H. Hager, T.A. Herring, K.W. Hudnut, R.W. King, S. Larsen, J.-B. Minster, K. Stark, S. Wdowinski and F.K. Wyatt (1993):

Detection of Crustal Deformation from the Landers Earthquake Sequence Using Continuous Geodetic Measurements, Nature, 361, 337-340.

Bock, Y., S. Wdowinski, P. Fang, J. Zhang, S. Williams, H. Johnson, J. Behr, J. Genrich, J. Dean, M. van Domselaar, D. Agnew, F. Wyatt, K. Stark, B. Oral, K. Hudnut, R. King, T. Herring, S. Dinardo, W. Young, D. Jackson and W. Gurtner (1997): *Southern California Permanent GPS Array: Continuous Measurements of Regional Crustal Deformation Between the 1992 Landers and 1994 Northridge Earthquakes*, Journal of Geophysical Research, 102(B8), 18013-18033.

Bonasia, V. and F. Pingue (1981): *Ground Deformations on Mt. Vesuvius from 1977 to 1981*, Bulletin of Volcanology, 44, 513-520.

Borchers, S. and R. Heer (2002): *Some Results of Deformation Measurements with GOCA (GPS-Based Online Control and Alarm System) at Lock Uelzen I*, Proc. 2nd Symp. on Geodesy for Geotechnical and Structural Engineering, Berlin, Germany, 21-24 May, 38-50.

Briole, P., D. Massonnet and C. Delacourt (1997): *Post-Eruptive Deformation Associated with the 1986-87 and 1989 Lava Flows of Etna Detected by Radar Interferometry*, Geophysical Research Letters, 24(1), 37-40.

Brunner, F.K., H. Hartinger and B. Richter (2000): *Continuous Monitoring of Landslides Using GPS: A Progress Report*, in: Bauer, S.J. and F. Weber (Eds.): *Proceedings Geophysical Aspects of Mass Movement*, Austrian Academy of Sciences, Vienna, 75-88.

Camargo, P.O., J.F.G. Monico and L.D.D. Ferreira (2000): *Application of Ionospheric Corrections in the Equatorial Region for L1 GPS Users*, Earth Planets Space, 52(11), 1083-1089.

Celebi, M. and A. Sanli (2002): *GPS for Recording Dynamic Displacements of Long-Period Structures – Engineering Implications*, Proc. 2nd Symp. on Geodesy for Geotechnical and Structural Engineering, Berlin, Germany, 21-24 May, 51-60.

Chen, D. (1993): *Fast Ambiguity Search Filtering (FASF): A Novel Concept for GPS Ambiguity Resolution*, Proc. ION GPS-93, Salt Lake City, Utah, 22-24 September, 781-787.

Chen, H.Y. (2001): *A Study on Real-Time Medium-Range Carrier Phase-Based GPS Multiple Reference Stations*, PhD Dissertation, UNISURV S-64, School of Geomatic Engineering, The University of New South Wales, Sydney, Australia, 185pp.

Chen, H.Y., C. Rizos and S. Han (1999): *Rapid Static, Medium-Range GPS Positioning Techniques for Geodynamic Applications*, Proc. 4th Int. Symp. on Satellite Navigation Technology & Applications (SatNav), Brisbane, Australia, 20-23 July, paper 49, 12pp.

Chen, H.Y., C. Rizos and S. Han (2001a): *From Simulation to Implementation: Low-Cost Densification of Permanent GPS Networks in Support of Geodetic Applications*, Journal of Geodesy, 75(9/10), 515-526.

Chen, W., C. Hu, Y. Chen, X. Ding and S.C.W. Kwok (2001b): *Rapid Static and Kinematic Positioning with Hong Kong GPS Active Network*, Proc. ION GPS-2001, Salt Lake City, Utah, 11-14 September, 346-352.

Chen, X., S. Han, C. Rizos and P.C. Goh (2000): *Improving Real Time Positioning Efficiency Using the Singapore Integrated Multiple Reference Station Network (SIMRSN)*, Proc. ION GPS-2000, Salt Lake City, Utah, 19-22 September, 9-16.

Comp, C.J. and P. Axelrad (1996): *An Adaptive SNR-Based Carrier Phase Multipath Mitigation Technique*, Proc. ION GPS-96, Kansas City, Missouri, 17-20 September, 683-697.

Condor (2000): Condor Earth Technologies Inc. website: http://www.3d-gps.com/.

Craymer, M.R. and N. Beck (1992): *Session Versus Single-Baseline GPS Processing*, Proc. ION GPS-92, Albuquerque, New Mexico, 16-18 September, 995-1004.

Decker, R. and B. Decker (1997): *Volcanoes*, 3rd edition, W.H. Freeman and Company, New York, 321pp.

Ding, X.L., G.X. Liu, Z.W. Li, Z.L. Li, Y.Q. Chen (2002): *Ground Subsidence Monitoring in Hong Kong with Satellite SAR Interferometry*, Proc. Advanced Workshop on InSAR for Measuring Topography and Deformation of the Earth Surface, Hong Kong, P.R. China, 16-17 December, 25-37.

Dixon, T.H., A. Mao, M. Bursik, M. Heflin, J. Langbein, R. Stein and F. Webb (1997): *Continuous Monitoring of Surface Deformation at Long Valley Caldera, California, with GPS*, Journal of Geophysical Research, 102(B6), 12017-12034.

Dodson, A., P. Shordlow, L. Hubbard, G. Elgered and P. Jarlemark (1996): *Wet Tropospheric Effects on Precise Relative GPS Height Determination*, Journal of Geodesy, 70, 188-202.

Dodson, A., T. Moore, M.H.O. Aquino and S. Waugh (2001): *Ionospheric Scintillation Monitoring in Northern Europe*, Proc. ION GPS-2001, Salt Lake City, Utah, 11-14 September, 2490-2498.

Doherty, P.H., S.H. Delay, C.E. Valladares and J.A. Klobuchar (2000): *Ionospheric Scintillation Effects in the Equatorial and Auroral Regions*, Proc. ION GPS-2000, Salt Lake City, Utah, 19-22 September, 662-671.

Duffy, M.A. and C. Whitaker (1999): *Deformation Monitoring Scheme Using Static GPS and Continuous Operating Reference Stations (CORS) in California*, Proc. ION GPS-99, Nashville, Tennessee, 14-17 September, 63-70.

Dvorak, J. and D. Dzurisin (1997): *Volcano Geodesy: The Search for Magma Reservoirs and the Formation of Eruptive Events*, Rev. Geophys., 35(3), 343-384.

Essex, E.A., R. Birsa, N. Shilo, R.M. Thomas, M.A. Cervera and A.M. Breed (2001): *Global Positioning System Signals under Solar Maximun Conditions*, Proc. 5th Int.

Symp. on Satellite Navigation Technology & Applications (SatNav), Canberra, Australia, 24-27 July, paper 14, 10pp.

Euler, H.-J. and H. Landau (1992): *Fast GPS Ambiguity Resolution On-The-Fly for Real-Time Applications*, Proc. 6th Int. Geodetic Symp. on Satellite Positioning, Columbus, Ohio, 17-20 March, 650-659.

Ewert, J.W. and D.A. Swanson (Eds.) (1992): *United States Geological Survey Bulletin 1966, Monitoring Volcanoes: Techniques and Strategies Used by Staff of the Cascades Volcano Observatory 1980-90*, Washington DC, United States Government Printing Office.

Fedrizzi, M., R.B. Langley, A. Komjathy, M.C. Santos, E.R. de Paula and I.J. Kantor (2001): *The Low-Latitude Ionosphere: Monitoring its Behaviour with GPS*, Proc. ION GPS-2001, Salt Lake City, Utah, 11-14 September, 2468-2475.

Foulger, G.R., R. Bilham, J. Morgan and P. Einarsson (1987): *The Iceland Geodetic Field Campaign 1986*, Eos, 68, 1801-1818.

Foxworthy, B.L. and M. Hill (1982): *Volcanic Eruptions of 1980 at Mount St. Helens: The First 100 Days*, U.S. Geological Survey Professional Paper 1249, 125pp.

Frei, E. and G. Beutler (1990): *Rapid Static Positioning Based on the Fast Ambiguity Resolution Approach FARA: Theory and First Results*, Manuscripta Geodaetica, 15, 325-356.

Fu, W., S. Han, C. Rizos, M. Knight and A. Finn (1999): *Real-Time Ionospheric Scintillation Monitoring*, Proc. ION GPS-99, Nashville, Tennessee, 14-17 September, 1461-1471.

Fujiwara, S., T. Nishimura, M. Murakami, H. Nakagawa, M. Tobita and P.A. Rosen (2000): *2.5-D Surface Deformation of M6.1 Earthquake near Mt. Iwate Detected by SAR Interferometry*, Geophysical Research Letters, 27, 2049-2052.

Ge, L., S. Han and C. Rizos (2000a): *Multipath Mitigation of Continuous GPS Measurements Using an Adaptive Filter*, GPS Solutions, 4(2), 19-30.

Ge, L., S. Han and C. Rizos (2000b): *The Double Interpolation and Double Prediction (DIDP) Approach for InSAR and GPS Integration*, Int. Archives of Photogrammetry & Remote Sensing (IAPRS), Vol. XXXIII, Amsterdam, Netherlands, 205-212.

Ge, L., V. Janssen, Y. Wang and C. Rizos (2003): *A Double-Differencing Algorithm for GPS-Derived Topographic Delay Corrections to Differential Radar Interferometry*, submitted to Journal of Geodesy.

Ge, L., C. Rizos, M. Omura and S. Kobayashi (2001): *Integrated Space Geodetic Techniques for Monitoring Ground Subsidence due to Underground Mining*, Proc. 5th Int. Symp. on Satellite Navigation Technology & Applications (SatNav), Canberra, Australia, 24-27 July, paper 19, 12pp.

GEODEV (2002): GEODEV Earth Technologies website: http://www.geodev.ch.

Georgiadou, Y. and A. Kleusberg (1988): *On Carrier Signal Multipath Effects in Relative GPS Positioning*, Manuscripta Geodaetica, 13, 172-179.

Geoscience Australia (2002): Geoscience Australia, National Mapping Division website: http://www.auslig.gov.au/geodesy/sgc/wwwgps/.

Goodman, J.M. and J. Aarons (1990): *Ionospheric Effects on Modern Electronic Systems*, Proc. IEEE, Vol. 78, 512-528.

Gourgaud, A., G. Camus, M.-C. Gerbe, J.-M. Morel, A. Sudradjat and P.M. Vincent (1989): *The 1982-83 Eruption of Galunggung (Indonesia): A Case Study of Volcanic Hazards with Particular Relevance to Air Navigation*, in: Latter, J.H. (Ed.): *Volcanic Hazards: Assessment and Monitoring*, Springer-Verlag, Berlin-New York, 151-162.

GSI (2002): Geographical Survey Institute website: http://www.gsi.go.jp/ENGLISH/ABOUT/about.html.

GVN (1991): *Unzen (Kyushu)*, Bulletin, Global Volcanism Network (GVN), 16, 8-11.

Han, S. (1995): *Ambiguity Recovery for GPS Long Range Kinematic Positioning*, Proc. ION GPS-95, Palm Springs, California, 12-15 September, 349-360.

Han, S. (1997): *Carrier Phase-Based Long-Range GPS Kinematic Positioning*, PhD Dissertation, UNISURV S-49, School of Geomatic Engineering, The University of New South Wales, Sydney, Australia, 185pp.

Han, S. and C. Rizos (1995): *Selection and Scaling of Simultaneous Baselines for GPS Network Adjustment, or Correct Procedures for Processing Trivial Baselines*, Geomatics Research Australasia, 63, 51-66.

Han, S. and C. Rizos (1996a): *A New Operation Mode and Processing Procedure for Centimetre Accuracy Rapid Static Positioning and Kinematic Positioning Using Single Frequency GPS Receivers*, Proc. 37th Australian Surveyor Congress, Perth, Australia, 13-19 April, 203-212.

Han, S. and C. Rizos (1996b): *Integrated Method for Instantaneous Ambiguity Resolution Using New Generation GPS Receivers*, Proc. IEEE Position Location & Navigation Symp. (PLANS'96), Atlanta, Georgia, 22-26 April, 254-161.

Han, S. and C. Rizos (1996c): *Comparison of GPS Ambiguity Resolution Techniques*, Proc. Int. Symp. on Global Positioning Systems, Digital Photogrammetry Systems, Remote Sensing and Geographical Systems (Geo-Informatics '96), Wuhan, P.R. China, 16-19 October, 136-146.

Han, S. and C. Rizos (1996d): *GPS Network Design and Error Mitigation for Real-Time Continuous Array Monitoring Systems*, Proc. ION GPS-96, Kansas City, Missouri, 17-20 September, 1827-1836.

Han, S. and C. Rizos (1997): *Multipath Effects on GPS in Mine Environments*, Proc. Xth International Congress on the International Society for Mine Surveying, Fremantle, Australia, 2-6 November, 447-457.

Hardwick, C.D. and J. Liu (1995): *Characterization of Phase and Multipath Errors for an Aircraft GPS Antenna*, Proc. ION GPS-95, Palm Springs, California, 12-15 September, 491-498.

Hartinger, H. and F.K. Brunner (2000): *Development of a Monitoring System of Landslide Motions Using GPS*, Proc. 9th FIG Int. Symp. on Deformation Measurements, Olsztyn, Poland, September 1999, 29-38.

Harvey, B.R. (1994): *Practical Least Squares and Statistics for Surveyors*, Monograph 13, School of Geomatic Engineering, The University of New South Wales, Sydney, Australia, 319pp.

Hatch, R.R. (1990): *Instantaneous Ambiguity Resolution*, in: Schwarz, K.P. and G. Lachapelle (Eds.): *Kinematic Systems in Geodesy, Surveying and Remote Sensing*, IAG Symp. 107, Springer-Verlag, 299-308.

Hinkley, D.V. (1971): *Inference About the Change Point from Cumulative Sum-Tests*, Biometrika, 58, 509-523.

Hofmann-Wellenhof, B., H. Lichtenegger and J. Collins (2001): *GPS: Theory and Practice*, 5th edition, Springer-Verlag, Vienna-New York, 382pp.

Huang, Y.-N. and K. Cheng (1991): *Ionospheric Disturbances at the Equatorial Anomaly Crest Region During the March 1989 Magnatic Storms*, Journal of Geophysical Research, 96(A8), 13953-13965.

Hudnut, K.W., Y. Bock, J.E. Galetzka, F.H. Webb and W.H. Young (2001): *The Southern California Integrated GPS Network (SCIGN)*, Proc. 10th FIG Int. Symp. on Deformation Measurements, Orange, California, 19-22 March, 129-148.

IGS (2002a): International GPS Service website: http://igscb.jpl.nasa.gov/components/prods.html.

IGS (2002b): International GPS Service website: http://igscb.jpl.nasa.gov/.

IPS (2002): IPS Radio & Space Services website: http://www.ips.gov.au/.

Janssen, V. (2001): *Optimizing the Number of Double-Differenced Observations for GPS Networks in Support of Deformation Monitoring Applications*, GPS Solutions, 4(3), 41-46.

Janssen, V., C. Roberts, C. Rizos and H.Z. Abidin (2001): *Experiences with a Mixed-Mode GPS-Based Volcano Monitoring System at Mt. Papandayan, Indonesia*, Geomatics Research Australasia, 74, 43-58.

Kälber, S., R. Jäger and R. Schwäble (2000): *A GPS-Based Online Control and Alarm System*, GPS Solutions, 3(3), 18-25.

Kato, T., Y. Terada, M. Kinoshita, H. Kakimoto, H. Issiki, M. Matsuishi, A. Yokoyama and T. Tanno (2000): *Real-Time Observation of Tsunami by RTK-GPS*, Earth Planets Space, 52(10), 841-845.

Kimberly, P., L. Siebert, J.F. Luhr and T. Simkin (1998): *Volcanoes of Indonesia*, V.1.0 (CD-ROM), Smithsonian Institution, Global Volcanism Program, Digital Information Series, GVP-1.

King, R.W. and Y. Bock (1995): *Documentation of the GAMIT GPS Analysis Software Version 9.3*, Massachusetts Institute of Technology, Cambridge.

Kleusberg, A. and P.J.G. Teunissen (Eds.) (1996): *GPS for Geodesy*, Springer-Verlag, Berlin-Heidelberg-New York, 407pp.

Klobuchar, J.A. (1987): *Ionospheric Time-Delay Algorithm for Single-Frequency GPS Users*, IEEE Transactions on Aerospace and Electronic Systems, AES-23(3), 325-331.

Klobuchar, J.A. (1996): *Ionospheric Effects on GPS*, in: Parkinson, B.W. and J.J. Spilker (Eds.): *Global Positioning System: Theory and Applications Volume I*, Progress in Astronautics and Aeronautics, 163, American Institute of Aeronautics and Astronautics, Washington, 485-515.

Knecht, A. and L. Manetti (2001): *Using GPS in Structural Health Monitoring*, Proc. SPIE's 8th Annual Int. Symp. on Smart Structures and Materials, Newport Beach, California, 4-8 March, 8pp.

Knight, M., M. Cervera and A. Finn (1999): *A Comparison of Predicted and Measured GPS Performance in an Ionospheric Scintillation Environment*, Proc. ION GPS-99, Nashville, Tennessee, 14-17 September, 1437-1450.

Knight, M., (2000): *Ionospheric Scintillation Effects on Global Positioning System Receivers*, PhD Dissertation, Department of Electrical and Electronic Engineering, The University of Adelaide, Australia, 304pp.

Koch, K.R. (1990): *Bayesian Inference with Geodetic Applications*, Lecture Notes in Earth Sciences Vol. 31, Springer-Verlag, Berlin-Heidelberg-New York, 198pp.

Koch, K.R. (1999): *Parameter Estimation and Hypothesis Testing in Linear Models*, 2nd edition, Springer-Verlag, Berlin-Heidelberg-New York, 333pp.

Kondo, H. and M.E. Cannon (1995): *Real-Time Landslide Detection System Using Precise Carrier Phase GPS*, Proc. ION GPS-95, Palm Springs, California, 12-15 September, 1877-1884.

Kunches, J.M. and J.A. Klobuchar (2001): *Eye on the Ionosphere: GPS after SA*, GPS Solutions, 4(3), 52-54.

Kusumadinata, K. (1979): *Data Dasar Gunungapi Indonesia (Catalogue of References on Indonesian Volcanoes with Eruptions in Historical Time)*, Volcanological Survey of Indonesia, 166-177.

Langley, R.B. (1993): *The GPS Observables*, GPS World, 4(4), 52-59.

Larson, K.M., P. Cervelli, M. Lisowski, A. Miklius, P. Segall and S. Owen (2001): *Volcano Monitoring Using the Global Positioning System: Filtering Strategies*, Journal of Geophysical Research, 106(B9), 19453-19464.

Leick, A. (1995): *GPS Satellite Surveying*, 2nd edition, Wiley, New York, 560pp.

Lovse, J.W., W.F. Teskey, G. Lachapelle and M.E. Cannon (1995): *Dynamic Deformation Monitoring of Tall Structures Using GPS Technology*, Journal of Surveying Engineering, 121(1), 35-40.

Lowry, A. and R. MacLeod (1997): *PMoS – A Real Time Precise DGPS Continuous Deformation Monitoring System*, Proc. ION GPS-97, Kansas City, Missouri, 16-19 September, 923-927.

Lu, Z., R. Fatland, M. Wyss, S. Li, J. Eichelberger, K. Dean and J. Freymueller (1997): *Deformation of New Trident Volcano Measured by ERS-1 SAR Interferometry, Katmai National Park, Alaska*, Geophysical Research Letters, 24(6), 695-698.

Mader, G.L. and R.J. MacKay (1996): *Calibration of GPS Antennas*, Proc. IGS Analysis Centers Workshop, Silver Springs, Maryland, 19-21 March, 81-105.

Marshall, G.A., J. Langbein, R.S. Stein, M. Lisowski and J. Svarc (1997): *Inflation of Long Valley Caldera, California, Basin and Range Strain, and Possible Mono Craters Dike Opening from 1990-94 GPS Surveys*, Geophysical Research Letters, 24(9), 1003-1006.

Mattioli, G.S., T.H. Dixon, F. Farina, E.S. Howell, P.E. Jansma and A.L. Smith (1998): *GPS Measurement of Surface Deformation Around Soufriere Hills Volcano, Montserrat, from October 1995 to July 1996*, Geophysical Research Letters, 25(18), 3417-3420.

McGuire, W.J. (1995): *Monitoring Active Volcanoes – An Introduction*, in: McGuire, W.J., C. Kilburn and J. Murray (Eds.): *Monitoring Active Volcanoes*, UCL Press, London, 1-31.

Meertens, C. (1999): *Development of a L1-Phase GPS Volcano Monitoring System – Progress Report for the Period 12 August 1998 – 15 May 1999*, http://www.unavco.ucar.edu/~chuckm/l1prog99.pdf.

Mendes, V.B. (1999): *Modeling the Neutral-Atmosphere Propagation Delay in Radiometric Space Techniques*, PhD Dissertation, Dept. of Geodesy & Geomatics Eng. Tech. Rept. No. 199, University of New Brunswick, Fredericton, Canada, 353pp.

Mertikas, S.P. (2001): *Automatic and Online Detection of Small But Persistent Shifts in GPS Station Coordinates by Statistical Process Control*, GPS Solutions, 5(1), 39-50.

Miura, S., S. Ueki, T. Sato, K. Tachibana and H. Hamaguchi (2000): *Crustal Deformation Associated with the 1998 Seismo-Volcanic Crisis of Iwate Volcano, Northeastern Japan, as Observed by a Dense GPS Network*, Earth Planets Space, 52(11), 1003-1008.

Miyazaki, S., T. Saito, M. Sasaki, Y. Hatanaka and Y. Iimura (1997): *Expantion of GSI's Nationwide GPS Array*, Bulletin of the Geographical Survey Institute, 43, 23-34.

Miyazaki, S., Y. Hatanaka, T. Sagiya and T. Tada (1998): *The Nationwide GPS Array as an Earth Observation System*, Bulletin of the Geographical Survey Institute, 44, 11-22.

Mogi, K. (1958): *Relations Between the Eruptions of Various Volcanoes and the Deformation of the Ground Surface Around Them*, Bull. Earthquake Res. Inst. Univ. Tokyo, 36, 99-134.

Murray, J.B., H. Rymer and C.A. Locke (2000): *Ground Deformation, Gravity, and Magnetics*, in: Sigurdsson, H. (Ed.): *Encyclopedia of Volcanoes*, Academic Press, 1121-1140.

NASA (2002): National Aeronautics and Space Administration website: http://science.msfc.nasa.gov/ssl/pad/solar/sunspots.htm.

Newhall, C.G. and S. Self (1982): *The Volcanic Explosivity Index (VEI): An Estimate of Explosive Magnitude for Historical Volcanism,* Journal of Geophysical Research, 87(C2), 1231-1238.

Newhall, C.G. and R.S. Punongbayan (Eds.) (1996): *Fire and Mud: Eruptions and Lahars of Mount Pinatubo, Philippines*, University of Washington Press, Seattle.

NGS (2002): U.S. National Geodetic Survey website: http://www.ngs.noaa.gov/ ANTCAL/.

Nichols, J., A. Hansen, T. Walter and P. Enge (1999): *Observations of Equatorial Scintillation Using GPS Receivers*, Proc. ION GPS-99, Nashville, Tennessee, 14-17 September, 1451-1460.

Nishi, K., H. Ono and H. Mori (1999): *Global Positioning System Measurements of Ground Deformation Caused by Magma Intrusion and Lava Discharge: The 1990-1995 Eruption at Unzendake Volcano, Kyushu, Japan*, Journal of Volcanology and Geothermal Research, 89, 23-34.

Nunnari, G. and G. Puglisi (1994): *The Global Positioning System as a Useful Technique for Measuring Ground Deformations in Volcanic Areas,* Journal of Volcanology and Geothermal Research, 61, 267-280.

Odijk, D. (2000): *Weighting Ionospheric Corrections to Improve Fast GPS Positioning Over Medium Distances,* Proc. ION GPS-2000, Salt Lake City, Utah, 19-22 September, 1113-1123.

Odijk, D., H. van der Marel and I. Song (2000): *Precise GPS Positioning by Applying Ionospheric Corrections from an Active Control Network*, GPS Solutions, 3(3), 49-57.

Ogaja, C. (2002a): *A Software Implementation of Multi-Sensor Data Analysis and GPS Integrity Assesment for Real-Time Monitoring Applications*, Proc. 2nd Symp. on Geodesy for Geotechnical and Structural Engineering, Berlin, Germany, 21-24 May, 27-37.

Ogaja, C. (2002b): *A Framework in Support of Structural Monitoring by Real Time Kinematic GPS and Mulitsensor Data*, PhD Dissertation, UNISURV S-71, School of Surveying and Spatial Information Systems, The University of New South Wales, Sydney, Australia, 191pp.

Ogaja, C., C. Rizos, J. Wang and J. Brownjohn (2001): *A Dynamic GPS System for On-line Structural Monitoring*, Proc. Int. Symp. on Kinematic Systems in Geodesy, Geomatics & Navigation (KIS 2001), Banff, Canada, 5-8 June, 290-297.

Omori, F. (1914): *The Sakura-jima Eruptions and Earthquakes*, Bulletin of the Imperial Earthquake Investigation Committee 8, Nos 1-6, 525.

Owen, S., P. Segall, M. Lisowski, A. Miklius, R. Denlinger and M. Sako (2000a): *Rapid Deformation of Kilauea Volcano: Global Positioning System Measurements between 1990 and 1996*, Journal of Geophysical Research, 105(B8), 18983-18998.

Owen, S., P. Segall, M. Lisowski, A. Miklius, M. Murray, M. Bevis and J. Foster (2000b): *January 30, 1997 Eruptive Event on Kilauea Volcano, Hawaii, as Monitored by Continuous GPS*, Geophysical Research Letters, 27(17), 2757-2760.

Page, E. (1954): *Continuous Inspection Schemes*, Biometrika, 41, 100-115.

Page, E. (1957): *Estimating the Point of Change in a Continuous Process*, Biometrika, 44, 248-252.

Parkinson, B.W. and J.J. Spilker (Eds.) (1996): *Global Positioning System: Theory and Applications Vol. 1+2*, Progress in Astronautics and Aeronautics, 163+164, American Institute of Aeronautics and Astronautics, Washington, 793pp + 643pp.

Puglisi, J., A. Bonforte and S.R. Maugeri (2001): *Ground Deformation Patterns on Mount Etna, 1992 to 1994, Inferred from GPS Data*, Bulletin of Volcanology, 62, 371-384.

Remondi, B.W. (1988): *Kinematic and Pseudo-Kinematic GPS*, Proc. ION GPS-88, Colorado Springs, Colorado, 19-23 September, 115-121.

Remondi, B.W. (1989): *Pseudo-Kinematic GPS Results using the Ambiguity Function Method*, Navigation, 38(1), 17-36.

Rizos, C. (1997): *Principles and Practice of GPS Surveying*, Monograph 17, School of Geomatic Engineering, The University of New South Wales, Sydney, Australia, 555pp.

Rizos, C., S. Han, C. Roberts, R. Galas and C. Reigber (1997a): *Low-Cost Densification of Permanent GPS Networks for Natural Hazard Mitigation*, Int. GEODYSSEA Symp., Penang, Malaysia, 14-18 April, 10pp.

Rizos, C., S. Han and C. Roberts (1997b): *Permanent Automatic Low-Cost GPS Deformation Monitoring Systems: Error Mitigation Strategies and System Architecture*, Proc. ION GPS-97, Kansas City, Missouri, 16-19 September, 909-917.

Rizos, C., S. Han, C. Roberts, X. Han, H.Z. Abidin, O.K. Suganda and A.D. Wirakusumah (2000): *Continuously Operating GPS-Based Volcano Deformation Monitoring in Indonesia: The Technical and Logistical Challenges*, in: Schwarz, K.-P. (Ed.): *Geodesy Beyond 2000: The Challenges of the First Decade*, Proc. IAG General Assembly, Birmingham, UK, 19-30 July 1999, Springer-Verlag, 361-366.

Rizos, C. and C. Satirapod (2001): *GPS with SA off: How Good Is It?*, Measure & Map, 12, 19-21.

Roberts, C. (2002): *A Continuous Low-Cost GPS-Based Volcano Deformation Monitoring System in Indonesia*, PhD Dissertation, UNISURV S-73, School of Surveying and Spatial Information Systems, The University of New South Wales, Sydney, Australia, 287pp.

Roberts, C. and C. Rizos (2001): *Mitigating Differential Troposphere Effects for GPS-Based Volcano Monitoring*, Proc. 5th Int. Symp. on Satellite Navigation Technology & Applications (SatNav), Canberra, Australia, 24-27 July, paper 38, 10pp.

Rocken, C., J.M. Johnson, J.J. Braun, H. Kawawa, Y. Hatanaka and T. Imakiire (2000): *Improving GPS Surveying with Modeled Ionospheric Corrections*, Geophysical Research Letters, 27(23), 3821-3824.

Rosen, P.A., S. Hensley, H.A. Zebker, F.H. Webb and E.J. Fielding (1996): *Surface Deformation and Coherence Measurements of Kilauea Volcano, Hawaii, from SIR-C Radar Interferometry*, Journal of Geophysical Research, 101, 23109-23125.

Rothacher, M. and L. Mervart (Eds.) (1996): *Bernese GPS Software Version 4.0*, Astronomical Institute, University of Berne, Switzerland, 418pp.

Saalfeld, A. (1999): *Generating Basis Sets of Double Differences*, Journal of Geodesy, 73, 291-297.

Santos, M.C., P. Vani◊ek and R.B. Langley (1997): *Effect of Mathematical Correlation on GPS Network Computation*, Journal of Surveying Engineering, 123(3), 101-112.

Schaer, S., G. Beutler, M. Rothacher and T.A. Springer (1996): *Daily Global Ionosphere Maps Based on GPS Carrier Phase Data Routinely Produced by the CODE Analysis Center*, Proc. IGS Analysis Centers Workshop, Silver Springs, Maryland, 19-21 March, 12pp.

SCIGN (2002): Southern California Integrated GPS Network (SCIGN) website: http://www.scign.org/.

Seeber, G. (1993): *Satellite Geodesy*, de Gruyter, Berlin, Germany, 531pp.

Shepherd, J.B., R.A. Herd, P. Jackson and R. Watts (1998): *Ground Deformation Measurements at the Sourfriere Hills Volcano, Montserrat: II: Rapid Static GPS Measurements June 1996 – June 1997*, Geophysical Research Letters, 25(18), 3413-3416.

Shimada, S., Y. Fujinawa, S. Sekiguchi, S. Ohmi, T. Eguchi and Y. Okada (1990): *Detection of a Volcanic Fracture Opening in Japan Using Global Positioning System Measurements*, Nature, 343, 631-633.

SI (2002): Smithsonian Institution website: http://www.volcano.si.edu/gvp/usgs/maps.htm.

Sigmundsson, F., P. Einarsson and R. Bilham (1992): *Magma Chamber Deflation Recorded by the Global Positioning System: The Hekla 1991 Eruption*, Geophysical Research Letters, 19(14), 1483-1486.

Simkin, T. and L. Siebert (1994): *Volcanoes of the World*, 2nd edition, Smithsonian Institution, Geoscience Press, Tucson, Arizona, 349pp.

Simkin, T. and L. Siebert (2000): *Earth's Volcanoes and Eruptions: An Overview*, in: Sigurdsson, H. (Ed.): *Encyclopedia of Volcanoes*, Academic Press, 249-261.

Skone, S.H. (2000): *Wide Area Ionosphere Modeling at Low Latitudes – Specifications and Limitations*, Proc. ION GPS-2000, Salt Lake City, Utah, 19-22 September, 643-652.

SOPAC (2002): Scripps Orbit and Permanent Array Center (SOPAC) website: http://sopac.ucsd.edu/cgi-bin/SCOUT.cgi.

Spilker, J.J. (1996): *Tropospheric Effects on GPS*, in: Parkinson, B.W. and J.J. Spilker (Eds.): *Global Positioning System: Theory and Applications Volume 1*, Progress in Astronautics and Aeronautics, 163, American Institute of Aeronautics and Astronautics, Washington, 517-546.

Stewart, M. and M. Tsakiri (2001): *The Application of GPS to Dam Surface Monitoring*, Journal of Geospatial Engineering, 3(1), 45-57.

Suganda, O.K. (1993): *Analysis of EDM Data in Association with the 1992 Eruption at Merapi Volcano, Indonesia,* Masters Thesis, Department of Geophysics, Kyoto University, Japan.

Swanson, D., T.J. Casadevall, D. Dzurisin, S.D. Malone, C.G. Newhall and C.S. Weaver (1983): *Predicting Eruptions at Mount St. Helens, June 1980 through December 1982*, Science, 221, 1369-1376.

Tazieff, H. and J.-C. Sabroux (Eds.) (1983): *Forcasting Volcanic Events*, Elsevier, Amsterdam-New York-Tokyo, 635pp.

Teunissen, P.J.G. (1995): *The Least-Squares Ambiguity Decorrelation Adjustment: A Method for Fast Integer Ambiguity Estimation*, Journal of Geodesy, 70, 65-82.

Tobita, M., M. Murakami, H. Nakagawa, H. Yarai and S. Fujiwara (2001): *3-D Surface Deformation of the 2000 Usu Eruption Measured by Matching of SAR Images*, Geophysical Research Letters, 28(22), 4291-4294.

Tsuji, H., Y. Hatanaka, T. Sagiya and M. Hashimoto (1995): *Coseismic Crustal Deformation from the 1994 Hokkaido-Toho-Oki Earthquake Monitored by a Nationwide Continuous GPS Array in Japan*, Geophysical Research Letters, 22(13), 1669-1672.

Turner, L. (2002): *What's Shaking? Earthquake Trials Test Networked RTK*, GPS World, 13(4), 16-22.

UNAM (2002): Universidad Nacional Autonoma de Mexico (UNAM) website: http://charro.igeofcu. unam.mx/L1/L1sys.html.

USCG (2003): U.S. Coast Guard Navigation Center website: http://www.navcen.uscg. gov/gps/status_and_outage_info.htm.

USGS (2002a): U.S. Geological Survey website: http://volcanoes.usgs.gov/About/ What/Monitor/monitor.html.

USGS (2002b): U.S. Geological Survey website: http://vulcan.wr.usgs.gov/Projects/Augustine/augustine_monitoring_intro.html.

USGS (2002c): U.S. Geological Survey website: http://volcanoes.usgs.gov/About/What/Monitor/Deformation/GPSKilauea.html.

USGS (2002d): U.S. Geological Survey website: http://volcanoes.usgs.gov/Hazards/What/hazards.html.

Vani◊ek, P. and E.J. Krakiwsky (1986): *Geodesy: The Concepts*, 2nd edition, North-Holland, Amsterdam, The Netherlands, 697pp.

VSI (2002a): Volcanological Survey of Indonesia website: http://www.vsi.dpe.go.id/volcanoes/papandayan/geninfo.html.

VSI (2002b): Volcanological Survey of Indonesia website: http://www.vsi.dpe.go.id/news/previous.htm.

Walker, R.A., B. Hannah and K. Kubik (1998): *Multipath Issues in GPS Monitoring*, Proc. Int. Workshop on Advances in GPS Deformation Monitoring, Curtin University of Technology, Perth, Australia, 24-25 September, 9pp.

Wanninger, L. (1993): *Effects of the Equatorial Ionosphere on GPS*, GPS World, 4(7), 48-54.

Wanninger, L. (1995): *Improved Ambiguity Resolution by Regional Differential Modelling of the Ionosphere*, Proc. ION GPS-95, Palm Springs, California, 12-15 September, 55-62.

Wanninger, L. (1999): *The Performance of Virtual Reference Stations in Active Geodetic GPS-Networks under Solar Maximum Conditions*, Proc. ION GPS-99, Nashville, Tennessee, 14-17 September, 1419-1427.

Watson, C. and R. Coleman (1998): *The Batman Bridge: Structural Monitoring Using GPS*, Proc. Int. Workshop on Advances in GPS Deformation Monitoring, Perth, Australia, 24-25 September, paper 16, 8pp.

Wells, D.E., N. Beck, D. Delikaraoglou, A. Kleusberg, E.J. Krakiwsky, G. Lachapelle, R.B. Langley, M. Nakiboglu, K.P. Schwarz, J.M. Tranquilla and P. Vani◊ek (1987): *Guide to GPS Positioning*, 2nd edition, Canadian GPS Associates, Fredericton, New Brunswick, Canada, 503pp.

Whitaker, C., M.A. Duffy and A. Chrzanowski (1998): *Design of a Continuous Monitoring Scheme for the Eastside Reservoir in Southern California*, Proc. XXI Int. Congress of FIG, Commission 6, Brighton, UK, 19-25 July, 329-344.

Williams, S., Y. Bock, P. Fang, Cecil H. and I.M. Green (1998): *Integrated Satellite Interferometry: Tropospheric Noise, GPS Estimates and Implications for Interferometric Synthetic Aperture Radar Products*, Journal of Geophysical Research, 103(B11), 27051-27068.

Wong, K.-Y., K.-L. Man and W.-Y. Chan (2001): *Monitoring Hong Kong's Bridges – Real-Time Kinematic Spans the Gap*, GPS World, 12(7), 10-18.

Wooden, W.H. (1985): *Navstar Global Positioning System: 1985*, Proc. of the First Int. Symp. on Precise Positioning with the Global Positioning System, Rockville, Maryland, 15-19 April, Vol. 1, 23-32.

Wu, J.T. (1994): *Weighted Differential GPS Method for Reducing Ephemeris Error*, Manuscripta Geodaetica, 20, 1-7.

Yuan, Y. and J. Ou (2001): *An Improvement to Ionospheric Delay Correction for Single-Frequency GPS Users – The APR-I Scheme*, Journal of Geodesy, 75(5/6), 331-336.

Zhang, Q.J. and K.P. Schwarz (1996): *Estimating Double Difference GPS Multipath under Kinematic Conditions*, Proc. IEEE Position Location & Navigation Symp. (PLANS'96), Atlanta, Georgia, 22-26 April, 285-291.

Appendix

THE NOVEMBER 2002 ERUPTION AT GUNUNG PAPANDAYAN

As this thesis was being completed, Gunung Papandayan spectacularly demonstrated the importance of continuously monitoring active volcanoes.

In October 2002 seismographs operated by the VSI recorded first deep and then shallow volcanic earthquakes and tremors beneath the volcano, indicating magma migration towards the surface. The number and intensity of these earthquakes increased during the next four weeks.

Then, on November 11, 2002, a *phreatic* eruption occurred from Kawah Baru (formed in 1942), which also triggered a landslide at the west wall of the old crater complex (see Fig. A.4). A phreatic eruption is an explosive volcanic eruption caused when water and heated volcanic rocks interact to produce a violent expulsion of steam and pulverised rocks; magma is not involved (Foxworthy & Hill, 1982). The material taken along the small rivers turned into *lahars* (volcanic mudflows consisting of a mixture of water-saturated ash, mud and debris), destroying several houses in nearby villages during the next few days.

The eruption progressed into a few sporadic magmatic eruptions and continuous ash eruptions up to 1km high. On November 15, at 6.30am local time, a large eruption occurred, producing dark-thick eruption ash, which was ejected up to 6km above the crater (Fig. A.1). Smaller ash and gas explosions continued during the following days.

On November 20 a large ash eruption occurred in the Nangklak crater as a directed lateral blast towards the northeast, reaching as far as 2km, stripping all trees along the inside of the horseshoe-shaped crater and leaving a deposit of blocks and smaller fragments of altered rocks covered by a wet 4-8cm thick layer of ash. In a radius of 500m from the crater, several trees were charred by the high temperature of the gas emitted (Fig. A.2). However, this eruption was not dominated by high temperatures, but rather by high-pressure steam and gas.

Fig. A.1: Eruption on 14 November 2002 (left), and the major eruption on 15 November 2002 that produced a 6km high ash cloud (right)

Fig. A.2: Tree blowdown at a radius of 400m from the crater due to the directed blast of Kawah Nangklak (left), and charred trees located 300m from the crater (right) (VSI, 2002b)

The following days were characterised by ash explosions of up to 600m high at Nangklak crater, while six other craters emitted white plumes as high as 200-400m. A more detailed description of the events can be found on the VSI website (VSI, 2002b). At the time of writing volcanic activity remains high (Fig. A.3).

Fig. A.3: Four eruption points in the horseshoe-shaped crater of Gunung Papandayan (left), and a close-up of Kawah Baru (right) (VSI, 2002b)

The eruptive activity changed the topography inside the horseshoe-shaped crater of Gunung Papandayan. New craters were formed, emitting large amounts of steam and ash, and a lot of material was transported over long distances inside the old crater complex. Most of the trees were flattened and the whole area was covered in a thick layer of wet ash. Fortunately the population of the nearby villages had been evacuated in time, so there were no human casualties. However, several tea plantations and rice fields were damaged by ashfall. At least 20 houses were destroyed by lahars along the Cileutik, Cibeureum and Cimanuk Rivers (Fig. A.4). The heavy rainfalls expected during the rainy season will certainly cause additional landslides and collapses of the very fragile volcanic landscape, and may result in further lahars threatening the surrounding villages.

Fig. A.4: Damage caused by ashfall at a tea plantation (left) and by a lahar in a nearby village (right) (VSI, 2002b)

Although there was no GPS equipment installed on the volcano during the eruption, the three ‘slave’ stations were affected significantly. Nangklak, which was located on the edge of the old crater wall, was completely destroyed by the November 11 landslide (Fig. A.5). At Kawah the radio antenna pole, all fence posts and the PVC tubing were demolished. Due to its location away from the main point of volcanic activity, the GPS station Bukit Maung survived the eruption relatively well, although one solar panel disappeared while the other (as well as the solar panel frame) was badly damaged. In both cases the monuments, plastic drums and GPS antenna poles remained unharmed. Figure A.6 shows the condition of these two stations on December 4, 2002. (The EDM reflector at Kawah was used by the VSI for ground deformation monitoring.)

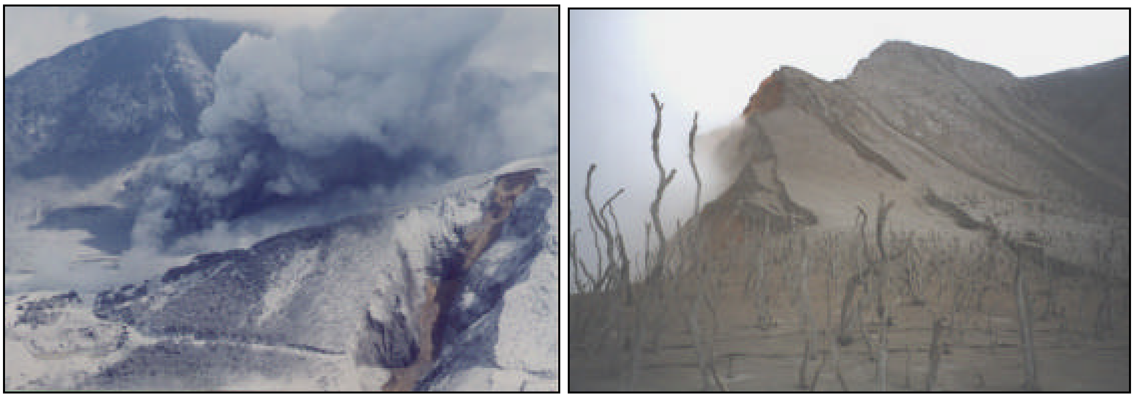

Fig. A.5: Landslide with ash emission from Kawah Baru in the background (left), and the former location of Nangklak (right)

Fig. A.6: Damage at Kawah (left) and Bukit Maung (right)

This eruption stresses the importance of monitoring active volcanoes in a continuous manner. After a very long period of silence it took Gunung Papandayan only four weeks to transform from a ‘lazing beauty’ into a ‘raging beast’. If it had been installed on the volcano at the time, the GPS volcano deformation monitoring system described in this thesis would certainly have picked up the signs of the impending eruption. In combination with the seismic measurements routinely carried out by the VSI, this would have created a more detailed picture of the volcano's behaviour leading up to the eruption. This information would also be very useful in helping to detect and analyse future periods of heightened activity, thereby contributing to volcanic hazard mitigation.

The advantage of operating a low-cost volcano deformation monitoring system is obvious. In the case of monitoring sites getting damaged or destroyed during an eruption, the relatively low cost of the equipment permits rapid repair and replacement.